Realization of current density imaging using ultra-low-field MRI

DISSERTATION

Zur Erlangung des akademischen Grades

Doktoringenieur (Dr.-Ing.)

vorgelegt der Fakultät für Informatik und Automatisierung

der Technischen Universität Ilmenau

von M. Sc. Peter Hömmen

vorgelegt am: 28.10.2020

Tag der wissenschaftlichen Aussprache: 15.06.2021

Gutacher: Univ.-Prof. Dr.-Ing. habil. Jens Haueisen

Prof. Dr. Lutz Trahms

Prof. Dr. Lauri Parkkonen

URN: urn:nbn:de:gbv:ilm1-2021000183

DOI: 10.22032/dbt.49343

Abstract

Reliable *in-vivo* current density imaging (CDI) of currents impressed to the human head would enable individual and spatially resolved conductivity mapping, much valuable for neuroimaging, neuromodulation, and possibly other applications. Magnetic resonance imaging (MRI) can be used for non-invasive CDI. However, conventional high-field MRI can only detect one component of the magnetic field $\boldsymbol{B}_\mathrm{J}$, associated with a current density $\boldsymbol{J}$, hampering the reconstruction of the $\boldsymbol{J}$-vector. MRI in the ultra-low-field (ULF) regime offers unique possibilities for CDI. The use of non-persistent magnets allows to switch all fields within a pulse sequence facilitating zero-field encoding, a sequence where all components of $\boldsymbol{B}_\mathrm{J}$ can be detected in the absence of the MRI fields. Prior to this work, zero-field encoding could not be realized using ULF MRI due to hardware limitations. Furthermore, the application of currents to a human is limited by safety regulations demanding a high signal-to-noise ratio (SNR).

This thesis describes the development and characterization of an ULF-MRI setup that enables *in-vivo* zero-field-encoded CDI. Key features are the defined manipulation of the magnetization's orientation, the ability to switch all MRI fields nearly instantaneously, and an outstanding sensitivity. Moreover, modifications to the sequence include a calibration procedure that decomposes phase effects due to $\boldsymbol{B}_\mathrm{J}$ from those due to the imaging fields. The method was successfully validated in phantom measurements. $\boldsymbol{B}_\mathrm{J}$ and $\boldsymbol{J}$ could be reconstructed reliably for 2 mA currents in different directions. This demonstration of CDI represents the first reconstruction of the full $\boldsymbol{J}$ vector based on a non-invasive method. However, the validation measurements also revealed a gap in SNR required to image the low current densities expected in an *in-vivo* application. The sensitivity of the method was further investigated by studying the relationship between the image SNR and the uncertainty of the $\boldsymbol{B}_\mathrm{J}$-reconstructions. The insights of the validation measurements and the sensitivity analysis prompted an upgrade of the setup, ensuring sufficient SNR for reliable $\boldsymbol{B}_\mathrm{J}$- and $\boldsymbol{J}$-reconstructions. MRI simulations using a realistic head model verified that the sensitivity of the final setup is sufficient to reconstruct the magnetic field $\boldsymbol{B}_\mathrm{J}$, associated with the current density $\boldsymbol{J}$, intra-cranially with an $\mathrm{SNR}[\boldsymbol{B}_\mathrm{J}] > 10$. Finally, two demonstration measurements with both, a realistic head phantom and a volunteer in an actual *in-vivo* application, were performed. With some room for improvement of the setup pending, the reconstructions agreed well with the simulations.

Zusammenfassung

In-vivo Stromdichtebildgebung (CDI) von Strömen, die dem menschlichen Kopf aufgeprägt werden, würde eine individuelle und ortsaufgelöste Abbildung der Gewebeleitfähigkeit ermöglichen. Diese ist für eine zuverlässige funktionale Bildgebung neuronaler Aktivität und für Neuromodulation von zentraler Bedeutung. Magnetresonanztomographie (MRT) ermöglicht CDI nicht-invasiv über die Erfassung des Magnetfeldes $\boldsymbol{B}_\mathrm{J}$, welches aus der Stromdichte $\boldsymbol{J}$ resultiert. Die konventionelle MRT im Hochfeld ist bei der Messung von $\boldsymbol{B}_\mathrm{J}$ auf eine Raumrichtung limitiert, was die Rekonstruktion des vollen Stromdichtevektors deutlich erschwert. MRT im Ultra-Niedrigfeld (ULF) eröffnet neue Möglichkeiten für CDI. Magnetfelder, erzeugt von Raumtemperaturspulen, können innerhalb einer Pulssequenz beliebig geschalten werden. Dies ermöglicht *zero-field encoding*, eine Sequenz bei der alle Komponenten von $\boldsymbol{B}_\mathrm{J}$ im Nullfeld detektiert werden. Bisher konnte *zero-field encoding* mittels ULF MRT nicht realisiert werden, vorwiegend wegen Schwierigkeiten beim definierten Schalten der Magnetfelder. Darüber hinaus ist ein hohes Signal-Rausch-Verhältnis (SNR) erforderlich, weil die an einen Menschen angelegten Ströme durch Sicherheitsvorschriften begrenzt sind.

Diese Arbeit beschreibt die Entwicklung und Charakterisierung eines ULF-MRT-Aufbaus, der *in-vivo* CDI ermöglicht. Hauptmerkmale sind die Möglichkeit zur definierten Manipulation der Magnetisierungsrichtung, die Fähigkeit alle MRT-Felder nahezu instantan zu schalten und eine sehr hohe Sensitivität. Außerdem wurde die Sequenz modifiziert, sodass durch ein Kalibrierverfahren Phasenverschiebungen, resultierend aus $\boldsymbol{B}_\mathrm{J}$, von den Effekten der Pulssequenz getrennt werden können. Die Methoden wurden erfolgreich in Phantommessungen validiert. $\boldsymbol{B}_\mathrm{J}$ und $\boldsymbol{J}$ wurden für 2 mA starke Ströme in verschiedenen Richtungen zuverlässig rekonstruiert. Diese Demonstration ist die erste Rekonstruktion des vollen $\boldsymbol{J}$-Vektors auf der Grundlage einer nicht-invasiven Methodik. Bei Stromdichteverteilungen im Bereich der *in-vivo* erwartbaren Größenordnungen zeigte sich jedoch eine weitere notwendige Verbesserung des SNR. Die Sensitivität wurde zusätzlich theoretisch untersucht, wobei eine Beziehung zwischen dem SNR im Bildbereich und der Unsicherheit der Feldrekonstruktionen zugrundegelegt wurde. Die Erkenntnisse aus den Phantommessungen und der Sensitivitätsanalyse veranlassten eine Weiterentwicklung des ULF-MRT-Aufbaus. In MRT-Simulationen mit einem realistischen Kopfmodell konnte gezeigt werden, dass die Empfindlichkeit des Systems ausreichend ist um $\boldsymbol{B}_\mathrm{J}$ intrakraniell mit einem $\mathrm{SNR}[\boldsymbol{B}_\mathrm{J}] > 10$ darzustellen. Schließlich wurden zwei Demonstrationsmessungen durchgeführt, eine mit einem realistischen Kopfphantom und die andere an einem Freiwilligen, in einer tatsächlichen *in-vivo* Anwendung. Unter Berücksichtigung weiterer möglicher Verbesserungen stimmten die Rekonstruktionen gut mit den Simulationen überein.

Acknowledgment

I express my sincere gratitude to all people who supported me during the time of this thesis.

First and foremost, my gratitude belongs to my mentor, Dr. Rainer Körber, who introduced me to the field of ULF MRI, and showed large and continuous interest in my work. Without his guidance, the goal of this project would not have been realized.

I would also like to express my sincere gratitude to Prof. Dr. Jens Haueisen for the scientific supervision of my research, and his thoughtful comments and recommendations on this dissertation.

I would like to thank Dr. Lutz Trahms, and Prof. Dr. Tobias Schäffter, who gave me the opportunity to join the biosignals department of PTB. Furthermore, I want to thank all members of the department. Particularly, I express my gratitude to the people in the ultra-low-field MRI group, Andrea Rahn, Jan-Hendrik Storm, Nora Höfner, and René Bösel, for their valuable contributions and mutual support. It was a pleasure working together.

Most of this work was conducted within the BREAKBEN project, which was funded by the European Union's Horizon 2020 FET-Open programme under grant agreement No 686865. As part of this project, Alexander Hunold, René Machts, and Prof. Dr. Jens Haueisen, from the Technische Universität Ilmenau, developed a head model and phantom. Many thanks to the Ilmenau group, who provided the phantom and contributed FEM simulations to this dissertation. Also as part of the BREAKBEN project, Antti J. Mäkinen from Aalto University visited our lab. This led to a fruitful collaboration far beyond Antti's time at PTB and I am very thankful for his contributions and enthusiasm.

Last but not least, I want to express my warmest thanks to my family, my mother, my sister, and my grandmothers, who always supported me. I am deeply thankful for my wife Christina, for her support, her understanding, and her kind words of encouragement when I needed them. Finally, I'm forever grateful for my father, who always believed in me.

Thank you!

Contents

Abbreviations

AC alternating current

aCDI adiabatic current density imaging

APF additional positive feedback

BMSR2 Berlin magnetically shielded Room 2

CDI current density imaging

CDII current density impedance imaging

CNC computerized numerical control

CSF cerebrospinal fluid

CT computer tomography

DC direct current

dc-SQUID dc superconducting quantum interference device

DFT discrete *Fourier* transform

DIFT discrete inverse *Fourier* transform

DTI diffusion tensor imaging

DT CDII diffusion tensor CDII

DT MREIT diffusion tensor MREIT

EEG electroencephalography

EIT electrical impedance tomography

EPT electric properties tomography

FEM finite element method

FPD free precession decay

FLL flux locked loop

FOV field of view

GM gray matter tissue

GMRES generalized minimal residual method

IC MREIT induced current MREIT

IGBT insulated gate bipolar transistor

lHe liquid helium

LINOD low-intrinsic-noise dewar

MEG magnetoencephalography

MOSFET metal oxide semiconductor field effect transistor

MR CDI magnetic resonance current density imaging

MREIT magnetic resonance electrical impedance tomography

MRI magnetic resonance imaging

NCI neuronal current imaging

NMR nuclear magnetic resonance

PTB Physikalisch-Technische Bundesanstalt

rf radio frequency

SD standard deviation

SNR signal-to-noise ratio

sps samples per second

SQUID superconducting quantum interference device

SRF spatial response function

tDCS transcranial direct current stimulation

TTL transistor-transistor logic

TVS transient voltage suppression

ULF ultra-low-field

WM white matter tissue

zCDI zero-field-encoded current density imaging

Symbols

2D two dimensional

3D three dimensional

a pick-up-loop radius

$\boldsymbol{a}$ unit vector describing instantaneous rotation

$\boldsymbol{a}^{\times}$ infinitesimal generator to $\boldsymbol{a}$

α shape parameter for *Tukey* window, or the temperature coefficient of pure copper

A_{S} effective pick-up-loop area

$\boldsymbol{A}^{\times}$ rotation generator matrix associated with rotation due to magnetic field $\boldsymbol{B}$

$\boldsymbol{A}_{\mathrm{J}}^{\times}$ rotation generator matrix associated with rotation due to magnetic field $\boldsymbol{B}_{\mathrm{J}}$

$\boldsymbol{b}$ unit vector to $\boldsymbol{B}$

$\boldsymbol{b}^{\times}$ infinitesimal generator to $\boldsymbol{b}$

β coupling coefficients converted to complex representation ($\beta = C_z + iC_y$, for a $\boldsymbol{B}_0$-field in $\boldsymbol{e}_x$ and a sensor sensitive in $\boldsymbol{e}_z$)

$\boldsymbol{B}$ magnetic flux density (often referred to by the term magnetic field)

$\hat{\boldsymbol{B}}$ reconstructed $\boldsymbol{B}$-field from zCDI

$\boldsymbol{B}_0$ MRI main field

$\boldsymbol{B}_1$ static or dynamic magnetic field used for $\pi/2$ spin flip

$\boldsymbol{B}_{\mathrm{B}}$ static or dynamic, unknown background field

$\boldsymbol{B}_{\mathrm{cal}}$ well known, homogeneous magnetic field, used for calibrating the reference phase ρ in the zCDI reconstruction

$\boldsymbol{B}_{\mathrm{ext}}$ magnetic field with known strength and direction, used in aCDI

$\boldsymbol{B}_{\mathrm{g}}$ guiding field oriented in $\boldsymbol{e}_x$, $\boldsymbol{e}_y$, or $\boldsymbol{e}_z$ to manipulate the orientation of the magnetization by adiabatic turn-off of the polarization field

$\boldsymbol{B}_{\mathrm{J}}$ magnetic field associated with a current density

$\boldsymbol{B}_{\mathrm{P}}$ magnetic polarization field

$\boldsymbol{B}_s$ magnetic field per unit current emanated by a receiver coil, used for principle of reciprocity

c $|\boldsymbol{B}|$-dependent scaling factor for standard deviation of $\hat{\boldsymbol{B}}_{\mathrm{J}}$

$\boldsymbol{C}$ matrix containing coupling coefficients to receiver coil

d dimension, distance, or depth

δ phase offset in zCDI due to imaging sequence

$\boldsymbol{D}$ electric flux density

Ds symbol for transient-voltage-suppression diode

$\boldsymbol{e}$ vector denoting basis direction ($\boldsymbol{e}_x = [1, 0, 0]$, $\boldsymbol{e}_y = [0, 1, 0]$, $\boldsymbol{e}_z = [0, 0, 1]$)

ϵ symmetric, complex Gaussian noise

ϵ_0 permittivity of free space

ϵ_r material permittivity

$\boldsymbol{E}$ electric field

E energy level

f frequency

f_L Larmor frequency

$g_{ij}(\boldsymbol{\Phi})$ $|\boldsymbol{B}|$-dependent scaling factor for noise standard deviation $\sigma_{\Phi_{ij}}$

γ gyromagnetic ratio

$\boldsymbol{G}_x$ magnetic field gradient $d\boldsymbol{B}_x/dx$ (frequency-encoding gradient, $\boldsymbol{B}_0$ is x-directional)

$\boldsymbol{G}_y$ magnetic field gradient $d\boldsymbol{B}_x/dy$ (phase-encoding gradient)

$|\boldsymbol{G}_{yi}|$ incremental $\boldsymbol{G}_y$-amplitude during k-space sampling

$\boldsymbol{G}_z$ magnetic field gradient $d\boldsymbol{B}_x/dz$ (phase-encoding gradient)

$|\boldsymbol{G}_{zi}|$ incremental $\boldsymbol{G}_z$-amplitude during k-space sampling

$\hbar$ Planck's constant over 2π

$\boldsymbol{H}$ magnetic field

i imaginary unit

I spin quantum number, or electric current

I_{P} polarization current

$\boldsymbol{I}$ nuclear spin, or identity matrix

I_b bias current in flux locked loop

I_C critical current

Im imaginary part

$\boldsymbol{J}$ total angular momentum, or current density

k Boltzmann's constant, or k-step in MRI

L_F SQUID feedback coil

L_{Fin} SQUID feedback coil in the input circuit, L_F and L_{Fin} form a feedback transformer

L_{i} SQUID input inductance

L_{in} SQUID input coil

L_{P} inductance of polarization coil

L_{S} pick-up loop inductance

L_{tot} total inductance of the input circuit comprising L_{S} and L_{i}

m_I magnetic quantum number

$\boldsymbol{\mu}$ magnetic moment of the nucleus

μ_0 permeability of free space

μ_r material permeability

M_{i} mutual inductance between the input coil and the SQUID

$\boldsymbol{M}$ magnetization vector

$\tilde{M}$ complex integral form of rotating magnetization ($\tilde{M} = M_z + iM_y$, for a $\boldsymbol{B}_0$-field in $\boldsymbol{e}_x$ and a sensor sensitive in $\boldsymbol{e}_z$)

$\boldsymbol{M}'$ magnetization vector in the rotating frame

$\boldsymbol{M}_0$ equilibrium magnetization

$\boldsymbol{M}_1$ magnetization after zero-field time with starting magnetization $\boldsymbol{M}_0\boldsymbol{e}_x$

$\boldsymbol{M}_2$ magnetization after zero-field time with starting magnetization $\boldsymbol{M}_0\boldsymbol{e}_y$

$\boldsymbol{M}_3$ magnetization after zero-field time with starting magnetization $\boldsymbol{M}_0\boldsymbol{e}_z$

N total number of spins (protons)

N_f number of *Fourier* terms

N_{vol} number of protons per unit volume

ΔN spin excess

ω Larmor angular frequency

$\omega_{\mathbf{J}}$ Larmor angular frequency associated with $\boldsymbol{B}_{\mathrm{J}}$ (specific case used for multiple $\boldsymbol{B}$-fields in aCDI)

p ratio between Larmor angular frequency ω and angular rate of magnetic field change ψ in aCDI

φ rotation angle associated with a spin precession

Φ magnetic flux

Φ_0 flux quantum

$\boldsymbol{\Phi}$ rotation matrix defining spin evolution during zero-field time in zCDI

ψ angular velocity of field change

$\boldsymbol{r}$ position vector

ρ electric charge, or phase in a non-referenced zCDI measurement

ρ_{cal} phase used to calibrate the reference phase in zCDI such that $\delta = \rho_{\mathrm{ref}} + \rho_{\mathrm{cal}}$

ρ_{ref} uncalibrated reference phase in zCDI

R ohmic resistor

$\mathrm{R_D}$ ohmic dummy resistor

$\boldsymbol{R}$ rotation matrix defining spin evolution in a magnetic field $\boldsymbol{B}$ (general)

$\boldsymbol{R}_1$ rotation of $\boldsymbol{M}_0$ to $|\boldsymbol{M}_0|\boldsymbol{e}_x$ in zCDI

$\boldsymbol{R}_2$ rotation of $\boldsymbol{M}_0$ to $|\boldsymbol{M}_0|\boldsymbol{e}_y$ in zCDI

$\boldsymbol{R}_3$ rotation of $\boldsymbol{M}_0$ to $|\boldsymbol{M}_0|\boldsymbol{e}_z$ in zCDI

$\boldsymbol{R}_{\mathrm{det}}$ rotation matrix defining spin evolution in $\boldsymbol{B}_0$-field

$\boldsymbol{R}_{\mathrm{G}}$ rotation matrix defining spin evolution during gradient time t_{G}

$\boldsymbol{R}_{\mathrm{E}}$ rotation matrix defining spin evolution during echo time t_{E}

Re real part

$s(t)$ signal time-course

S potential-free solid state relay

$S_{B,\mathrm{m}}$ total magnetic field noise density

$S_{B,\mathrm{amp}}$ equivalent magnetic field noise density from SQUID electronics

$S_{B,\mathrm{i}}$ SQUID-intrinsic equivalent magnetic field noise density

$S_{\Phi,\mathrm{i}}$ SQUID-intrinsic magnetic flux noise density

σ electric conductivity, or noise standard deviation

$\boldsymbol{\Sigma}$ diagonal matrix containing singular values

t time

t_{E} echo time

t_{G} gradient time

t_{M} time interval, where $\boldsymbol{B}_{\mathrm{P}}$ is turned off adiabatically into a guiding field $\boldsymbol{B}_{\mathrm{g}}$

t_{P} polarization time

Δt sampling period

τ zero-field time in zCDI

T temperature

T_C critical temperature for superconductivity

T_1 spin-lattice relaxation time

T_2 intrinsic spin-spin relaxation time

T_2' spin-spin relaxation time subject to external magnetic fields

T_2^* effective spin-spin relaxation time

u complex voxel value of reference in zCDI

U scalar potential

U_b bias voltage in flux locked loop

U_{Ds} breakthrough voltage of TVS diodes

$\boldsymbol{U}$ left singular matrix in singular-value decomposition

v complex voxel value in zCDI

v_{d} voxel side length

$\boldsymbol{V}$ right singular matrix in singular value decomposition

W_k width of k-space

Z gaussian noise

List of Figures

List of Tables

Chapter 1

Introduction

1.1 Motivation

The study of human brain activity is an ongoing field of research with the primary goal of understanding the brain function. This knowledge may help to find new ways of treating neurological and psychiatric disorders. Brain activity comprises electrochemical processes inside a highly complex neuronal network. Several non-invasive methods to record or image brain activity on a macroscopic level have been established in the last decades. They vary substantially in the underlying physical principles and have distinct benefits and drawbacks. None of these methods obtains both sufficient temporal and spatial resolution to fully understand and interpret the networks behind our actions and perceptions. Nevertheless, as we do know that "the brain [...] always behaves according to the known laws of physics" [1, p. 2], there is a great potential for improvement by gathering more profound and individual information on the electric properties of head tissue, most importantly conductivity.

Accurate and individual knowledge of tissue conductivity is difficult to obtain *in vivo* and non-invasively. Quantitative imaging of currents, impressed in the head via scalp electrodes, possibly enables to derive conductivity distributions inside the head due to a direct linear relation connecting electric field, conductivity, and current density. Consequently, much effort in research is spent to exploit this relation. Based on magnetic resonance imaging (MRI), methods have been established that pursue current density imaging (CDI) via the magnetic field $\boldsymbol{B}_\mathrm{J}$ associated with the current density $\boldsymbol{J}$. The spatial resolution of MRI machines in the order of millimeter promises conductivity mapping at discretization levels, much valuable for functional brain research. However, in high-field MRI, the magnetic field detection is restricted to the $\boldsymbol{B}_\mathrm{J}$-component parallel to the MRI main field, hampering a direct conversion from magnetic field to current density without additional information.

This thesis aims at non-invasive and *in-vivo* CDI using MRI in the ultra-low-field (ULF) regime. ULF MRI offers new possibilities for CDI as the relative difference between $\boldsymbol{B}_\mathrm{J}$ and the MRI main field is orders of magnitudes smaller, facilitating the detection of small phase changes in the MRI signal due to $\boldsymbol{B}_\mathrm{J}$. Furthermore, the use of non-persistent magnets allows to switch all MRI fields within a pulse sequence, potentially enabling the detection of all components of $\boldsymbol{B}_\mathrm{J}$. This flexibility is unique to MRI in the low-field regime, but comes at the cost of inferior signal-to-noise ratio (SNR) and lower spatial resolution due to the reduced magnetic field strength. Regarding CDI in the human brain, the SNR is most crucial because the strength of applied currents is limited by safety regulations to the low milliampère range [2, 3]. Furthermore, the experimental realization of specialized sequences for CDI in the ULF regime requires dedicated hardware.

So far, CDI could not be realized using ULF MRI due to hardware limitations of existing setups. Preliminary research and experimental studies, such as [4, 5], have not bridged feasibility investigation. Nevertheless, simulation studies imply that sequences designed for ULF MRI have the potential to yield the information required for a reconstruction of the full current density vector, without any additional information [6, 7]. Besides, continual advancements in sensor performance and noise reduction over the last two decades have lifted ULF MRI to a state where it is worth pursuing *in-vivo* CDI.

In this thesis, the focus will be on the demonstration of *in-vivo* CDI on the human head. Evidently, reliable and non-invasive CDI would impact other medical applications involving electric and magnetic stimulation. Beyond medicine, non-destructive battery diagnosis is a research topic of growing interest. MRI with it's unique capabilities for non-destructive CDI has recently been used for this purpose [8].

The remainder of this chapter expounds the potential of ULF MRI for non-invasive and individual CDI and thereby conductivity imaging. To this end, a short introduction on human brain anatomy and tissue conductivity is followed by a description of the value of accurate information on electric properties for methods in functional neuroimaging and neuromodulation. Subsequently, a short review on methods, mainly based on high-field MRI, that potentially enable a non-invasive acquisition of individual information on tissue conductivity is given, before the benefits and challenges of ULF MRI are presented. Finally, the aim and the outline of this thesis are set out in detail.

1.2 Human brain anatomy and tissue conductivity

The human brain forms the main part of the central nervous system. It is dominated by two types of cells, neurons, which are electrically excitable cells responsible for brain activity, and glia, providing support and electrical insulation for neurons, and maintain homeostasis. The structure of the brain is commonly divided into three parts: brainstem, cerebellum, and cerebrum. The biggest part is the cerebrum. It is wrinkled, forming gyri (bulges) and sulci (grooves), and consists of the left and right hemispheres. Each hemisphere is structured in lobes (compare figure 1.1), which yet can be sub-divided into distinct functional areas. The outer surface of the cerebrum is called the cortex, an up to 5 mm thick structure consisting of gray matter tissue (GM). The inner part is formed by white matter tissue (WM). Meninges, consisting of the three membranes pia mater, arachnoid mater, and dura mater, envelope the cerebrum (compare figure 1.2). Blood vessels pass through the meninges, where their distinct structures create a blood–brain barrier. Subarachnoid, the pia mater is suspended in cerebrospinal fluid (CSF). The system of meninges and CSF protect the brain from injury and mechanically damps shock motion. The skull (cranium) forms a rigid protective structure and gives the head and the face its unique shape. The skull is surrounded by the scalp, consisting of several layers, including periosteum, fat and fibrous tissue, connective tissue, and the skin.

In terms of electric properties, the relatively low conductive skull divides the head into three main compartments: intra-cranial, cranium, and extra-cranial. However, large variations especially for measured or estimated bulk skull conductivities are reported in the literature. Haueisen and Knösche [11] present compartment conductivity ratios scalp:skull:brain based on literature values ranging in the extreme cases from

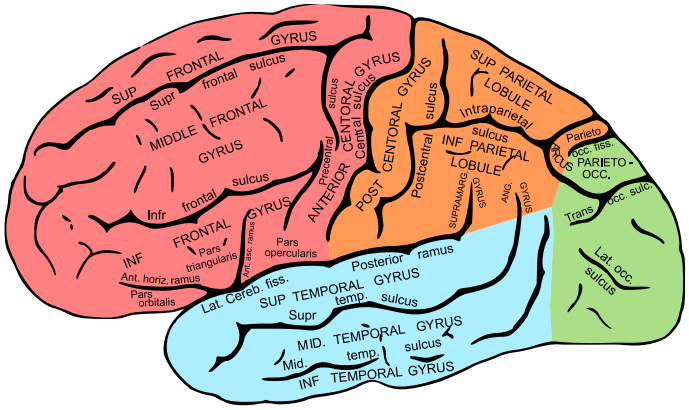

Figure 1.1: Lateral surface of left cerebral hemisphere of the human brain, viewed from the side. The figure is modified from [9]. The colors were added to the figure and show frontal lobe (red), parietal lobe (orange), temporal lobe (blue), and occipital lobe (green).

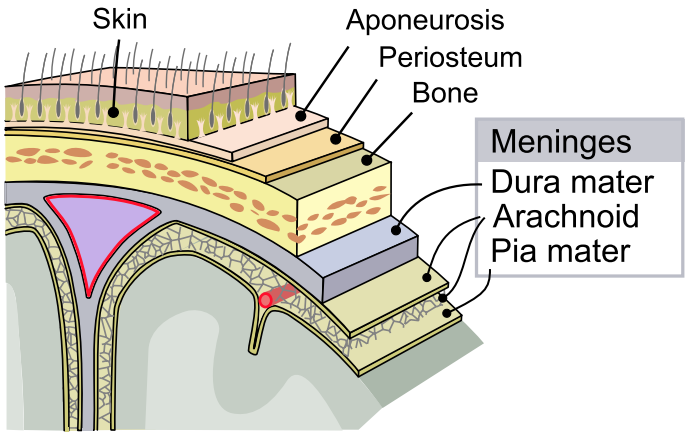

Figure 1.2: Meninges of the central nervous parts. Extracted from [10].

1:1/180:1 (based on [12][1]) to 1:1/8:1 (based on [13][2]). They state that recent studies indicate that a ratio of 1:1/80:1, often applied in modeling studies, might be too high. As these ratios do neither account for single tissue types, nor blood or CSF compartments, intra- and extra-cranial tissue is treated equally, which is reasonable in comparison to the large differences in skull conductivity. However, different intracranial tissues also show conductivity differences with a rough ratio WM:GM:CSF of 1:4:18, where the WM and GM values show large variations [11]. The conductivity value of CSF is most reliable and reported with approximately 0.179 S/m [14]. Conductivity of the dura layer is reported approximately 0.04 times that of CSF [15, 16]. Modeling studies often simplify the space between skull and GM by only one CSF compartment, which may be inaccurate [16, 17]. Figure 1.3 sketches such a model qualitatively, based on the ratios presented above.

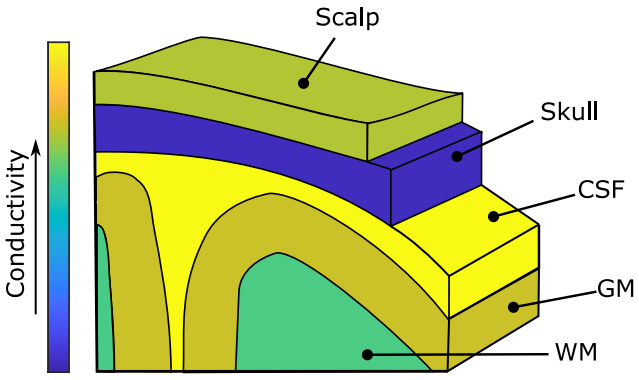

Figure 1.3: Qualitative visualization of bulk tissue conductivity

[1] In [12] skull conductivities were estimated in a calibration procedure using somatosensory evoked potentials and fields.

[2] In [13] skull conductivities were measured from surgically removed skull using a four-point electrode method.

1.3 The relevance of tissue conductivity for human brain research

Individual knowledge on electric properties of head tissue is of utmost importance for neuroimaging and neuromodulation techniques that rely on accurate models of the volume conductor.

Electromagnetic neuroimaging represents the only method that measures human brain activity directly. Net effects of ionic currents flowing through the dendrites of neurons are monitored either via the resulting electric field using scalp electrodes in electroencephalography (EEG) or via the emanated magnetic field using sensitive magnetic field sensors in magnetoencephalography (MEG) [18]. Thus, EEG and MEG measurements reflect weighted superposition of brain activity, depending on tissue geometries and sensor arrangement [1]. Both methods are characterized by real-time signal acquisition and a sub-millisecond temporal resolution. Spatial source localization requires to solve an inverse problem based on a proposed transfer function between a source model and the sensor array. This transfer function is commonly denoted as the bioelectromagnetic forward problem and most accurate when geometries and electromagnetic properties of head tissue, most importantly conductivity, are included [11]. The inverse problem is ill-posed making source localization error-prone and ambiguous yielding a high localization uncertainty of several millimeters [1, 18].

Neuromodulation on the other hand aims at manipulation of brain function, for example, by suppression or enhancement of neuron excitability. Methods such as transcranial electric stimulation, or transcranial magnetic stimulation are available to influence or evoke electric brain activity directly, without peripheral nerve stimulation. The most popular variant is transcranial direct current stimulation (tDCS), which can result in long-lasting changes in the excitability of the human cortex [19, 20]. This feature makes tDCS feasible for the treatment of numerous psychiatric diseases, e.g., depression, schizophrenia, addiction, and dementia [21, 22, and references therein], as well as for the treatment of several neurological disorders, e.g., epilepsy, post-stroke motor rehabilitation, Alzheimer's disease, and Parkinson's disease [23, and references therein]. Besides number, position, and shape of the stimulation electrodes, anatomical characteristics such as tissue thickness and electrical conductivity have a significant influence on the resulting electric field distribution and thereby the propagation and effect of the impressed current. To target a specific brain region, models that enable computational optimization of the stimulation parameters are utilized (e.g., [24, 25, 26, 27, 28]). Therefore, solving a bioelectromagnetic forward problem similar to electromagnetic neuroimaging is required.

In conclusion, individual information on tissue conductivity is key to electromagnetic neuroimaging and neuromodulation techniques. However, these are difficult to obtain *in vivo* and non-invasively. Besides, tissue conductivity is frequency-dependent, and robust values for the relevant low-frequency range are scarce. Direction dependent conductivity (anisotropy), as found for WM tissue, is even harder to quantify *in vivo*. Therefore, most studies employ scalar bulk conductivity values based on *in-vitro* samples of animal and human tissue. Literature values show large variations based on the utilized measurement method and procedure. Gabriel et al. [29] give an extensive literature review on tissue conductivity over a wide frequency range up to 1 MHz. In a recent publication by McCann et al. [30], 3121 reports on conductivity were identified, where 56 were taken into closer consideration for data analysis. Due to the large observed variations, they emphasize, that individually acquired conductivity estimates are necessary for accurate volume conductor models. Haueisen and Knösche [11] assess reported literature values and techniques by their relevance for neuroimaging. They point out that extensive volume conductor models based on finite element method (FEM) should incorporate inhomogeneity and anisotropy. Further, if these are not available, there might be no superior results by the elaborate discretization in FEM and Boundary Element Methods can be utilized. The relevance of anisotropy in tDCS remains controversial [28, 31, 32, 33].

1.4 State of the art in *in-vivo* electric properties estimation

Several methods have been presented, that pursue non-invasive and individual estimation of electric properties, such as conductivity. Most, but not all, use spatially encoded information acquired by MRI. They can be categorized as direct or indirect methods, and by the frequency range at which the properties are determined. In the following, the most relevant are explained briefly, considering only methods that are non-invasive and potentially applicable *in vivo*.

1.4.1 Electrical impedance tomography

Electrical impedance tomography (EIT) is the only method discussed in this thesis that is not supported by MRI. It provides dynamic measures of tissue conductivity accessible by an inverse reconstruction based on potential measurements (e.g., [34]). Therefore, multiple surface electrodes are positioned on the head. Resistive tissue structures forming the current path yield a unique voltage pattern for each stimula-

tion configuration. EIT has the benefit of relatively low-cost hardware and potentially easy implementation in a clinical or non-clinical environment. However, the method is suffering from low spatial resolution, a low sensitivity in deeper brain areas, and the necessity to solve an ill-posed inverse problem.

1.4.2 High-field-MRI-based methods

MRI in the high-field regime at MHz Larmor frequencies can be used for non-invasive CDI [35, 36, 37, 38]. In magnetic resonance current density imaging (MR CDI), the local magnetic fields $\boldsymbol{B}_\mathrm{J}$ generated by a current density $\boldsymbol{J}$ result in a measurable phase change of the MR signal. The safe application of currents to the head is limited to a few milliampère [2, 3], corresponding to magnetic fields in the nanotesla range. As the MRI main field $\boldsymbol{B}_0$ is approximately 7–9 orders of magnitudes stronger than $\boldsymbol{B}_\mathrm{J}$, MR CDI is insensitive to magnetic field components perpendicular to $\boldsymbol{B}_0$. Later in this thesis, it will be shown that a full 3D-acquisition of the $\boldsymbol{B}_\mathrm{J}$-vector is required for $\boldsymbol{J}$-reconstruction. To image all components of $\boldsymbol{B}_\mathrm{J}$, a rotation of the subject inside the scanner is necessary. Making use of a resonance phenomenon by alternating current (AC) stimulation at the MHz Larmor frequency partly relaxes the constraint of only one sensitive direction [39, 40]. However, not all components of $\boldsymbol{J}$ can be recovered and the estimates are acquired at frequencies far beyond relevance for functional physiological processes.

Although stand-alone applications for CDI exist, conductivity estimation based on imaged current density distributions represents a strong objective in many studies from the early stages of CDI [41, 42, 43]. Extensions to MR CDI are often referred to by magnetic resonance electrical impedance tomography (MREIT). The idea is that current pathways obtained by MR CDI could be used *a priori* to stabilize the ill-posed inverse problem in EIT. Another terminology was given by Hasanov et al. [44], who coined the expression current density impedance imaging (CDII) and intended it for methods that estimate conductivity based on current density without the use of boundary voltage measurements as in EIT. Although this seems reasonable, most studies use the terminology MREIT regardless of the reconstruction approach. Methods, that Hasanov et al. refer to as CDII, estimate the conductivity based on $\boldsymbol{J}$. Therefore, all components of $\boldsymbol{B}_\mathrm{J}$ are required. The necessary subject rotation, however, is impracticable during an *in-vivo* application and would further cause misalignment problems [45]. Additionally, unique solutions require current injection from several directions such that the current density at every point in the imaging slice is not collinear for at least two of the injec-

tion currents [46]. Absolute conductivity determination requires the incorporation of at least one potential measurement [46, 47], the algorithms in [48] and [49] need even more. Due to the problem of only one sensitive direction in the MR measurements, mathematical frameworks have been developed that pursue the estimation of 3D conductivity images based on only one component of $\boldsymbol{B}_\mathrm{J}$ [50, 51, 52, 53]. However, the requirement of current impression from multiple directions remains. According to [44], the solutions might not be unique and the computational effort is high.

Induced current MREIT (IC MREIT), presented by Özparlak and Ider [54], can be considered as a modification to MREIT and CDII. Instead of impressing currents via scalp electrodes, eddy currents are induced via excitation coils driven at kHz frequencies. In theory, the method manages to reconstruct absolute conductivity values without additional potential measurements, due to a change in the electromagnetic inverse problem [55]. However, an implementation of the method in an MR environment is difficult with regard to the strong, pulsed magnetic field gradients. The usage of the available MRI gradient coils for eddy current induction reduces the instrumental effort. However, simulation studies revealed that the acquired signals are below the noise level, and sufficient sensitivity for *in-vivo* conductivity reconstruction cannot be achieved [56].

Electric properties tomography (EPT) [57, 58] uses a similar concept as IC MREIT, although the frequency range at which electric properties are obtained is much higher. Eddy currents due to the radio frequency (rf) field ($\boldsymbol{B}_1$) cause field distortions. In MRI, these distortions result in false estimations of quantitative MR parameters, usually taken care of by $\boldsymbol{B}_1$ mapping [59]. The eddy current distributions and thereby the $\boldsymbol{B}_1$ distortions are highly dependent on permittivity and conductivity of the body tissue. In EPT, $\boldsymbol{B}_1$ mapping forms the basis for the estimation of electric properties [60]. However, the values are obtained at frequencies in the MHz range, far beyond relevance for functional processes or tDCS.

Diffusion tensor imaging (DTI) [61, 62] measures the effect of molecular movement on the echo intensity in MRI. Although diffusion of water molecules and conductivity are physical independent tissue properties, an effective-medium approach showed that diffusion tensors and conductivity tensors share the same eigenvectors [63]. Hence, DTI can be considered an indirect method that estimates conductivity. However, the relation between diffusion of water molecules and ion mobility is unclear [64] and correlation seems to be originating in the cellular structures [65]. Off note, by means of the tensor information on diffusion, DTI can be used to derive conductivity anisotropy [63, 66].

Recent developments pursue to gain more information based on a combination of the before described methods. An approach called diffusion tensor CDII (DT CDII) was proposed by Ma et al. [67] in 2013, combining anisotropy information from DTI with conductivity reconstructions from CDII. One year later, a different approach was presented by Kwon et al. [68], combing DTI with MREIT. Using this technique, called diffusion tensor MREIT (DT MREIT), Chauhan et al. [69] recently reconstructed *in-vivo* acquired cross-sectional conductivity maps at a frequency of approximately 10 Hz.

In conclusion, all the here presented methods suffer from distinct disadvantages regarding their potential value for neuroimaging and neuromodulation. EIT relies on an ill-posed inverse problem. The reconstructions in MR CDI and MREIT are more stable, but the methods are impracticable due to a necessary rotation of the subject inside the scanner. EPT provides reliable conductivity estimates, but the frequency range at which the values are obtained is far beyond physiological processes. Finally, the diffusivity obtained by DTI can be related to conductivity and yield even anisotropy, but the correlation between the two measures is not clearly defined.

1.4.3 Methods using ultra-low-field MRI

Superconducting quantum interference device (SQUID)-based ULF MRI, working at microtesla fields (kHz Larmor frequencies) offers new possibilities for CDI. The relative difference between $\boldsymbol{B}_\mathrm{J}$ and the MRI main field is orders of magnitude smaller, facilitating the detection of small phase changes in the MRI signal. Furthermore, not only direct current (DC) impression, but also the exploitation of AC currents at the Larmor frequency have the potential to provide conductivity estimates in the relevant frequency range. Last but not least, the use of non-persistent magnets gives a new flexibility in sequence design, potentially enabling to image the full vector of $\boldsymbol{B}_\mathrm{J}$ without the need of subject rotation. ULF MRI is comparably new and preliminary research on MR CDI is scarce. Nevertheless, methods in the ultra-low-field regime have been suggested for AC [4, 5] and DC [4, 6, 7] impression.

Lee et al. [5] measured the influence of impressed AC currents on 2D spin density and phase images in phantom experiments. The current was applied at the Larmor frequency during a defined time interval with only the main field of 34.3 μT present. They report a lack of sensitivity in the direction of the main field, which could possibly be overcome when expanding the experiment to 3D. Quantitative reconstruction of current density could not be achieved. Kraus et al. [4, p. 218 ff.] showed influences of DC currents on phase images in phantoms. In comparison to Lee et al., the current was applied during phase encoding. The resulting DC magnetic field, superimposing

the MRI fields, caused a phase shift in the MR signal. Similar to high-field MR CDI, the sensitivity is limited to the main field direction. They propose an additional AC current to employ resonant absorption for the detection of the orthogonal components. Both, Lee et al. [5] and Kraus et al. [4], refer to their work as a step towards ULF MREIT. Regarding that, both approaches have not yet passed the status of preliminary experiments and it was not specified how the methods could be utilized to extract conductivity information. Nevertheless, both experiments demonstrated qualitatively that the effect of impressed currents in the milliampére range can be detected by ULF MRI.

In 2014, Vesanen et al. [6] and Nieminen et al. [7] presented two sequences for ULF MR CDI. These works were the first aiming at the quantitative detection of all components of the magnetic field associated with the current density with a pulsed ULF-MRI sequence, and without subject rotation. Both sequences were validated in simulations, but could not be demonstrated experimentally, due to hardware limitations. The two approaches are explained in more detail in chapter 3, including an evaluation of their feasibility for in-vivo applications.

Despite the promising benefits regarding CDI, the small magnetization poses restrictions unique to ULF MRI. A pre-polarization pulse in the order of several tens of millitesla is essential to gain sufficient SNR [70]. Besides, the method requires shielding from the earth's magnetic field and environmental noise, in most cases achieved by the utilization of magnetically shielded rooms.

1.5 Scope of the thesis

It was described in the previous section, that MRI in the ULF regime offers unique possibilities for CDI. Currently, it is the only modality that potentially enables imaging all components of the current density vector. However, so far, CDI could not be realized due to hardware limitations of the existing setups.

This thesis describes the experimental realization of CDI using ULF MRI. To this end, an appropriate sequence is chosen based on previous work by Vesanen et al. [6] and Nieminen et al. [7]. The development of an ULF-MRI scanner, that meets the requirements for the sequence, is described. Phantom measurements are used to validate the conducted methods. Furthermore, an investigation of the theoretical sensitivity is presented, prompting an upgrade of the setup with regard to the necessary SNR in an *in-vivo* application. Finally, measurements in phantom, and *in vivo* are shown that demonstrate the achievements.

Conductivity estimation, which is the primary motivation for the work on CDI, is explicitly not covered in this thesis. Nevertheless, this work will pave the way for *in-vivo* and individual conductivity mapping by demonstrating CDI.

1.6 Outline of the thesis

Following this Introduction, Chapter 2 provides the fundamentals to the methods conducted in this work. First, the physical relations between current density and magnetic field are reviewed, before the basics of nuclear magnetic resonance are briefly described. Subsequently, spatial encoding for MRI is explained, followed by an overview of the distinct benefits and requirements for MRI at ultra-low fields.

The third chapter focuses on sequences for CDI using ULF MRI. Based on the requirements for an *in vivo* application, available sequences are assessed regarding feasibility and practicability. Necessary modifications are identified, before the approach that is pursued in this thesis is explained in detail.

Chapter 4 gives a description of the hardware developments necessary to perform CDI. Starting with a comprehensive review on previous developments and the status of the ULF-MRI facilities at the Physikalisch-Technische Bundesanstalt (PTB), the specialized hardware for the CDI sequence is explained. This includes the generation of all MRI fields, as well as the development a custom-built ultra-low-noise magnetic field sensor based on a SQUID. The possible implementation of an *in-vivo* application represents a strong focus during all development stages.

A proof of principle is presented in chapter 5. CDI measurements in phantoms and structural *in-vivo* imaging of a human head demonstrate the feasibility of the method and provide first insights into the performance of the setup.

An in-depth analysis of the theoretical sensitivity of the new method is given in chapter 6. A linearization of the reconstruction algorithm gives an approximate relation between image SNR and reconstruction uncertainty. Furthermore, Monte-Carlo simulations are employed to quantify effects of the non-linearity.

Chapter 7 describes the efforts towards an *in-vivo* application of the method. Based on the findings in the chapters 5 and 6, the system is upgraded for improved performance. Accompanied by simulations using a realistic three-compartment head model, measurements in phantom and *in vivo* are utilized to demonstrate the feasibility of the final setup.

Finally, the achievements of this thesis are summarized and discussed with regards to potential future developments in chapter 8.

1.7 Related publications of the author

This thesis is based in part on the publications listed below. The entries are arranged chronologically.

[71] — J.-H. Storm, P. Hömmen, D. Drung, and R. Körber, An ultra-sensitive and wideband magnetometer based on a superconducting quantum interference device, Applied Physics Letters, vol. 110, p. 072603, feb 2017.
The author's contribution to [71] includes development of the novel methods, experiments, the data acquisition and evaluation, and reviewing the manuscript.

[72] — P. Hömmen, J.-H. Storm, N. Höfner, and R. Körber, Demonstration of full tensor current density imaging using ultra-low field MRI, Magnetic Resonance Imaging, vol. 60, pp. 137–144, jul 2019.
The author's contribution to [72] includes reviewing the literature, development of the novel methods, experiments, the data acquisition and evaluation, discussion of the results, visualization of the methods and results, writing the manuscript, and revising the manuscript based on annotations and suggestions of the co-authors.

[73] — R. Körber, O. Kieler, P. Hömmen, N. Höfner, and J.-H. Storm, Ultra-sensitive SQUID systems for applications in biomagnetism and ultra-low field MRI, in 2019 IEEE International Superconductive Electronics Conference (ISEC), pp. 1–3, 2019.
The author's contribution to [73] includes parts of the experiments and reviewing the manuscript.

[74] — J.-H. Storm, P. Hömmen, N. Höfner, and R. Körber, Detection of body noise with an ultra-sensitive SQUID system, Measurement Science and Technology, vol. 30, p. 125103, sep 2019.
The author's contribution to [74] includes development of the novel methods, experiments, the data acquisition and evaluation, and reviewing the manuscript.

[75] — P. Hömmen*, A. J. Mäkinen*, A. Hunold, R. Machts, J. Haueisen, K. C. J. Zevenhoven, R. J. Ilmoniemi, and R. Körber, Evaluating the performance of ultra-low-field MRI for in-vivo 3D current density imaging of the human head, Frontiers in Physics, vol. 8, p. 105, apr 2020.
**Both authors contributed equally to [75], including reviewing the literature, development of the novel methods, experiments, the data acquisition and evaluation, discussion of the results, visualization of the methods and results, writing the manuscript, and revising the manuscript based on annotations and suggestions of the co-authors.*

Chapter 2

Fundamentals

The methods applied in this thesis require multi-disciplinary fundamental background. This chapter briefly describes the physical principles behind the used procedures. For more detailed information, I refer to the literature that is referenced at the beginning of each section.

2.1 Impressed currents

This section gives an introduction to the electrodynamics behind MR-based CDI. The physical principles are presented in many textbooks, e.g., [76], which was consulted for this section.

The impression of currents to the head is realized through scalp electrodes connected to a current source and closely related to the field of transcranial electric stimulation. A potential difference ΔU between anode and cathode causes a current flow. The current density distribution $\boldsymbol{J}$ depends on the geometry and electric properties of the underlying medium following the electric field. In MR CDI, the current density distribution is examined via the associated magnetic field $\boldsymbol{B}_{\mathrm{J}}$.

In classical electrodynamics, the electric and magnetic field, $\boldsymbol{E}$ and $\boldsymbol{H}$ respectively, as well as the electric and magnetic flux densities, $\boldsymbol{D}$ and $\boldsymbol{B}$ respectively, are linked in *Maxwell's equations*. In differential form, these are:
1. *Gauss's law*: charge ρ is a source of an electric field

$$\mathrm{div}\boldsymbol{D} = \nabla \cdot \boldsymbol{D} = \rho, \tag{2.1}$$

2. *Gauss's law for magnetism*: there are no magnetic monopoles

$$\mathrm{div}\boldsymbol{B} = \nabla \cdot \boldsymbol{B} = 0, \tag{2.2}$$

3. *Faraday's law of induction*: A changing magnetic field induces an electric field

$$\mathrm{rot}\boldsymbol{E} = \nabla \times \boldsymbol{E} = -\frac{d\boldsymbol{B}}{dt}, \text{ and} \tag{2.3}$$

4. *Ampere's law (with Maxwell's extension of electric flux)*: Current density and changing electric flux densities both generate magnetic fields

$$\mathrm{rot}\boldsymbol{H} = \nabla \times \boldsymbol{H} = \frac{d\boldsymbol{D}}{dt} + \boldsymbol{J}. \tag{2.4}$$

Further, a set of material properties link electric field and electric flux density, current density and electric field, and magnetic field and magnetic flux density:

$$\boldsymbol{D} = \epsilon_0\epsilon_r\boldsymbol{E} = \epsilon\boldsymbol{E}, \tag{2.5}$$

$$\boldsymbol{J} = \sigma\boldsymbol{E}, \tag{2.6}$$

$$\boldsymbol{B} = \mu_0\mu_r\boldsymbol{H} = \mu\boldsymbol{H}. \tag{2.7}$$

Here, ϵ_r and μ_r represent material-specific values for permittivity and permeability, respectively, and ϵ_0 and μ_0 denote the values for free-space. The electric conductivity is given by σ.

For the low-frequency case, equations (2.1–2.4) can be reduced to a quasi-static form, where all time variant terms can be neglected. Now, *Faraday's law* (2.3) simply states that the electric field is curl-free

$$\nabla \times \boldsymbol{E} = 0. \tag{2.8}$$

Taking into account (2.5) and assuming permittivity and charge density are not functions of position $\boldsymbol{r}$ ($\epsilon_r(\boldsymbol{r}) = \epsilon_r$, $\rho(\boldsymbol{r}) = \rho$), *Gauss's law* can be rewritten as:

$$\nabla \cdot \boldsymbol{E} = \frac{\rho}{\epsilon_0\epsilon_r}. \tag{2.9}$$

Further, knowing that any vector field can be described by curl and divergence, and that the divergence is equivalent to the gradient of a scalar potential, the electric field can be described by:

$$\boldsymbol{E} = -\mathrm{grad}U = -\nabla U, \tag{2.10}$$

where U is the position dependent scalar potential.
The combination of (2.9) and (2.10) finally yields *Poisson's equation*

$$\nabla^2 U = -\frac{\rho}{\epsilon_0\epsilon_r}, \tag{2.11}$$

which forms the basis for the solution to the boundary-constraint, discrete, electrostatic problem. A practical requirement to a numerical solution to *Poisson's equation* is the

formulation of boundary constraints usually employed by a combination of *Dirichlet* and *Neumann conditions*. The *Dirichlet condition* forces a fixed potential at the boundary of a discrete grid, whereas the *Neumann condition* forces a fixed gradient of the potential in the direction normal to the boundary. In the case of tDCS, the electrode surfaces would be characterized by a fixed voltage using *Dirichlet condition* and the head surface fulfills *Neumann condition*. Loosely spoken, this defines the source of the electric field at the electrodes and bounds the field to the head volume.

As mentioned before, in MR-based CDI the magnetic field $\boldsymbol{B}_\mathrm{J}$ due to $\boldsymbol{J}$ is measured. Since the quasi-static approach to the electromagnetic problem fulfills the original version of *Ampere's law* and under the assumption that the material is non-magnetic ($\mu_r = 1$), (2.4) can be rewritten as

$$\frac{1}{\mu_0}\nabla \times \boldsymbol{B}_\mathrm{J} = \boldsymbol{J}. \tag{2.12}$$

Having $\boldsymbol{J}$, it should be possible to extract quantitative information on tissue-dependent conductivities using the formalism in (2.6). However, it should be kept in mind that using a current source does not result in a fixed potential at the electrodes, but rather in a fixed current flow through the electrode area. As mentioned before, this thesis focuses on the demonstration of CDI and does not further evaluate methods to extract conductivities from the obtained data.

2.2 Nuclear magnetic resonance

Quantum mechanical descriptions can gain a thorough understanding of nuclear magnetic resonance (NMR) principles. More often, phenomenological approaches are presented, as employed in this thesis. For a deeper understanding of the theory, I refer the reader to e.g., [77]. The matrix representation of spin evolution in section 2.2.2 is based on the notations in [4].

2.2.1 Nuclear spin, magnetic moment, and magnetization

Several atomic nuclei and elementary particles possess a fundamental quantum mechanical property called spin angular momentum. The total angular momentum $\hbar\boldsymbol{I}$[1] is connected to the magnetic moment of the nucleus $\boldsymbol{\mu}$ by

$$\boldsymbol{\mu} = \gamma\hbar\boldsymbol{I}, \tag{2.13}$$

[1] In this section $\boldsymbol{I}$ and I denote the nuclear spin and the spin quantum number, respectively. Please note that in the rest of this thesis I represents electric current, or the identity matrix ($\boldsymbol{I}$).

where γ is the isotope-specific gyromagnetic ratio and $\hbar$ is Planck's constant over 2π. It is characteristic, that $\hbar\boldsymbol{I}$ is quantized in discrete values, where the spin quantum number I can take either integer or half integer values depending on the spin system. The angular momentum $\hbar\boldsymbol{I}$ is connected with I by

$$\boldsymbol{I}^2 = I(I+1). \tag{2.14}$$

Exposed to a magnetic field $|\boldsymbol{B}|\boldsymbol{e}_z$, $\hbar\boldsymbol{I}$ is quantized in the z-direction and given in terms of the magnetic quantum number $m_I = -I, -I+1, ..., I-1, I$:

$$\boldsymbol{I}_z = m_I. \tag{2.15}$$

In a magnetic field $\boldsymbol{B}$, each state possesses a specific energy level E associated with the magnetic moment

$$E = -\boldsymbol{\mu}\boldsymbol{B} = -m_I\hbar\gamma|\boldsymbol{B}| = -\hbar m_I\omega, \tag{2.16}$$

where $\omega = \gamma|\boldsymbol{B}|$ is the Larmor angular frequency associated with $|\boldsymbol{B}|$. In medical imaging ^{1}H nuclei are usually employed, where γ is $26.7513 \cdot 10^{-7}$ rad s^{-1} T^{-1}, corresponding to 42.576 MHz T^{-1}.

^{1}H atoms are characterized by spin-one-half ($I = 1/2$). Here, the energy splits into two states so that m_I can take values of $+1/2$ or $-1/2$, corresponding to spin alignment parallel and anti-parallel to $\boldsymbol{B}$, respectively. This is called Zeeman splitting and illustrated in figure 2.1. According to equation (2.16), an energy difference $\Delta E = \hbar\gamma\boldsymbol{B}$ between the two states exists, where anti-parallel spins possess the higher energy level. The energy gap results in a population difference ΔN, also called spin excess, towards the lower energy level. In thermal equilibrium, the proportion is governed by Boltzmann statistics,

$$\frac{N\downarrow}{N\uparrow} = \exp\left(-\frac{\Delta E}{kT}\right), \tag{2.17}$$

where $N\downarrow$ and $N\uparrow$ are populations at higher and lower energy level, respectively, T is the temperature, and k represents Boltzmann's constant. It can be shown that if ΔE is much smaller than the thermal energy ($\hbar\gamma\boldsymbol{B} << 2kT$), which is the case at human body temperature and/or at low magnetic fields, the spin excess is given by

$$\Delta N \approx N\frac{\hbar\gamma\boldsymbol{B}}{2kT}, \tag{2.18}$$

where N refers to the total number of protons in the sample. The spin excess is forming a net magnetization. Taking into account the proton magnetic moment component $\gamma\hbar/2$ and the number of protons per unit volume N_{vol}, the equilibrium magnetization $\boldsymbol{M}_0$ is given by Curie's Law:

$$\boldsymbol{M}_0 = \boldsymbol{B}\frac{N_{\text{vol}}\gamma^2\hbar^2}{4kT}. \tag{2.19}$$

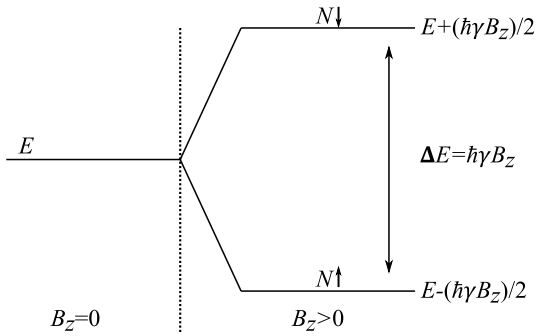

Figure 2.1: Nuclear Zeeman splitting for a spin-one-half system in a magnetic field $\boldsymbol{B} = B_z$.

2.2.2 Precession

For the following descriptions it is convenient to consider a macroscopic magnetization $\boldsymbol{M} = \frac{1}{\text{vol}} \sum_{n=1}^{N_{\text{vol}}} \boldsymbol{\mu}_n$. In the presence of a magnetic field $\boldsymbol{B}$, $\boldsymbol{M}$ precesses about $\boldsymbol{B}$, according to

$$\frac{d\boldsymbol{M}}{dt} = \gamma \left[\boldsymbol{M} \times \boldsymbol{B}\right], \tag{2.20}$$

with the specific Larmor frequency $f_L = \frac{\omega}{2\pi} = \frac{\gamma}{2\pi}|\boldsymbol{B}|$. This basically describes a rotation, as shown by Kraus et al. [4], and equation 2.20 can be written in matrix notation

$$\frac{d\boldsymbol{M}}{dt} = \boldsymbol{A}^{\times}\boldsymbol{M}, \tag{2.21}$$

where $\boldsymbol{A}^{\times}$ is a rotation generator[2] defining the rotation about $\boldsymbol{B}$:

$$\boldsymbol{A}^{\times} = \gamma \begin{bmatrix} 0 & B_z & -B_y \\ -B_z & 0 & B_x \\ B_y & -B_x & 0 \end{bmatrix}. \tag{2.22}$$

For a given duration t and a constant $\boldsymbol{B}$, the rotation matrix is given by the matrix exponential of the rotation generator and the solution to (2.21) is:

$$\boldsymbol{M}(t) = e^{\boldsymbol{A}^{\times} t}\boldsymbol{M}(0) = \boldsymbol{R}\boldsymbol{M}(0). \tag{2.23}$$

Here, $\boldsymbol{M}(0) = \boldsymbol{M}(t = 0)$ and $\boldsymbol{R}$ denotes the rotation matrix. Utilizing the unit vector in field direction $\boldsymbol{b} = \boldsymbol{B}/|\boldsymbol{B}|$ and it's infinitesimal generator $\boldsymbol{b}^{\times}$ a relation called *General*

[2] Following the notations in [4], in this thesis rotation generators are denoted by $^{\times}$. A rotation generator matrix associated with a unit vector is called infinitesimal generator [4, 78]. For example, the corresponding infinitesimal generator to the unit vector $\boldsymbol{a} = (a_1, a_2, a_3)^T$ is the skew-symmetric cross product matrix $\boldsymbol{a}^{\times}$:

$$\boldsymbol{a}^{\times} = \begin{bmatrix} 0 & -a_3 & a_2 \\ a_3 & 0 & -a_1 \\ -a_2 & a_1 & 0 \end{bmatrix}$$

Formula of Rodriguez can be utilized to derive $\boldsymbol{R}$ from $\boldsymbol{B}$ at t:

$$\boldsymbol{R} = e^{\boldsymbol{A}^{\times} t} = e^{\varphi \boldsymbol{b}^{\times}} = \boldsymbol{I} + \sin \cdot(\varphi)\boldsymbol{b}^{\times} + (1 - \cos(\varphi)) \cdot (\boldsymbol{b}^{\times})^2. \tag{2.24}$$

Here $\boldsymbol{I}$ is the identity matrix and $\varphi = \gamma|\boldsymbol{B}|t$ represents the rotation angle.

Precession forms the basis for signal detection in any NMR experiment. Receiver coils pick up magnetic flux from the rotating magnetization vectors through magnetic induction. However, if $\boldsymbol{M}$ is aligned with $\boldsymbol{B}$, precession does not occur. Hence, manipulation of the spin system, in the best case 90° to $\boldsymbol{B}$ (transverse magnetization), is required. An *rf* pulse, tuned to the Larmor frequency, can be utilized to apply a torque, tipping $\boldsymbol{M}$ out of the longitudinal axis defined by $\boldsymbol{B}$. The initial Boltzmann distribution is hereby preserved. Figure 2.2 visualizes this process for a $\boldsymbol{B}_0$-field in the x-direction and a circularly-rotating tipping pulse $\boldsymbol{B}_1$ in the yz-plane. In many cases, it is convenient to describe spin evolution in a rotating frame[3], where the coordinate system rotates about the longitudinal axis at the Larmor frequency. In this rotating frame, precession of $\boldsymbol{M}'$ about $\boldsymbol{B}_0$ does not take place (see figure 2.2(d)). In addition to *rf*-induced tipping, the orientation of magnetization can be manipulated by rapid field switching or an adiabatic field change. The two processes differ in the slopes of the magnetic field ramps and require magnet systems that can be switched flexibly. Please note that the usage of superconducting magnets, as realized in conventional high-field MRI machines for medical imaging, strongly limits this requirement.

The change in the magnetic field $\boldsymbol{B}(t)$ can be described in matrix form by a rotation

$$\boldsymbol{B}(t) = \frac{\omega(t)}{\gamma}\boldsymbol{R}(t)\boldsymbol{b}, \tag{2.25}$$

where $\boldsymbol{R}(t)$ is the underlying rotation matrix, i.e., $\boldsymbol{R}(t = 0)$ is the identity matrix $\boldsymbol{I}$ and $\boldsymbol{b}$ is a unit vector associated with $\boldsymbol{B}$. For the magnetization follows

$$\frac{d\boldsymbol{M}}{dt} = \omega(t)\left(\boldsymbol{R}(t)\boldsymbol{b}\right)^{\times}\boldsymbol{M}. \tag{2.26}$$

To distinguish the dependencies of $d\boldsymbol{M}/dt$ with $\boldsymbol{B}(t)$ and $\boldsymbol{R}(t)$, equation (2.26) can be transferred to the rotating frame, where the coordinate system moves along with the instantaneous effective field [4]. Consequently, the magnetization transforms as

$$\frac{d\boldsymbol{M}}{dt} = \frac{d}{dt}(\boldsymbol{R}\boldsymbol{M}') \tag{2.27}$$

and equation (2.26) becomes:

$$\frac{d\boldsymbol{M}'}{dt} = \left(\omega\boldsymbol{R}^{\mathrm{T}}(\boldsymbol{R}\boldsymbol{b})^{\times}\boldsymbol{R} + \boldsymbol{R}^{\mathrm{T}}\frac{d\boldsymbol{R}}{dt}\right)\boldsymbol{M}'. \tag{2.28}$$

[3]In this thesis, the rotating frame occurs only in this section and is explicitly indicated when used. Quantities associated with the rotating frame are denoted by $'$.

As the rotation is ideal ($\boldsymbol{R}^T = \boldsymbol{R}^{-1},\ \det(\boldsymbol{R}) = \pm 1$), a general relation

$$(\boldsymbol{R} \cdot \boldsymbol{b})^{\times} = \boldsymbol{R} \cdot \boldsymbol{b}^{\times} \cdot \boldsymbol{R}^{\mathrm{T}} \cdot \det(\boldsymbol{R}),$$

can be applied. Furthermore, substituting

$$\frac{d\boldsymbol{R}}{dt} \text{ with } \psi \boldsymbol{a}^{\times} \boldsymbol{R},$$

where $\boldsymbol{a}$ describes a unit vector of the instantaneous rotation and ψ is the angular velocity of the field change, equation. (2.28) reduces to:

$$\frac{d\boldsymbol{M}'}{dt} = \left(\omega \boldsymbol{b}^{\times} + \psi \boldsymbol{a}^{\times}\right) \boldsymbol{M}'. \tag{2.29}$$

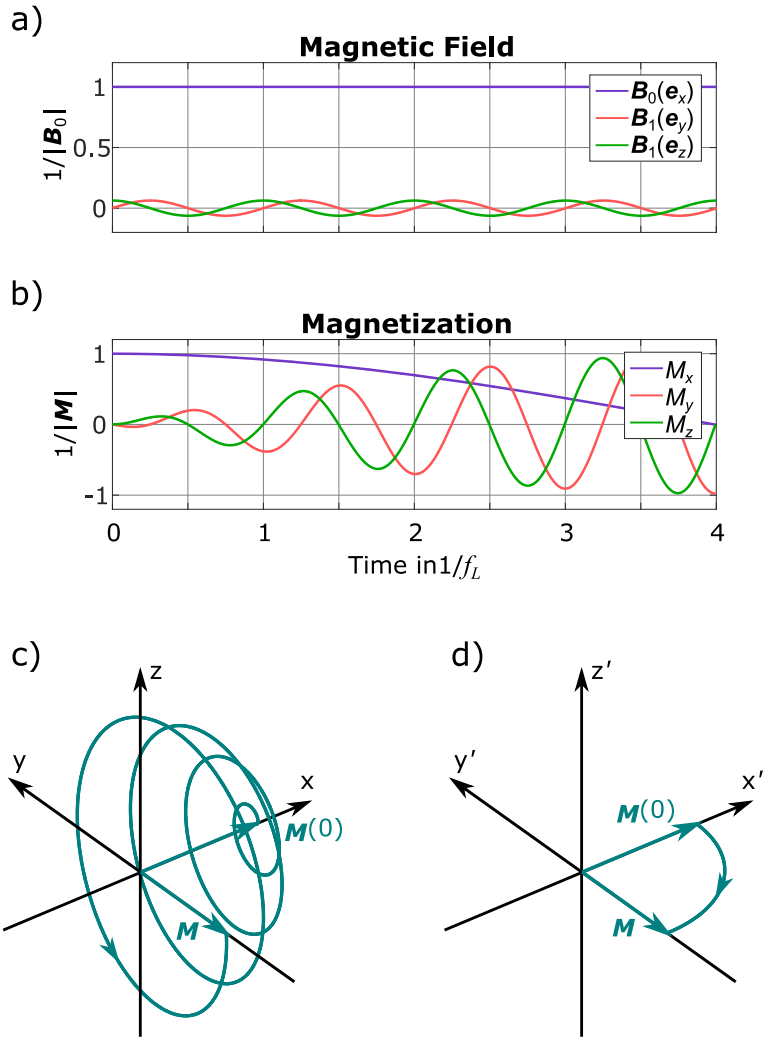

Figure 2.2: Representations of a $\pi/2$ resonant spin flip. The time course of the co-rotating field $\boldsymbol{B}_1$ is displayed with respect to the main field $\boldsymbol{B}_0$ in a), and b) gives the evolution of the magnetization. The corresponding trace of the magnetization is shown in the laboratory frame in c), and in the rotating frame in d). In the rotating frame, $\boldsymbol{B}_1$ is parallel to z'.

Considering $\boldsymbol{b}$ and $\boldsymbol{a}$ are unit vectors it is easy to see, that if one of the quantities ω or ψ is much greater compared to the other, it governs spin evolution.
The authors in Kraus et al. [4] yield for $|\omega| >> |\psi|$

$$\boldsymbol{M'} = e^{\varphi \boldsymbol{b}^\times} \boldsymbol{M'}(0) \text{ (rotating frame)},$$

$$\text{and } \boldsymbol{M} = \boldsymbol{R} \cdot e^{\varphi \boldsymbol{b}^\times} \boldsymbol{M}(0) \text{ (laboratory frame)}, \tag{2.30}$$

$$\text{where } \varphi = \varphi(t) = \int_0^t \omega(t) dt.$$

Hence, the magnetization $\boldsymbol{M}$ precesses about $\boldsymbol{B}(t)$ at a constant angle and this is called adiabatic field change.
For the case of $|\omega| << |\psi|$ they constitute:

$$\boldsymbol{M'} = e^{\theta \boldsymbol{a}^\times} \boldsymbol{M'}(0) = \boldsymbol{R}^{\mathrm{T}} \boldsymbol{M'}(0) \text{ (rotating frame)},$$

$$\text{and } \boldsymbol{M} = \boldsymbol{R}\boldsymbol{R}^{\mathrm{T}} \boldsymbol{M}(0) = \boldsymbol{M}(0) \text{ (laboratory frame)}, \tag{2.31}$$

$$\text{where } \theta = \theta(t) = \int_0^t \psi(t) dt.$$

It follows that the magnetization is not affected by rapid field switching.

The question remains of how big the difference between ω and ψ should be to obtain adiabatic or non-adiabatic behavior. Kraus et al. [4] present a formalism to derive the most efficient, i.e., the fastest, waveform for an adiabatic field change. Nieminen et al. [7] suggest a practical approach to generate waveforms for the same purpose. The methods presented by [7] are described in detail in section 3.2.1.

At this point, an example shall be presented that utilizes adiabatic field switching and rapid field switching consecutively. This is visualized in figure 2.3. A magnetization built by an arbitrarily oriented field $\boldsymbol{B}_2$ and an x-directional detection field $\boldsymbol{B}_0$ is assumed. To measure the precession signal, transverse magnetization in the yz-plane is desired. Using a y-directional guiding field $\boldsymbol{B}_1$, $\boldsymbol{B}_2$ can be turned off slowly allowing an adiabatic field change between $\boldsymbol{B}_2$ and $\boldsymbol{B}_1$. Thereby, $\boldsymbol{B}_1$ can be orders of magnitudes smaller than $\boldsymbol{B}_2$, as long as the slope of $\boldsymbol{B}_2$ is chosen such that $|\omega| >> |\psi|$. The magnetization follows the effective field and ends at $\boldsymbol{e}_y$. Now, turning off $\boldsymbol{B}_1$ rapidly and at the same time turning on $\boldsymbol{B}_0$, precession about $\boldsymbol{B}_0$ starts instantaneously. This example is applicable for MRI scanners that do not use persistent magnets to create magnetization. As explained later, in ULF MRI, magnetization is built by a millitesla polarization field while readout is conducted at microtesla $\boldsymbol{B}_0$-fields.

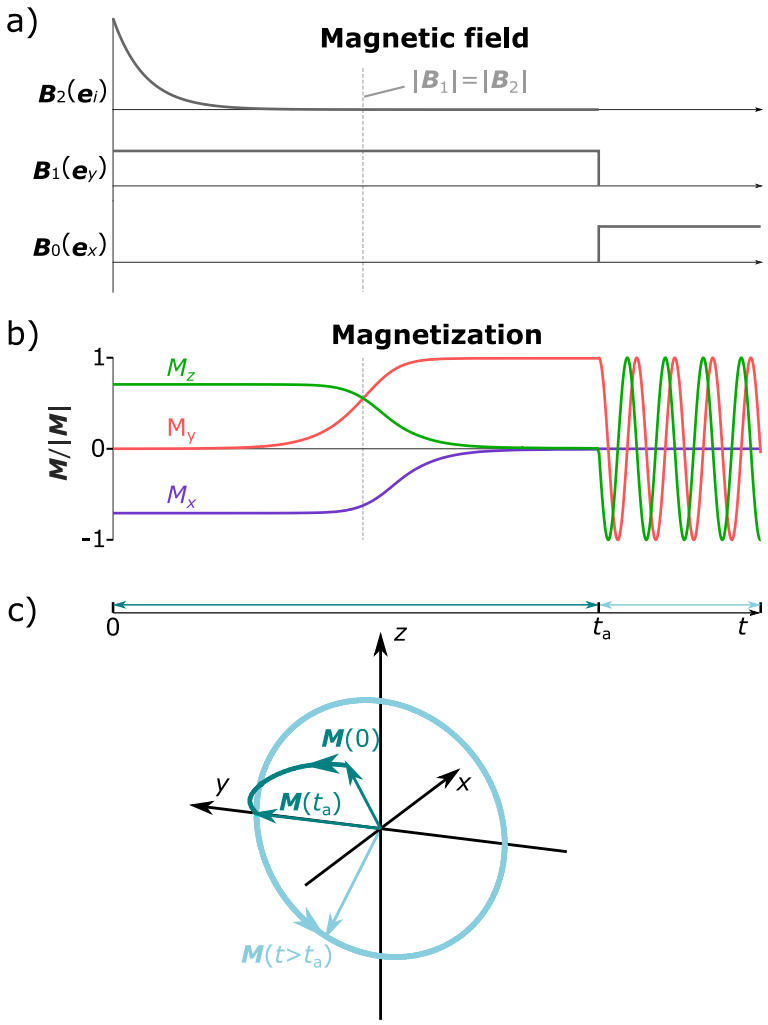

Figure 2.3: Adiabatic turn-off of an arbitrarily-oriented field $\boldsymbol{B}_2$ into a y-directional field $\boldsymbol{B}_1$ and subsequent rapid field switch between $\boldsymbol{B}_1$ and $\boldsymbol{B}_0$ (x-directional). Equilibrium magnetization along $\boldsymbol{B}_2$ is assumed at $t = 0$. a) displays the time course of the applied magnetic fields and b) the corresponding evolution of magnetization. c) shows the trace of b) in the laboratory frame. Note that $|\boldsymbol{B}_2(0)| >> |\boldsymbol{B}_1|$ and $|\boldsymbol{B}_1| \approx |\boldsymbol{B}_0|$.

2.2.3 Relaxation

Starting with a magnetization transverse to a static magnetic field $\boldsymbol{B}_0$, without relaxation, precession could be measured indefinitely. In fact, MR signals decay with time, subject to different relaxation processes.

Energy exchange of the spin ensemble with its surrounding lattice will cause relaxation of the transverse component of the net magnetization while obtaining a regrowth towards it's initial equilibrium $\boldsymbol{M}_0$ in the longitudinal direction. Consequently, this process is called spin-lattice relaxation. The governing material-dependent time constant is called T_1 relaxation time.

Another (non-dissipative) relaxation process arises from dephasing of the single mag-

netic moments within a spin ensemble. Random field alterations superimposing $\boldsymbol{B}_0$ on a local (nuclei-position) level cause small differences in the Larmor frequency between nuclei. Also resulting in a decaying net magnetization, this process is called spin-spin relaxation. It obeys the specific T_2 relaxation time constant. External fields can also cause spin dephasing according to T_2'. The combined relaxation time constant T_2^* is given by:

$$\frac{1}{T_2} + \frac{1}{T_2'} = \frac{1}{T_2^*}. \tag{2.32}$$

It should be mentioned that the instrumental effects due to T_2' can be reversed by refocusing pulses.

Bloch [79] presented a phenomenological approach to describe spin evolution including relaxation:

$$\begin{aligned} \frac{d\boldsymbol{M}_{\parallel}}{dt} &= \gamma \left[\boldsymbol{M} \times \boldsymbol{B}\right]_{\parallel} + \frac{1}{T_1}(\boldsymbol{M}_0 - M_{\parallel}), \\ \frac{d\boldsymbol{M}_{\perp}}{dt} &= \gamma \left[\boldsymbol{M} \times \boldsymbol{B}\right]_{\perp} - \frac{1}{T_2} M_{\perp}. \end{aligned} \tag{2.33}$$

$\boldsymbol{M}_0$ represents the equilibrium magnetization as derived by equation (2.19) and $\parallel$ and $\perp$ represent the components along and transverse to $\boldsymbol{B}$, respectively.

2.2.4 The signal equation

In this thesis, the NMR signal is acquired using receiver coils at a relatively far distance. Hence, the weighted sum of all precessing proton spins, form the measured signal $s(t)$. The signal equation can be written as

$$s(t) = \int_{Vol} \boldsymbol{C}(\boldsymbol{r})^{\mathrm{T}} \boldsymbol{M}(\boldsymbol{r}, t) dV, \tag{2.34}$$

where $\boldsymbol{r}$ is a position vector and $\boldsymbol{C}(\boldsymbol{r})$ defines the coupling to the sensor. For the simple experiment measuring the decay of the precessing transverse magnetization this signal is called the free precession decay (FPD). Figure 2.4 displays the FPD signal decaying with $\exp(-t/T_2^*)$. The signal strength is proportional to the transverse magnetization. After a time of $t = 3T_2^*$, approximately 95 % of the transverse magnetization are gone.

As the receiver is only sensitive to the transverse components of the precessing magnetization vectors, the matrix notation introduced in section 2.2.2 can be utilized to describe the signal equation. Assuming a homogeneous $\boldsymbol{B}_0$-field, this becomes:

$$s_{\mathrm{FPD}}(t) = \int_{Vol} \boldsymbol{C}(\boldsymbol{r})^{\mathrm{T}} \boldsymbol{R}_{\mathrm{det}}(t) \boldsymbol{M}_0 e^{-t/T_2^*(\boldsymbol{r})} dV. \tag{2.35}$$

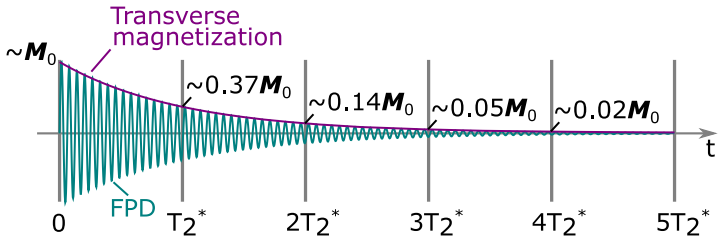

Figure 2.4: Illustration of a free precession decay

Here $\boldsymbol{R}_{\text{det}}(t)$ is a rotation matrix corresponding to the phase evolution $\varphi = \gamma|\boldsymbol{B}_0|t$ of the precessing signal.

In most MRI experiments, the sensor coupling $\boldsymbol{C}(\boldsymbol{r})$ can be neglected, as quantities such as frequency and relaxation are independent from signal amplitude. Theoretical examinations of SNR and realistic NMR simulations, however, require accurate knowledge on sensitivity including the sensor coupling coefficients. It has been shown that these can be derived from the principle of reciprocity, stating that a flux through a loop wire Φ emanated by a magnetization source $\boldsymbol{M}(\boldsymbol{r})$ at point $\boldsymbol{r}$ can be related to a flux due to the loop that goes through the magnetization. In other words, the sensor coupling is equal to the magnetic field per unit current $\boldsymbol{B}_s(\boldsymbol{r})$ emanated by the receiver coil, replacing the problem of a surface integration over the receiver coil area with a volume integration over the sample:

$$\Phi = \int_{area} \boldsymbol{B} d\boldsymbol{S} \equiv \int_{Vol} d^3 r \boldsymbol{B}_s(\boldsymbol{r}) \cdot \boldsymbol{M}(\boldsymbol{r}). \tag{2.36}$$

A complete derivation of the relation via the vector potential $\boldsymbol{A}$ using *Stokes'* theorem is given in, e.g., [77, p. 97 ff.]. MRI simulations over a larger field of view (FOV) can easily involve millions of field calculations. A computationally efficient calculation based on elliptical integrals, or numerical integration over filamentary line segments, is presented in the Appendix in section D.1.

2.3 Magnetic resonance imaging

MRI describes the process of spatially encoding the NMR through magnetic field gradients. Again, for more information on the underlying principles, I refer the reader to, e.g., [77]. The extraction of adequate imaging parameters for a desired FOV and resolution is nicely described in [80].

2.3.1 The Fourier gradient-echo signal

In MRI, magnetic field gradients modulate the Larmor frequency as a function of space. A frequency gradient $\boldsymbol{G}_x = (dB_x/dx)$ in the direction of $|\boldsymbol{B}_0|\boldsymbol{e}_x$, applied during

readout, encodes one dimension. The other two dimensions can be encoded using gradient pulses $\boldsymbol{G}_y = (dB_x/dy)$ and $\boldsymbol{G}_z = (dB_x/dz)$, applied before readout, that cause a defined spatially-depended phase offset.

During gradient application, the gradient fields dominate the T_2^* relaxation time (compare (2.32)), and the signal amplitude decreases quickly. In a gradient-echo sequence, the phase accumulation due to the frequency gradient is reversed, forming an echo signal. Dephase and rephase can be repeated until the transverse magnetization has vanished. A typical gradient-echo sequence is shown in figure 2.5, illustrating the generation of two subsequent echos. It is visible that the echo time t_E is two times the gradient time t_G, where $\boldsymbol{M}$ has a maximum at $t_\mathrm{E}/2$.

The precession due to the gradient fields can be explained by further rotations which can be included in the signal equation as:

$$s_\mathrm{Echo}(t) = \int_{Vol} \boldsymbol{C}(\boldsymbol{r})^\mathrm{T} \boldsymbol{R}_\mathrm{E}(\boldsymbol{r}, t) \boldsymbol{R}_\mathrm{G}(\boldsymbol{r}) \boldsymbol{M}_0 e^{-t/T_2^*(\boldsymbol{r})} dV. \tag{2.37}$$

Here, $\boldsymbol{R}_\mathrm{G}(\boldsymbol{r})$ represents the spatially-dependent phase accumulation during the gradient time t_G. $\boldsymbol{R}_\mathrm{E}(\boldsymbol{r}, t)$ stands for the spatially-, and time-dependent phase accumulation in the echo time t_E.

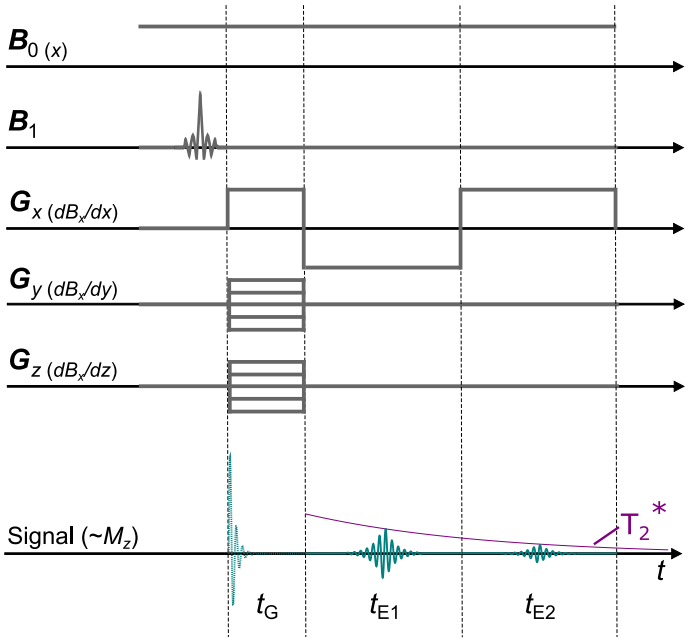

Figure 2.5: Typical sequence for gradient-echo imaging. The application of phase gradients $\boldsymbol{G}_y$ and $\boldsymbol{G}_z$ causes a quick dephasing of the spin ensemble during the time t_G. Subsequent inversion of the frequency gradient $\boldsymbol{G}_x$ causes rephasing which partly recovers the net magnetization.

2.3.2 *k*-space

For 3D spatial encoding, the sequence displayed in figure 2.5 has to be repeated with different gradient strengths in $\boldsymbol{G}_y$ and $\boldsymbol{G}_z$, corresponding to unique spatial frequencies along the axes y and z, respectively.

The collection of data points is called k-space, which is visualized in a 2D-representation in figure 2.6 taking into account only the phase-encoded axes. The number of points in this representation equals the number of pixels in the displayed dimensions and consequently also the number of sequence runs necessary. Since the frequency gradient is active during readout, the third dimension of k-space (x) is filled with each echo, where each sample represents one point in k-space.

It is important to understand, that points in k-space do not match voxels in the image, although both contain the same information and can be transferred to one-another by discrete *Fourier* transform (DFT) and discrete inverse *Fourier* transform (DIFT). Generally, points in k-space close to the center represent low spatial frequencies, corresponding to overall shapes and forms in the image, whereas points in the periphery of k-space represent higher spatial frequencies, corresponding to edges in the image.

In figure 2.6, points are equidistantly distributed, which is the case for all images presented in this thesis. The trajectory through k-space is not very important in this work. However, using the presented spiral-shaped trajectory, equal sets of spatial frequencies are obtained for both dimensions with each round of the spiral. If the

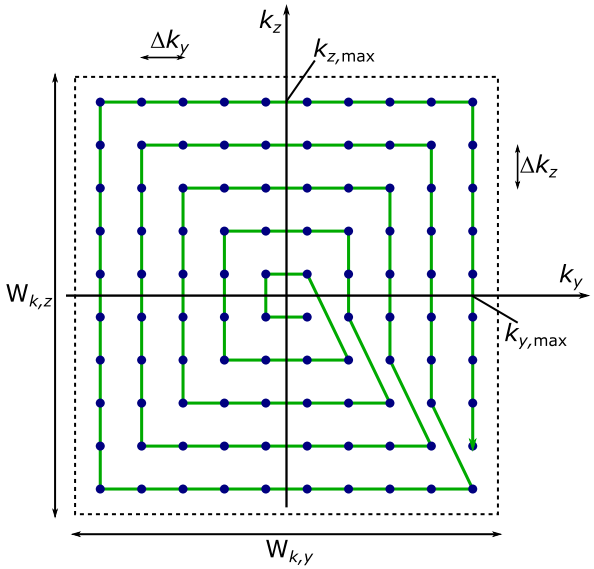

Figure 2.6: 2D-representation of k-space. Displayed are only the phase-encoded directions. The blue dots represent the samples in k-space and the green line shows the trajectory. The figure was adapted from [80, p. 85]

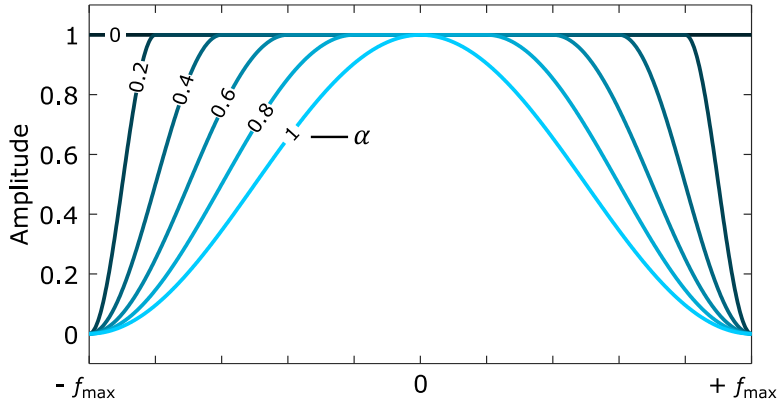

Figure 2.7: 1D-Illustration of the *Tukey kernel* with different shape parameters α. The function resembles a *Dirichlet kernel* for $\alpha = 0$ and a Hanning kernel for $\alpha = 1$.

measurement has to be interrupted for any reason, the image might still be usable even though the higher spatial frequencies are missing. This might be especially helpful for long *in-vivo* measurements.

After applying the 3D-DFT, and considering only the frequency components close to the Larmor frequency, the complex voxel value corresponding to the MR signal generated close to $\boldsymbol{r}$ can be approximated by:

$$v_n = \int_{Vol} \mathrm{SRF}(\boldsymbol{r} - \boldsymbol{r}_n)\beta(\boldsymbol{r})^* \tilde{M}(\boldsymbol{r}) dV. \tag{2.38}$$

Here, $\beta = C_z + iC_y$[4] is the coupling profile $\boldsymbol{C}$ converted to complex representation, where i is the imaginary unit, and $\tilde{M} = M_z + iM_y$ corresponds to the complex integral form of the rotating magnetization, including relaxation. The unique spatial response function (SRF) results from finite k-space sampling. In an ideal case the SRF would be defined by a *Dirac peak*, i.e., each voxel value $v_n(\boldsymbol{r}_n)$ reflects exclusively the MR signal generated at the position $\boldsymbol{r}$ [81]. However, the frequency truncation is equivalent to a convolution of the image with a *sinc kernel*, also known as *Dirichlet kernel*. The resultant SRF picks up signal from a volume around $\boldsymbol{r}$ and leakage from distant areas. It causes a truncation artifact, also known as *Gibbs ringing*, which appears most prominent at sharp contrast edges and in the phase-encode directions.

Multi-dimensional k-space filtering helps to attenuate the side lobes, but broadens the main peak and thereby reduces image resolution. Mäkinen et al. [82] surveyed the SRF for the unmodified k-space (*Dirichlet kernel*) and for a *Hanning*-windowed k-space. They pursued automated spatial registration, not structural or functional imaging, and concluded that the *Hanning kernel* provides the best compromise between attenuation

[4] $\boldsymbol{B}_0$ is considered x-directional, thus precession occurs in the yz-plane. The sensor is sensitive in the z-direction.

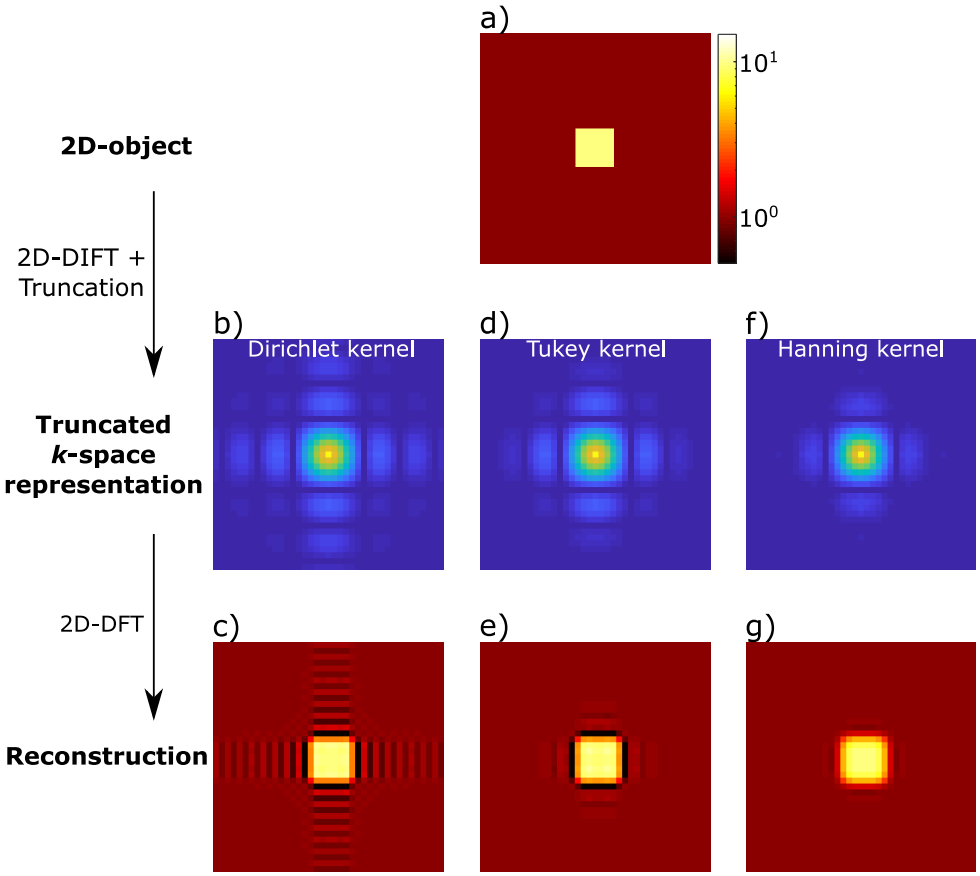

Figure 2.8: Visualization of k-space windowing. k-space was truncated to 40 spatial harmonics and multiplied with a *Dirichlet kernel* in b), a *Tukey kernel* with $\alpha = 0.5$ in d), and a *Hanning kernel* in f). Panels c), e), and g) show the corresponding image reconstructions.

of side lobes and main-peak broadening for their purpose. An intermediate function is given by the *Tukey window*. This comprises a cosine lobe of width $\alpha(N_f + 1)/2$ convoluted with a rectangular window of width $(N_f + 1) - \alpha(N_f + 1)/2$. Here, N_f is the number of *Fourier terms* after truncation and α is a shape parameter, enabling flexible attenuation of the side lobes. The *Tukey* window is illustrated for a 1D-example in figure 2.7 using different shape parameters. It results in a *Dirichlet kernel* for α=0 and a Hanning kernel for α=1.

The effect of windowing the truncated k-space is demonstrated in figure 2.8 using a 2D-example, emulating the two phase-encoding directions. Panel a) shows a box shaped object. The panels b), d), and f) visualize the k-space representation after truncation to 40 spatial harmonics. The data were generated, using 2D-DIFT of the box signal and multiplication with a *Dirichlet kernel* (b), a *Tukey kernel* where α=0.5 (d), and a *Hanning kernel* (f). The reconstruction using 2D-DFT is presented in figures 2.8(c, e, g). The *Dirichlet kernel* yields a ringing inside and outside of the box object,

expanding the signal up to the margins of the FOV. This ringing is attenuated by the *Tukey* kernel but still visible. The *Hanning kernel* results in the closest approximation of the amplitude showing negligible ringing inside and outside of the box. However, the reconstructed edges appear gradually smoothed, hindering an accurate estimation of the object boundaries.

2.3.3 Imaging parameters

Imaging parameters such as FOV and voxel size are defined by coverage of k-space. Knowing that sampling points in k-space represent spatial frequencies, it becomes clear that the lowest sampled frequency determines the FOV, which corresponds to exactly one cycle of the harmonic sine wave:

$$\mathrm{FOV} = \frac{1}{\Delta k}. \tag{2.39}$$

To avoid aliasing, the *Nyquist* criterion in k-space has to be met. Image information from outside the FOV are folded into the reconstructed data, thus sampling density below the *Nyquist* density yields aliasing artifacts. Loosely spoken, the sampling density Δk needs to be chosen such that the FOV exceeds the object to be imaged. For the frequency-encoded direction, the spatial sampling period depends on the gradient amplitude $|\boldsymbol{G}_x|$ and the sampling period of the echo signal Δt:

$$\Delta k_x = \frac{\gamma}{2\pi}|\boldsymbol{G}_x|\Delta t. \tag{2.40}$$

For the phase-encoded directions, this transfers to the incremental gradient amplitudes $|\boldsymbol{G}_{yi}|$ and $|\boldsymbol{G}_{zi}|$ and the gradient time t_G:

$$\Delta k_y = \frac{\gamma}{2\pi}|\boldsymbol{G}_{yi}|t_\mathrm{G}. \tag{2.41}$$

The spatial discretization of an image is determined by the width of k-space W_k given by:

$$\mathrm{W}_k = 2k_\mathrm{max} + \Delta k. \tag{2.42}$$

In line with the number of k-steps equaling the number of voxels in the image, the voxel size v_d amounts

$$v_d = \frac{\mathrm{FOV}}{N} = \frac{1}{\mathrm{W}_k}, \tag{2.43}$$

where N represents the number of readout samples. In [80, p. 89 f.] it is explained how points in k-space are functions of gradient area, therefore k_max can be expressed for the frequency-encoding domain as

$$k_{x,\mathrm{max}} = \frac{\gamma}{2\pi}|\boldsymbol{G}_x|\frac{t_\mathrm{E}}{2}, \tag{2.44}$$

and for the phase-encoding domain as:

$$k_{y,\max} = \frac{\gamma}{2\pi}|\boldsymbol{G}_y|t_{\mathrm{G}}. \tag{2.45}$$

Now, the voxel size can be determined by (2.43), using (2.40)/(2.41), and (2.44)/(2.45). For the frequency-encoding direction this is

$$v_{\mathrm{d}x} = \frac{1}{\frac{\gamma}{2\pi}|\boldsymbol{G}_x|(t_{\mathrm{E}} + \Delta t)}, \tag{2.46}$$

and for the phase-encoding in y-direction:

$$v_{\mathrm{d}y} = \frac{1}{\frac{\gamma}{2\pi}(2|\boldsymbol{G}_y| + \boldsymbol{G}_{yi})t_{\mathrm{G}}}. \tag{2.47}$$

$v_{\mathrm{d}z}$ is determined similarly using (2.47) with $\boldsymbol{G}_z$.

2.4 Ultra-low-field magnetic resonance imaging

The terminology "ultra-low field" that is used in this thesis refers to Larmor fields up to 100 μT, corresponding kHz Larmor frequencies. NMR experiments in the ULF regime have been performed at fields as low as some nanotesla [83, 84]. The measurements conducted in this thesis were recorded at 38.64 μT, corresponding to 1645 Hz.

NMR and MRI in the ULF regime obey the same physical principles as in the high field. However, there are important differences in parameters and instrumentation, resulting in distinct benefits but also disadvantages compared to the high-field regime. A great overview of methods and applications for ULF MRI is given by Kraus et al. [4].

2.4.1 Instrumental requirements for ULF MRI

The operation at or below the earth's magnetic field requires magnetic shielding, usually realized by a combination of magnetically shielded rooms, eddy current shields, rf shields, and possibly active compensation [85]. It should be noted, that NMR experiments in the earth's magnetic field have been performed without shielding, where the earth's field served as the Larmor field [86].

One of the biggest challenges in ULF MRI is the low signal strength. Inferring from equation (2.19), the equilibrium magnetization is directly proportional to the magnetic-field strength. Therefore, virtually all ULF-MRI sequences contain a pre-polarization period, where magnetization is built in a field of several tens of millitesla. Figure 2.9 visualizes an exemplary ULF-MRI sequence, including the polarization period, based

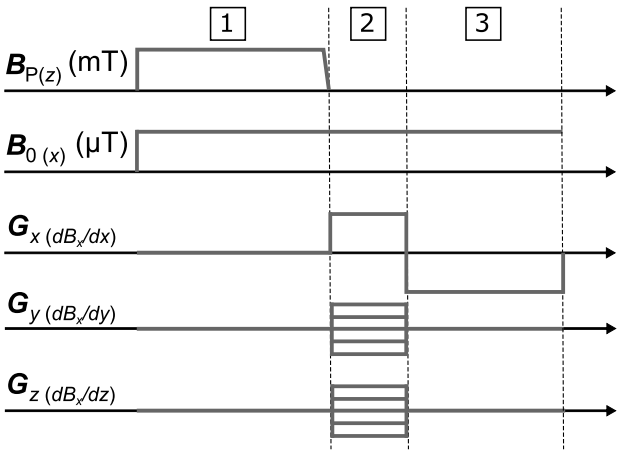

Figure 2.9: Gradient-echo sequence modified for ULF MRI. The sequence is divided into three stages: 1–polarization, 2–gradient time, and 3–echo time.

on the previously described gradient-echo sequence. Several polarization systems have been presented, that reach field strengths of 100 mT or higher [88, 89].

Previous to spatial encoding in the microtesla field, the polarization field is switched off adiabatically or non-adiabatically depending on the application [4, p. 91 ff.]. This process is critical as eddy currents and magnetization, induced in the conductive walls of the shielded room, cause transient decaying magnetic fields. Dynamic cancellation [90], as well as self-shielded coil designs [91] have been developed to reduce these transients. Further, exploiting symmetry by placing the system centrally in the room effectively cancels some of the room responses [92].

In addition to a strong magnetization, signal acquisition with sufficient SNR requires highly sensitive magnetic field sensors. In most systems this is realized by means of low-T_C dc superconducting quantum interference devices (dc-SQUIDs), coupled to

Table 2.1: Relaxation times in the microtesla regime, as reported by Zotev et al. [87] and Inglis et al. [88].

	T_2(ms)	T_1(ms)		
Tissue	46 μT [87]	46 μT [87]	130 μT [88]	80–150 mT [88]
GM	106 ± 11	103 ± 5	—	—
WM	79 ± 11	75 ± 2	—	—
Brain	—	—	85 ± 3	453 ± 117
CSF	355 ± 15	344 ± 9	1770 ± 130	4360 ± 600
Scalp	120 ± 7	124 ± 7	96 ± 2	223 ± 45
Blood			190 ± 39	450

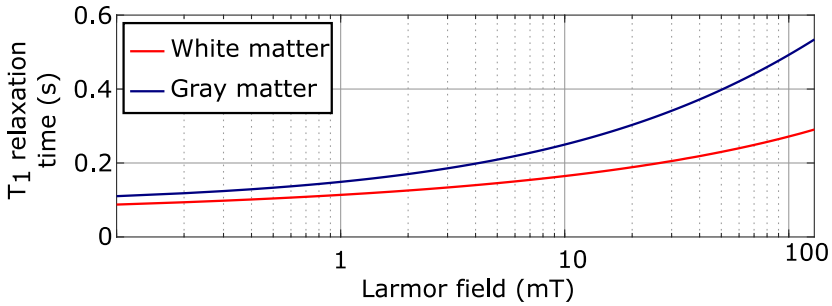

Figure 2.10: T_1 relaxation dispersion of GM and WM. The curves were generated using the relaxation model by Fischer et al. [101].

superconductive receiver coils [93, 94, 95, 88, 6, 96]. ULF MRI using high-T_C SQUIDs [97] and optically pumped magnetometers [98, 99] have been demonstrated as well, but superior noise performance over a wide frequency range can be achieved with low-T_C SQUIDs [100, 71]. Section 2.4.3 gives a short introduction to dc-SQUIDs that are usable for MRI.

As mentioned before, relaxation influences the signal strength and thereby the SNR. This needs to be considered when planning adequate polarization times and sequences. Relaxation times of head tissue in the microtesla regime were determined by Zotev et al. [87] and Inglis et al. [88], using $\boldsymbol{B}_0$-fields of 46 μT and 130 μT, respectively. The findings of both studies are listed in table 2.1. Zotev et al. surveyed both T_2 and T_1 relaxation times, which converge at microtesla fields. They even report slightly shorter T_1 times for some tissue, but clarify that this is not significant. Except for CSF, the relaxation times of all tissue types are close to 100 ms. T_1 and T_2 of CSF were measured at approximately 350 ms. This value is smaller compared to other literature findings, which the authors attribute to partial volume effects. T_1 values obtained by [88] at 130 μT generally agree with the values in [87], except for a much larger T_1 relaxation of CSF, which is closer to other literature values obtained at higher field strengths (e.g., [102]).

Tissue relaxation rates show a dispersion visible towards higher fields. T_1 values for different tissue types obtained by Inglis et al. [88] at 88–130 mT are approximately 2–5 times longer, compared to the microtesla regime. This generally agrees with dispersion curves presented by Fischer at al. [101] and Bottomley et al. [103] for GM and WM tissue. Figure 2.10 shows the T_1 dispersion over Larmor fields from 100 μT to 130 mT, as derived from [101, Equation 1, Table 5]. It can be observed that T_1 relaxation times become longer towards higher field strengths.

The relevance of T_1 and T_2 relaxation for the timing in an ULF-MRI sequence is visualized in figure 2.11, approximately for the brain relaxation times. To obtain

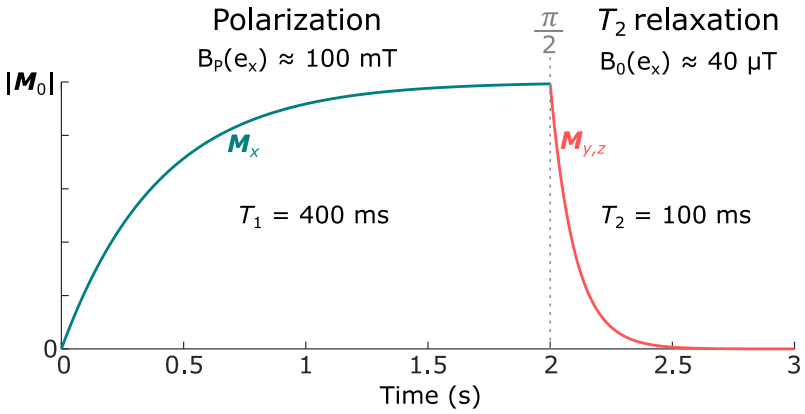

Figure 2.11: T_1 relaxation of magnetization in polarization field (mT) and T_2 relaxation in imaging field (μT).

sufficient SNR, polarizing times of approximately $3T_1$ (here 1.2 s) should be realized. Signal encoding and detection should take place as fast as possible.

2.4.2 Benefits and applications for ULF MRI

Despite the mentioned challenges, MRI in the ultra-low-field regime offers distinct advantages by means of flexibility, contrast mechanisms, safety, portability, and cost, all with restrictions [104]. The latter two are more or less constrained to an operation in a non-shielded environment, e.g., [105].

The utilization of SQUID sensors for signal acquisition facilitates a hybrid MEG-MRI device [106, 107, 108]. Here, co-registration between MEG and MRI coordinates, a central part of MEG source localization, is obsolete [82].

The low magnetic fields enable safe imaging in the presence of metal [109, 110]. In high-field MRI, susceptibility differences between metallic objects and tissue can cause field distortions, resulting in local changes of the Larmor frequency. The so-called susceptibility artifact scales with the strength of the applied main field and appears negligible in the microtesla regime [4, p. 184 ff.].

The insensitivity to susceptibility changes might also promote neuronal current imaging (NCI), which is referring to methods that try to detect changes in local spin dynamics caused by magnetic fields generated by neuronal activity [111, 112, 113, 114, 115]. Reliable NCI measurements would enable direct, spatially resolved, and possibly real-time localization of neuronal activity. In high-field MRI, artifacts arising from susceptibility changes in oxygenated and deoxygenated hemoglobin mask the frequency shift generated by neuronal currents [116].

A benefit of ULF MRI, most important for the methods employed in this thesis,

is given by increased flexibility in sequence design. Unlike superconducting magnets, room-temperature coils enable the application of arbitrary MRI fields. In section 3.2, it is explained how this feature is key for CDI as proposed by [6, 7].

2.4.3 SQUID sensors for ULF MRI

SQUIDs are the most sensitive, wide-band magnetic field sensors to date, and therefore the number one choice for signal acquisition in ULF MRI. This subsection gives a brief overview of the working procedure of a dc-SQUID used in ULF MRI. A very detailed description of SQUIDs and applications is presented in [117, 118]. A short overview is given by, e.g., [119, 104].

The dc-SQUID is a superconductive ring interrupted by two small normal-resistive, or insulating barriers, the *Josephson junctions*. In the superconductive state, electrons form so-called Cooper pairs that can tunnel these barriers, the *Josephson effect*. If the SQUID is biased appropriately with a current I_b, the voltage across the junctions changes periodically with the applied flux, forming a characteristic U-Φ curve. The period is given by the magnetic flux quantum Φ_0. The bias current I_b, together with a bias voltage U_b, set a defined working point on the U-Φ curve. External feedback is used to compensate the flux inside the SQUID loop with a counter flux, effectively linearizing the U-Φ characteristic. This is called flux locked loop (FLL), where the feedback current becomes a measure of the flux. Optimal noise performance is given, when the working point is at the steepest point of the U-Φ curve. Here, the noise contribution of the room-temperature electronics is minimal. Figure 2.12 shows a measured U-Φ curve of a dc-SQUID. Additional positive feedback (APF) is applied to form asymmetric U-Φ characteristics, yielding a steeper slope around the working point [120].

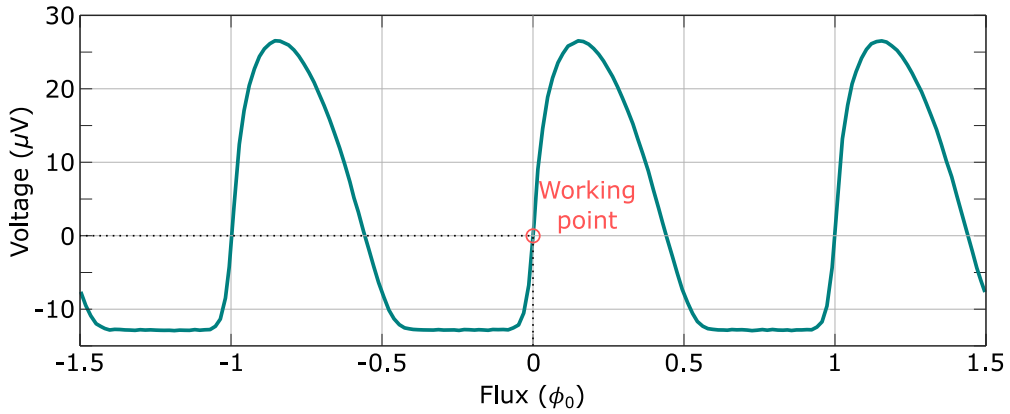

Figure 2.12: Exemplary U-Φ curve of a dc-SQUID with APF. For this sensor the slope at the working point was measured at approximately 600 $\mu V/\Phi_0$.

Often, the SQUID is inductively coupled to a receiver coil via an input coil L_{in}. In this configuration, the SQUID is called current sensor, as the SQUID loop itself amplifies the current in the pick-up loop. Feedback can be applied directly to the SQUID loop or with a feedback transformer to the input circuit. The chip carrier holding the SQUID with its input coil and the feedback loop can be placed in larger distance and shielded using superconductive shields (for instance niobium capsules) [100]. This is especially helpful in ULF MRI, where the sensor is exposed to strong magnetic fields during the pulse sequence.

Figure 2.13 sketches a current-sensor SQUID with APF. The pick-up coil, in this case an axial 1st-order gradiometer, connected to the on-chip input coil L_{in} form a superconducting flux transformer. Within the input circuit, a current limiter consisting of 16 unshunted SQUIDs in series and a feedback transformer formed by L_{Fin} and L_F is realized. As the name says, the current limiter restricts the current in the input circuit to a value below I_C (nominally 20 μA). Significantly larger currents would cause trapped flux in the SQUID structure and thereby worsen SQUID performance. The figure displays a simplified scheme of a sensor as used for instance in [100].

The design of the pick-up coil is critical for SNR as it defines the sensor coupling. Generally, an increase in the pick-up-loop area improves the sensitivity to external fields [119]. Körber [121] examined optimum pick-up-loop sizes in dependence of different noise sources. Taking into account external noise, such as thermal noise originating in

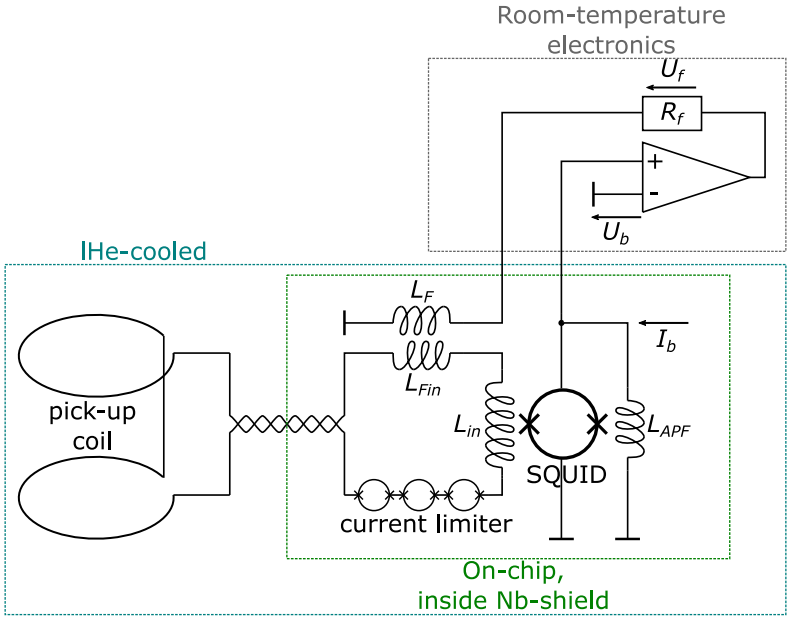

Figure 2.13: Schematic of current-sensor dc-SQUID with inductively coupled pick-up coil, both in liquid helium (lHe) bath, and room-temperature electronics for FLL. The figure was adapted from [120].

the cryostat material, yields substantially different optimum pick-up-loop areas.

The pick-up-loop arrangement should be optimized for the application. Magnetometers cover one surface and respond linearly to the field integrated over the surface area. Gradiometers form a closed path over two or more surface areas and give 1^{st}- or higher-order derivatives of the field. This attenuates homogeneous (far-field) components and gradients, depending on the order. An overview for different sensor geometries in ULF MRI is given by Zevenhoven et al. [122], who computationally examined existing and potential sensor arrangements regarding their sensitivity. They conclude that gradiometers yield less image SNR, but potentially attenuate transient fields from eddy currents in the shielded walls. It will be shown later in this thesis, that a 2^{nd}-order gradiometer can also be used to supress noise associated with the MRI gradients.

Chapter 3

Sequence design based on specifications for *in-vivo* CDI

In this chapter, sequences for CDI in the ULF regime are evaluated regarding their feasibility in a possible *in-vivo* application. Two sequences, namely adiabatic current density imaging (aCDI) by Nieminen et al. [7] and zero-field-encoded current density imaging (zCDI) by Vesanen et al. [6], have been identified that promise the reconstruction of all components of the magnetic field $\boldsymbol{B}_\mathrm{J}$ associated with the current density $\boldsymbol{J}$. Both sequences have not been validated experimentally due to hardware limitations.

This chapter starts with an analysis of the requirements for *in-vivo* CDI in section 3.1. Subsequently, the two sequences are explained in detail, followed by an assessment based on the before specified requirements. Finally, necessary modifications are identified, before the sequence applied in this thesis is explained in detail.

The methods and results presented in this chapter have partly been previously published in [72]. Parts of the text and figures are extracted from that publication.

3.1 Requirements for *in-vivo* CDI

In this thesis, the demonstration of 3D-CDI is pursued. Thereby, a possible *in-vivo* application of the method poses a strong focus in all development stages. Consequently, methods and sequences have to be capable of imaging weak magnetic fields, related to the impressed currents.

Several simulation studies present quantitative information on electric field and current density distribution $\boldsymbol{J}$ due to DC-stimulation via scalp electrodes, e.g. [27, 28, 123]. Depending on the accuracy of the underlying head model, the utilized conductivities, and the electrode montage, current densities of 0.1–0.2 A/m^2 are reported in the brain

tissue for 1 mA applied current [27, 124]. Scalp values are approximately ten times higher. The magnetic field $\boldsymbol{B}_\mathrm{J}$, due to $\boldsymbol{J}$, is not important for applications in transcranial electric stimulation, therefore, usually not investigated. MR CDI and MREIT on the other hand, rely on accurate measurements of at least one component of $\boldsymbol{B}_\mathrm{J}$. However, studies reporting on *in-vivo* acquired head images are scare. Chauhan et al. [69] show measured (but optimized) B_z maps, with values between 2–3 nT intra-cranially, for 1.5 mA applied current via scalp electrodes. The results of an earlier study by the same group largely agrees with these values [125]. The values reported by Göksu et al. [126] are slightly lower. Based on these numbers, and assuming a safe application of 4 mA current, $\boldsymbol{B}_\mathrm{J}$ strengths below 10 nT are expected. Later in this thesis, in chapter 7, FEM simulations based on a three-compartment head phantom are presented that reach $\boldsymbol{B}_\mathrm{J}$ values of approximately 12 nT in the intra-cranial cavity.

In addition to the sensitivity for weak magnetic fields, it should be kept in mind that relaxation times for brain tissue in the microtesla regime range at approximately 100 ms, as described before in section 2.4.1. To obtain adequate SNR, signal encoding needs to be sufficiently fast.

Last but not least, current density reconstruction from $\boldsymbol{B}_\mathrm{J}$ using *Ampere's Law* (compare equation (2.12)) requires an adequate imaging resolution with voxel side lengths smaller than the tissue thickness. A high imaging resolution is in conflict with a low overall measurement time, which is required for *in-vivo* measurements. The measurement time is also connected to the FOV, which should be sufficiently large to prevent aliasing.

In conclusion, the following requirements have been identified for a successful *in-vivo* application of CDI:

- sensitivity for weak magnetic fields < 10 nT,
- encoding within T_2 (≈ 100 ms) for optimum SNR, and
- a reasonable overall measurement time to obtain a fine resolution sufficient for $\boldsymbol{J}$-reconstruction.

In the following, two sequences for CDI using ULF MRI will be presented in sections 3.2.1 and 3.2.2, and assessed in section 3.2.3 based on the above listed requirements.

3.2 Sequences for CDI in ULF MRI in a detailed review

3.2.1 Adiabatic current density imaging (aCDI)

Nieminen et al. [7] presented the aCDI sequence in 2014. By making use of the physical principle of adiabaticity (compare section 2.2.2), aCDI possibly enables the detection of the full $\boldsymbol{B}_{\mathrm{J}}$-vector. Considering a pre-polarized pulse sequence, Nieminen et al. suggest to decrease the polarizing field $\boldsymbol{B}_{\mathrm{P}}$ slowly into a static $\boldsymbol{B}_{\mathrm{J}}$-field, where the condition

$$\omega(t) >> \psi(t) \tag{3.1}$$

has to be satisfied. Here, $\omega(t)$ is the Larmor angular frequency defined by $\gamma(\boldsymbol{B}_{\mathrm{P}}(t)+\boldsymbol{B}_{\mathrm{J}})$ and $\psi(t)$ is the angular rate at which the orientation of the field changes. Hence, the slope of the ramp-down of $\boldsymbol{B}_{\mathrm{P}}$ is the critical parameter that has to be defined precisely. A polarizing waveform that fulfills the requirements in equation (3.1) can be obtained using a practical approach, fixing the ratio between Larmor frequency and angular rate of field change to a constant $p >> 1$:

$$p = \frac{\omega(t)}{\psi(t)}. \tag{3.2}$$

Now, the polarizing turn-off can be obtained by

$$\boldsymbol{B}_P(t) = \frac{\sqrt{\dfrac{(p-\omega_{\mathrm{J}}t)^2}{p^2-(p-\omega_{\mathrm{J}}t)^2}}}{\boldsymbol{B}_{\mathrm{J}}}, \tag{3.3}$$

where $\omega_{\mathrm{J}}= \gamma\boldsymbol{B}_{\mathrm{J}}$ is the Larmor angular frequency associated with $\boldsymbol{B}_{\mathrm{J}}$. The time duration $(0 - t_{\mathrm{end}})$ is given by:

$$t_{\mathrm{end}} \approx \frac{p}{\omega_{\mathrm{J}}}. \tag{3.4}$$

After the adiabatic turn-off of $\boldsymbol{B}_{\mathrm{P}}$, the magnetization $\boldsymbol{M}$ is aligned with $\boldsymbol{B}_{\mathrm{J}}$. Subsequently, spatial information can be encoded employing frequency and phase gradients.

Nieminen et al. [7] give the details on the quantitative reconstruction of $\boldsymbol{B}_{\mathrm{J}}$. Besides measuring $\boldsymbol{B}_{\mathrm{J}}$, it involves a sequence run with an additional, well-known, external field $\boldsymbol{B}_{\mathrm{ext}}$. Furthermore, the authors clarify that additional fields, such as a static background field $\boldsymbol{B}_{\mathrm{B}}$, will superimpose $\boldsymbol{B}_{\mathrm{J}}$ and $\boldsymbol{B}_{\mathrm{ext}}$ and have to be subtracted by a full reconstruction of $\boldsymbol{B}_{\mathrm{B}}$ only.

The aCDI sequence was validated in simulations, under the idealized assumption of no present background field. Equation (3.3) was utilized to create a 250 ms long waveform for the $\boldsymbol{B}_{\mathrm{P}}$ turn-off, where a constant $\boldsymbol{B}_{\mathrm{J}} = 5\ \mu\mathrm{T}$ was assumed. The ratio

p can be approximated to 335 using equation (3.2). The polarizing field strength was set to 100 mT, the main field to 50 μT, and the external field $\boldsymbol{B}_{\text{ext}}$ to 1 μT. Spatial encoding was simulated for 20 k-space lines in each of the phase-encoding directions to derive 1 mm^3 voxels. The sample was constructed as three orthogonal tubes (6 mm in diameter), each carrying a current of 40 mA.

3.2.2 Zero-field-encoded current density imaging (zCDI)

Similar to aCDI, zCDI by Vesanen et al. [6] promises imaging the full $\boldsymbol{B}_{\text{J}}$-vector, where the encoding of the magnetic field is performed using different principles. $\boldsymbol{B}_{\text{J}}$ is applied in the absence of all MRI fields, including the $\boldsymbol{B}_0$-field. Hence, the precession axis and frequency are set only by $\boldsymbol{B}_{\text{J}}$:

$$\frac{d\boldsymbol{M}}{dt} = \gamma \boldsymbol{M} \times \boldsymbol{B}_{\text{J}}. \tag{3.5}$$

During the zero-field time τ, the precessing magnetization vector can be described by a rotation in matrix notation, as introduced in section 2.2.2:

$$\boldsymbol{M}(\tau) = e^{\tau \boldsymbol{A}_{\text{J}}^{\times}} \boldsymbol{M}_0 = \boldsymbol{\Phi} \boldsymbol{M}_0. \tag{3.6}$$

Here the rotation generator $\boldsymbol{A}_{\text{J}}^{\times}$ to the rotation matrix $\boldsymbol{\Phi}$ is given by:

$$\boldsymbol{A}_{\text{J}}^{\times} = \gamma \begin{bmatrix} 0 & B_{\text{J},z} & -B_{\text{J},y} \\ -B_{\text{J},z} & 0 & B_{\text{J},x} \\ B_{\text{J},y} & -B_{\text{J},x} & 0 \end{bmatrix}. \tag{3.7}$$

When the elements of $\boldsymbol{\Phi}$ are known, all components of $\boldsymbol{B}_{\text{J}}$ can be derived from a non-linear inversion of the matrix exponential:

$$\tau \boldsymbol{A}_{\text{J}}^{\times} = \frac{\varphi}{2 \sin \varphi} (\boldsymbol{\Phi} - \boldsymbol{\Phi}^{\top}) \tag{3.8}$$

where $\varphi = \arccos[(\text{tr}(\boldsymbol{\Phi}) - 1)/2]$ represents the rotation angle of $\boldsymbol{\Phi}$.

Applying a gradient-echo sequence, Vesanen et al. [6] give the details, how the elements of $\boldsymbol{\Phi}$ can be derived from the real and imaginary parts of detected signals from three different measurements with starting magnetizations $\boldsymbol{M_0}$ in the three basis directions $\boldsymbol{e}_x$, $\boldsymbol{e}_y$, and $\boldsymbol{e}_z$, respectively. For the case of a z-directional $\boldsymbol{B}_{\text{P}}$, $\boldsymbol{M}_0$ after the polarization appears as $|\boldsymbol{M}_0|\boldsymbol{e}_z$. The three measurements can be described by

$$\begin{aligned} \boldsymbol{M}_1 &= \boldsymbol{\Phi} \boldsymbol{R}_1 \boldsymbol{M}_0, \\ \boldsymbol{M}_2 &= \boldsymbol{\Phi} \boldsymbol{R}_2 \boldsymbol{M}_0, \\ \text{and } \boldsymbol{M}_3 &= \boldsymbol{\Phi} \boldsymbol{M}_0, \end{aligned} \tag{3.9}$$

where $\boldsymbol{R}_1$ and $\boldsymbol{R}_2$ represent $\pi/2$ rotations of $\boldsymbol{M}_0$ to $\boldsymbol{e}_x$ and $\boldsymbol{e}_y$, respectively. As in aCDI, a background field superimposing $\boldsymbol{B}_\mathrm{J}$ during τ needs to be acquired separately. That gives a total of six full images, i.e. six sequence runs per k-step, required for a full-vector $\boldsymbol{B}_\mathrm{J}$-reconstruction.

The sequence was validated in a simulation setup, similar to the one for aCDI [7], with no present background field. 20 k-space lines were acquired, resulting in voxel-side-lengths of 4 mm. The polarizing field strength was set to 100 mT, the main field to 50 μT. The sample comprised three orthogonal tubes (24 mm diameter) each carrying a current of 12 mA, corresponding to a current density of 27 A/m^2. An experimental validation could not be realized due to technical difficulties with switching the low-noise currents in the $\boldsymbol{B}_0$-coil and the frequency-gradient coil.

3.2.3 Assessment of feasibility

The simulations by Nieminen et al. [7] using the aCDI sequence were performed at a mean current density of approximately 1415 A/m^2. Based on literature values, realizable current densities in the brain range around 0.5 A/m^2, thus around 2800 times smaller compared to the values in [7]. In the discussion of [7], it is mentioned that imaging weak current density requires long turn-off times of $\boldsymbol{B}_\mathrm{P}$. In detail, it is estimated that t_end for $|\boldsymbol{B}_\mathrm{J}|$ of 1 μT must be greater than 200 ms. Inserting these numbers into equation (3.4), a corresponding ratio $p \approx 53$ can be estimated, which is about five times lower than what was used in the simulations. An appropriate value for p was not further evaluated, but the error angle between $\boldsymbol{M}$ and $\boldsymbol{B}_\mathrm{J}$ at t_end was obtained for the simulated data and presented as a function of $|\boldsymbol{B}_\mathrm{J}|$. They found that their ramp was adiabatic for most voxels with $|\boldsymbol{B}_\mathrm{J}| > 1\mu$T. However, they also found that the orientation of $\boldsymbol{B}_\mathrm{J}$ has a strong effect on the alignment. Assuming a constant $\boldsymbol{B}_\mathrm{J}$ of 10 nT, as estimated from literature values, and choosing a p-ratio of 50, the slope of the $\boldsymbol{B}_\mathrm{P}$ turn-off would have to be 18 s long according to equation (3.4). Even if the p-ratio is reduced to two, where the adiabatic condition hardly holds, a turn-off time of 750 ms is required. Recalling the relaxation time constants of brain tissue in the μT regime of approximately 100 ms, the feasibility of aCDI for an *in-vivo* application can be safely ruled out.

The simulations of Vesanen et al. [6] using the zCDI sequence comprised a current density of 27 A/m^2, which is approximately a factor of 55 higher than realistic *in-vivo* values. The noise level matched that of their ULF-MRI system with sensor noise levels as low as 2–4 fT Hz$^{1/2}$ [108]. Again, assuming a $\boldsymbol{B}_\mathrm{J}$ of 10 nT and choosing τ=100 ms according to the relaxation time constants, a rotation angle of the precession due to

$\boldsymbol{B}_\mathrm{J}$ during τ can be estimated to $\varphi = \gamma\tau|\boldsymbol{B}_\mathrm{J}| \approx 15°$. Based on these estimations and provided the SNR is substantially higher compared to the system examined by Vesanen et al., the zCDI sequence seems feasible for *in-vivo* application. A detailed examination of the theoretical sensitivity of the sequence as a function of SNR follows in chapter 6.

3.3 Towards an experimental implementation

3.3.1 The zCDI reconstruction in detail

In the last section, it was evaluated that zCDI by Vesanen et al. [6] is most promising regarding an *in-vivo* implementation. To provide a better understanding on the procedure, the reconstruction is explained in detail using an idealized case.

After the zero-field time, the magnetization has been rotated to $\boldsymbol{M}_1$, $\boldsymbol{M}_2$, or $\boldsymbol{M}_3$ by the magnetic field during τ as

$$\begin{aligned}\boldsymbol{M}_1(\boldsymbol{r}) &= \boldsymbol{\Phi}(\boldsymbol{r})\left(|\boldsymbol{M}_0(\boldsymbol{r})|\boldsymbol{e}_x\right),\\ \boldsymbol{M}_2(\boldsymbol{r}) &= \boldsymbol{\Phi}(\boldsymbol{r})\left(|\boldsymbol{M}_0(\boldsymbol{r})|\boldsymbol{e}_y\right),\\ \boldsymbol{M}_3(\boldsymbol{r}) &= \boldsymbol{\Phi}(\boldsymbol{r})\left(|\boldsymbol{M}_0(\boldsymbol{r})|\boldsymbol{e}_z\right),\end{aligned} \tag{3.10}$$

where, $|\boldsymbol{M}_0|\boldsymbol{e}_i$ is the starting magnetization rotated to one of the three basis directions $i = x, y,$ or z. Ideally, the rotation matrix $\boldsymbol{\Phi}$ is solely determined by the magnetic field $\boldsymbol{B}_\mathrm{J}$, associated with $\boldsymbol{J}$ and τ. The traces of the magnetization during τ are visualized in figure 3.1.

Following τ, the main field $\boldsymbol{B}_0$ is turned on, and the magnetization is manipulated by gradient fields to encode spatial information in the phase and frequency of the resulting signal. From now on and for all experiments described in this thesis, the main field $\boldsymbol{B}_0$ is x-directional and the frequency gradient $\boldsymbol{G}_x$ encodes in $d\boldsymbol{B}_x/dx$ and the phase gradients $\boldsymbol{G}_y$ and $\boldsymbol{G}_z$ in $d\boldsymbol{B}_x/dy$ and $d\boldsymbol{B}_x/dz$, respectively. According to equation (2.37) and ignoring relaxation, the magnetic signal recorded at a sensor during the echo, exemplary for $\boldsymbol{M}_1$, can be written as

$$s(t) = \int \boldsymbol{C}(\boldsymbol{r})^\top \mathbf{R}_\mathrm{E}(\boldsymbol{r}, t)\mathbf{R}_\mathrm{G}(\boldsymbol{r})\boldsymbol{M}_1(\boldsymbol{r})dV. \tag{3.11}$$

As before, the matrices $\mathbf{R}_\mathrm{G}$ and $\mathbf{R}_\mathrm{E}$ represent rotations during the gradient time t_G and the echo time t_E, respectively, and $\boldsymbol{C}$ defines the coupling to the sensor.

The precession signal contains information on two components of the magnetization. Therefore, six values (2 rows) of $\boldsymbol{\Phi}$ can be extracted from the real and imaginary parts of the three measurements after applying the *Fourier transformation*. Since rotation

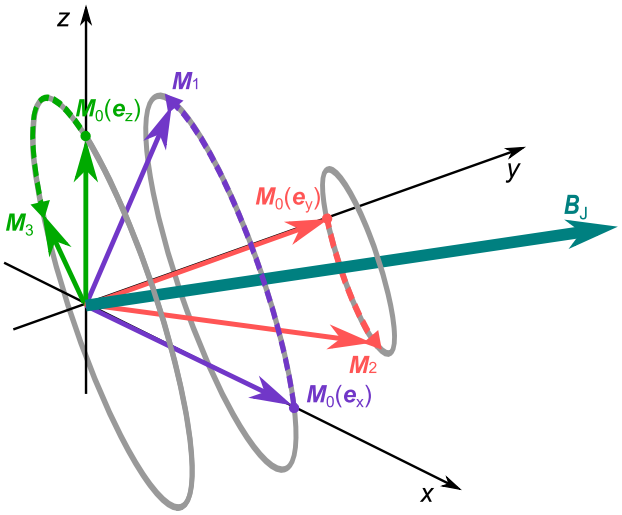

Figure 3.1: Rotation of magnetization about $\boldsymbol{B}_\mathrm{J}$ during zero-field time. Displayed are magnetization vectors and traces for three measurements with starting magnetizations $\boldsymbol{M}_0$ in $\boldsymbol{e}_x$ (purple), $\boldsymbol{e}_y$ (red), and $\boldsymbol{e}_z$ (green).

matrices are orthogonal, the last row is given by the cross-product of the two measured rows. Assuming a receiver coil sensitive in the z-direction, the z-component and the y-component of $\boldsymbol{M}$ correspond to the real and imaginary parts of the signal converted to complex representation ($\tilde{M} = M_z + iM_y$). For now ignoring the effects of $\mathbf{R}_\mathrm{G}$, $\mathbf{R}_\mathrm{E}$, $\boldsymbol{C}$, and relaxation, two rows of the rotation matrix $\boldsymbol{\Phi}$ are included in the magnetization vectors as:

$$\boldsymbol{\Phi}\begin{bmatrix} |\boldsymbol{M}_0| & 0 & 0 \\ 0 & |\boldsymbol{M}_0| & 0 \\ 0 & 0 & |\boldsymbol{M}_0| \end{bmatrix} = \begin{bmatrix} - & - & - \\ \mathrm{Im}(\tilde{M}_1) & \mathrm{Im}(\tilde{M}_2) & \mathrm{Im}(\tilde{M}_3) \\ \mathrm{Re}(\tilde{M}_1) & \mathrm{Re}(\tilde{M}_2) & \mathrm{Re}(\tilde{M}_3) \end{bmatrix}. \tag{3.12}$$

Therefore, $\boldsymbol{\Phi}$ can be recovered by a normalization of the real and imaginary parts with $|\boldsymbol{M}_0|$. Having $\boldsymbol{\Phi}$, the components of $\boldsymbol{B}_\mathrm{J}$ can be reconstructed using (3.8) and (3.7). A practical requirement in zCDI is limiting the angle φ to $-\pi < \varphi < \pi$, effectively avoiding ambiguity. This can be achieved by choosing τ accordingly.

3.3.2 The zCDI reconstruction under realistic conditions

In the idealized case, as explained in section 3.3.1 and simulated by Vesanen et al. [6], the reconstruction of $\boldsymbol{B}_\mathrm{J}$ is straight forward. The only unknown, affecting the reconstruction, is measurement noise. Since rotation matrices are orthogonal by nature, matrix orthogonalization can be utilized to stabilize the reconstruction. As proposed by Vesanen et al. [6], this could be done, for instance, using *Löwdin's* transformation, which yields the closest orthogonalization in the least-squares sense [127, 128]. The

singular value decomposition gives a simple implementation

$$\begin{aligned} \boldsymbol{\Phi} &= \boldsymbol{U}\boldsymbol{\Sigma}\boldsymbol{V}^T, \\ \boldsymbol{U}\boldsymbol{V}^T &= \tilde{\boldsymbol{\Phi}}, \end{aligned} \tag{3.13}$$

where $\tilde{\boldsymbol{\Phi}}$ represents the orthogonalization of $\boldsymbol{\Phi}$ [129]. $\boldsymbol{U}$ and $\boldsymbol{V}$ are unitary matrices containing left and right singular vectors, respectively. $\boldsymbol{\Sigma}$ is diagonal and contains the singular values.

A realistic setting, however, is more difficult. First of all, a superposition of a static background field and transient fields due to pulsing (combined in the term $\boldsymbol{B}_\mathrm{B}$) are present. Therefore, $\boldsymbol{B}_\mathrm{B}$ needs to be detected without $\boldsymbol{B}_\mathrm{J}$, where the reconstruction of $\boldsymbol{B}_\mathrm{B}$ is subtracted from the reconstruction of ($\boldsymbol{B}_\mathrm{B}$+$\boldsymbol{B}_\mathrm{J}$).

Furthermore, the effects of $\mathbf{R}_\mathrm{G}$, $\mathbf{R}_\mathrm{E}$, $\boldsymbol{C}$, and relaxation, are included in the measurements $\boldsymbol{M}_1$, $\boldsymbol{M}_2$, and $\boldsymbol{M}_3$, and hamper the determination of $\boldsymbol{\Phi}$ using equation (3.12). As the relaxation profile is unknown, its influence given by $|\boldsymbol{M}_0| \exp\left(-\frac{t}{T_{1,2}}\right)$ is also unknown and could only be measured in a true zero-field. With regard to the always present background field, this is not achievable. Nevertheless, as rotation matrices have row-norm one by definition, a normalization of the rows in the right term of (3.12) gives the correct magnitude reference. It should be noted that this works on the assumption of $T_1 = T_2$, which is reasonable in the nanotesla regime (compare section 2.4.1).

More difficult to derive are the influences of the MRI fields on the phase of the complex voxel values. The rotation matrices $\mathbf{R}_\mathrm{G}$ and $\mathbf{R}_\mathrm{E}$ correspond to rotations in the yz-plane and result in a spatially dependent phase offset δ in the MR signal. This can be best explained using a simple example, where all imaging fields, as well as $\boldsymbol{B}_\mathrm{B}$, and $\boldsymbol{B}_\mathrm{J}$ are purely x-directional. In this scenario, the magnetization precesses about the *x-axis* in each part of the sequence, where information on the field strengths of $\boldsymbol{B}_\mathrm{B}$ and $\boldsymbol{B}_\mathrm{J}$ is encoded solely in the phase of the resulting signal. Figure 3.2(a) visualizes the evolution of the magnetization in the yz-plane for the measurements with starting magnetizations in $\boldsymbol{e}_y$ ($\boldsymbol{M}_2$) and $\boldsymbol{e}_z$ ($\boldsymbol{M}_3$). The measurement with starting magnetization in the x-direction ($\boldsymbol{M}_1$) would not yield a precessing magnetization and is therefore not visualized in the figure. Both, $\boldsymbol{M}_2$ and $\boldsymbol{M}_3$ are displayed for the case where only $\boldsymbol{B}_\mathrm{B}$ is present ($\boldsymbol{B}1$) during τ and for the case of $\boldsymbol{B}_\mathrm{B}$+$\boldsymbol{B}_\mathrm{J}$ ($\boldsymbol{B}2$). It can be observed, that all measurements are subject to the same phase offset δ, which originates from the imaging fields. In the case of figure 3.2(a) where $|\boldsymbol{M}_0| = 1$ and relaxation is ignored, the rotation matrix yields:

$$\boldsymbol{\Phi} = \begin{bmatrix} 1 & 0 & 0 \\ 0 & \mathrm{Im}(\tilde{M}_2) & \mathrm{Im}(\tilde{M}_3) \\ 0 & \mathrm{Re}(\tilde{M}_2) & \mathrm{Re}(\tilde{M}_3) \end{bmatrix}.$$

Now, recalling equation (3.6), $\boldsymbol{M}(\tau) = \boldsymbol{\Phi}\boldsymbol{M}_0 = e^{\tau \boldsymbol{A}^\times}\boldsymbol{M}_0$, with

$$\boldsymbol{A}^\times = \gamma \begin{bmatrix} 0 & B_z & -B_y \\ -B_z & 0 & B_x \\ B_y & -B_x & 0 \end{bmatrix},$$

one can see that $\boldsymbol{B}_x$ is probed twice.

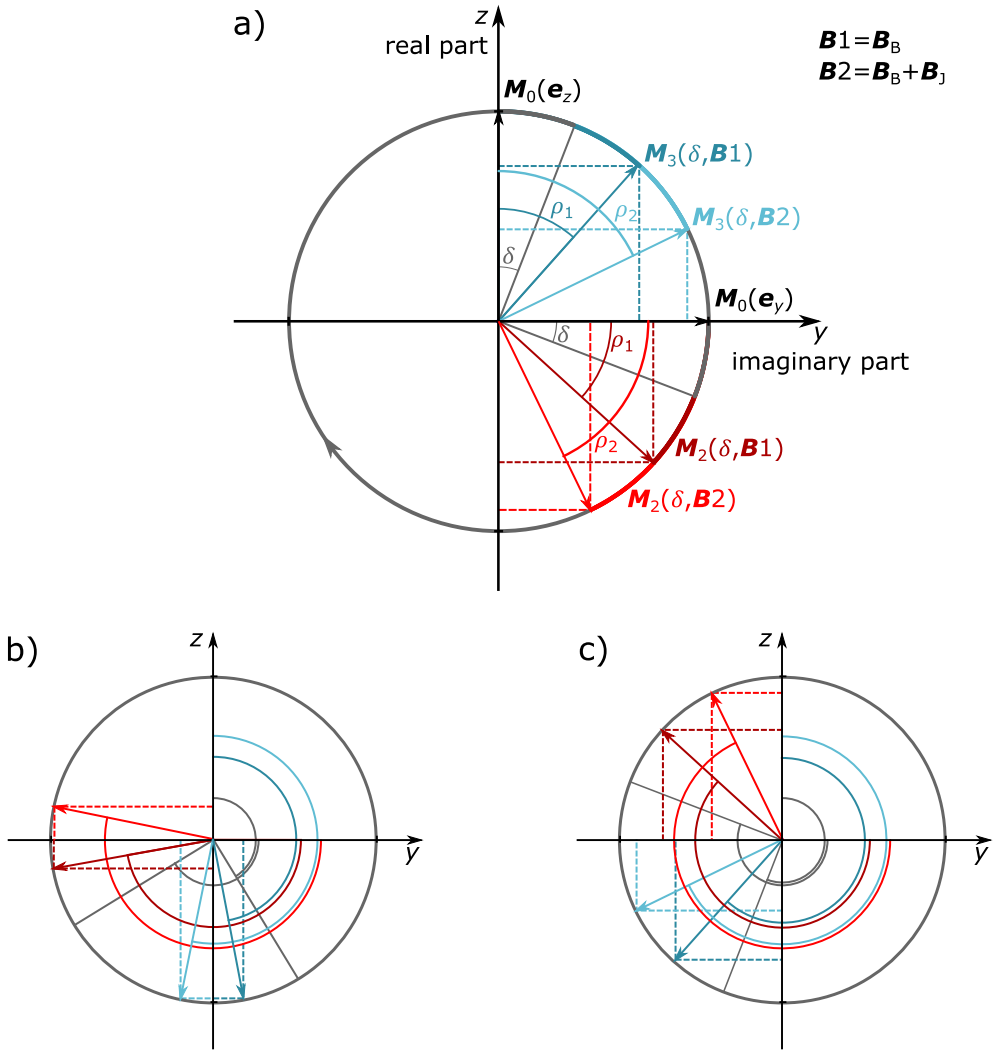

Figure 3.2: Single-voxel example for phase accumulation in zCDI, displayed in a 2D-plane. All fields ($\boldsymbol{B}_\mathrm{B}$, $\boldsymbol{B}_\mathrm{J}$, $\boldsymbol{G}$, $\boldsymbol{B}_0$) are assumed purely x-directional. Each panel shows four measurements ($\boldsymbol{B}1$ and $\boldsymbol{B}2$, with starting magnetizations in $\boldsymbol{e}_y$ ($\boldsymbol{M}_2$) and $\boldsymbol{e}_z$ ($\boldsymbol{M}_3$), respectively). Since the rotation axis is $\boldsymbol{e}_x$, the z- and y-components of the magnetization vectors correspond directly to real and imaginary parts of the resulting MR signal, converted to complex representation. The associated phase is given by ρ. All measurements are subject to the same phase offset δ, originating from the imaging fields. The panels visualize the three cases for phase offsets δ, so that phase wrapping does not occur (a), phase wrapping occurs for measurements of $\boldsymbol{B}_2$, but not for $\boldsymbol{B}_1$ (b), and phase wrapping occurs equally for all measurements (c).

In this example, where $\mathrm{Re}(\tilde{M}_2) = \mathrm{Im}(\tilde{M}_3)$, one of the two measurements would be sufficient to extract the amplitude of $\boldsymbol{B}_x$, which can be derived from equation (3.8). The phase offset δ causes overestimation of $\boldsymbol{B}1$ ($\boldsymbol{B}_\mathrm{B}$) and $\boldsymbol{B}2$ ($\boldsymbol{B}_\mathrm{B}$+$\boldsymbol{B}_\mathrm{J}$). Nevertheless, subtraction of the two reconstructions gives the correct estimation of $\boldsymbol{B}_\mathrm{J}$:

$$\hat{\boldsymbol{B}}_\mathrm{J} = \hat{\boldsymbol{B}}2 - \hat{\boldsymbol{B}}1. \tag{3.14}$$

Here, the $\hat{}$ symbol stands for the reconstruction of $\boldsymbol{B}$. Since ρ_1 and ρ_2 are smaller than π, no phase wrapping occurs.

However, the phase offset δ could range anywhere between $-\pi$ and π, easily pushing the phase ρ into a critical range. This scenario is illustrated in figure 3.2(b), where the large δ results in an overall phase ρ_2 above π, causing incorrect reconstruction in the negative amplitude range. As ρ_1 still ranges below π, the subtraction using (3.14) cannot compensate for the phase offset. If the phase offset is $\pi < \rho < 2\pi$, the reconstruction after (3.14) yields the correct result again, as shown in figure 3.2(c).

At this point, it should be noted that a realistic case is not subject to all fields being purely x-directional. The information on $\boldsymbol{B}$ is encoded in the phase and amplitude of the resulting signals and $\rho(\tilde{M}_1) \neq \rho(\tilde{M}_2) \neq \rho(\tilde{M}_3)$. In addition, the phase shift δ depends on the gradient parameters and non-ideality; hence is spatially-dependent and unpredictable. In conclusion, to obtain reliable reconstruction results, the phase offset δ should be eliminated beforehand, effectively preventing phase wrapping. Therefore, a reference phase is required. In the next section, it is explained how this reference phase can be determined using a calibration measurement.

3.3.3 Correct referencing in presence of a background field using a calibration measurement

The unknown phase shift δ hinders the correct interpretation of the amplitude and phase data acquired in the three measurements with starting magnetization in the three basis directions. As δ depends on the gradient parameters and timing, this reference should cover the same image space as the reconstruction. Recalling the sequence diagram in figure 3.4, the most obvious way to take a reference covering all phase shifts due to imaging fields would be to set $\tau = 0$ s. However, one has to keep in mind that the $\boldsymbol{B}_\mathrm{P}$ turn-off causes a transient room response. In the case of $\tau = 0$ s this transient would superimpose t_G and t_E, instead of τ, thereby falsify the reference. Therefore, the reference phase cannot be measured conventionally, but must be constructed from the measurements.

In conclusion, a method extracting δ from the measurements of $\boldsymbol{M}_1$–$\boldsymbol{M}_3$ is desired. I suggest a practical approach involving a calibration procedure. A well known, homogeneous magnetic field $\boldsymbol{B}_{\mathrm{cal}}$ could be used instead of $\boldsymbol{B}_{\mathrm{J}}$ to adjust the phase in the referenced reconstruction, such that $\boldsymbol{B}_{\mathrm{cal}}$ is recovered correctly. Thereby the operating procedure would be as follows:

- Measure $\boldsymbol{M}_1$, $\boldsymbol{M}_1$, and $\boldsymbol{M}_3$, for the fields $\boldsymbol{B}1$ ($\boldsymbol{B}_{\mathrm{B}}$) and $\boldsymbol{B}2$ ($\boldsymbol{B}_{\mathrm{B}}$+$\boldsymbol{B}_{\mathrm{cal}}$).
- Convert to complex representation $\tilde{M}_1$, $\tilde{M}_2$, and $\tilde{M}_3$, by Fourier transform.
- Extract the phase ρ_{ref} of $\tilde{M}_3(\boldsymbol{B}_{\mathrm{B}})$. This phase comprises δ and the phase accumulation due to the background field ρ_1.
- Reference all measurements $\tilde{M}$ by: $\tilde{M}_{\mathrm{referenced}} = |\tilde{M}|e^{(\rho - p_{\mathrm{ref}} + p_{\mathrm{cal}})}$.
- Now, ρ_{cal} is an additional phase, used to calibrate the reference phase p_{ref}. p_{cal} needs to be adjusted until $\delta = p_{\mathrm{ref}} + p_{\mathrm{cal}}$, such that the reconstruction $\hat{\boldsymbol{B}}_{\mathrm{cal}} = \hat{\boldsymbol{B}}2 - \hat{\boldsymbol{B}}1$ gives the correct amplitude of $\boldsymbol{B}_{\mathrm{cal}}$.

Later, when imaging $\boldsymbol{B}_{\mathrm{J}}$, the same procedure is executed, but with the fixed value p_{cal} from the calibration step.

The calibration procedure effectively decomposes the phases ρ and δ, enabling to compensate phase offsets from the imaging sequence, individually for each voxel. Nevertheless, the method is subject to some limitations. First, the calibration field should not be x-directional (or the direction of the main field for other setups). As one can see from figure 3.2, there are several sets of offset phases δ, that allow sufficient reconstruction even without calibration. Recalling equation (3.6), it becomes evident that y- and z-directional fields are more vulnerable to phase offsets. Secondly, the method relies on a reproducible phase offset, gained during the imaging sequence. In other words, non-ideality in the imaging fields should be stable. Fluctuations in the field ramps and amplitudes will cause errors, as the calibration phase causes under- or over-compensation.

3.3.4 Modifications to zCDI due to instrumental limitations

The reliable preparation of the magnetization to the three basis directions $\boldsymbol{e}_x$, $\boldsymbol{e}_y$, and $\boldsymbol{e}_z$, before the zero-field period is essential for successfull $\boldsymbol{B}_{\mathrm{J}}$-reconstruction. To manipulate the magnetization, Vesanen et al. [6] suggest to pulse $\boldsymbol{B}_0\boldsymbol{e}_x$ and $\boldsymbol{B}_1\boldsymbol{e}_y$, after the polarization field $\boldsymbol{B}_{\mathrm{P}}\boldsymbol{e}_z$ is turned-off. Here, the precession due to the pulses describes a rotation with the angle $\gamma t|\boldsymbol{B}| = \pi/2$. To be less sensitive to non-ideal

pulse ramps, t should be relatively long. On the other hand, fast spin manipulation is desired to prevent from magnetization losses due to relaxation. It can be estimated that small deviations of a few percent in the pulse length or amplitude cause error angles of some degree. Hence, this method is susceptible to non-ideal pulsing, thus difficult to implement experimentally. Furthermore, if the polarization field $\boldsymbol{B}_\mathrm{P}\boldsymbol{e}_z$ is not perfectly homogeneous, there will be an additional spatially-dependent error angle. In conclusion, pulsed fields as proposed by Vesanen et al. are not suitable to manipulate the orientation of the magnetization reliably.

The use of an adiabatic field switch between polarization field and defined guiding fields, as introduced in section 2.2.2 would be more stable. In this case, guiding fields oriented $\boldsymbol{e}_x$, $\boldsymbol{e}_y$, and $\boldsymbol{e}_z$, define the magnetization orientation after the turn-off. Figure 3.3 visualizes that a magnetization vector generated, for instance, by a 30 mT $\boldsymbol{B}_\mathrm{P}\boldsymbol{e}_z$ can be manipulated to $\boldsymbol{e}_y$ within 15 ms using a guiding field $\boldsymbol{B}_\mathrm{g}\boldsymbol{e}_y$ of approximately 30 μT. The data were generated solving equation (2.20) numerically. Therefore, a differential equation solver was implemented based on the notes in [130], using the standard 4$^{\mathrm{th}}$-order Runge-Kutta method with a fixed step size of 0.1 μs. Please note, that the technical realization of the $\boldsymbol{B}_\mathrm{P}$ waveform depends on the coil characteristics, mainly the coil inductance. Therefore, it might be necessary to increase the length of the waveform slightly. Besides, one might deal with angles between $\boldsymbol{B}_\mathrm{P}$ and $\boldsymbol{B}_\mathrm{g}$ that are larger than 90°, also requiring longer turn-off times. Nonetheless, waveform lengths

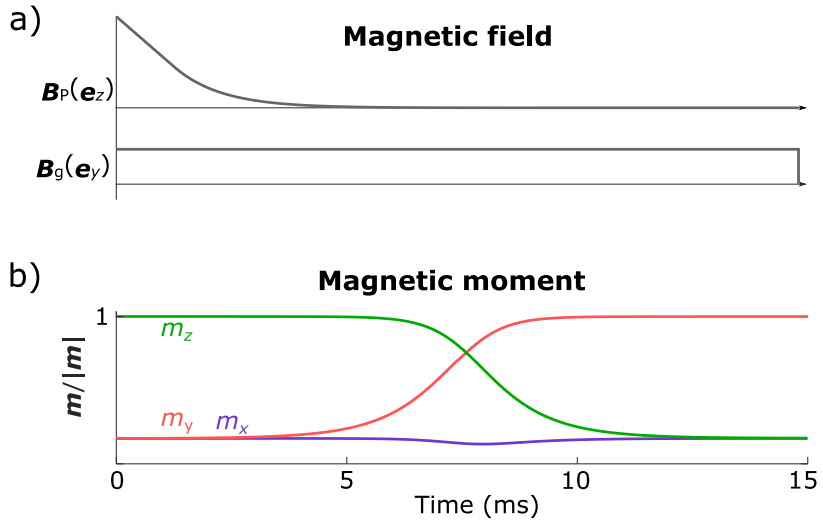

Figure 3.3: Adiabatic turn-off of $\boldsymbol{B}_\mathrm{P}\boldsymbol{e}_z$ (30 mT) into $\boldsymbol{B}_\mathrm{g}\boldsymbol{e}_y$ (30 μT). a) displays the magnetic field waveform of $\boldsymbol{B}_\mathrm{P}$ and $\boldsymbol{B}_\mathrm{g}$, where $\boldsymbol{B}_\mathrm{P}$ consists of a linear decay at the beginning, turning into an exponential decay after approximately 1.4 ms. b) shows the corresponding evolution of the magnetization vector. Note, equilibrium magnetization at $t = 0$ is assumed according to $\boldsymbol{B}_\mathrm{P}$.

of approximately 20 ms have proven sufficient for many sets of conditions, tested in simulations.

A modified sequence including the adiabatic turn-off of $\boldsymbol{B}_\mathrm{P}$ is illustrated in figure 3.4. It can be divided into five different periods, the polarization time t_P, the interval t_M for the manipulation of the orientation of $\boldsymbol{M}$, the zero-field period τ, the phase-encoding time t_G, and the echo time t_E. At first, magnetization is built up by a polarization field active during t_P. As mentioned before, to achieve equilibrium magnetization, t_P should be approximately three times the T_1 relaxation time constant in the millitesla regime. In the second stage, during t_M, the magnetization is manipulated into $\boldsymbol{e}_x$, $\boldsymbol{e}_y$, or $\boldsymbol{e}_z$ by an adiabatic field switch of the polarization field into defined guiding fields $\boldsymbol{B}_\mathrm{g}$. This takes approximately 15–20 ms depending on the strength of the polarization field. Subsequently, all MRI fields are turned off, and the current density $\boldsymbol{J}$ is applied during a defined zero-field time τ. When choosing the length τ, the trade-off between SNR-loss due to relaxation and SNR-gain due to an increasing rotation angle φ needs to be taken into account. Vesanen et al. [6] state that the optimum length of τ is given by the T_2 relaxation time, provided that phase wrapping can be excluded. In section 2.4.1, it was elaborated that the T_2 relaxation time of brain tissue in the microtesla regime can be expected at around 100 ms.

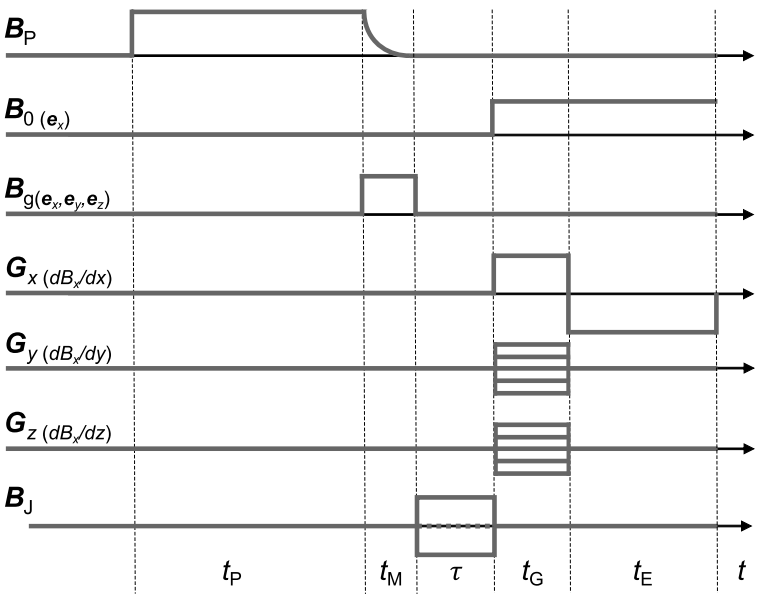

Figure 3.4: Fourier gradient echo sequence for zCDI. The sequence is devided into five stages (t_P – polarization, t_M – manipulating the orientation of the magnetization, t_Z – zero-field encoding, t_G – spatial encoding, and t_E – echo time).

3.3.5 Challenges towards the technical realization of zCDI

The successful realization of the zCDI sequence requires all field ramps to be sufficiently fast to satisfy a non-adiabatic field change (with the exception of $\boldsymbol{B}_\mathrm{P}$). In that regard, Vesanen et al. [6] reported switching the low-noise currents in the $\boldsymbol{B}_0$-coil and the frequency-gradient coil most challenging.

As both coils are active during readout, they are usually driven by current sources with heavily filtered output stages, limiting bandwidth and slew-rate. Vesanen et al. [6] state that ULF-MRI setups, able to pulse all MRI fields sufficiently fast, exist (e.g., Zotev et al. [107]). However, in [107], field switching was limited to current reversal to obtain gradient echos. Zotev et al. do not clarify how field switching was realized, but it seems like current reversal can be easily achieved by switching the polarity of the coils, e.g., using solid state relays [95]. This way, the current source itself would not be involved in the switching procedure at all. Turning the current off, as required for the zero-field period, is more difficult.

Shortly after [6] was published, a concept of a fast and low-noise current amplifier was presented by the same group [131], potentially overcoming the difficulties in field switching. The amplifier features a kHz-bandwidth and an ultra-low-noise mode, where current feedback is disabled during the short period of readout (t_E). This is effectively freezing the output current, providing a noise performance of approximately 60 pA/Hz$^{1/2}$. A potential drawback of this method is that the source is not regulating the current during the time interval of the readout. Especially during gradient-echo sequences, where the current in the coils needs to be reversed, this method's reliability appears questionable.

A more simple approach, that is pursued in this thesis, involves a dummy load and a switching circuit that bypasses the coil current during the zero-field time. If the dummy load is chosen carefully to mimic the coils ohmic resistance, and if the switching times are sufficiently fast, the current source does not have to regulate the current. The technical realization of this procedure is presented in the following chapter, section 4.2.3.

3.4 Chapter summary and discussion

In this chapter, requirements for *in-vivo* applicability of CDI have been formulated based on literature values for $\boldsymbol{B}_\mathrm{J}$, $\boldsymbol{J}$, and relaxation times. Three demands on a potential sequence have been identified: sensitivity for weak magnetic fields < 10 nT, $\boldsymbol{B}_\mathrm{J}$-encoding within 100 ms, and a reasonable overall measurement time to obtain

sufficient resolution and SNR. Two sequences, namely aCDI by Nieminen et al. [7], and zCDI by Vesanen et al. [6] were assessed with regard to the formulated requirements.

It has been found, that aCDI is not suitable to detect magnetic fields as low as expected during the *in-vivo* impression of currents to the human head. The turn-off times for $\boldsymbol{B}_\mathrm{P}$ required to satisfy the adiabatic condition are too long with respect to the relaxation times of head tissue.

The zCDI sequence seems feasible. However, approximated rotation angles of 15° due to precession according to $\boldsymbol{B}_\mathrm{J}$ during $\tau = 100$ ms are relatively small. Full exploitation of the sensitivity would require much longer zero-field times. However, this is impracticable regarding the short relaxation times of brain tissue. Hence, a sensor setup with an extraordinary noise performance and a strong polarization field is desired to compensate for the sensitivity losses. Section 4.3 gives a detailed description of the sensor developed during this work. A survey of the sensitivity as function of SNR is presented in chapter 6.

Due to hardware limitations, Vesanen et al. [6] validated zCDI in simulations. Experimental issues, such as the preparation of the magnetization's orientation, or defined field switching, were not covered in detail. In this chapter, an adiabatic field change between polarization field $\boldsymbol{B}_\mathrm{P}$ and defined guiding fields $\boldsymbol{B}_\mathrm{g}$ was proposed for the preparation of the magnetization. The technical realization is explained in section 4.2.2. Flexible switching of all MRI fields will be realized by switching circuits and low-noise current sources. This issue will be revisited in section 4.2.3.

A slightly modified sequence was presented, including a calibration procedure that compensates for phase shifts due to the imaging fields. A drawback of the proposed operation is the substantial requirement of reproducible magnetic field ramps and amplitudes. Fluctuations will cause reconstruction errors, manifesting either as increased noise, if the fields are constantly changing, or as systematic offsets, if the setting changes between calibration and measurement. In any case, the calibration procedure seems unavoidable in a realistic situation.

Chapter 4

Development of the ULF-MRI setup for zCDI

The experimental implementation of zCDI requires an ULF-MRI scanner that enables 3D-MRI, provides high sensitivity, and allows the necessary flexibility in field switching. The developed scanner is a joint project of the working group 8.25 (Ultra-Low-Field MRI) of the PTB. In this chapter, all hardware necessary for the implementation of zCDI are listed and explained in detail. Besides zCDI, the scanner is intended to be used for NCI and possibly other ULF-MRI or ULF-NMR experiments. The sensor itself is also used as a stand-alone device.

The methods and results presented in this chapter have partly been previously published in [71, 72, 74]. Parts of the text and figures are extracted from those publications.

4.1 Status of the PTB-ULF-MRI scanner

The concept of the coil system for zCDI is based on the development of Ingo Hilschenz [95]. For his doctoral thesis, he designed a prototype 2D-ULF-MRI setup for structural imaging based on proton density. The setup comprised a Helmholz coil for the generation of a main field in the x-direction, a Maxwell coil to provide a gradient field $d\mathrm{B}_x/dx$, and bi-planar coils for phase gradients $d\mathrm{B}_x/dy$ or $d\mathrm{B}_x/dz$. The pre-polarization, necessary for sample magnetization, was generated using a small solenoid coil. Transverse magnetization was generated by a non-adiabatic field change of $\boldsymbol{B}_\mathrm{P}\boldsymbol{e}_z$ into $\boldsymbol{B}_0\boldsymbol{e}_x$. Gradient echoes were acquired using a switching circuit, as displayed in figure 4.1, that changes the polarity in the frequency gradient. Using this system, Hilschenz et al. [132] were able to perform 2D imaging at Larmor frequencies down to 100 Hz.

Based on that prototype a more sophisticated ULF-MRI setup was designed by Hilschenz, where computerized numerical control (CNC) manufacturing ensured de-

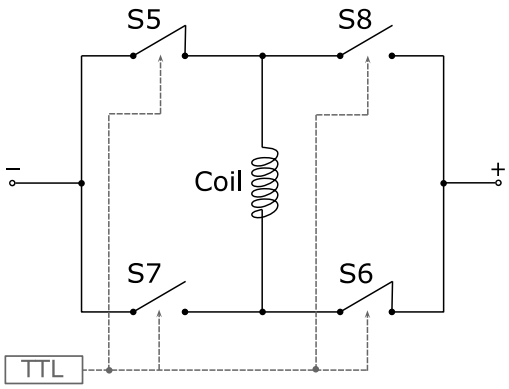

Figure 4.1: Schematic of the swithing circuit designed by Ingo Hilschenz to change the polarity in the frequency-gradient coil. The figure was modified from [95].

fined geometries. In addition to the Helmholz coil that generates the main field in the x-direction, two Helmholz coils for homogeneous fields in the y- and z-directions were installed. Although not used at this stage, these coils could potentially be employed to generate rf pulses that tip the magnetization in 90° or 180° which would relax the constraint of a polarization field perpendicular to the main field. A picture of the setup is shown in figure 4.2. It was operated inside a custom-designed magnetically shielded room, the ZUSE chamber, which is based on the commercially available AK3b (Vacuumschmelze GmbH & Co. KG, Hanau, Germany). This room consists of two layers of MUMETAL®, one eddy current shield, and it is situated inside a rf-shielded room made of 2 mm thick zinc-plated steel panels. Outside the magnetic shield, several power amplifiers and current sources drove the MRI coils. Switching circuits were installed that decouple the amplifiers from the coils during readout. In-house-built low-noise current sources operated the main field and the frequency gradient which are active during readout.

The sensor system comprised a one-channel 1st-order axial gradiometer, inductively coupled to a current-sensor SQUID. The lHe dewar holding the sensor was modified for low noise performance and from then on called "low-intrinsic-noise dewar (LINOD)". Therefore, mylar foil, commonly used as a radiation heat shield, was replaced by aluminum vaporized polyester, resulting in reduced thermal noise. The white noise level of the sensor system was reported at approximately 0.5 fT Hz$^{-1/2}$.

Coil setup and data acquisition were controlled via a PXI™ (National Instruments™ (NI™), Austin, Texas, USA). A multi-input/output card (NI™ 6289), an RS 232 connector (NI™ 8432/2), and an analogue-output module (NI™ 6733) was used to control the various hardware components. A dynamic-signal-acquisition card (NI™ 4462) allowed simultaneous sampling of four channels with 24-bit resolution and a maximum sampling rate of 204.8 ksps. A counter module (NI™ 6602) was employed

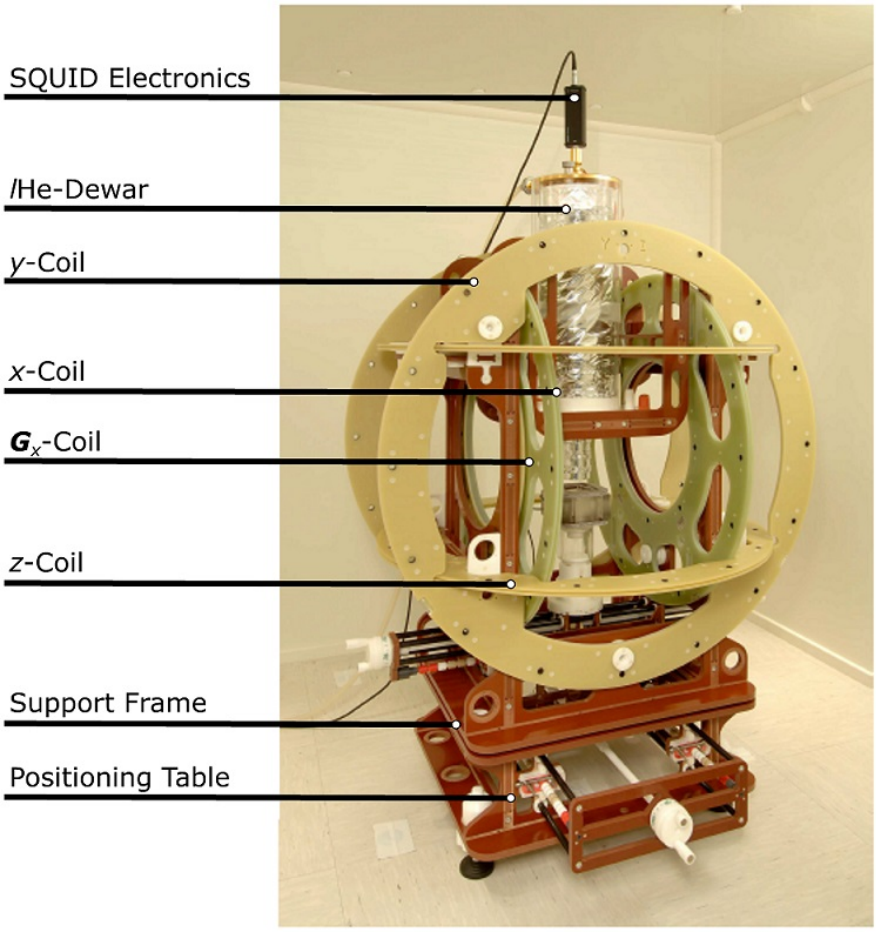

Figure 4.2: ULF-MRI setup, designed by Ingo Hilschenz, that served as basis for this work. The picture was extracted from [95].

for the timings, and a multi-system-extension interface (NI™ MXI-4) was used to connect the PXI™ chassis to a control computer outside the rf room via an optical link. LabVIEW™-based control software was developed to initiate pulse sequences.

Körber et al. [113] and Höfner et al. [133, Chapter 6] used the setup with modifications in the polarization setup for phantom studies on NCI. Later, a self-shielded Helmholz-type pre-polarization coil, similar to [91], was designed by Jaakko O. Nieminen. This coil enables the generation of nearly homogeneous polarizing fields in the x-direction while reducing the magnetization of the MUMETAL® walls and thereby additional transient fields to a minimum. As the polarization is now in parallel to the main field, a subsequent spin flip is required to record FPDs.

The described developments formed a basis for the ULF-MRI scanner that was optimized for zCDI. Therefore, the system needed to be upgraded for 3D-imaging and equipped with additional coils and switches to realize different orientations of the magnetization and the zero-field period. The hardware components were chosen based on the requirements for each specific section of the zCDI sequence. A detailed

description is given in section 4.2. The zCDI sequence was implemented in the existing LabVIEW™ framework by Hilschenz. Furthermore, the sensor was modified for ultra-low-noise operation, as described in section 4.3. A validation using phantoms is given in chapter 5.

4.2 The coil setup for zCDI

This section describes the hardware chosen to realize zCDI. Please refer to figure 3.4 for a sequence diagram.

4.2.1 Stage 1: The polarization period

The most substantial requirement regarding the polarization field is the generation of a strong magnetization. However, the zero-field period in zCDI poses unique restrictions to the polarization setup. Transient room responses, as present after $\boldsymbol{B}_\mathrm{P}$-turn-off, will superimpose $\boldsymbol{B}_\mathrm{J}$ and have to be treated as part of the background field $\boldsymbol{B}_\mathrm{B}$. $\boldsymbol{B}_\mathrm{J}$ and $\boldsymbol{B}_\mathrm{B}$ both contribute to the phase φ accumulated during the zero-field time τ. To avoid phase wrapping ($-\pi < \varphi < \pi$), the length of τ needs to be chosen carefully. At the same time, a large phase accumulation due to $\boldsymbol{B}_\mathrm{J}$ is required, thus $\boldsymbol{B}_\mathrm{B}$ should be on the order of $\boldsymbol{B}_\mathrm{J}$ or smaller. Consequently, a self-shielded polarization setup is desired, reducing magnetization and eddy currents in the shielded walls.

The self-shielded coil designed by Nieminen is well suited for this purpose, albeit it possesses several limitations. The overall wire length of the Helmholtz-type coil, including the shield, is long compared to a non-shielded design, resulting in relatively high resistance of approximately 7.5 Ω at 293 K. Furthermore, the compact design with many windings limits the heat dissipation to the surrounding air-conditioned environment. An increased resistance that is proportional to the temperature rise (at least up to temperatures of ≈ 470 K) is the consequence, which can be estimated by a linear approximation taking into account the temperature coefficient of pure copper $\alpha = 3.93^{-3}$ K^{-1} at 293 K [134]:

$$R(T) = R_{T_0}[1 + \alpha(T - T_0)]. \tag{4.1}$$

The high resistance demands for a power reserve of the amplifier driving the coil. The available amplifier, HERO®POWER PA2032A (Rohrer® GmbH, Munich, Germany), enables the application of 4.5 kW; either 30 A and 150 V or 60 A and 75 V. Figure 4.3 illustrates the estimated coil resistance in a range between 293 K and 393 K and the

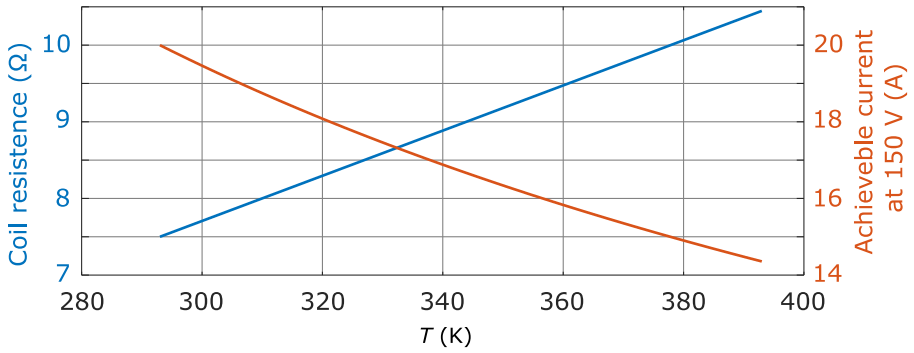

Figure 4.3: Estimated change of resistance with temperature T in self-shielded polarization coil (blue – left y-axis) and corresponding polarization current at 150 V (red – right y-axis).

corresponding current at 150 V. Exemplary for a current of 17 A, the increase in temperature must be limited to a maximum of 45 K. A sufficient duty cycle and possibly longer measurement breaks need to be planned accordingly. In measurements, monitoring the amplifier output voltage, it was determined that a current of 17 A at a polarization time of 0.5 s requires a duty cycle $\approx 1/3$ and a longer break after approximately 1600 polarization runs. Please note, the zCDI sequence accompanied by a structural image with 30×30 k-steps requires $30 \times 30 \times 7 = 6300$ runs.

Balancing the benefits and limitations, I decided to use the self-shielded coil for a demonstration of zCDI in phantoms. Subsequently, the need for a possible modification of the setup towards *in-vivo* measurements could be assessed based on the conducted measurements and simulations.

During readout, the power amplifier needs to be decoupled from the polarization coil to eliminate noise interference. Figure 4.4 visualizes the utilized decoupling scheme, which is based on a development by Hilschenz [95]. The circuit is controlled by the PXI™ system via five digital inputs using transistor-transistor logic (TTL). To initiate the polarization, the amplifier is set to current mode via TTL 1 and TTL 2. After the polarization period, the switches S1–S3 disconnect the coil from the amplifier. Simultaneously, the switches S4 and S5 set one side of the coil and intermediate elements in the circuit to ground potential. Additionally, the power amplifier is switched to a voltage-source mode via TTL 3. Modifications to the setup include the transient voltage suppression (TVS) diodes Ds and the resistor R, which set a defined turn-off slope for the coil current. As explained in the next section, the slope, combined with defined guiding fields, is key to the adiabatic field change intended to manipulate the orientation of the magnetization prior to the zero-field period. For a detailed visualization of the timing in the zCDI sequence, please see figure A.5 in the appendix.

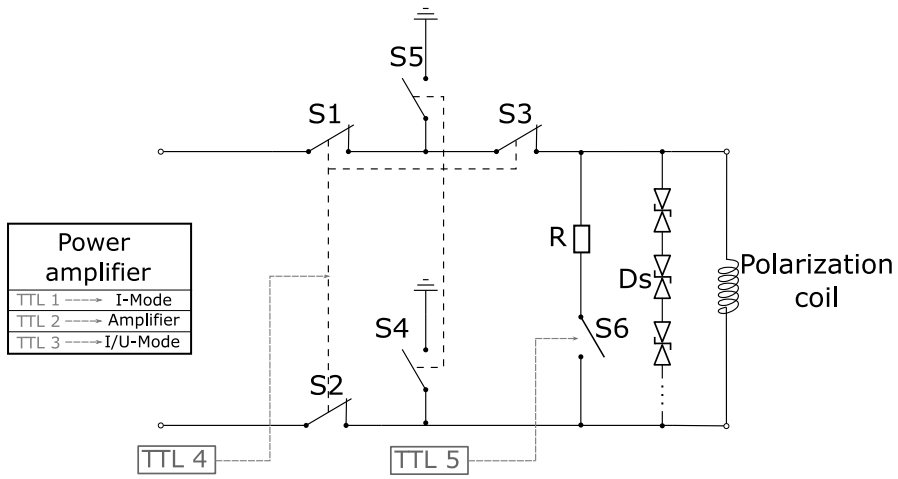

Figure 4.4: Decoupling Scheme for polarization setup. The switches S1–S3 disconnect the coil from the power amplifier, while S4 and S5 set the coil and intermediate circuits to ground potential. S6 activates the parallel resistor R, that sets a defined waveform for the turn-off of the polarization current. The circuit is controlled by the PXI™ system via the digital control signals TTL 1–5.

The switches S1–S6, and all further switching circuits presented in this thesis, represent bipolar potential-free solid state relays based on either metal oxide semiconductor field effect transistors (MOSFETs) or insulated gate bipolar transistors (IGBTs), as explained in appendix A.1. They feature electrical isolation from the signal input ensuring a low-noise operation of the circuit.

4.2.2 Stage 2: Manipulating the orientation of the magnetization

The polarizing field is turned off adiabatically into defined guiding fields $\boldsymbol{B}_\mathrm{g}$ to accomplish the different magnetization orientations. In section 3.3, it was shown that an adiabatic field switch can be achieved using a 30 mT polarization field and a 30 μT perpendicular guiding field within 15 ms. In this setup, the polarization setup can only generate 17 A polarization current, yielding approximately 17 mT polarization field. The guiding field strength can be lowered due to the reduced current, possibly decreasing transient room responses due to guiding-field switching.

Figure 4.5 illustrates the adiabatic turn-off of a 17 mT polarizing field in the x-direction into a 20 μT $\boldsymbol{B}_\mathrm{g}$ in the y-direction. The slope of $\boldsymbol{B}_\mathrm{P}$ is shown in figure 4.5(a) on a logarithmic scale. It was generated using a hardware-realistic calculation, simulating a parallel network of ohmic resistors and TVS diodes. The corresponding circuit is sketched in figure 4.4. At TTL-level input, the switches S1–S3 decouple the polar-

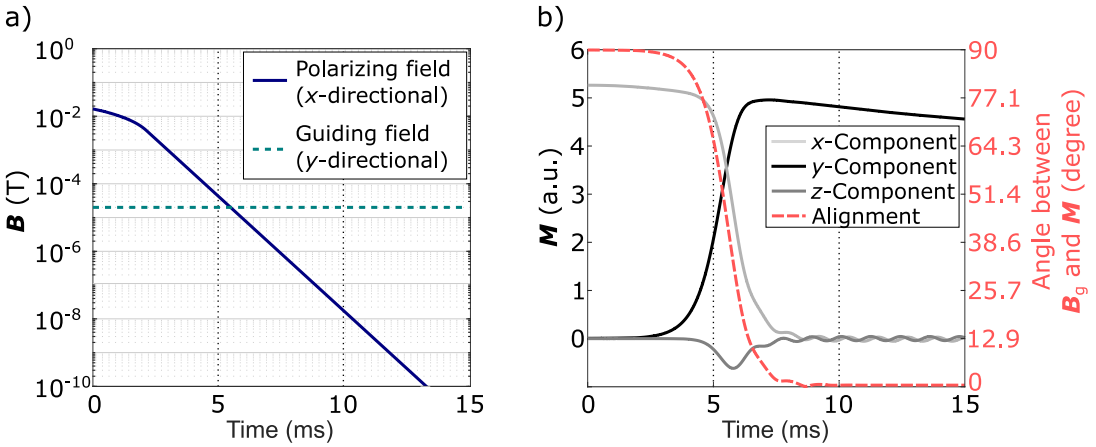

Figure 4.5: Simulation of magnetization reorientation via adiabatic turn-off during t_{M}. a) shows the time dependence of the simulated turn-off of a 17 mT polarizing field in the x-direction and a 20 μT guiding field in the y-direction. b) displays the time dependence of the simulated evolution of the magnetization (left y-axis). The alignment between $\boldsymbol{M}$ and the guiding field is displayed in red (right y-axis).

ization coil from the power amplifier. The resulting induction voltage U in the coil is limited by the TVS diodes Ds to the breakthrough voltage U_{Ds} causing the current in the coil to discharge, following a linear regime:

$$\frac{dI_{\mathrm{P}}}{dt} = \frac{-U_{\mathrm{Ds}}}{L_{\mathrm{P}}}. \tag{4.2}$$

Here, L_{P} is the inductance of the polarization coil, and I_{P} the polarization current. Once the current falls to a value at which the resulting voltage across R would be below U_{Ds},

$$U(t) = \left(I_{\mathrm{P}}(0) + t\frac{dI_{\mathrm{P}}}{dt} \right) R < U_{\mathrm{Ds}}, \tag{4.3}$$

Ds become highly-resistive, and the energy is dissipated only via the ohmic resistor R. This causes an exponential decay with the time constant L_{P}/R. The current discharge $I_{\mathrm{P}}(t)$ can finally be estimated by

$$\begin{aligned} &I_{\mathrm{P}}(0) + t\frac{dI_{\mathrm{P}}}{dt} && \text{, when } I_{\mathrm{P}}(t)R > U_{\mathrm{Ds}}, \text{ and} \\ &\frac{-U_{\mathrm{Ds}}}{R} \exp\left(-\frac{tR}{L_{\mathrm{P}}}\right) && \text{, when } I_{\mathrm{P}}(t)R < U_{\mathrm{Ds}}. \end{aligned} \tag{4.4}$$

After the coil is fully discharged, the closed circuit is disconnected via S6 (compare figure 4.4) preventing noise interference.

The values $L_{\mathrm{P}} = 173$ mH, $R = 270\ \Omega$, and $U_{\mathrm{Ds}} = 1090$ V yield the waveform shown in figure 4.5(a) and were implemented in the hardware. The simulated spin

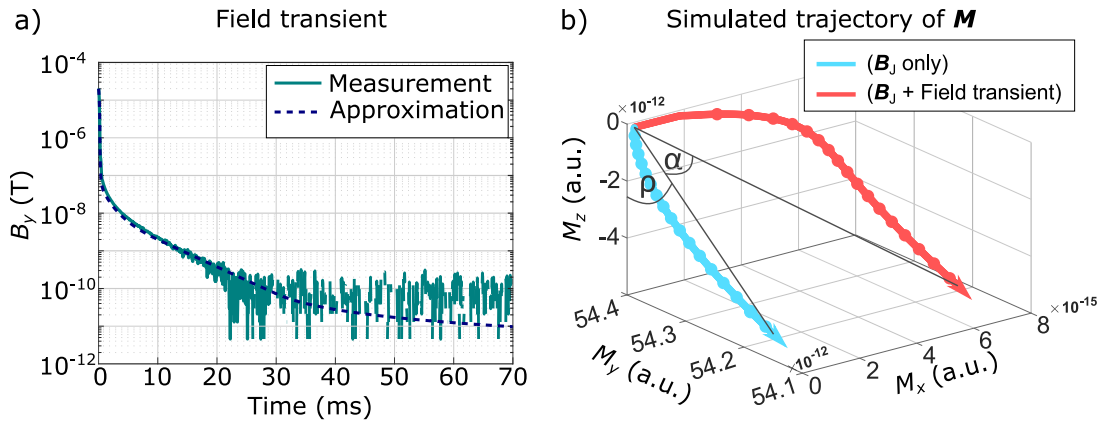

Figure 4.6: The influence of transients generated by the guiding fields on spin dynamics during $\tau = 70$ ms. a) shows a fluxgate measurement of the transient magnetic field in the y-direction after turn-off of $\boldsymbol{B}_g\boldsymbol{e}_y$ and approximation by combination of several exponential decays. b) displays the simulated evolution of magnetization during the zero-field encoding period for $\boldsymbol{B}_J\boldsymbol{e}_x$ (light blue), and $\boldsymbol{B}_J\boldsymbol{e}_x$ plus the transient field in $\boldsymbol{e}_y$ (red). The time scale is given by bold dots in 4-ms steps. The angles ρ and α represent the evolution of magnetization due to $\boldsymbol{B}_J$ and the error angle due to the transient field, respectively. Please note the x-axis is blown up by three orders of magnitude.

dynamics corresponding to the field change are given in 4.5(b). They show that a $\boldsymbol{B}_g$ of approximately 20 μT is sufficient for spin reorientation within 15 ms and an alignment error of approximately 0.5°. Unlike in figure 3.3, this simulation incorporates relaxation $T_1 = T_2 = 100$ ms, hence visualizes a realistic evolution of the magnetization.

Enlarging the guiding fields would reduce the alignment error. However, they could induce magnetization and eddy currents in the MUMETAL® walls yielding transient decays after turn-off parallel to $\boldsymbol{B}_g$. Therefore, setting the strength of $\boldsymbol{B}_g$ is a compromise between an alignment error of the starting magnetization and influences of the transient fields on spin dynamics during τ. Using a three-axis fluxgate with a 3 dB bandwidth of 3 kHz (Mag-03MS, Bartington), the transient fields during τ after ramping down $\boldsymbol{B}_g\boldsymbol{e}_y$ were recorded as shown in figure 4.6 (a). A fast decay due to the current ramp down in the coil within 1 ms and the slower MUMETAL® response decreasing from about 90 nT down to less than 1 nT in 15 ms were observed. An approximation of the field transient by several combined exponential decays was used to simulate the influence on the evolution of the magnetization in the presence of a perpendicular $\boldsymbol{B}_J$ varying between 1 and 50 nT. An illustration for the case of $\boldsymbol{B}_J = 10$ nT is given in figure 4.6 (b). The transient in parallel to the starting magnetization influences spin dynamics only slightly, yielding an error angle smaller than 0.13 %. For reasons of illustration, these simulations were performed ignoring relaxation.

Table 4.1: Parameters of the guiding-field coils

Coil	Dimension (mm)	d (mm)	Windings per coil arm [layers, rows]	Resistance (Ω)	Inductance (mH)	B/I in center (μT/A)
$B_{g,x}$	947 (⌀)	472	[1, 3]	0.6	0.07	5.7
$B_{g,y}$	670 × 484	640	[1, 3]	0.4	0.04	4.2
$B_{g,z}$	1047 (⌀)	522	[1, 3]	0.9	0.08	5.3

⌀ – diameter; d – distance between coil arms;
B/I – field-to-current ratio

The reconstruction of all three components of a magnetic field using zCDI requires three different measurements with starting magnetizations in $\boldsymbol{e}_x$, $\boldsymbol{e}_y$, and $\boldsymbol{e}_z$, respectively. Theoretically, perfect alignment in the three directions is required. Misalignment will result in systematic reconstruction uncertainty, where the relative error depends on the total rotation angle due to $\boldsymbol{B}$ during τ. In reality, the systematic misalignment will cause an error field, which will be assigned to the background field, thereby compensated by background field subtraction. Nevertheless, the misalignment should be minimal, to prevent phase wrapping and ensure stable reconstruction.

The Helmholtz coils in the coil setup from Hilschenz, oriented in the x-, y-, and z-direction, could be exploited to generate guiding fields for the manipulation of the spin orientation using adiabatic turn off of $\boldsymbol{B}_\mathrm{P}$. The field orientations and strengths were evaluated in measurements using a 3-axis fluxgate to detect a possible misalignment. The methodology and the results are explained in detail in appendix A.2. Including measurement uncertainty, the total sum of error angles in the system comprising $\boldsymbol{B}_\mathrm{g}\boldsymbol{e}_x$, $\boldsymbol{B}_\mathrm{g}\boldsymbol{e}_y$, and $\boldsymbol{B}_\mathrm{g}\boldsymbol{e}_z$ was estimated to be below 0.9°, corresponding to an error field of 0.59 nT. Hence, the coil system by Hilschenz fulfills the orthogonality requirements for zCDI using adiabatic turn-off for manipulating the magnetization orientation. The reconstruction uncertainty due to the orthogonality error of the coil system is well below 1 nT and poses no risk for phase wrapping.

However, the reliable operation of the coil setup required some practical modifications. To yield sufficiently fast switching times for the guiding fields $\boldsymbol{B}_\mathrm{g}\boldsymbol{e}_x$, $\boldsymbol{B}_\mathrm{g}\boldsymbol{e}_y$, and $\boldsymbol{B}_\mathrm{g}\boldsymbol{e}_z$, the coil inductances and resistances were lowered as listed in table 4.1 (compare table A.1 for the original parameters). The number of windings in each coil was reduced to three. In addition, the size of the y-coil required modification, as transient room responses of several tens of nT superimposed the zero-field time after the turn-

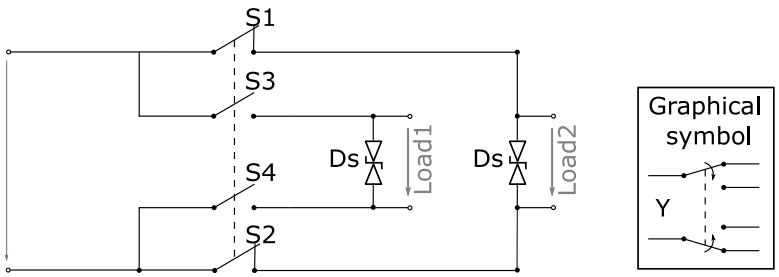

Figure 4.7: Switching circuit to discriminate between two different loads (Y-Switch)

off of $\boldsymbol{B}_{\mathrm{g}}\boldsymbol{e}_y$. The coil was replaced by a quadratic 3-turn coil arrangement, yielding a sufficiently low chamber response, which is illustrated in figure 4.6. The same CNC-manufactured coil arms were utilized, which is why the orthogonality was not inspected again.

Since the guiding fields in $\boldsymbol{e}_x$, $\boldsymbol{e}_y$, and $\boldsymbol{e}_z$ are operated sequentially and only during the time of the $\boldsymbol{B}_{\mathrm{P}}$ turn-off, they can be driven by one power amplifier, which can also be shared with one of the phase-gradient coils. For this purpose, the precision power amplifier Hubert® A1110-16 (Dr. Hubert GmbH, Bochum, Germany) is employed. My colleagues Nora Höfner and René Bösel developed a decoupling scheme that allows one to choose between two different loads on a millisecond time-scale. An internal logic based on a processing unit was realized that ensures sequential activation of both outputs.

For the zCDI sequence, four coils shall be driven by one power amplifier. Therefore, the decoupler was expanded by two additional Y-switches (see figure 4.7) that enable choosing between two different loads, respectively, on TTL-level input. Four bipolar relays (compare figure A.1) connect or disconnect both ends of the coils. In principle, this operation could have been realized by two relays, but disconnecting both ends of the coils prevents potential disturbances. TVS diodes in parallel to the coils ensure fast discharge of the coil currents and protect the circuit from high induction-voltage peaks.

The entire switching circuit, including the logic for the TTL input, is sketched in figure 4.8. Here, the switches S1–S10 decouple the coils and require two TTL inputs ensuring sequential activation. The Y-switches Y1–2 can be controlled with one TTL level to discriminate between two outputs, respectively. Two of the guiding-field coils are not set to ground potential, when inactive. As this is usually avoided to prevent floating potentials, it also means lower complexity of the circuit, which already consists of 36 power MOSFETs in total. Since all coils but the $\boldsymbol{G}_y$-coil can be activated well before piloting the power amplifier, switching under load is not required and switching times are not critical.

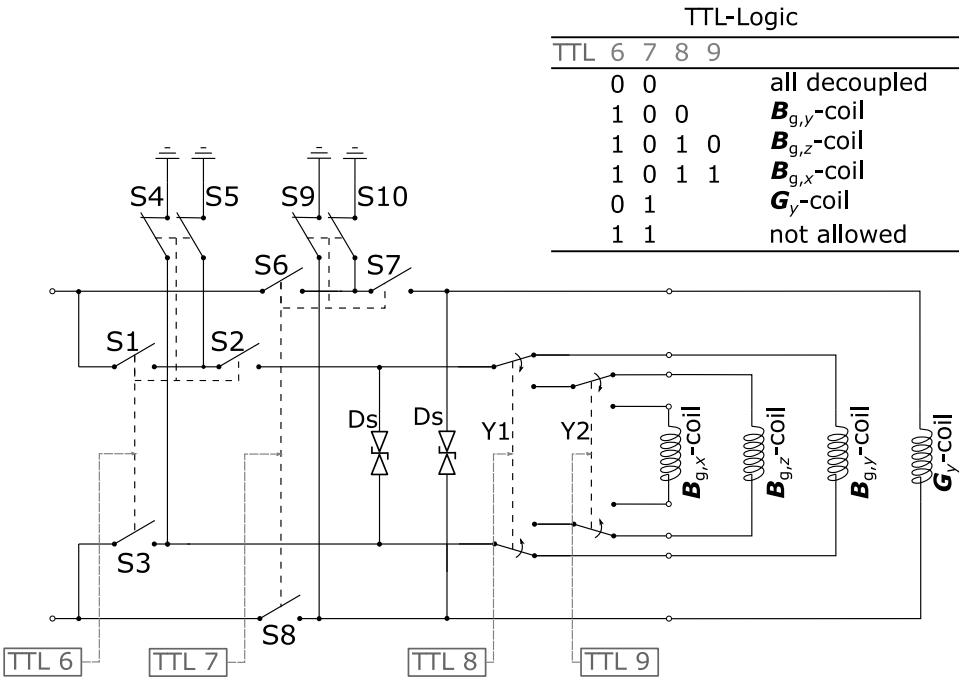

Figure 4.8: Circuitry and decoupling scheme for the guiding fields and one phase gradient. The switches S1–S10 decouple the coils and discriminate between phase gradient or guiding fields. An internal TTL-logic (upper right) ensures sequential activation. The Y-switches Y1–2 discriminate between the three guiding-field coils.

4.2.3 Stage 3: The zero-field period

After the magnetization is oriented in $\boldsymbol{e}_x$, $\boldsymbol{e}_y$, or $\boldsymbol{e}_z$, all MRI fields are turned off and the spins evolve in $\boldsymbol{B}_\mathrm{B}+\boldsymbol{B}_\mathrm{J}$, or just in $\boldsymbol{B}_\mathrm{B}$. The polarization coil is fully discharged during the adiabatic turn-off and the guiding fields can be quickly turned off and decoupled, as presented in the previous section. The $\boldsymbol{B}_0$-field and the frequency gradient, however, need to be switched off as well. During a conventional ULF-MRI sequence, these fields are persistently active, allowing the use of low noise current sources. These usually exhibit heavily filtered output stages, limiting bandwidth and slew-rate. The resulting response times make fast switching impracticable.

Two in-house-built current sources, are available for the main field and the frequency gradient, respectively. The feedback circuits of the current sources, in combination with the coils, have a 3 dB small-signal bandwidth of approximately 10 kHz. The current noise was measured to be approximately 360 pA $\mathrm{Hz}^{-1/2}$. Fast switching is pursued via dummy circuits, mimicking the coils' ohmic resistances. Here, the current is switched between coil and dummy load. Figure 4.9 illustrates the dummy circuit connected to the frequency gradient. During the zero-field time, a TTL-voltage level switches S1–S4, where S1–S3 redirect the current between coil and dummy and S4 fixes the coil potential to ground. The dummy load is carefully chosen to match the nominal ohmic

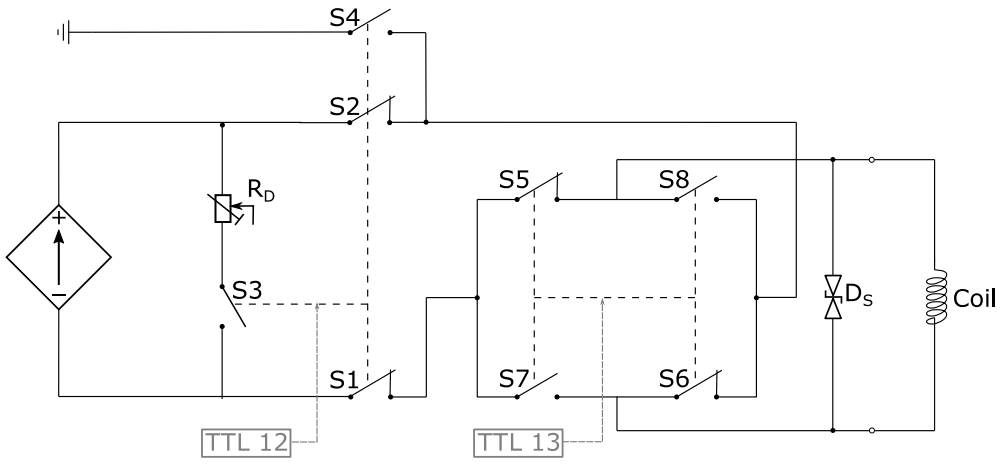

Figure 4.9: Circuitry for fast switching of low-noise currents. S1–S3 switch the current between the coil and a dummy load R_D that can be tuned precisely via potentiometer. During active dummy load, the coil is simultaneously grounded via S4. All switches are controlled via TTL-level. S5–S8 represent the field switching circuit by Hilschenz (compare figure 4.1) that reverts the polarity of the current in the coil.

resistance of the coil, ensuring the current sources level out quickly when switching between the loads. The TVS diode D_S protects the circuit from voltage peaks due to induction voltages. S5–S8 represent the circuit designed by Hilschenz (compare figure 4.1) that reverts the current in the frequency gradient coil, to generate a gradient echo. This circuit was included in the new setup without modification.

Figure 4.10 shows time courses of measured currents in the $\boldsymbol{B}_0$-coil and the frequency-gradient coil, as applied in the zCDI sequence. The currents are turned off well before the zero-field time τ, before the $\boldsymbol{B}_P$ ramp-down starts. After τ, the currents are redirected to the coils and stay constant during the phase encoding (t_G). Subsequently, to initiate the echo time t_E, the current in the frequency-gradient coil is inverted. The inset to figure 4.10 shows that recovery times of the current range well below 1 ms. The stability of the current in the $\boldsymbol{B}_0$-coil during readout was determined to about 10 ppm within one sequence run, and to approximately 80 ppm over entire measurements of several hours.

The $\boldsymbol{B}_0$-coil and the frequency-gradient coil were equipped with a similar switching circuit. In principle, both, $\boldsymbol{B}_0$ and $\boldsymbol{G}_x$ could be reversed to generate echo signals. This would be beneficial as inhomogeneity in both fields would be compensated. However, reverting the $\boldsymbol{B}_0$-field also causes larger transient room responses in the center of the MRI setup, as symmetry effects cannot be exploited. Therefore, for the zCDI sequence, an inversion of the $\boldsymbol{B}_0$-field was not pursued.

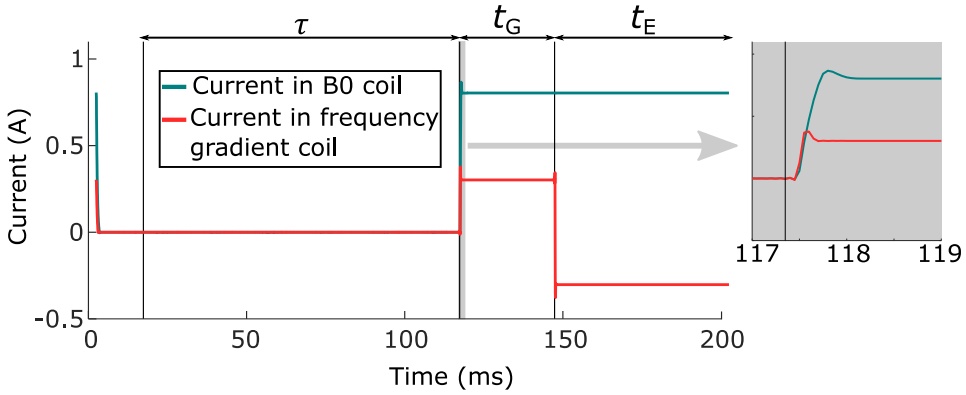

Figure 4.10: Step response of current in $\boldsymbol{B}_0$-coil and frequency-gradient coil during the zCDI sequence (starting at the end of the polarization period). The inset shows a zoom-in at around 118 ms.

4.2.4 Stage 4: The gradient time

After the zero-field time, spatial encoding is initiated during t_G by activating the $\boldsymbol{B}_0$-field, the frequency gradient $\boldsymbol{G}_x$ (dB_x/dx), and the phase-encoding gradients $\boldsymbol{G}_y$ (dB_x/dy) and $\boldsymbol{G}_z$ (dB_x/dz). The operation of the $\boldsymbol{B}_0$-coil and the frequency gradient is performed via the switching circuit illustrated in figure 4.9. The switch-on times, presented in figure 4.10, are sufficiently fast.

Commercial power amplifiers switch the currents in the phase-gradient coils. It has been shown in the previous section, that the $\boldsymbol{G}_y$-gradient coil is operated via the switching network illustrated in figure 4.8, which also decouples the coil during readout in the subsequent echo time t_E. The $\boldsymbol{G}_z$-gradient is operated simultaneously. Therefore, a separate power amplifier and a corresponding decoupling scheme are required. For this purpose, an AE TECHRON® (Elkhart, Indiana, USA) Model 7548 is employed. This precision amplifier features a stand-by mode which is automatically activated during read-out, effectively preventing noise interference.

4.2.5 Stage 5: The echo time

The echo time t_E is initiated by a current inversion in the frequency-gradient coil. Therefore, the circuit sketched in figure 4.9 is utilized. Additionally, the SQUID sensor is set to FLL mode, enabling to read the echo signal. The timing can be reviewed in figure A.5, where the digital signals TTL 15 and TTL 16 reset the SQUID-current-limiter and set the SQUID-feedback-loop to FLL, respectively.

4.3 The sensor system for zCDI

4.3.1 Description of the sensor system

The sensor system consists of a single-channel SQUID sensor, inductively coupled to a wire-wound pick-up loop. It comprises a low-noise, single-stage current-sensor SQUID with additional positive feedback [120, 135]. On-chip within the input circuit, a current limiter consisting of 16 hysteretic SQUIDs is implemented (compare figure 2.13). The SQUID is housed inside a niobium capsule to shield it from the MRI fields [100].

As mentioned before, the SNR is most crucial regarding the successful realization of CDI. Several steps were taken to achieve an outstanding sensitivity of the sensor setup. The lHe dewar, holding the SQUID sensor, was modified to exhibit negligible thermal noise which is described in the next section 4.3.2. Furthermore, the pick-up loop design comprises a 2^{nd}-order axial gradiometer. It was optimized for cortical magnetization sources and minimal mutual inductance to the MRI coils as explained in the subsequent section 4.3.3.

4.3.2 The low-noise liquid helium dewar

The SQUID probe is operated inside a custom-built ultra-low-noise fiberglass dewar. The lHe vessel holds 6.5 l and is surrounded by a vacuum space containing insulation material. A radiation shield comprising several layers of aluminized mylar foil, the so-called superinsulation, and two heat exchangers made of copper mesh are inserted. The distance between the lower loop of the gradiometer and the outside of the flat bottom dewar was measured to be 12.9 mm at 4.2 K, as explained in appendix A.3.

As both, the radiation shield and the heat exchanger, are electrically conductive, they are subject to thermal agitation of charge carriers resulting in *Nyquist-Johnson noise*. In the proximity of the pick-up loop equivalent magnetic field noise couples to the sensor and decreases the overall noise performance.

Thermal noise increases with the radius of the conducting paths. Therefore, an often applied practice to reduce cryostat noise is to break metalized radiation shields into small electrically isolated areas, e.g., by manual wrinkling. Seton et al. [136] introduced an ultra-low-noise cryostat making use of aluminized polyester for the radiation shield near the sensor. Using a commercialized process, they report metalized areas approximately two-to-three orders of magnitude smaller than achievable with wrinkled aluminized foil. Besides, they used aluminum oxide (Al_2O_3), instead of copper, for the heat exchanger material near the sensor. At 77 K, Al_2O_3 has a thermal conductiv-

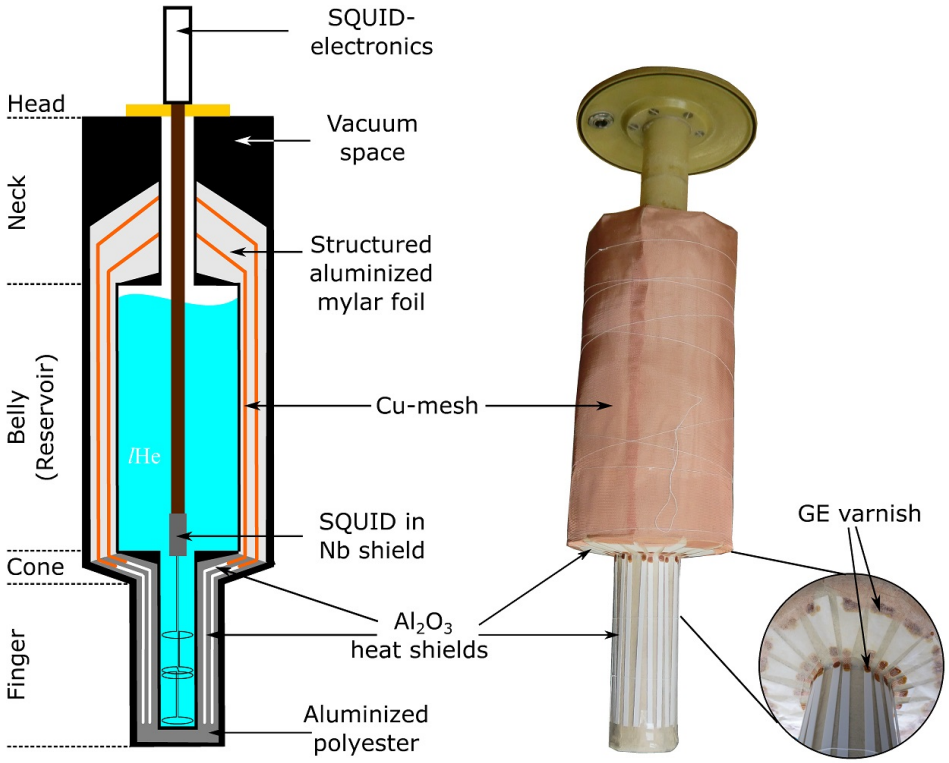

Figure 4.11: Remodeling of the low-intrinsic-noise dewar (LINOD). The final version (LINOD2) comprised aluminized polyester and stripes of Al_2O_3 in the proximity of the sensor loop, ensuring negligible thermal noise.

ity slightly lower than pure copper, but exhibits negligible electric conductivity. The design proved to be successful for a tuned system operated at 414 kHz.

In a first attempt by former colleagues, aluminized polyester was partly used as superinsulation in the finger- and the cone-section of the dewar (compare figure 4.11). This improved the sensitivity of the system to the sub-femtotesla level. However, the heat exchangers, made from copper mesh, were left untouched, leaving an equivalent field noise of 0.5 fT $Hz^{1/2}$ for a 45-mm diameter pick-up loop. [137]

In a second upgrade, we replaced the copper mesh in the finger- and cone-section with commercially available strips and plates of Al_2O_3 (LCP GmbH, Hermsdorf, Germany), as proposed by Seton et al. [136]. The separate plates were connected via strips of copper mesh, glued with GE Varnish to ensure good thermal contact. The remaining parts comprised the original assembly with structured aluminized mylar foil and copper mesh. Figure 4.11 sketches a cut through the dewar, showing the helium vessel and the surrounding vacuum space, including the different layers of heat shields. On the right, the photograph shows the inner heat exchanger made of copper-mesh in the neck- and belly-section, and the connection to the Al_2O_3 stripes in the cone- and finger-section. With the SQUID system installed, the dewar's hold-time is about four

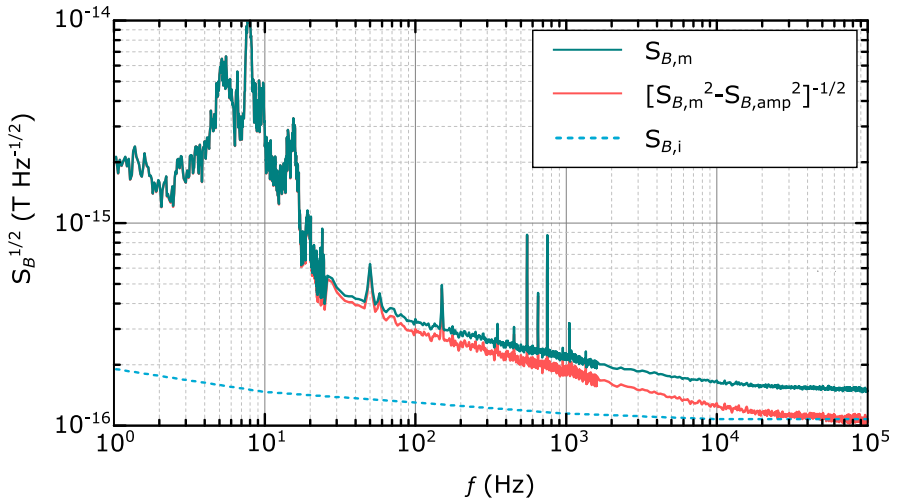

Figure 4.12: Noise performance of a 45-mm-diameter magnetometer in the LINOD2 dewar in the magnetically shielded room BMSR2. The three curves show the total noise density $S_{B,\mathrm{m}}$, noise density with amplifier contribution $S_{B,\mathrm{amp}}$ subtracted, and the intrinsic SQUID-noise-density $S_{B,\mathrm{i}}$.

days, which is equal to before the modification. The average boil-off rate in the first 3.5 days is 1.45 l per day measured with a vibrating-membrane dip stick.

The improved noise performance was verified by field-noise measurements in the center of the Berlin magnetically shielded Room 2 (BMSR2), a magnetically extremely well-shielded environment comprising seven layers of MUMETAL®, one electrically conductive eddy current shield, and all enclosed in a large rf room [138]. Figure 4.12 visualizes the result. A white-noise-level of approximately 150 aT Hz$^{-1/2}$ was measured using a 45 mm magnetometer pick-up loop. The subtraction of the noise component of the room-temperature SQUID electronics shows that the intrinsic SQUID noise is reached, proving there are negligible noise contributions from the dewar material. Between 20 Hz and 20 kHz, the noise density shows a $1/f$ behavior. By comparison to a gradiometer-pick-up-loop, it could be shown that this results from a far-field noise source. In FEM simulations, employing the fluctuation-dissipation theorem, my colleague Jan-Hendrik Storm could show that this noise source originates in thermal noise in the conducting walls of the shielded room. For more information on the simulations and the utilized SQUID sensors, I refer the reader to [71].

4.3.3 The receiver coil

The receiver coil is one of the main components determining the sensitivity of the ULF-MRI setup. The design has to enable a good coupling to cortical magnetization sources while ensuring ultra-low-noise performance. Therefore, several design para-

meters must be considered, such as diameter, mutual inductance to the MRI coils, and self-inductance. Hence, figure of merit should be the SNR.

The signal strength is given by the amount of flux picked up by the receiver coil. For a given source depth d, the optimum diameter of the pick-up loop is $2\sqrt{2}d$, according to Storm et al. [100]. However, the loop diameter also determines the amount of picked-up extrinsic noise and indirectly affects sensor noise. For instance, in the presence of thermal noise in the Dewar material, Körber [121] derives substantially different optimum pick-up-loop diameters. The field noise $S_{B,\mathrm{i}}^{1/2}$, equivalent to SQUID intrinsic flux noise ${S_{\Phi,\mathrm{i}}}^{1/2}$, is given by

$$S_{B,\mathrm{i}}^{1/2} = \frac{S_{\Phi,\mathrm{i}}^{1/2} L_{\mathrm{tot}}}{2 M_{\mathrm{i}} A_{\mathrm{S}}}, \tag{4.5}$$

where A_{S} is the effective pick-up-loop area, L_{tot} is the total inductance of the input circuit comprising the pick-up-loop inductance L_{S} and the SQUID inductance L_{i}, and M_{i} is the mutual inductance between the input coil and the SQUID. It becomes evident, that increasing A_{S} reduces $S_{B,i}^{1/2}$. For the case of circular, single-turn loops and perfect matching ($L_{\mathrm{i}} = L_{\mathrm{S}}$), $S_B^{1/2} \propto 2a^{-3/2}$, where a is the pick-up-loop radius. If the pick-up loop comprises an axial gradiometer, L_{tot} is increased in comparison to a magnetometer design with equal radius. The effective area on the other hand is mostly determined by the lowest loop, most sensitive to the desired magnetization sources below the sensor. According to equation (4.5), this results in a higher equivalent field noise for the gradiometric pick-up loop design.

Another parameter influencing SNR is extrinsic noise due to the MRI fields. One of the key features for ultra-low-noise performance of our setup is minimal mutual inductance between sensor loop and MRI coils, ensuring low equivalent magnetic noise due to the current noise from the current sources, measured at 360 pA $\mathrm{Hz}^{-1/2}$. This concerns the main-field coil and the frequency gradient $\boldsymbol{G}_x$, as these are active during readout and cannot be decoupled. An axial sensor loop oriented in $\boldsymbol{e}_z$ ensures negligible mutual inductance to the main-field coil $\boldsymbol{B}_0\boldsymbol{e}_x$. The frequency gradient $d\boldsymbol{B}x/dx$, however, exhibits concomitant terms $d\boldsymbol{B}y/dy$ and $d\boldsymbol{B}z/dz$, where the latter couples directly to the pick-up loop. A 2$^{\mathrm{nd}}$-order gradiometer can be used to compensate the flux due to $\boldsymbol{G}_x$ picked up by the lowest loop. Such a pick-up loop was developed by my colleagues Rainer Körber and Jan-Hendrik Storm for the purpose of NCI. It comprises a 2$^{\mathrm{nd}}$-order axial gradiometer with 45 mm diameter and 125 mm overall baseline. The diameter was optimized for source depths corresponding to the cortex [121] while reducing mutual inductance to the MRI fields, mainly the frequency gradient $\boldsymbol{G}_x$. In the following, I will briefly explain the reasoning for the gradiometric design and show that the sensor arrangement is also suitable for CDI.

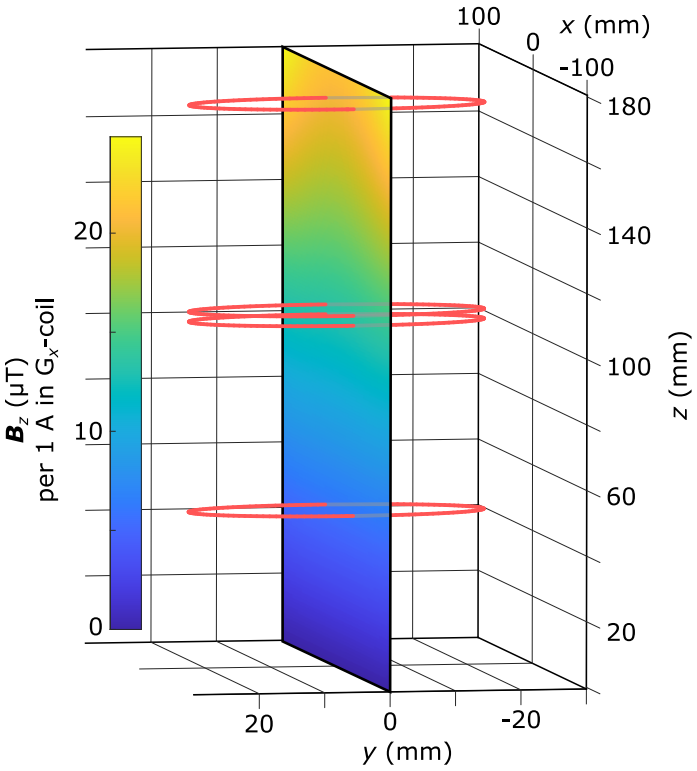

Figure 4.13: z-component of the field generated by 1 A in the frequency-gradient coil at the sensor position.

Figure 4.13 visualizes the z-component of the field generated by 1 A in the $\boldsymbol{G}_x$-coil at the sensor position. Numerical integration of the flux over the pick-up loop area reveals that the coupling between $\boldsymbol{G}_x$-coil and sensor is attenuated by approximately 97% by the gradiometer, compared to a magnetometer in a similar arrangement. Taking into account the current noise of 360 pA $\mathrm{Hz}^{-1/2}$, originating in the current source driving the $\boldsymbol{G}_x$-coil, the equivalent field noise picked-up by the sensor is approximately 60 aT $\mathrm{Hz}^{-1/2}$, compared to approximately 2 fT $\mathrm{Hz}^{-1/2}$ for the magnetometer.

However, the intrinsic equivalent field noise of a gradiometer is higher, compared to a magnetometer, due to the increased total inductance. Figure 4.14 shows that we reached a white noise level above 1 kHz of approximately 350 aT $\mathrm{Hz}^{-1/2}$ with the 2$^{\mathrm{nd}}$ order gradiometer in LINOD2, with the MRI fields in operation. The noise level with the MRI coils disconnected is also shown and appears similar in the frequency range above 100 Hz. The data were taken in the ZUSE chamber, the magnetically shielded room consisting of two layers of MUMETAL® and one eddy current shield. Since the coil setup is installed in this room, all ULF-MRI experiments shown in this thesis were performed here.

For SNR comparison, the coupling should be taken into account as well. The gradiometer attenuates the signal from a dipolar magnetization source depending on the

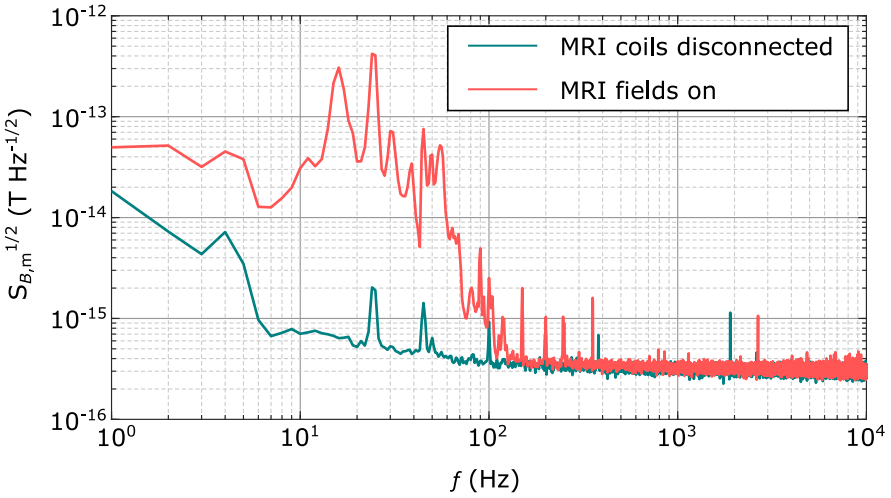

Figure 4.14: Noise performance of the 2nd-order gradiometer in the LINOD2 dewar and inside the ZUSE chamber.

baseline. In the NCI experiment, my colleagues aimed for cortical sources at approximately 30 mm depth. Considering the warm-cold distance of LINOD2, the overall distance to the lowest loop of the pick-up coil amounts 47.9 mm. Here, the coupling of a magnetization vector centrally below the pick-up coil is approximately 20% lower for the 2nd-order gradiometer, compared to a magnetometer setup. Increasing the gradiometer baseline would increase the coupling. However, due to geometrical constraint of LINOD2 this is not possible.

Figure 4.15 visualizes the sensor coupling in a cross-sectional plot for sources starting directly below the dewar bottom (z=0.035) down to depths of 35 mm (z=0) and over an area xy of (150×150) mm^2. The values resemble the magnetic field per unit current in the receiver coil, as required by reciprocity (see section 2.2.4). The highest sensitivity is found centrally and directly below the dewar, both for the 2nd-order gradiometer (panel a) and the magnetometer (panel b). Panel c) displays the ratio between the two, showing that the gradiometer sensitivity decreases slightly stronger with depth. Both, magnetometer and gradiometer exhibit two directions of very low sensitivity, diagonally oriented in the xz-plane. As the magnetization vectors rotate about $\boldsymbol{B}_0\boldsymbol{e}_x$, the sensor is only sensitive to y- and z-components which results in distinct blind angles in the xz-plane. In the case of the gradiometer, the blind angles are closer to the center.

In conclusion, the increase in SNR due to reduced mutual inductance to the $\boldsymbol{G}_x$-coil, and the decrease in SNR due to a reduced coupling to magnetization vectors, should be balanced. For a representative voxel at [0,0,0] (x,y,z), this combines to a 4.6-fold SNR in case of the 2nd-order gradiometer.

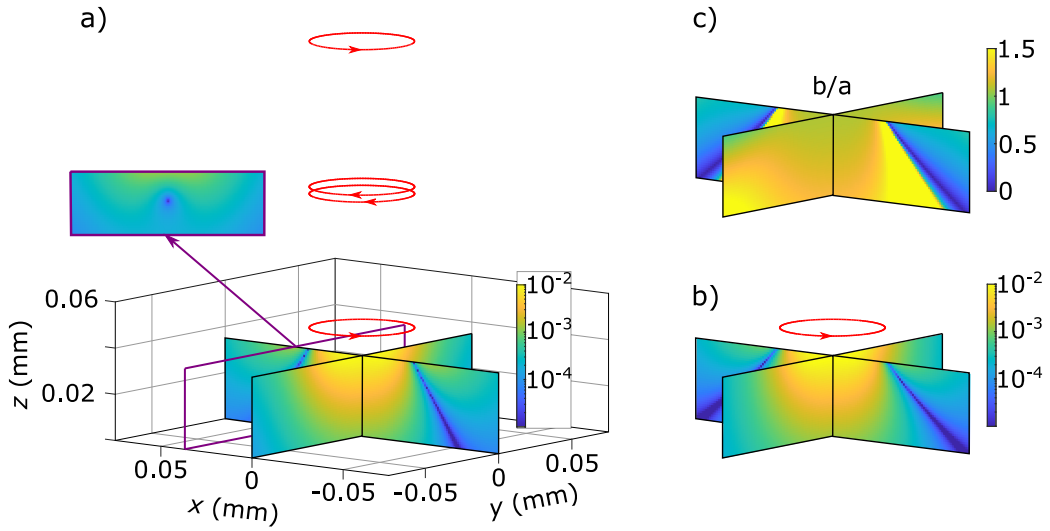

Figure 4.15: Coupling field for a 2nd-order gradiometer with overall baseline of 125 mm and 45 mm loop diameter (a), magnetometer with the same diameter (b), and the ratio between the two (c).

4.4 The final assembly of the ULF-MRI setup for zCDI

Figure 4.16 illustrates the final assembly of the ULF-MRI setup used for zCDI. Three different coil pairs form the polarization setup, where the inner pair creates the magnetization. Directly attached, a shielding pair with a larger diameter canceling the magnetic moments of the inner pair is realized. This self-shielded coil was designed by Nieminen (compare section 4.1). The outer pair was added, as in the original setup a fast $\boldsymbol{B}_\mathrm{P}$ turn-off caused large induction voltage peaks in the collinearly arranged $\boldsymbol{B}_0$-coil. The voltage peaks hampered the control of the constant current in the $\boldsymbol{B}_0$-coil due to the high response time of the low-noise current source. The outer coil pair effectively reduces mutual inductance between the polarization setup and the $\boldsymbol{B}_0$-coil.

The guiding fields are realized by three Helmholtz-type coils oriented in x-, y-, and z-direction. Please note, the $\boldsymbol{B}_{\mathrm{g},x}$-coil is not visible in the figure, as it shares the same geometry with the $\boldsymbol{B}_0$-coil. As mentioned before, the large y-coil in the system of Hilschenz had to be replaced by a smaller quadratic-shaped coil, to reduce transient responses from the walls of the shielded room. Originally, the inner door cover of the shielded room was made of a thin aluminum panel resulting in eddy-current transients after switching the y-coil. After removal of the door cover, I did not revert back to the larger coil arrangement since the quadratic $\boldsymbol{B}_{\mathrm{g},y}$-coil proved sufficient, as will be shown in chapter 5.

The $\boldsymbol{B}_0$-coil for the main field and the gradient coils were adopted without modifi-

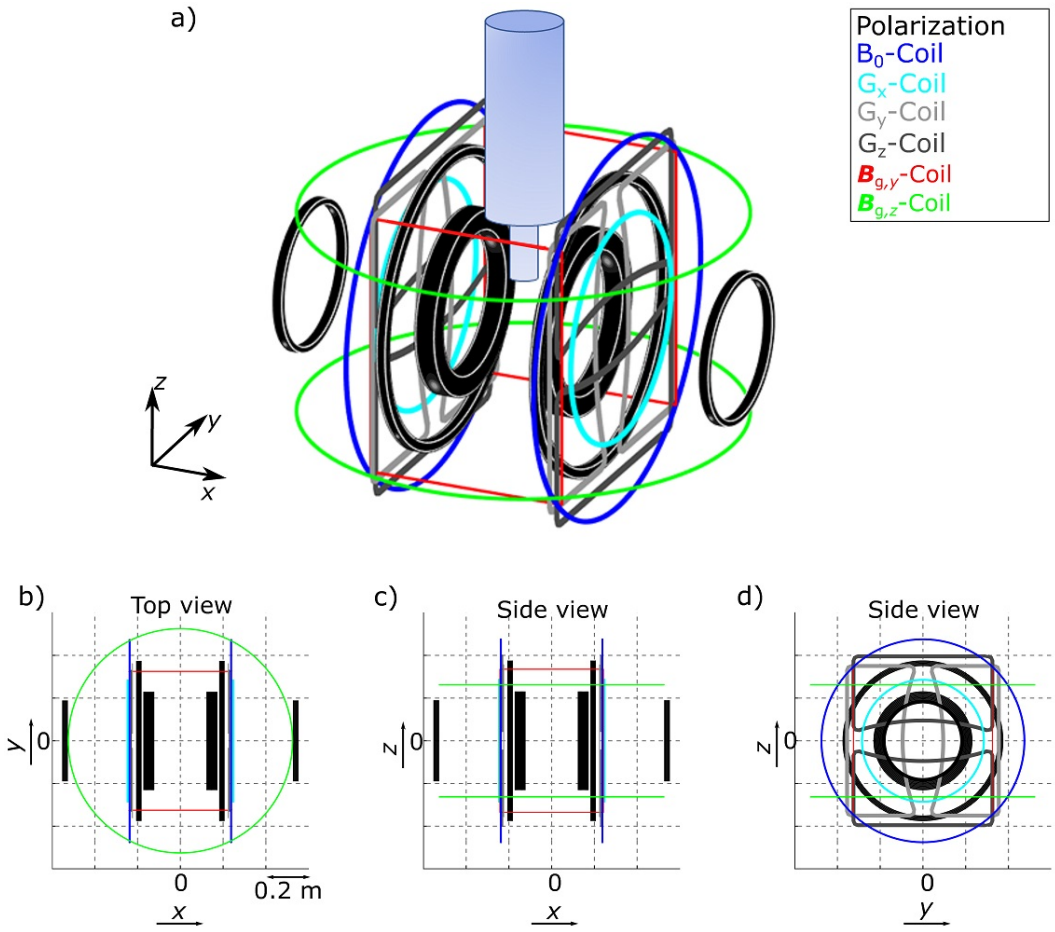

Figure 4.16: Illustration of the coil setup for zCDI in an overview including the lHe dewar (a), in a topview (b), and the two sideviews xz (c), and yz (d).

cations from the setup designed by Hilschenz. All coils were connected to the previously described current sources and power amplifiers via the introduced switches and decouplers. The zCDI sequence was implemented in the LabVIEW™ framework by Hilschenz, using the existing PXI™ setup for timings and data acquisition. A diagram of the timings is given in figure A.5.

4.5 Chapter summary and discussion

The existing PTB-ULF-MRI setup was evaluated and updated for zCDI. The coil system comprises a Helmholtz-type self-shielded polarization coil enabling $\boldsymbol{B}_\mathrm{P}$ pulses of about 17 mT. Compared to other ULF-MRI studies, the achievable polarization is low. Fields around 100 mT have been reached using water-cooled [88] or liquid-nitrogen-cooled [89] coil arrangements. However, these setups have lower homogeneity and expectedly higher transient room responses after pulsing, possibly causing severe problems for the defined manipulation of the magnetization and the zero-field requirements

in zCDI. Besides, both systems described in [88] and [89] operated at Larmor frequencies > 5 kHz, due to excess low-frequency noise after pulsing. Although expecting that the SNR requirements for *in-vivo* zCDI cannot be met using the existing self-shielded coil arrangement, this setup is employed for a proof of principle using phantoms (chapter 5). The results will point to a necessary improvement in SNR and thereby facilitate the design of a polarization setup sufficient for *in-vivo* zCDI.

Guiding-field coils were installed that tip the magnetization to $\boldsymbol{e}_x$, $\boldsymbol{e}_y$, or $\boldsymbol{e}_z$ during an adiabatic turn-off of $\boldsymbol{B}_\mathrm{P}$. The orthogonality, switching times, and effects of transient room responses were evaluated in fluxgate measurements and simulations. Error angles are expected below 0.9°, corresponding to magnetic-field errors below 0.6 nT. The misalignment errors are systematic, which is why their effects on $\boldsymbol{B}_\mathrm{J}$-reconstruction are canceled in the background-field subtraction.

The zero-field time was realized by dummy circuits that bypass the current in the $\boldsymbol{B}_0$-coil and the frequency-gradient coil. Turn-off and recovery times well below 1 ms could be achieved. A field switch enables inversion of the frequency gradient and thereby generation of gradient echoes. Besides, spatial encoding is realized by means of phase-gradient pulses.

The sensor system comprises a single-channel 2$^{\mathrm{nd}}$-order SQUID gradiometer housed in a lHe dewar modified for ultra-low-noise operation. With the MRI fields on, noise levels as low as 350 aT Hz$^{-1/2}$ were measured in the relevant frequency range around the Larmor frequency. The performance is approximately 10–20 times better than commercially available SQUID systems and 2–15 times better than ULF-MRI studies reported so far [88, 89, 108].

In a magnetometer setting and without operating additional magnetic fields, we were able to measure noise levels as low as 150 aT Hz$^{-1/2}$ [71], implying there is still room for improvement. Therefore, ultra-low-noise current amplifiers, for instance, as suggested by [131], need to be employed for the MRI fields. As elaborated before, it needs to be determined if such amplifiers are suitable for gradient-echo sequences.

A natural limit for noise improvement is given by body noise, the thermal agitation of charge carriers in conductive human body tissue. Using a 1$^{\mathrm{st}}$-order gradiometer in LINOD2, we were able to give an upper limit for body noise in the human head of 80 aT Hz$^{-1/2}$ and an expected value of 55 aT Hz$^{-1/2}$ based on a phenomenological approach. Recent developments in SQUID design using sub-micron-sized junctions could lead to sensors that are body-noise-limited in the near future [73, 139, 140, 141]. For more information on the measurement of body noise using SQUIDs, I refer the reader to [74].

Chapter 5

Proof of principle

In this chapter, a demonstration of the successful operation of the ULF-MRI setup for zCDI is presented. At first, the 3D-imaging capabilities are evaluated performing *in-vivo* imaging of a human head. 3D-imaging forms the basis for CDI as the reconstruction of $\boldsymbol{J}$ using *Ampère's law* requires complete information on the vector-field $\boldsymbol{B}_{\mathrm{J}}$. The obtained images verify that the setup is suitable for spatial encoding of the MR signal and further allow determination of the image SNR. Subsequently, the implemented zCDI sequence is validated in phantom measurements.

The methods and results presented in this chapter have partly been previously published in [72]. Parts of the text and figures are extracted from that publication.

5.1 3D structural imaging

5.1.1 Image parameters

To verify that the ULF-MRI setup is sufficient for spatial encoding of the MR signal, a structural image was acquired of a human head. The applied sequence resembled the zCDI sequence with $\tau = 0$ s. The guiding field $\boldsymbol{B}_{\mathrm{g}}$ was always z-directional, creating transverse magnetization after the polarization. The strength of the polarization field was 17 mT, and the polarization time 500 ms. The $\boldsymbol{B}_0$-field was set to 38.64 μT, corresponding to a Larmor frequency of 1645 Hz. The frequency gradient $\boldsymbol{G}_x$ was set to 125 μT/m, and the maximum phase-encoding gradients $\boldsymbol{G}_y$ and $\boldsymbol{G}_z$ to $\pm$ 95 μT/m with a phase-encoding time of 30 ms. 35 k-steps for each y- and z-direction were acquired, resulting in a voxel volume of $(4.1 \times 3.9 \times 3.9)$ mm^3. The total measurement time for the 1225 combinations of encoding steps amounted to approximately 40 minutes, including a duty cycle of one-third for the polarization.

5.1.2 Data processing

Data handling was entirely performed using MATLAB® (©1994–2020 The MathWorks, Inc.). The echo signals, converted to magnetic flux density, are superimposed by transients, low-frequency vibrations, and external low-frequency interferences. Subtraction of a lower-order polynomial, fitted to the data, yields the mean- and trend-adjusted echo signal. Figure 5.1 shows the bias removal for an echo signal where no phase gradients were applied during t_G. The echo is not perfectly centered at 1/2 t_E, which is probably subject to additional time-varying x-directional background fields.

Besides bias removal, the time-domain data were tapered using a *Tukey* window with $\alpha = 0.1$ (compare figure 2.7) and sorted in a 3D-array, according to the phase gradients. Now, also the phase-encoding directions were windowed using a *Tukey* kernel with $\alpha = 0.1$ (compare section 2.3.2). Subsequently, the array was transformed into the image domain applying 3D-*Fourier transform*. As the frequency-encoded direction obtains a larger FOV, the transformed array was cut according to the FOV given by the phase-encoding parameters. Finally, the derived complex voxel values were rearranged, moving the lowest spatial frequencies to the center.

Images were computed by the magnitude of the complex voxel values. Further, the complex image SNR was calculated as

$$\mathrm{SNR} = \frac{|u|}{\mathrm{SD}[e]}, \tag{5.1}$$

where u represents the complex image values, and e a complex noise estimate taken from a noise-only region in the image. SD is the standard deviation.

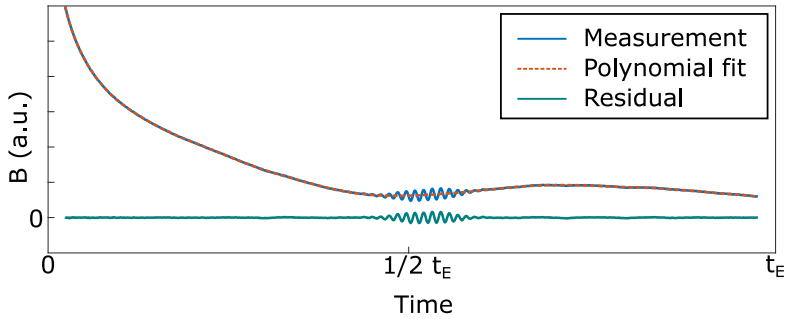

Figure 5.1: Pre-processing of the echo signals. Superimposing transient fields are removed by subtraction of a polynomial.

5.1.3 Results

Figures 5.2(a, b) show how the subject is placed in a lateral position in the scanner. The sensor is located above the temporal lobe. The panels c)–e) give the reconstructed magnitude images, not corrected for the sensitivity profile of the sensor. Therefore, the voxel values are weighted by the coupling profile, visualized in figure 4.15(a). Three different slices are displayed in 5.2, a central yz-slice (c), and two xy-slices at distances of 18.3 mm (d) and 10.6 mm (e), respectively to the dewar bottom. Note, the dewar bottom was positioned at $z = 30$ mm, centrally in the MR-coordinate system, resulting in a position of the lowest loop of the gradiometer of approximately 42 mm. Signal above noise level could be observed down to depths of approximately 5 cm below the dewar bottom, and about $\pm$ 8 cm in the x- and y-direction depending on the depth. Anatomical structures like scalp, skull, and intracranial tissue could be distinguished. CSF, which should obtain a much longer T_2 relaxation time, could not be distinguished from the other tissue.

Figure 5.3(a) shows the calculated image SNR, corresponding to the slice in figure 5.2(c). In the scalp, SNR values up to 71 could be observed. Intra-cranially, peak SNR ranged around 35. Figure 5.3(b) shows the same data as 5.3(a) but scaled according to the approximate relaxation during a possible zero-field time $\tau = 100$ ms.

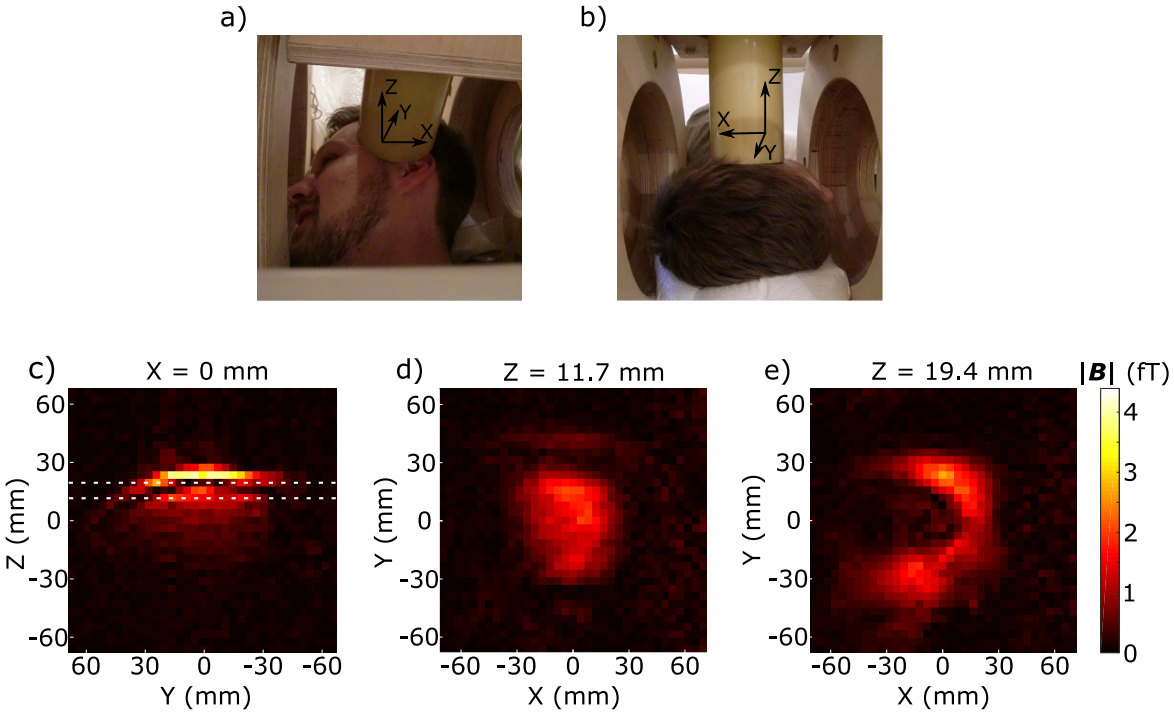

Figure 5.2: Structural image of the human head. Displayed is the positioning of the subject in a) and b), an MR amplitude image in the central yz-slice in c), and in two xy-slices in d) and e).

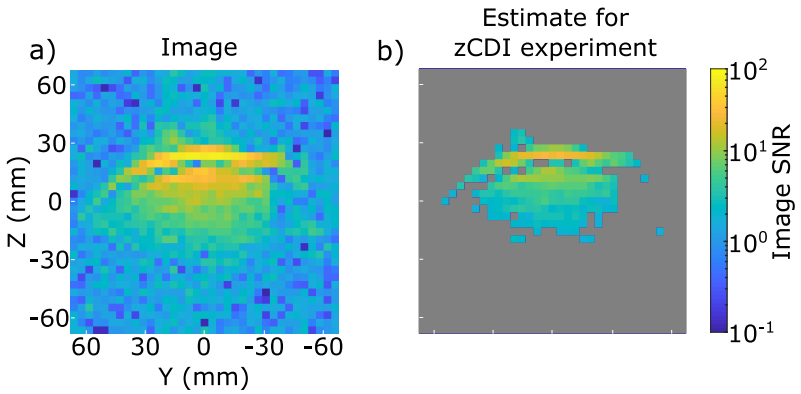

Figure 5.3: SNR of structural head image (a), corresponding to figure 5.2(c). Panel b) shows the SNR when the image is scaled according to an additional zero-field time $\tau = 100$ ms, assuming a T_2 relaxation time of 100 ms over all tissue. Pixels with SNR below five in a) were excluded from the visualization in b) (gray area).

Therefore, the figure represents an estimate of the image SNR during a CDI experiment, with the same image parameters. The scaling factor was calculated using a relaxation time $T_2 = 100$ ms for all tissue, yielding $|u|e^{-(\tau/T_2)} = |u|e^{-1} \approx |u|0.37$. Since noise was also scaled by the operation, voxels with SNR below five in panel a) were excluded from the illustration.

5.2 Current density imaging on phantoms

5.2.1 Phantom development

For the demonstration of 3D-zCDI, phantoms with different geometries (figure 5.4(a–c)) were produced using additive manufacturing. Each phantom has supports for flat electrodes of the dimension (50×70) mm^2, which were fabricated from fiber-reinforced plastic with a 35 μm copper-coating. Figure 5.4(d) shows how the copper coating was slit in a fish-bone shape, effectively reducing thermal noise within the electrode material. Thin rubber-insulated copper stripes connect the electrodes to the leads that were bound to a twisted pair below the phantom. The leads were positioned such that their emitted magnetic field is lowest in the region below the sensor.

For the experiments, the phantoms were filled with an aqueous solution of $CuSO_4$ (0.079 wt%) tuning the relaxation time $T_1 = T_2$ to approximately 100 ms [142], a value similar to relaxation times of brain matter in the microtesla regime (compare section 2.4.1). Phantom 1 has the dimensions $(140 \times 100 \times 110)$ mm^3 and contains a small current pathway with a cross-sectional area of 357 mm^2, yielding a nominal current density of 2.8 A/m^2 for 1 mA applied current. During experiments, it appeared

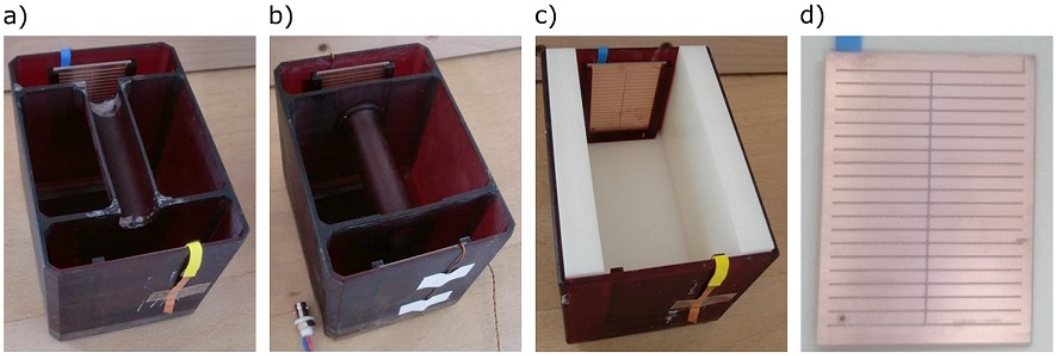

Figure 5.4: Pictures of the phantoms used for the experimental demonstration of zCDI. Phantoms 1 (a) and 2 (b) possess a current path at the top and at a depth of 30 mm, respectively. Phantom 3 (c) is a container allowing current flow through the entire volume. All phantoms have supports for (50×70) mm^2 electrodes (d).

practical not to fill the phantom up to the top. When leaving a one-millimeter gap, the cross-sectional area amounts approximately 340 mm^2, corresponding to a mean current density of 2.97 A/m^2 for 1 mA applied current. Phantom 2 with the same outer dimensions possesses a similar pathway (cross-sectional area of 315 mm^2, nominal current density 3.2 A/m^2 per mA applied current) 30 mm below the surface. Phantom 3 is a container with the dimensions $(140 \times 64 \times 70)$ mm^3, allowing current flow through the entire volume (nominal current density 0.22 A/m^2 per mA applied current).

A battery-powered, constant-current source was developed to drive the phantom currents. This source is based on a design by my colleagues Nora Höfner and René Bösel, which is visualized in figure 5.5. A voltage transformer scales the input voltage U_e by $\approx \frac{1}{19}$, before a difference amplifier is used for common-mode rejection. Finally, an inverting amplifier scales the output voltage such that the output current I_a is given by:

$$I_a = \frac{Ue}{19\mathrm{R8}} \left(1 + \frac{R9}{R10}\right), \tag{5.2}$$

yielding approximately $I_\mathrm{a} = -100\ \mu\mathrm{A} \frac{U_e}{1\ \mathrm{V}}$.

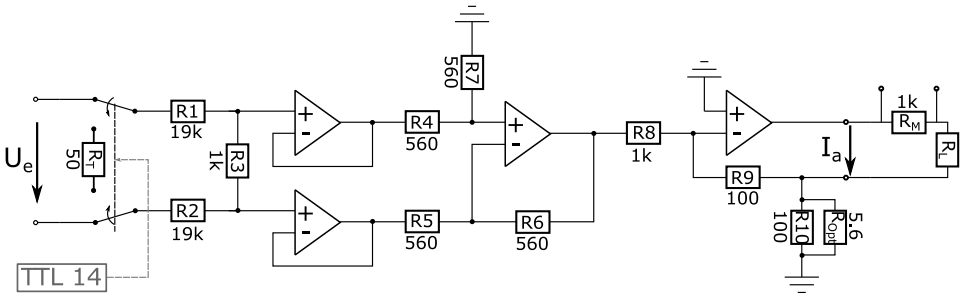

Figure 5.5: Scheme of voltage-to-current converter to drive the phantom current.

For a demonstration of CDI, this source was modified, in order to obtain currents in the low milliampere range. Therefore, the circuit was equipped with an optional resistor $R_{Opt} = 5.6\ \Omega$ in parallel to R10, tuning the transfer function to obtain

$$I_a = -1\ \text{mA}\frac{U_e}{1\ \text{V}}.$$

A monitor resistor $R_M = 1\ \text{k}\Omega$ was included in series to the load R_L, i.e., the phantom, to record the applied current with a transfer coefficient of

$$U_M = 1\ \text{V}\frac{I_a}{1\ \text{mA}}.$$

Furthermore, the input was equipped with a switchable resistor R_T that terminates the input to 0 V during readout, effectively eliminating noise from the voltage input. Due to the parameter adjustments, the original voltage supply was changed from ± 9 V to ± 18 V. This enables total current strengths up to approximately ± 4 mA, provided the phantom resistance ranges below 3 kΩ. The current noise of the source, including the modifications, was measured at 720 pA $\text{Hz}^{-1/2}$.

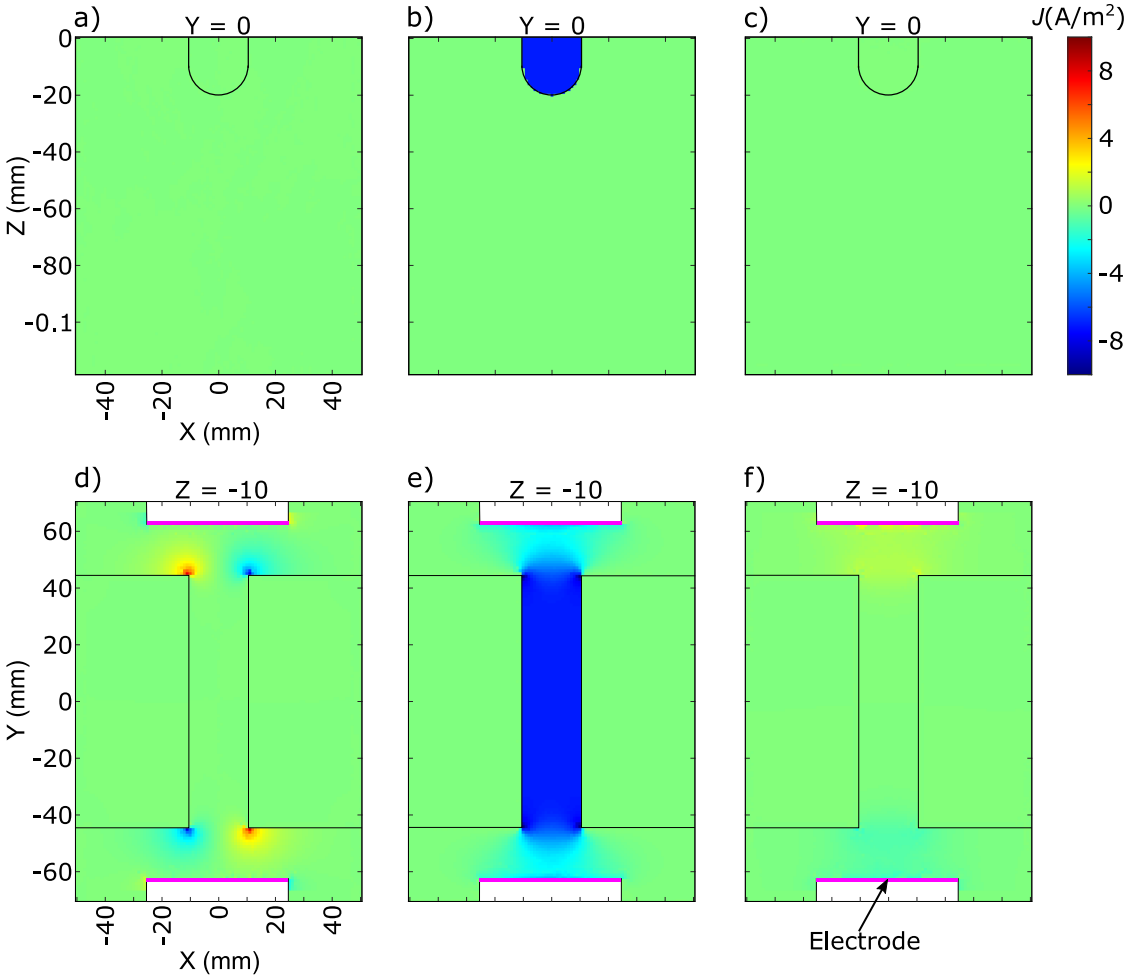

Figure 5.6: FEM-based $\boldsymbol{J}$-field simulations of Phantom 1 showing J_x in a) and d), J_y in b) and e), and J_z in c) and f).

5.2.2 Field simulations for Phantom 1

The CDI experiments with Phantom 1 were expected to yield the best results, as the current channel is close to the sensor. To assess the reconstructed field values, $\boldsymbol{J}$ and $\boldsymbol{B}_\mathrm{J}$ were simulated beforehand. Therefore, the phantom was modeled in COMSOL™ Multiphysics using the nominal dimensions, including the electrode positions. The conductivity ratio between plastic and the conductive solution was set to 1/200,000. The current flow between the electrodes was realized simulating the electric field due to fixed potentials at the electrode boundaries using the iterative conjugate gradients solver and scaling to a total current of 2.5 mA. Approximately 99% of the current was flowing through the current channel.

The results were exported to a regular 1 mm grid and are displayed in figure 5.6. Two slices, centrally through the current channel, are shown for J_x (a, d), J_y (b, e), and J_z (c, f), respectively. In the central cross-section at $y = 0$, current-flow was solely y-directional. The amplitude of 6.99 A/m^2 matched the approximation based on the cross-sectional area. The xy-slices d)–f) visualize how the current dispersed towards both ends of the channel. It shows x-components peaking at the corners of the channel and weaker, but broader z-components.

Based on the current density, the magnetic field $\boldsymbol{B}_\mathrm{J}$ was simulated using the generalized minimal residual method (GMRES). The result is displayed in figure 5.7 for a 2D-vector field corresponding to the cross-section visualized in figure 5.6(a–c). The plot reveals a rotation of the field around the center of the current channel. Absolute field values rose towards the boundary of the current channel and peaked at approximately 46 nT.

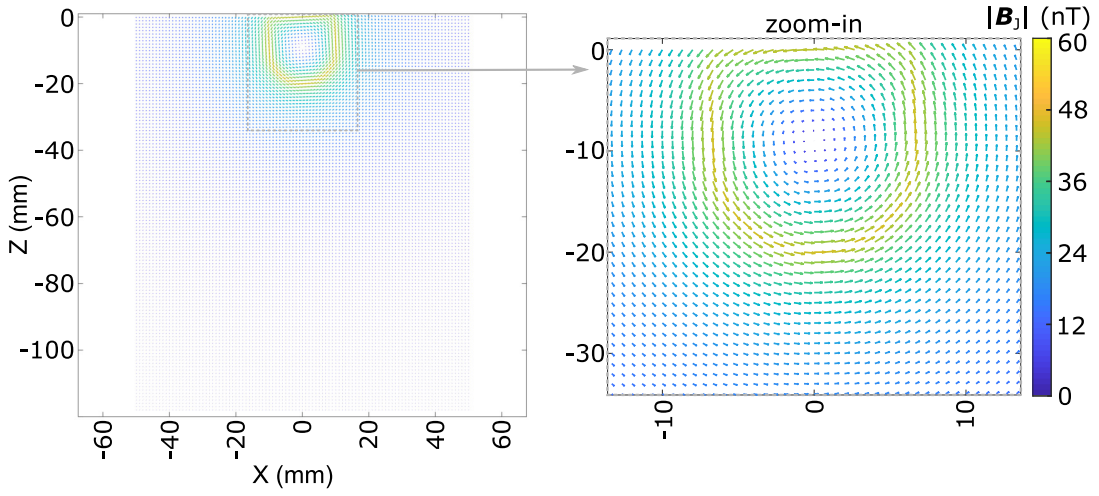

Figure 5.7: FEM-based $\boldsymbol{B}_\mathrm{J}$-field simulations of Phantom 1 showing a central xz-plane.

5.2.3 Calibration

As elaborated in section 3.3.3, a calibration measurement is required to compensate for the unknown phase shifts δ due to the imaging sequence. Therefore, a measurement was performed using Phantom 3 and a large Helmholtz coil oriented in the y-direction. This coil was driven by the above presented current source (compare figure 5.5) to create a 15 nT calibration field $\boldsymbol{B}_{\text{cal}}$ during τ. The electrodes were not inserted in the phantom. The full zCDI sequence was performed, and the calibration field was reconstructed. Therefore, the complex voxel values, obtained by *Fourier transform*, were adjusted by a phase offset p_{cal}, which was varied until the reconstruction $\hat{\boldsymbol{B}}_{\text{cal}}$ yielded the correct calibration field in the y-direction. Especially the y- and z-component of $\hat{\boldsymbol{B}}_{\text{cal}}$ appeared very sensitive to changes in the phase. An additional phase of $p_{\text{cal}} = 295°$ gave the best reconstruction for each part of the FOV. Figure 5.8 shows $\hat{\boldsymbol{B}}_{\text{cal}}$ using the offset of 295° in three voxel lines expanding over areas in the FOV with relatively high signal strength. A global phase offset was sufficient to image $\boldsymbol{B}_{\text{cal}}$ reliably. Deviations to the nominal field value were most likely subject to noise and possibly image artifacts. The experiment was repeated with x-, and z-directional calibration fields (not shown),

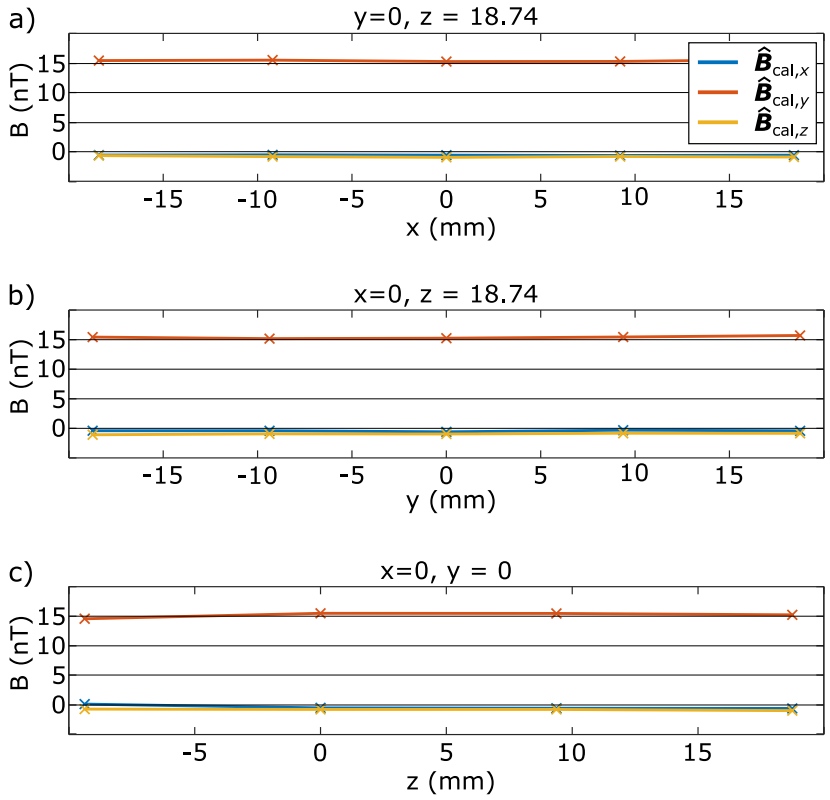

Figure 5.8: Reconstruction of a 15 nT y-directional calibration field using a global phase offset of 295°. For reasons of illustration, three lines of voxels expanding in the x-direction (a), the y-direction (b), and the z-direction (c) were extracted from the image.

yielding the same optimal offset $p_{\mathrm{cal}} = 295°$. This phase offset was employed as a calibration phase for each zCDI experiment following in this chapter.

5.2.4 Measurements

zCDI measurements were performed applying 2.5 mA current to Phantom 1 and Phantom 2, resulting in mean current densities in the current paths of 7.4 A/m^2 and 7.9 A/m^2, respectively. The phantoms were positioned centrally in the MRI-coordinate system (figure 5.9) such that current-flow was in the negative y-direction in case of Phantom 1 and in the positive x-direction in case of Phantom 2. The distance from the top level of the solution to the bottom of the dewar was less then 1 cm, yielding a distance phantom–gradiometer of approximately 2 cm. Spatial encoding was realized using 29 k-steps for each y- and z-direction, yielding a voxel size of $(4.8 \times 4.8 \times 4.8)$ mm^3 and a field of view $\mathrm{FOV}_{y,z} = 139$ mm. Equal to the *in-vivo* head image, the Larmor frequency was adjusted to 1645 Hz. The frequency gradient $\boldsymbol{G}_x$ was set to 121 μT/m and the maximum phase-encoding gradients $\boldsymbol{G}_y$ and $\boldsymbol{G}_z$ to $\pm$ 75.6 μT/m with a phase-encoding time t_{G} of 30 ms. The current was applied to the phantom in the zero-field encoding time $\tau = 70$ ms. The polarization field was 17 mT, applied for 500 ms, in-

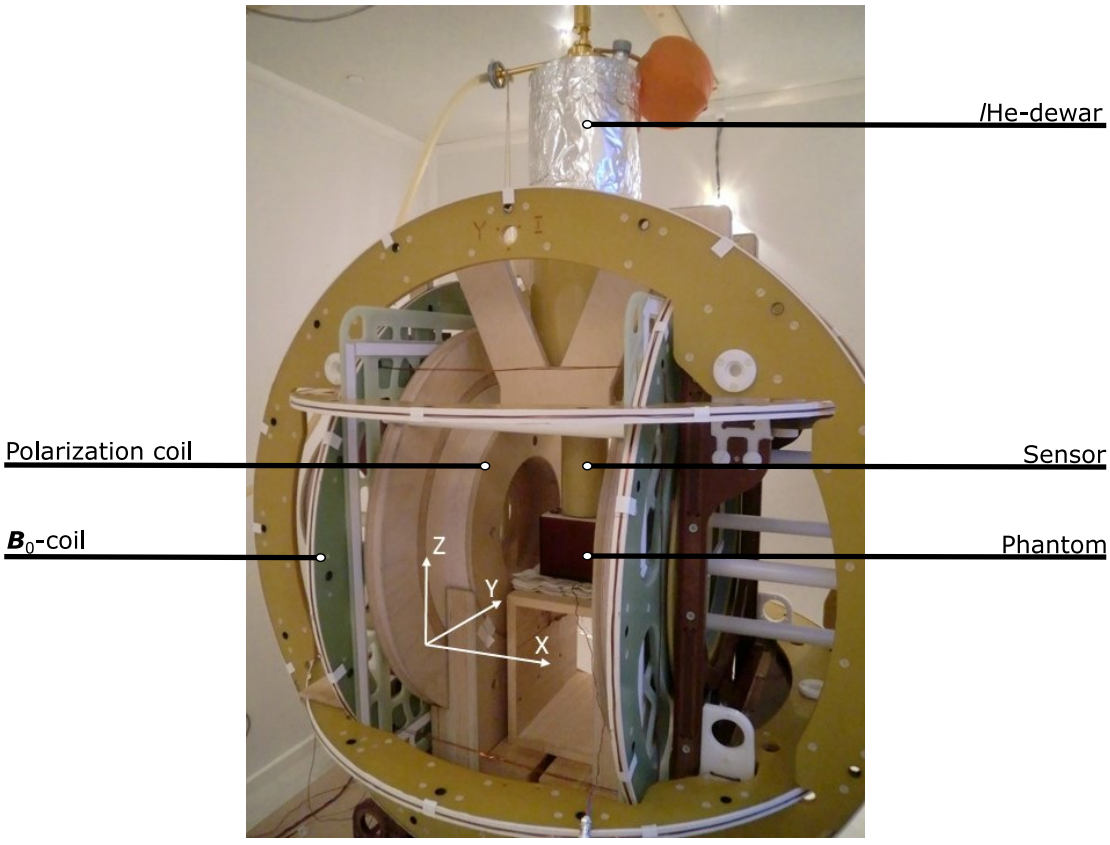

Figure 5.9: Picture of the phantom position, centrally inside the ULF-MRI setup.

cluding a 150 ms ramp up. As mentioned before, a full 3D-$\boldsymbol{B}_{\mathrm{J}}$-reconstruction requires six runs of the sequence per k-step. Together with a spin-density image using $\tau = 0$ s, this results in 5887 sequence runs for 29×29 k-steps. A necessary duty cycle of one-third and cool-down periods of at least two hours every 1500 shots resulted in a total measurement time of approximately nine hours.

For the examination of physiologically realistic current density, 2 mA current was applied to Phantom 3, resulting in a mean current density of approximately 0.45 A/m^2. The phantom was positioned in the MRI coordinate system to allow current-flow in the negative x-direction. As the current density was about 20 times lower compared to the experiments with Phantom 1 and 2, the voxel size was increased to $(9.4 \times 9.4 \times 9.4)$ mm^3, effectively increasing the signal strength. Furthermore, to reach an overall measurement time that could be executable *in vivo*, the imaging parameters were adjusted to yield a $\mathrm{FOV}_{y,z} = 141$ mm. The phantom was positioned with the longer side in the frequency-encoding direction (x), which obtains a significantly larger FOV, to avoid aliasing artifacts.

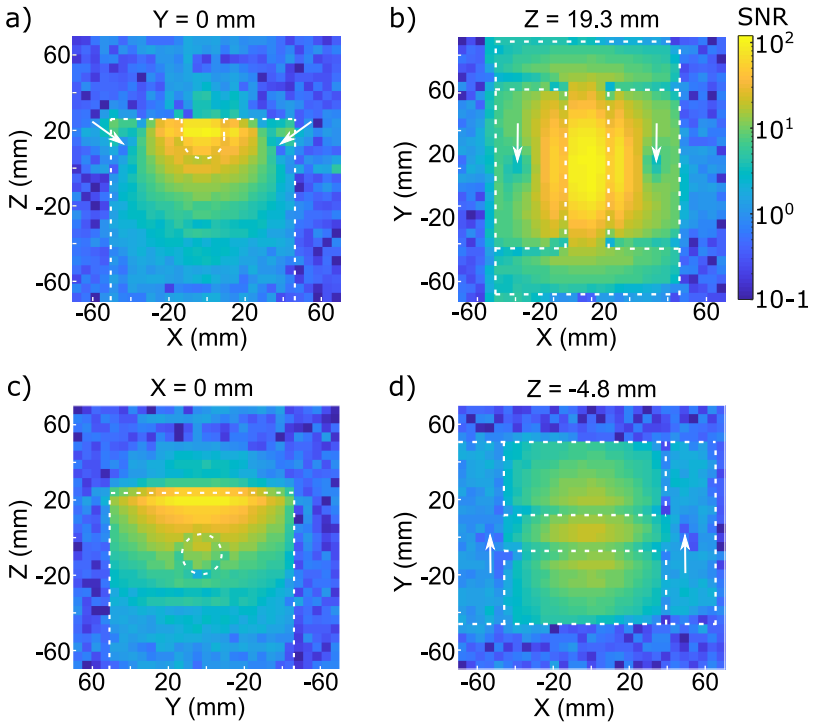

Figure 5.10: Image SNR of zCDI measurements with Phantom 1 (a, b) and Phantom 2 (c, d) on a logarithmic scale. Two slices centrally through the current channels are displayed for each phantom. The phantom outlines are drawn in white dashed lines. The white arrows indicate the blind angles, that originate from the system-specific sensitivity profile (compare section 4.3.3). For a sketch showing the phantoms in the MRI coordinates, see figures 5.12(b) and 5.13(b).

5.2.5 Results

The SNR of the spin density images of the experiments with Phantom 1 and 2 are illustrated in figure 5.10 on a logarithmic scale. An estimate for the complex noise variance was taken from the upper corners of the FOV, which contained solely air and showed negligible leakage artifacts. The outlines of the phantoms are visible in the images and drawn into the pictures in white dotted lines. Peak values are found in the second voxel layer from top and equal for both phantoms. This indicates that the upper most voxels with signal were only partially filled by the phantom. In the case of Phantom 1, the current channel was in the region of the highest SNR.

$\boldsymbol{B}_\mathrm{J}$ was reconstructed for the entire FOV. Since the reconstruction of $\boldsymbol{J}$ using Ampere's law (equation 2.12) requires the calculation of local gradients, an SNR-threshold of 5.5 was chosen to exclude voxels with poor signal strength. Thus, local field gradients were calculated in regions with sufficient SNR according to the rules defined in figure 5.11. Voxels with neighbors below the SNR threshold were taken into account, as long as one neighbor in each direction appeared above the threshold.

In figure 5.10 (a and b), one can spot two regions with low SNR. They appear centrally on the y-axis and originate from the sensitivity profile of the sensor in combination with a $\boldsymbol{B}_0$-field in the x-direction (compare figure 4.15). These regions trim the volume of sufficient SNR in the x-direction, which is visible when comparing the reconstructions in figures 5.12(c–e) and 5.13(c–e).

$\boldsymbol{B}_\mathrm{J}$-reconstructions of the experiments with Phantom 1 and Phantom 2 are displayed in the figures 5.12(a) and 5.13(a), respectively. When comparing the two experiments, please note the different positioning in the MRI coordinate system, as illustrated in panels (b). Both experiments yielded a rotation of $\boldsymbol{B}_\mathrm{J}$ around the center of the current

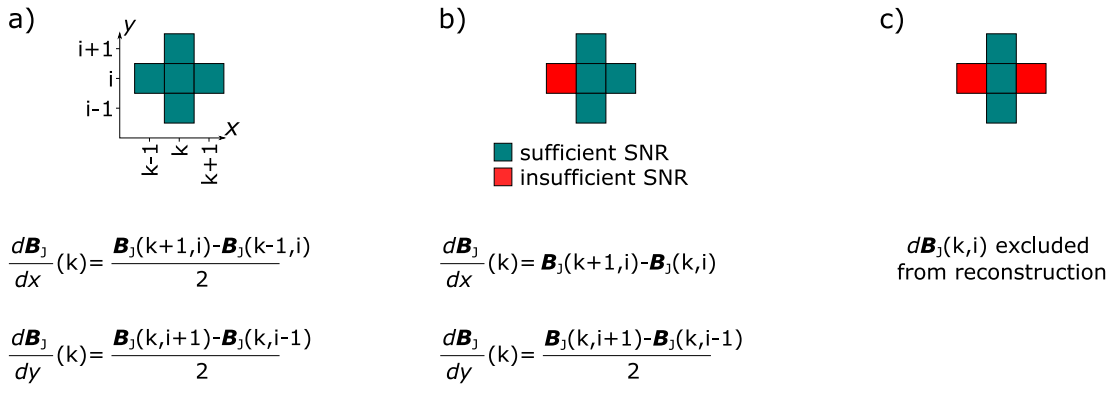

Figure 5.11: Rules for gradient calculation in demonstration measurements. Voxels were included if at least one neighbor in each direction was above the SNR threshold (a, b), otherwise not (c).

channels. However, the data of Phantom 2 showed larger variance, especially towards the lower bound of the channel. This is due to the significantly lower SNR in the region more remote to the sensor.

$\boldsymbol{J}$-reconstructions are displayed in the panels (c–h), where the gray areas represent voxels below the SNR threshold. The data are visualized for the same slices as the previously shown SNR images and separated in $\hat{J}_x$-, $\hat{J}_y$-, and $\hat{J}_z$-components. The

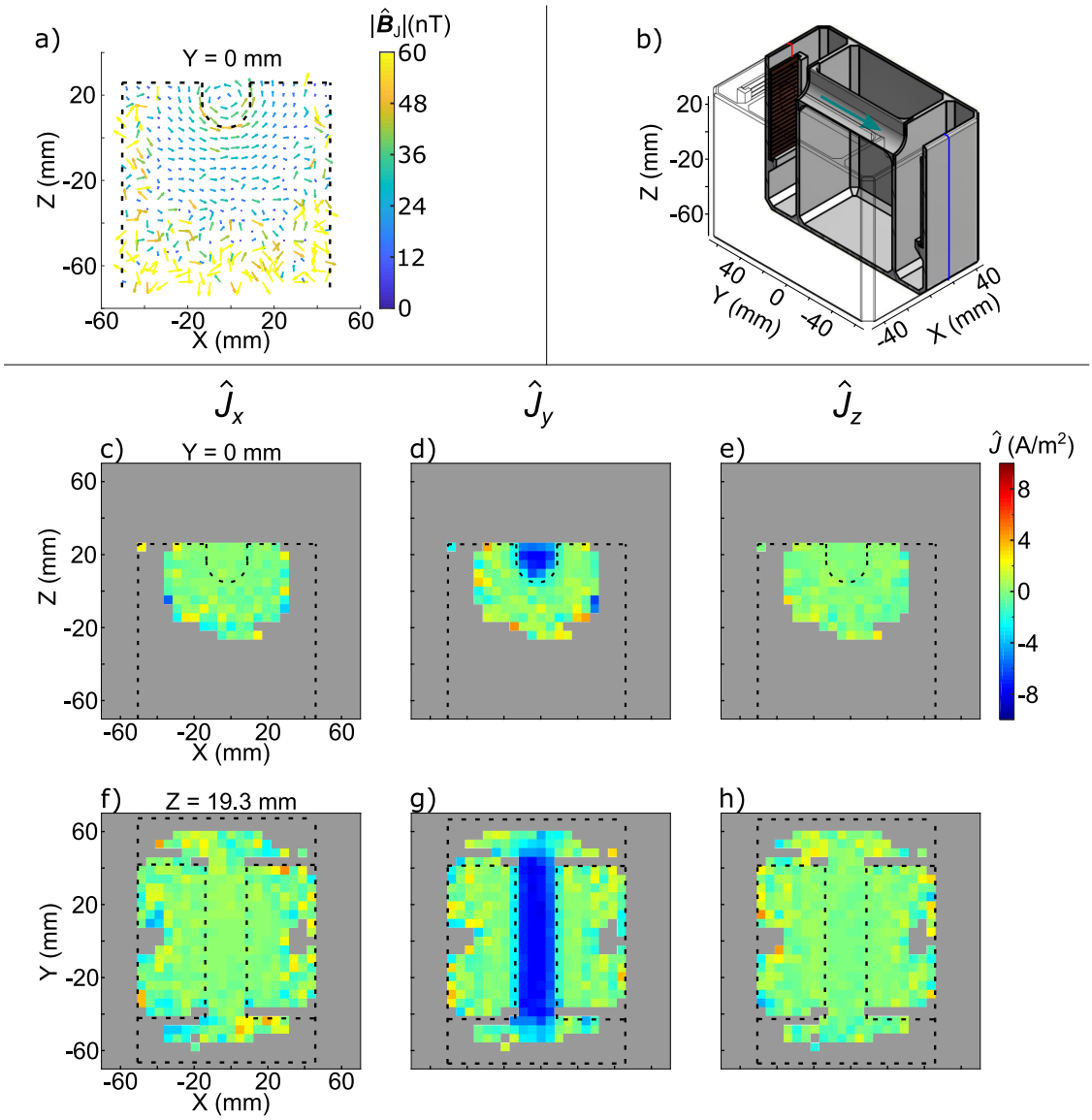

Figure 5.12: Results of 3D-zCDI measurements with Phantom 1. a) shows the reconstructed $\boldsymbol{B}_\mathrm{J}$ in a central xz-slice. Colorbar and arrow lengths were limited to 60 nT. b) illustrates the a cut-away view of the phantom. The axes show the positioning inside the MR scanner. Current-density reconstructions are shown in two slices centrally through the current channel (c–h). The gray areas represent voxels that were excluded from the reconstruction, due to insufficient SNR. The same data were published in [72] with a slightly different analysis.

experiment with Phantom 1 yielded a reconstruction of $\boldsymbol{J}$ in the negative y-direction. In the center of the current channel, the amplitudes agreed well with the estimated mean current density of 7.4 A/m^2. The reconstructed current inside the current channel was distinguishable to the outside where reconstructions vary stochastically close to zero. In the vicinity of the channel boundaries, $\hat{\boldsymbol{J}}$ appeared gradually decreasing, probably due to partial volume effects and leakage from neighboring voxels.

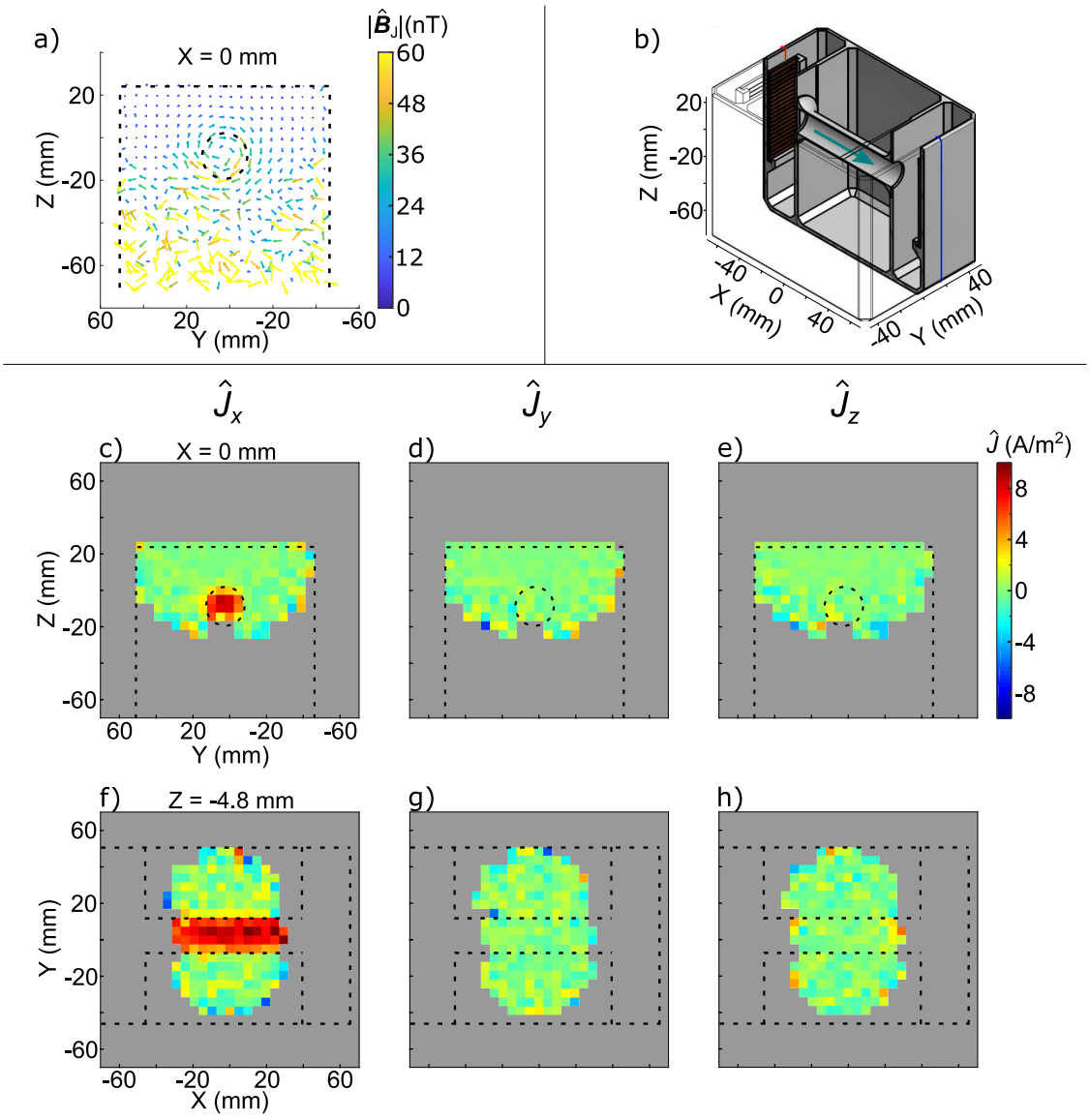

Figure 5.13: Results of 3D-zCDI measurements with Phantom 2. a) shows the reconstructed $\boldsymbol{B}_\mathrm{J}$ in a central yz-slice. Colorbar and arrow lengths were limited to 60 nT. b) illustrates the a cut-away view of the phantom. The axes show the positioning inside the MR scanner. Current-density reconstructions are shown in two slices centrally through the current channel (c–h). The gray areas represent voxels that were excluded from the reconstruction, due to insufficient SNR. The same data were published in [72] with a slightly different analysis.

Comparing figure 5.12(f–h), to the simulations displayed in figure 5.6(d–f), the focal $\hat{J}_x$-components at the corners of the channel are visible, although masked by noise due to the relatively poor SNR in those regions. In contrast to the simulations, $\hat{J}_z$-components in the areas between the current channel and electrodes cannot be observed. This is again due to the poor SNR.

In the experiment with Phantom 2, the current channel was 30 mm farther away from the sensor. The phantom was positioned such that the current inside the channel was x-directional. Referring to figure 5.10, one can see that the sensitivity decreases quickly with rising distance to the sensor. The $\boldsymbol{J}$-reconstruction images revealed that the current channel was barely in the region above the defined SNR threshold. The magnitudes of $\hat{\boldsymbol{J}}$ were in agreement with the predicted value of 7.9 A/m^2. Similar to the experiment with Phantom 1, the reconstructed current density was solely x-directional inside the current channel, and distinguishable to the outside. However, a larger variation of the current amplitudes is observable, which is due to the reduced SNR.

Figure 5.14 displays the SNR (a), and the $\boldsymbol{B}_\mathrm{J}$-reconstruction (b) in a yz-slice centrally through Phantom 3. Dotted lines indicate the phantom outline. Initially, the echo signals were k-space-windowed with a *Tukey kernel* using a shape parameter α=0.1, similar to the previous experiments. As this experiment showed much stronger ringing artifacts, α was enlarged to 0.5. However, ringing is still clearly visible in 5.14(a), which is emphasized by the logarithmic color scaling. In comparison to the previous experiments, voxel volumes were chosen about 7.5 times higher to gain sufficient SNR for the reconstruction of the significantly lower current density. However, maximum SNR values, as visible in figure 5.14(a) increased only by a factor 1.8, indicating that noise increased almost by the same factor as signal strength.

Despite the poor SNR conditions, the reconstructed magnetic field distribution in figure 5.14(b) revealed a circulation in the yz-plane, which is due to the applied current in the negative x-direction. However, the center of the circulation was not aligned with the center of the phantom, even though a nearly homogeneous current flow can be assumed according to the phantom geometry. It could be shown in simulations (explained in detail in appendix B) that this was due to the stray field of the leads connecting the electrodes. These were guided along the outside of the phantom and combined to a twisted pair approximately 20 mm below (compare figure B.1(a)).

The current-density reconstruction, displayed in figure 5.14(c), was not affected by the field of the leads because the curl operator in *Ampère's law* (2.12) is not sensitive to currents external to the phantom. Similar to the previous experiment, an SNR thresh-

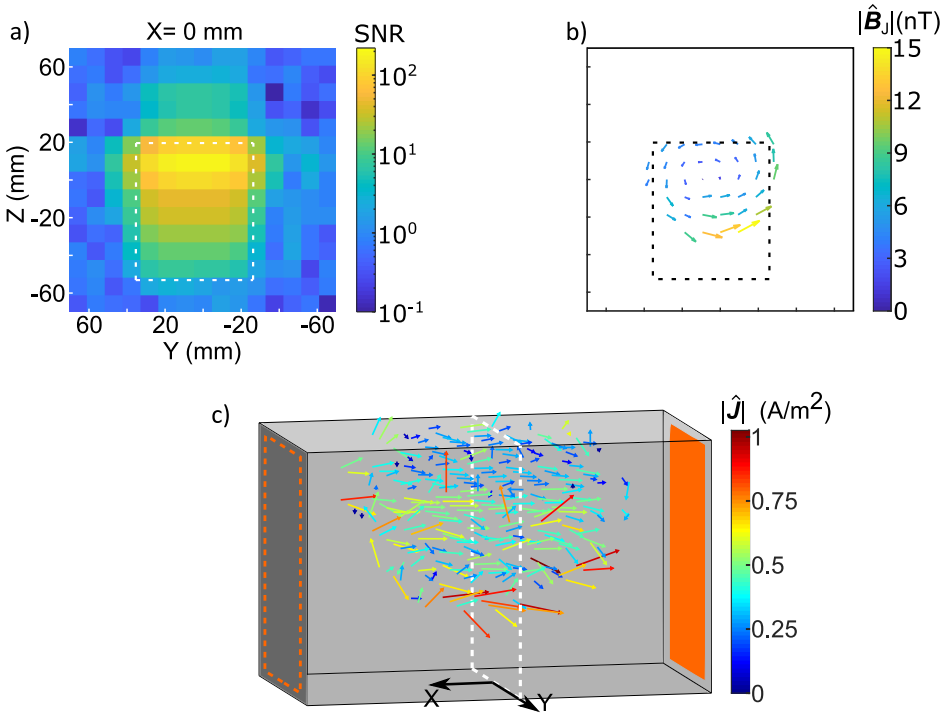

Figure 5.14: Results of 3D-zCDI measurements with Phantom 3. a) shows the image SNR in a yz-slice. The outline of the phantom is indicated by white dotted lines. b) displays the $\boldsymbol{B}_J$-reconstruction, inside the phantom (only for regions above SNR threshold). Note, colorbar and arrowlengths are limited to 15 nT. c) shows the $\boldsymbol{J}$-reconstruction in an overview plot of the entire phantom. The electrode dimensions are simplified by copper-colored planes. The slice illustrated in a) and b) is indicated by white dotted lines. The same data were published in [72] with a slightly different analysis.

old was defined for the volume of $\boldsymbol{J}$-reconstruction. However, due to the significantly lower $\boldsymbol{B}_J$-values, the SNR threshold in this experiment of 40 was chosen approximately 8 times higher. As can be seen in figure 5.14(c), this was still insufficient for most parts of the reconstruction volume. In general, $\boldsymbol{J}$ appeared in the negative x-direction. In the third voxel layer from the top, the magnitudes between 0.4 to 0.5 A/m^2 were in good agreement with the expected value calculated from the cross-sectional area. However, variations appeared larger than in the experiment with Phantoms 1 and 2.

5.3 Chapter summary and discussion

The experiments in this chapter demonstrated that full-vector $\boldsymbol{B}$-field mapping, and thereby current density imaging, is possible using MRI techniques in the ultra-low-field regime. The developed measurement setup enabled to resolve current densities as low as 0.45 A/m^2 for a voxel size of $(9.4 \times 9.4 \times 9.4)$ mm^3 and 7.4 A/m^2 for a voxel size of $(4.8 \times 4.8 \times 4.8)$ mm^3. Thereby, currents were applied from various directions, yielding

no visual direction-dependence for the quality of the result.

The measurements with Phantom 3 required more substantial attenuation of the high spatial frequencies using a *Tukey kernel* with shape parameter $\alpha = 0.5$. Still, the results showed visible ringing artifacts. Seven times higher voxel volumes yielded approximately two-fold peak SNR, compared to the previous experiments. This is probably due to several reasons. First, the sensor's sensitivity profile causes a non-linear relationship between voxel size and signal strength, especially when the voxel is expanding in the z-direction. Secondly, the image noise increases due to the lower amount of encoding steps. This is a known phenomenon in *Fourier*-based MRI. Finally, the visible ringing artifacts might expand to a low amount into all regions of the image. The noise was estimated from the voxels in the far-upper corner (air region). A noise-only image might give a better noise estimate in the case of significant ringing and leakage artifacts.

The reconstruction of $\boldsymbol{B}_{\mathrm{J}}$ in Phantom 3 revealed a strong influence of the wires connecting the electrodes, which could be verified in simulations. As the geometry of the phantom is quite simple, the basic finite difference method was utilized, even though it is computationally inefficient. For more complex phantoms, the definition of boundary constraints becomes cumbersome and simulation toolboxes such as COMSOL Multiphysics should be utilized. It could be shown that the stray field of the connecting wires is on the order of $\boldsymbol{B}_{\mathrm{J}}$, hence cannot be neglected for $\boldsymbol{B}$-field mapping. The reconstruction of $\boldsymbol{J}$, on the other hand, should not suffer from the interference, as fields from the outside are curl-free. In practice, the $\boldsymbol{J}$-reconstructions will be influenced as well, because the closed-loop integrals are approximated based on the discretized volume. Reviewing figures 5.12(a) and 5.13(a) with regards to the stray fields by the wires, one can also find a tendency of higher $\boldsymbol{B}$-field reconstructions below the current channels compared to regions above them. However, the effect is less prominent, due to the small dimensions of the current channels and the significantly higher $\boldsymbol{B}_{\mathrm{J}}$-values.

The imaging capabilities of the ULF-MRI setup were verified by an *in-vivo* 3D-magnitude image of the human head. During pre-processing, it was observed that the echo signal was not perfectly centered at $1/2\ t_{\mathrm{E}}$, which is probably subject to a time-varying x-directional background field, arising from the polarization. If this field is homogeneous, it causes a phase shift in the echo signal. On the other hand, if it shows a gradient characteristic, it yields additional dephasing of the spins, which is not recovered by inversion of the frequency gradient. In conclusion, a slightly longer time is required for spin alignment during t_{E}. During the CDI experiments, this additional gradient field should manifest as a spatially-dependent offset phase, that needs to be compensated by a spatially-adjusted calibration phase. However, a global calibration

phase proved sufficient for the $\boldsymbol{B}_{\mathrm{J}}$-reconstructions of the calibration fields. Therefore, the gradient strength must either be low, or quickly decreasing, such that the homogeneous background field components mainly influence the effective offset phase.

The head image showed three compartments (scalp, skull, and intra-cranial) that could be distinguished in regions of high SNR. Even though CSF has a much larger T_2 relaxation time in the microtesla regime, a significant amplitude difference between CSF and what is expected to be gray or white matter tissue could not be observed. Recalling the literature values of CSF relaxation time constants in the millitesla regime, listed in section 2.4.1, it becomes clear that CSF also has a much longer T_1 relaxation time relevant during polarization. Consequently, the magnetization of CSF was much lower, compared to the other tissue, compensating the lower T_2 relaxation in terms of magnitude during t_{E}.

The achieved voxel volume of $(4.1{\times}3.9{\times}3.9)$ mm^3 was slightly smaller than 3D-ULF-MRI images of the human head reported so far [89, 87, 108]. The SNR in a hypothetical expansion of the image to a CDI measurement was estimated by an additional signal loss in the zero-field time due to T_2 relaxation. The SNR values in the brain range below 20. A comparison with the CDI experiment using Phantom 3 reveals that an increase in SNR of approximately 8–10 is necessary to obtain results with similar quality. Reliable information on the SNR gap requires a thorough understanding of the effects of noise on the reconstruction quality. This will be accomplished by the methods presented in chapter 6.

An improvement in SNR by a factor of 2–3 could be gained by enlarging the voxel size to approximately $(6 \times 6 \times 6)$ mm^3. Depending on the field distribution and the tissue structure, even larger volumes are possible using non-isotropic voxels. However, to obtain similar noise values, the number of k-steps should be equal.

Besides, considering that the noise floor of the developed sensor system is already very low, substantial improvements in SNR are most likely possible by larger polarizing fields. The utilized polarization system comprises a self-shielded room-temperature coil in a quasi-Helmholtz configuration. While this arrangement has multiple upsides in terms of field homogeneity and negligible transient fields after pulsing, it limits the field strength due to a higher resistivity and the maximum number of applicable pulses due to overheating (compare section 4.2.1). This also affects the overall measurement time. A possible *in-vivo* application requires a polarization system that enables operation without duty cycle and cool-down periods. A cooled polarization coil could overcome the problems regarding SNR and measurement time.

Chapter 6

The theoretical sensitivity of zCDI

In the last chapter, it was demonstrated that $\boldsymbol{B}_\mathrm{J}$- and $\boldsymbol{J}$-distributions can be reconstructed from MRI data in the ultra-low-field regime using the zCDI sequence. It was shown that the reconstruction quality depends on image SNR. However, based on the experimental data, no confidence interval as a function of SNR could be defined.

In this chapter, the effect of measurement noise on the reconstruction of $\boldsymbol{B}_\mathrm{J}$ and $\boldsymbol{J}$ will be investigated theoretically. Therefore, the entire reconstruction algorithm will be reviewed with respect to the propagation of noise. Due to the strong non-linearity in the procedure, a small angle linear approximation will be employed, as well as a Monte-Carlo simulation for various strengths of $\boldsymbol{B}$.

The methods and results presented in this chapter have partly been previously published in [75]. Parts of the text and figures are extracted from that publication.

6.1 Noise in the rotation matrix

As elaborated before, after the zero-field time τ, the magnetization vectors $\boldsymbol{M}_1$, $\boldsymbol{M}_2$, and $\boldsymbol{M}_3$ are rotated as:

$$\begin{aligned} \boldsymbol{M}_1(\boldsymbol{r}) &= \boldsymbol{\Phi}\boldsymbol{R}_1\boldsymbol{M}_0 e^{-\left(T_2^*(\boldsymbol{r})/\tau\right)}, \\ \boldsymbol{M}_2(\boldsymbol{r}) &= \boldsymbol{\Phi}\boldsymbol{R}_2\boldsymbol{M}_0 e^{-\left(T_2^*(\boldsymbol{r})/\tau\right)}, \\ \text{and } \boldsymbol{M}_3(\boldsymbol{r}) &= \boldsymbol{\Phi}\boldsymbol{R}_3\boldsymbol{M}_0 e^{-\left(T_2^*(\boldsymbol{r})/\tau\right)}, \end{aligned} \tag{6.1}$$

where $\boldsymbol{\Phi}$ is the rotation matrix associated with $\tau\boldsymbol{A}^\times$. The manipulation of $\boldsymbol{M}_0$ before τ to $\boldsymbol{e}_x$, $\boldsymbol{e}_y$, and $\boldsymbol{e}_z$ was substituted by dedicated rotations $\boldsymbol{R}_1$, $\boldsymbol{R}_2$, and $\boldsymbol{R}_3$, respectively.

It is convenient to start with the signal acquisition when analyzing the influences of noise on the zCDI reconstruction. Inferring from equation (3.11), the echo signals obtained in the measurements are weighted integrals of the magnetization vectors plus

noise

$$s_1 = Z + \int_{Vol} \boldsymbol{C}(\boldsymbol{r})^{\mathrm{T}} \boldsymbol{R}_{\mathrm{E}}(\boldsymbol{r}, t) \boldsymbol{R}_{\mathrm{G}}(\boldsymbol{r}) \boldsymbol{M}_1 dV, \tag{6.2}$$

where $Z \sim \mathcal{N}(0, \sigma_s^2)$ is independent Gaussian noise, and $\boldsymbol{C}$ is the coupling field profile of the sensor. $\boldsymbol{R}_{\mathrm{G}}$, and $\boldsymbol{R}_{\mathrm{E}}$ are rotations in the yz-plane during gradient time and the echo time.

After applying the discrete *Fourier* transform to the frequency- and phase-encoded data and taking the relevant frequency bins, the magnitude and phase of the rotation of $\boldsymbol{M}$ can be estimated at the location of the corresponding voxel. The complex voxel value corresponding to the MR signal generated close to $\boldsymbol{r}_n$ is given by

$$v_{n,1} = \epsilon + \int \mathrm{SRF}(\boldsymbol{r} - \boldsymbol{r}_n) \beta(\boldsymbol{r})^* \tilde{M}_1(\boldsymbol{r}) dV, \tag{6.3}$$

where $\epsilon \sim \mathcal{N}(0, \sigma^2)$ is symmetric complex Gaussian noise. As before, $\mathrm{SRF}(\boldsymbol{r} - \boldsymbol{r}_n)$ is the spatial response function of the n^{th} voxel, $\beta = C_z + iC_y$ is the coupling profile converted to complex representation, and $\tilde{M}_1 = M_{1,z} + iM_{1,y}$ corresponds to the time integral of the rotating magnetization, including relaxation. Analogously, $v_{n,2}$ and $v_{n,3}$ can be derived using $\boldsymbol{M}_2$ and $\boldsymbol{M}_3$, respectively.

The voxel values v_n contain information about the zero-field-encoded magnetic field in both their magnitude and phase. To extract these information, the relative changes in v_n associated with the current density are recovered by normalization with a reference u_n, as elaborated in section 3.3.3. Repeating the sequence for all the three basis directions $\boldsymbol{e}_x$, $\boldsymbol{e}_y$, and $\boldsymbol{e}_z$, the last two rows of $\boldsymbol{\Phi}_n$ can be measured. Thereby the entries are given by

$$\boldsymbol{\Phi}_n = \begin{bmatrix} - & - & - \\ \mathrm{Im}[v_{n,1}/u_n] & \mathrm{Im}[v_{n,2}/u_n] & \mathrm{Im}[v_{n,3}/u_n] \\ \mathrm{Re}[v_{n,1}/u_n] & \mathrm{Re}[v_{n,2}/u_n] & \mathrm{Re}[v_{n,3}/u_n] \end{bmatrix}, \tag{6.4}$$

where $u = |u|e^{i\delta}$ is the complex reference, with $|u|$ being related to the magnitude of the magnetization after τ and δ to the phase accumulation due to effects that do not arise from the magnetic fields during τ, but mainly from the subsequent imaging sequence. As mentioned before, the first row of $\boldsymbol{\Phi}_n$ is derived by the cross product of the second and the third. It is clear that a unique rotation matrix $\boldsymbol{\Phi}_n$ is created for each voxel n. The following analysis concentrates on a voxel-wise reconstruction, where the index n is left out for simplicity.

Naturally, v and u are subject to noise, which would be equally distributed over the two data sets, if u was a separately acquired reference measurement. However, as elaborated in section 3.3.3, $|u|$ cannot be measured directly due to the always present

background field. Therefore, the reference is constructed from the real or imaginary parts of the three measurements of v by

$$|u| = \sqrt{\mathrm{Re}[v_1]^2 + \mathrm{Re}[v_2]^2 + \mathrm{Re}[v_3]^2}. \tag{6.5}$$

The reference phase δ, on the other hand, has to be acquired in a separate measurement in combination with a calibration procedure. The phase correction with the noisy reference phase δ causes the real part to leak to the imaginary part and vice versa, increasing the noise in the matrix elements. Dividing by the magnitude $|u|$ yields unit norm in the rows of $\mathbf{\Phi}$ decreasing the noise. This is derived in appendix C, which also shows that the noise SD in the elements of $\mathbf{\Phi}$ can be approximated as

$$\sigma_{\Phi_{ij}} = \frac{1}{\sqrt{2}\,\mathrm{SNR}} g_{ij}(\mathbf{\Phi})\,, \tag{6.6}$$

where the scaling $1 \leq g_{ij}(\mathbf{\Phi}) \leq \sqrt{2}$ depends on the associated measurement. $\sigma_{\Phi_{ij}}$ corresponds to the standard deviation of the elements in $\mathbf{\Phi}$.

The SNR is referred to the magnitude of the magnetization, i.e., $|u|$, and is defined as

$$\begin{aligned} \mathrm{SNR} &\overset{\mathrm{def}}{=} \frac{|\,\mathrm{E}[u]|}{\mathrm{SD}[e]} = \frac{|\,\mathrm{E}[u]|}{\sqrt{\mathrm{E}[\mathrm{Re}(\epsilon)^2] + \mathrm{E}[\mathrm{Im}(\epsilon)^2]}} \\ &= \frac{|\,\mathrm{E}[u]|}{\sigma}\,, \end{aligned} \tag{6.7}$$

where E denotes the expected value and SD the standard deviation. e is a noise estimate that can be extracted from a noise-only image, or from a noise-only region in any of the images v. This approximation is valid when $u \approx \mathrm{E}[u]$, *i.e.*, $\mathrm{SNR} \gg 1$.

6.2 Noise analysis of B-field reconstruction

6.2.1 Non-linearity in the reconstruction

In the reconstruction algorithm proposed by Vesanen et al. [6], all components of the magnetic field $\boldsymbol{B}$ can be derived from $\mathbf{\Phi}$ using a non-linear inversion of the matrix exponential

$$\mathbf{\Phi} = e^{\tau \boldsymbol{A}^{\times}},$$

where

$$\begin{aligned} \tau \mathbf{A}^{\times} &= \tau\gamma \begin{bmatrix} 0 & \hat{B}_z & -\hat{B}_y \\ -\hat{B}_z & 0 & \hat{B}_x \\ \hat{B}_y & -\hat{B}_x & 0 \end{bmatrix} \\ &= \frac{\varphi}{2\sin\varphi}(\mathbf{\Phi} - \mathbf{\Phi}^{\top}). \end{aligned} \tag{6.8}$$

Here, $\varphi = \arccos[(\mathrm{tr}(\mathbf{\Phi}) - 1)/2]$ represents the rotation angle of $\mathbf{\Phi}$, and $\hat{\boldsymbol{B}}$ is the reconstruction of $\boldsymbol{B}$. As this was already introduced in section 3.2.2, it is recaptured here to point out the non-linearity in the reconstruction procedure.

Analytical means to estimate the noise in the reconstruction are not applicable leaving simulation the only appropriate tool to assess the reconstruction quality as a function of noise. Nonetheless, in the following section, an investigation of the evolution of noise is employed based on a small-angle linear approximation of (6.8). This provides insights into the connection between image SNR and noise in the reconstruction. A more thorough analysis comprising the entire range of possible rotation angles is presented in section 6.2.3. Based on a Monte-Carlo simulation, noise in the reconstruction can be estimated for various field strengths and directions.

6.2.2 Linear approximation

To estimate the noise in the reconstruction of $\boldsymbol{B}$, an idealized case is discussed first where all three rows of $\mathbf{\Phi}$ can be measured, and no reference image u is needed. In this scenario, the noise in the elements of $\mathbf{\Phi}$ becomes independent and identically distributed with standard deviation of $1/(\sqrt{2}\,\mathrm{SNR})$. A first-order small-angle approximation of the rotation matrix is given by

$$\mathbf{\Phi} \approx \mathbf{I} + \tau \mathbf{A}^{\times} = \tau\gamma \begin{bmatrix} 1 & B_z & -B_y \\ -B_z & 1 & B_x \\ B_y & -B_x & 1 \end{bmatrix}, \tag{6.9}$$

where $\mathbf{I}$ is the identity matrix. The magnetic field components can be solved directly, and, as each component is measured twice, they can be averaged so that the noise SD in the angular quantity becomes $\sigma_{\gamma\tau\hat{B}_m} = 1/(2\,\mathrm{SNR})$. Here, m is any of the components x, y, or z, and the noise SD of a magnetic field component can be derived to $\sigma_{\hat{B}_m} = 1/(2\gamma\tau\ \mathrm{SNR})$.

In reality, the elements of $\mathbf{\Phi}$ are estimated with the help of a reference image, which modifies the noise in the elements as derived in appendix C. Additionally, only two rows of the rotation matrix $\mathbf{\Phi}$ can be obtained from the measurements. Therefore, one row (here the first row) has to be derived from the cross product of the adjacent rows, where the cross product contains information about the components of $\boldsymbol{B}$ orthogonal to the direction of $\boldsymbol{B}_0$. These components are no longer subject to independent random noise; consequently, the noise is not reduced by the averaging effect in the linear reconstruction.

So far, the noise analysis was discussed for the reconstruction of the effective $\boldsymbol{B}$-field. As mentioned before, in practice, the measurement of $\boldsymbol{B}_\mathrm{J}$ is contaminated by a

background field $\boldsymbol{B}_\mathrm{B}$. $\hat{\boldsymbol{B}}_\mathrm{J}$ and $\hat{\boldsymbol{B}}_\mathrm{B}$ can be decomposed from $\hat{\boldsymbol{B}}$ by the subtraction of another reconstruction. In chapter 5, this was performed by reconstructing

$$\hat{\boldsymbol{B}}1, \text{ subject to } \boldsymbol{B}_\mathrm{B} + \boldsymbol{B}_\mathrm{J}\,,$$
$$\text{and } \hat{\boldsymbol{B}}2, \text{ subject to } \boldsymbol{B}_\mathrm{B}\,,$$

and calculating

$$\hat{\boldsymbol{B}}_\mathrm{J} = \hat{\boldsymbol{B}}1 - \hat{\boldsymbol{B}}2. \tag{6.10}$$

In the first-order approximation, we finally obtain

$$\sigma_{\hat{B}_y} = \sigma_{\hat{B}_z} \approx \frac{1}{\gamma\tau\,\mathrm{SNR}} \tag{6.11}$$

and

$$\sigma_{\hat{B}_x} \approx \frac{1}{\sqrt{2}\gamma\tau\,\mathrm{SNR}}\,, \tag{6.12}$$

because B_x is measured twice. Of note, as the reference phase δ is the same for the two data sets, the additional noise due to referencing will cancel in the field subtraction.

Changing the experiment slightly, one can benefit from the field subtraction employing an averaging effect. Applying $\boldsymbol{B}_\mathrm{J}$ with opposite polarity, equation (6.10) becomes

$$\hat{\boldsymbol{B}}_\mathrm{J} = \frac{\hat{\boldsymbol{B}}1 - \hat{\boldsymbol{B}}2}{2}, \tag{6.13}$$

with

$$\hat{\boldsymbol{B}}1, \text{ subject to } \boldsymbol{B}_\mathrm{B} + \boldsymbol{B}_{\mathrm{J}(+)}\,,$$
$$\text{and } \hat{\boldsymbol{B}}2, \text{ subject to } \boldsymbol{B}_\mathrm{B} + \boldsymbol{B}_{\mathrm{J}(-)}.$$

Since the noise in the two reconstructions is independent, the noise in the field estimate is reduced. The small-angle approximation now yields:

$$\sigma_{\hat{B}_y} = \sigma_{\hat{B}_z} \approx \frac{1}{2\gamma\tau\,\mathrm{SNR}} \tag{6.14}$$

and

$$\sigma_{\hat{B}_x} \approx \frac{1}{2\sqrt{2}\gamma\tau\,\mathrm{SNR}}. \tag{6.15}$$

From now on, the reconstruction method given by equation (6.10) is called unipolar zCDI and the method in equation (6.13) bipolar zCDI.

6.2.3 Monte-Carlo simulations

From the first-order small-angle approximation one can gain intuitive understanding of the statistical uncertainty in the reconstruction of $\boldsymbol{B}_\mathrm{J}$. However, in reality, the rotation angle φ can obtain values up to π and the linear approximation breaks down. In order

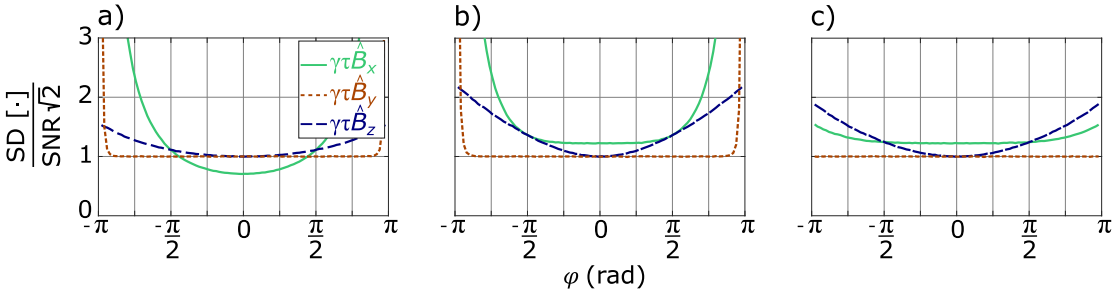

Figure 6.1: Single-voxel Monte-Carlo simulations to estimate the influence of noise on three different steps of the non-linear reconstruction as a function of the rotation angle φ. The shown data are based on simulated noisy rotation matrices, where the first row was derived by the cross product of the other two. Displayed are normalized standard deviations of each component of $\hat{\boldsymbol{B}}$, which is the reconstruction of y-directional field $\boldsymbol{B} = |\boldsymbol{B}_\mathrm{B}|\boldsymbol{e}_y$. $|\boldsymbol{B}_\mathrm{B}|$ was adjusted to generate the rotation angles φ with the negative angles corresponding to the field direction $-\boldsymbol{e}_y$. The main field $\boldsymbol{B}_0$ was x-directional. The panels show the standard deviations of reconstructions without pre-referencing (a), with pre-referencing (b), and with subsequent orthogonalization using *Löwdin's* transformation (c).

to estimate the influence of noise on the non-linear reconstruction, a series of Monte-Carlo simulations was carried out. Therefore, the last two rows of rotation matrices $\boldsymbol{\Phi}$ were generated for 100 different rotation angles $\varphi = \pm\gamma\tau|\boldsymbol{B}|$ taken uniformly between $-\pi < \varphi < \pi$, where the negative angles correspond to $-\boldsymbol{B}$. As before, $\boldsymbol{B} = \boldsymbol{B}_\mathrm{B} + \boldsymbol{B}_\mathrm{J}$, where $\boldsymbol{B}_\mathrm{J}$ was set to zero and φ was varied by adjusting $\boldsymbol{B}_\mathrm{B}$. The matrices $\boldsymbol{\Phi}$ were generated using the *General Formula of Rodriguez* (equation 2.24). Independent and Gaussian-distributed random noise was generated and superimposed with each element of $\boldsymbol{\Phi}$, according to equation (6.6). Subsequently, the first row was derived by the cross product of the other two. The procedure was repeated 100,000 times to obtain statistics for the reconstruction quality.

Figure 6.1 illustrates the standard deviation after three intermediate steps of the reconstruction of a y-directional field $\boldsymbol{B} = |\boldsymbol{B}_\mathrm{B}|\boldsymbol{e}_y$, showcasing their influences on the result. The data are normalized to the input noise $1/(\sqrt{2}\,\mathrm{SNR})$ corresponding to equation (6.6) without $g_{ij}(\boldsymbol{\Phi})$. Figure 6.1(a) illustrates a case where no referencing with u was applied. Each element of $\boldsymbol{\Phi}$ thus contained the same amount of Gaussian distributed noise. Although this may not be the case in an experimental implementation, one sees that B_x contains $1/\sqrt{2}$ the noise of the other components for small angles of φ, as predicted by the first-order approximation. However, with a rising field strength, i.e., larger rotation angle φ, the noise in this component increases non-linearly and more strongly compared to the components orthogonal to $\boldsymbol{B}_0$. The simulations un-

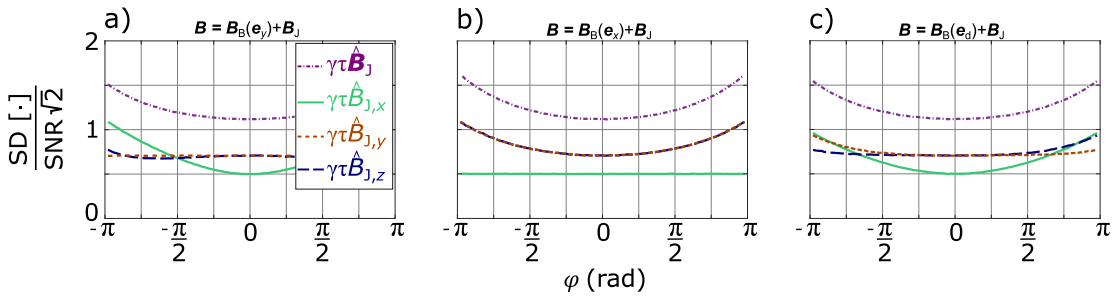

Figure 6.2: Single-voxel Monte-Carlo simulations to estimate the standard deviation of each component of $\hat{\boldsymbol{B}}_\mathrm{J}$ after bipolar reconstruction (equation 6.13), in dependence of the rotation angle φ. In addition, $\sqrt{\mathrm{tr}[\mathrm{cov}(\hat{\boldsymbol{B}}_\mathrm{J})]}$ (equation 6.16) is presented in purple, dash/dotted lines. $\boldsymbol{B}$ is the effective field $\boldsymbol{B}_\mathrm{B} + \boldsymbol{B}_\mathrm{J}$, where $\boldsymbol{B}_\mathrm{J}$ was set to zero and $\boldsymbol{B}_\mathrm{B}$ was adjusted to generate defined rotation angles φ with negative angles corresponding to $-\boldsymbol{B}$. The panels represent reconstructions, where $\boldsymbol{B}_\mathrm{B}$ was y-directional (a), x-directional (b), and diagonally oriented in $\boldsymbol{e}_\mathrm{d} = [1,1,1]/\sqrt{3}$ (c). The main field $\boldsymbol{B}_0$ was x-directional in all cases.

derlying figure 6.1(b) include the necessary pre-referencing. For very small angles, the extra phase noise due to the noisy reference phase δ affects the noise SD only in $\hat{B}_x$. Towards larger angles, this effect is visible in $\hat{B}_z$. The y-component of $\hat{\boldsymbol{B}}$ is not affected, which is in accordance with the analysis presented in appendix C. Figure 6.1(c) shows the results after subsequent orthogonalization using the *Löwdin* transformation. One observes a strong effect towards large angles φ, especially in the x-component, which is parallel to $\boldsymbol{B}_0$.

Figure 6.2 illustrates the standard deviations of the results of a simulated bipolar reconstruction. In comparison to figure 6.1, these data sets are arithmetic means of two similar fields (independent noise, identical reference), respectively equation (6.13) with $\boldsymbol{B}_\mathrm{J} = 0$. Reconstructions are given for y-directional fields (a), x-directional fields (b) and mixed directions (c), emphasizing the direction dependence of the reconstruction quality with respect to the main field direction (x). Note, figure 6.2(a) is the extension to the data shown in figure 6.1. Overall, the noise levels decrease by a factor of $\sqrt{2}$, in comparison to the reconstructions of the effective field $\boldsymbol{B}$ in figure 6.1. Further, the additional noise due to the reference phase δ, visible in figure 6.1(b–c), was subtracted entirely. Except for very large angles ($\varphi > 7\pi/8$), the noise SD in each component is lower than $1/(\mathrm{SNR}\sqrt{2})$.

Figure 6.2 also shows a measure to assess the expected deviation from the mean of $\hat{\boldsymbol{B}}_\mathrm{J}$ (purple, dash-dotted line), which can be derived to be the square root of the trace

of the covariance matrix:

$$\begin{aligned} \mathrm{SD}[\hat{\boldsymbol{B}}_J] &= \sqrt{\mathrm{E}\left[|\hat{\boldsymbol{B}}_\mathrm{J} - \mathrm{E}(\hat{\boldsymbol{B}}_\mathrm{J})|^2\right]} \\ &= \sqrt{\mathrm{tr}\left[\mathrm{cov}(\hat{\boldsymbol{B}}_\mathrm{J})\right]} \\ &= \sqrt{\sigma^2_{B_{\mathrm{J},x}} + \sigma^2_{B_{\mathrm{J},y}} + \sigma^2_{B_{\mathrm{J},z}}}\,. \end{aligned} \tag{6.16}$$

6.3 Noise analysis of J-field reconstruction

From equation (6.13), the full vector of the local field $\hat{\boldsymbol{B}}_\mathrm{J}$ is derived, enabling the estimation of $\hat{\boldsymbol{J}}$ by *Ampère's law* (equation 2.12). The noise in the reconstruction of $\boldsymbol{B}_\mathrm{J}$ gives rise to the noise in the current density reconstruction.

For an estimation, some simplifications are made. First, a constant current density in a homogeneous and isotropic medium is assumed. Secondly, a homogeneous background field that is much larger than $\boldsymbol{B}_\mathrm{J}$ shall be present. The spatial derivation is calculated, taking the two nearest neighbors into account

$$\frac{d\hat{\boldsymbol{B}}_\mathrm{J}}{dz}(z) = \frac{\hat{\boldsymbol{B}}_\mathrm{J}(z+l) - \hat{\boldsymbol{B}}_\mathrm{J}(z-l)}{2l}\,, \tag{6.17}$$

where z is the coordinate of the voxel in the z-direction and l is the voxel side-length. Assuming equal SNR at $z+l$ and $z-l$, the noise SD of the gradient is approximately $\sigma_{\boldsymbol{G}(z_n)} = \sigma_{\hat{\boldsymbol{B}}_\mathrm{J}(z_n)}/(l\sqrt{2})$. Applying the curl

$$\hat{J}_x = \frac{1}{\mu_0}\left(d\hat{B}_{\mathrm{J},z}/dy - d\hat{B}_{\mathrm{J},y}/dz\right) \tag{6.18}$$

and neglecting the small possible differences in $\sigma_{\hat{B}_{\mathrm{J},z}}$ and $\sigma_{\hat{B}_{\mathrm{J},y}}$, the noise SD of $\hat{J}_x$ can be approximated as

$$\sigma_{\hat{J}_x} = \sigma_{\hat{B}_{\mathrm{J},z}}/(l\mu_0). \tag{6.19}$$

$\sigma_{\hat{J}_y}$ and $\sigma_{\hat{J}_z}$ can be estimated analogously.

6.4 Field reconstruction quality in terms of image SNR

Using the definition of image SNR in equation (6.7) and the results of the Monte-Carlo simulations, the signal-to-noise ratio of the $\boldsymbol{B}_\mathrm{J}$-reconstruction ($\mathrm{SNR}[\hat{\boldsymbol{B}}_\mathrm{J}]$) can be estimated by

$$\begin{aligned} \mathrm{SNR}[\hat{\boldsymbol{B}}_\mathrm{J}] &\overset{\mathrm{def}}{=} \frac{|\hat{\boldsymbol{B}}_\mathrm{J}|}{\mathrm{SD}[\hat{\boldsymbol{B}}_\mathrm{J}]} \\ &= \frac{\gamma\tau|\hat{\boldsymbol{B}}_\mathrm{J}|\sqrt{2}}{c}\mathrm{SNR}\,, \end{aligned} \tag{6.20}$$

where $\mathrm{SD}[\hat{\boldsymbol{B}}_\mathrm{J}]$ is the measure for noise in the vector $\hat{\boldsymbol{B}}_\mathrm{J}$ defined in equation (6.16). Further, the scaling factor c depends on the strength and the orientation of $\boldsymbol{B}_\mathrm{B}$ and can be read directly from the purple, dash/dotted lines in figure 6.2. As c is highest for x-directional background fields, a polynomial, normalized to $1/\pi$, was fitted to the data presented in figure 6.2(b), to approximate c as a function of φ:

$$c(\varphi) \approx 0.17 \left(\frac{\varphi}{\pi}\right)^4 + 0.35 \left(\frac{\varphi}{\pi}\right)^2 + 1.118\,. \tag{6.21}$$

Note that the results presented in the figures 6.2 (a and c) only deviate slightly from equation (6.21). According to the figure, without any information on the background field, a representative value for the scaling factor would be $c = 1.3$. This is close to the worst-case scenario as higher rotation angles may cause phase wrapping.

To provide a numerical example, let us assume a $|\boldsymbol{B}_\mathrm{J}| = 10$ nT, a homogeneous x-directional background field of 60 nT, and a zero-field time $\tau = 100$ ms, taking into account the T_2 relaxation time of GM in the microtesla regime of approximately 100 ms. Substituting the rotation angle $\varphi = \gamma\tau|\boldsymbol{B}|$ in equation (6.21), c is approximated to be 1.2. According to equation (6.20), for a required $\mathrm{SNR}[\hat{\boldsymbol{B}}_\mathrm{J}] > 10$, the voxel SNR needs to be over 32.

The estimation of $\boldsymbol{J}$ using *Ampère's law* requires the determination of local field gradients, where the noise in the reconstruction is inversely proportional to the voxel side-length l. This effect should not be underestimated, as the signal strength already scales to the voxel volume l^3, the SNR of $\hat{\boldsymbol{J}}$ scales to the fourth power of the voxel side-length. The quality of the $\boldsymbol{J}$-reconstruction can be determined from the SNR of $\hat{\boldsymbol{B}}_\mathrm{J}$, by including the scaling factor $l\mu_0$ in equation (6.20):

$$\begin{aligned} \mathrm{SNR}[\hat{\boldsymbol{J}}] &\stackrel{\mathrm{def}}{=} \frac{|\hat{\boldsymbol{J}}|}{\mathrm{SD}\,[\hat{\boldsymbol{J}}]} \\ &\approx \frac{\gamma\tau l\mu_0|\hat{\boldsymbol{J}}|\sqrt{2}}{c}\mathrm{SNR}\,. \end{aligned} \tag{6.22}$$

The approximation in equation (6.22) is valid when the voxels involved in the gradient estimation are subject to equal complex voxel SNR. Especially at tissue boundaries, this can cause erroneous assessments due to different relaxation times.

Again, to provide an example, we assume a current-density distribution of 0.4 A/m^2, a value in accordance with the literature for a stimulation of approximately 4 mA [27]. Similar to the example above, $c \approx 1.2$ is assumed. If we want to derive $\hat{\boldsymbol{J}}$ with $\mathrm{SNR}[\hat{\boldsymbol{J}}] > 10$ and a voxel side-length of 5 mm, a required complex voxel SNR of 130 is estimated.

6.5 Comparison of zCDI sensitivity to high-field MR CDI

Already in 1992, Scott et al. [38] presented a sensitivity analysis for high-field MR CDI based on a standard spin-echo pulse sequence using slice selection[1]. As elaborated before, MR CDI relies on the impracticable subject rotation inside the scanner. At least for $\boldsymbol{B}_\mathrm{J}$ estimates, Scott et al. derive similar variance of the reconstructions:

$$\sigma_B = \frac{1}{2\gamma t_\mathrm{current}\mathrm{SNR}}.$$

Since each component of $\boldsymbol{B}$ is obtained equally (sequentially after subject rotation), no distinction between $\boldsymbol{B}_x$, $\boldsymbol{B}_y$, and $\boldsymbol{B}_z$ is given. Comparing $\boldsymbol{J}$-reconstruction quality is more difficult, due to differences in the sequence and the gradient calculations. Nevertheless, they give a numerical example similar to the parameters presented above ($t_\mathrm{current} = 60$ ms, $T_2^* = 100$ ms, voxel size = $(0.75 \times 0.75 \times 5)$ mm^3, SNR =40). Using a similar template for gradient calculation, they yield an SD$[\hat{\boldsymbol{J}}] = 0.48$. Expanding the approximations for SD$[\hat{\boldsymbol{J}}]$ in zCDI to the same voxel dimensions results in almost the same standard deviation for $\tau = 100$ ms. A comparison of SNR in high-field MRI and ULF MRI is difficult, with respect to the different sensitivity profiles and the substantially differing sequence. The exemplary value of 40, given in [38], seems well achievable with ULF MRI.

6.6 Chapter summary and discussion

The analysis in this chapter provides information on the influence of noise on the reconstruction of $\boldsymbol{B}_\mathrm{J}$ and $\boldsymbol{J}$. The linearization of the field reconstruction gives an approximate relationship between the image SNR and the statistical uncertainty in the field estimates. Further, Monte-Carlo simulations were used to derive the statistical uncertainty in the presence of large background fields where the non-linearity takes effect. The presented link between image SNR and noise in the reconstruction allows the determination of the necessary SNR for the reconstructions $\hat{\boldsymbol{B}}_\mathrm{J}$ and $\hat{\boldsymbol{J}}$ within a predefined uncertainty.

To retain constant image SNR in the Monte-Carlo simulations, $|\boldsymbol{B}_\mathrm{B}|$ was adjusted to vary $\varphi = \gamma\tau|\boldsymbol{B}_\mathrm{B}|$. τ was set equal to to T_2, which yields maximum SNR$[\boldsymbol{B}_\mathrm{J}]$ according to [6]. However, the non-linear dependence of SNR$[\boldsymbol{B}_\mathrm{J}]$ on φ suggests that there is an optimum set of parameters for each specific case. In reality, the effective background

[1] Slice selection is a method of spatially dependent excitation during the rf pulse. Since it is not further explained in this thesis, please see [38] directly, or [77] for general information.

field will be roughly constant over the measurement periods and τ should be adjusted to obtain maximum SNR[$\boldsymbol{B}_\mathrm{J}$]. If the relaxation times are known, equations (6.20) and (6.21) can be utilized to create a cost function that provides parameters for maximum reconstruction quality. It should be mentioned that the optima for τ are flat and close to T_2 for small background fields. An adjustment of τ seems worthwhile in the case of very large background fields, where up to 12% can be gained in SNR[$\hat{\boldsymbol{B}}_\mathrm{J}$] compared to $\tau = T_2$. Furthermore, it should be kept in mind that $\varphi < \pi$ should be fulfilled to prevent ambiguity in the field reconstruction.

This chapter provides means to evaluate the performance of a specific ULF-MRI system in zCDI directly from acquired or simulated image data. This will be used in chapter (7) to assess a modification to the setup introduced in chapter 4. As the sensitivity analysis is universally applicable, in [75], the methodology was applied to compare the performance of the here presented PTB-ULF-MRI setup to a setup comprising an MEG-based multi-channel system located at Aalto University in Espoo, Finland.

Chapter 7

Towards *in-vivo* CDI

In chapter 5, the feasibility of zCDI was demonstrated in phantoms. It was estimated, that a further boost in SNR is necessary towards an *in-vivo* implementation of the method. It was elaborated, that this is most likely achievable through improvements in the polarization setup. In chapter 6, the theoretical sensitivity was analyzed as function of image SNR, enabling to assess the performance of a setup by analytical means.

In this chapter an improved polarization setup optimized for *in-vivo* zCDI, is presented. The performance of the upgraded system is evaluated in simulations emulating the zCDI sequence under realistic conditions. Finally, a demonstration measurement using a realistic head phantom and an *in-vivo* measurement are shown, illustrating the current status.

Section 7.2.2 describes FEM simulations of current density and magnetic field distributions. The model design and the simulations were conducted by Alexander Hunold and René Machts at the Institute of Biomedical Engineering and Informatics, Technische Universität Ilmenau, Germany. The analysis of the simulation results was performed by me, Peter Hömmen, in close collaboration with Antti J. Mäkinen from the Department of Neuroscience and Biomedical Engineering of the Aalto University School of Science, Finland.

Section 7.3 describes a demonstration measurement using a realistic three-compartment head phantom. The phantom was provided by Alexander Hunold and René Machts of the Institute of Biomedical Engineering and Informatics of the Ilmenau, Technische Universität Ilmenau, Germany.

The methods and results presented in this chapter have partly been previously published in [75]. Parts of the text and figures are extracted from that publication.

7.1 An improved polarization setup

Retaining the existing power amplifier hardware for polarization, a new, optimized, coil design is needed that exploits the amplifiers capabilities more effectively. The utilized amplifier possesses two ranges of operation, 150 V and 30 A, or 70 V and 60 A. Therefore, the coil resistance should not exceed 5 Ω, or 1.17 Ω, respectively. Another constraint originates in the fact that the zCDI sequence requires multiple runs per k-step, yielding easily 3,000 runs and more for an image with a voxel size below 10 mm. The power of approximately 4.5 kW dissipates as heat, causing an increase of the coil resistance. Since cool-down periods of several hours are not applicable *in vivo*, a cooling system is required enabling nearly continuous polarizing steps. Naturally, another demand is a high field-to-current ratio within the imaging volume, while the field at the position of the MUMETAL® walls should be minimized to prevent transients due

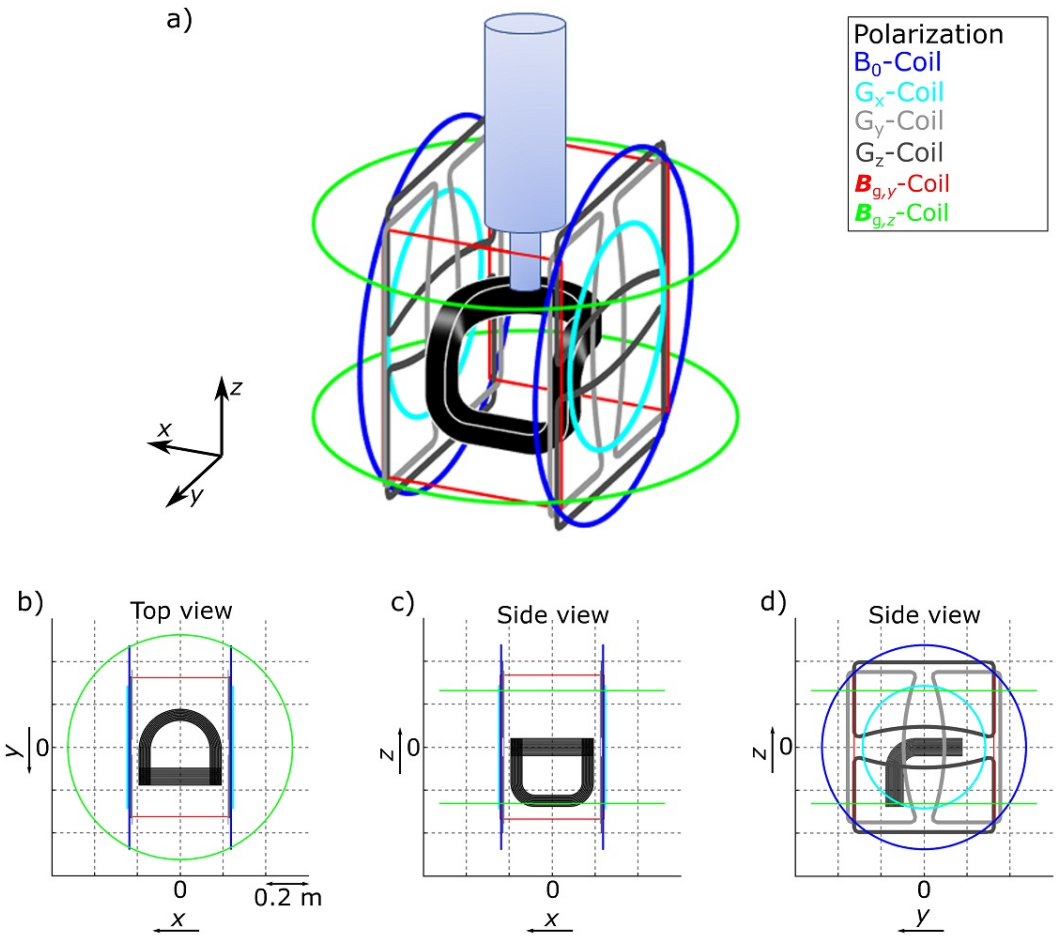

Figure 7.1: Illustration of the coil setup, optimized for *in-vivo* zCDI. a) shows an overview including the lHe dewar. b) shows a topview, and c), and d) give the two side-views xz, and yz, respectively. Not in the figure is a large shielding coil, that attenuates the field of the polarization coil at the walls of the shielded room.

to decaying magnetization and/or eddy currents. Consequently, a self-shielded coil is desired.

We built a 414-turn polarization coil, shape-optimized for the human head. Figure 7.1 visualizes the coil geometry in the ULF-MRI setup. The mean field-to-current ratio of the inhomogeneous polarization field over the FOV was measured at about 1.3 mT/A. My colleague Rainer Körber designed a large ($\approx 120 \times 120$ cm^2), un-cooled shielding coil (not displayed in figure 7.1), that was optimized to reduce transient room responses by a factor 50, while damping the polarization field in the FOV by only 3 %. Remaining transients after the turn-off of $\boldsymbol{B}_\mathrm{P}$ were measured via fluxgate at the center of the MRI setup to be approximately 0.5 nT per Ampére current in the coil.

One-millimeter spacing in between windings was realized, enabling immersion of the coil in a cooling agent. Initially, the coil was intended to be operated in a liquid nitrogen bath. However, the necessary cryostat dimensions exceeded the available space in the existing coil setup. Therefore, an oil bath connected via a pump to a heat exchanger outside of the shielded room was utilized. Figure 7.2 shows a photograph of the manufactured coil in the oil vessel. The resistance of the polarization setup, including the shielding coil, was 3.4 Ω. During extensive operation, the oil bath heats up to approximately 320 K and the shielding coil to more than 360 K, yielding a rise in resistance to approximately 4 Ω. In conclusion, the coil can be operated with 30 A polarization current using the Rohrer amplifier in range one (150 V, 30 A). Liquid nitrogen cooling, as initially intended, would reduce the coils ohmic resistance to approximately 0.5 Ω, allowing to use range two of the amplifier with 50 A and more.

Figure 7.2: Photograph showing a top view of the optimized polarization coil in the oil vessel (oil not inserted).

7.2 zCDI simulations using the modified setup

7.2.1 An MRI simulation setup for realistic zCDI emulation

To check whether the optimized coil setup provides sufficient magnetization for *in-vivo* zCDI, a simulation setup was established that emulates the entire sequence under realistic conditions. The main factors that determine the SNR profiles of ULF-MRI images are the sensor arrangement, system noise, and the polarizing field profile. To evaluate the sensitivity of the $\boldsymbol{B}_J$- and $\boldsymbol{J}$-field reconstruction in a realistic situation, the simulations incorporated the calculated polarization field profile (see figure 7.3(a)) and realistic coupling coefficients using the actual sensor geometry (see figure 7.3(b)). Both, the polarization field profile and the coupling of the magnetization to the sensor were calculated using the methods described in appendix D.1. Time-domain evolution of the magnetization was calculated using an analytical solution to equation (2.33) and assuming ideal gradient fields and instantaneous field switching. Based on measured values, sensor noise of 350 aT $Hz^{-1/2}$ was added to the simulated gradient-echo signals.

The simulation setup was validated using actual ULF-MRI measurements of a simple spherical phantom. The results of the measurement in comparison to simulations is presented in appendix D.2. It was shown that the simulation toolbox overestimated the MR amplitudes by approximately 25%, which could be attributed to effects of the shielding coil that was not considered in the simulations, winding errors in the actual polarization coil, and perhaps a somewhat different warm-cold distance of the sensor setup subject to helium level.

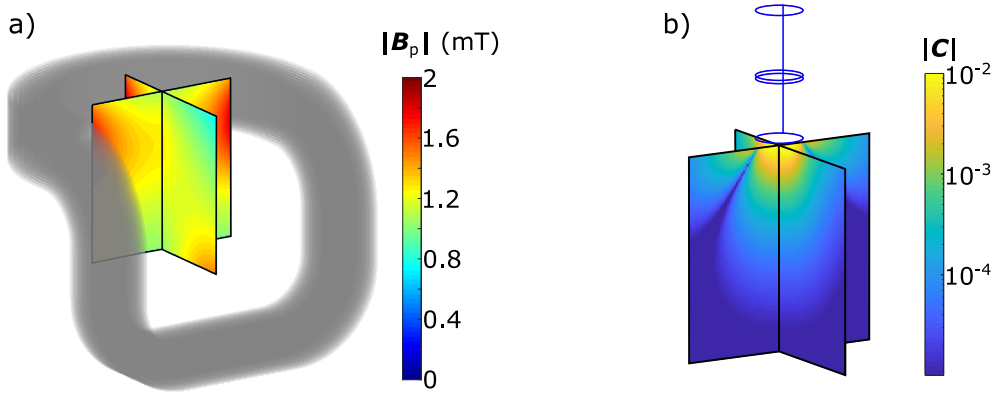

Figure 7.3: a) shows the calculated polarization field profile for 1 A in the optimized polarization coil (gray), and b) the coupling field profile of the 2nd-order gradiometer. Both were incorporated in the realistic zCDI simulations.

7.2.2 Realistic fields from FEM simulations based on a three-compartment head phantom

To emulate the zCDI sequence in a realistic setting, $\boldsymbol{B}_J$-distribution as found in a human head is desired. Therefore, a model based on computer tomography (CT) scans of a human head [143] was developed by the *Institute of Biomedical Engineering and Informatics* in Ilmenau, Germany. Figure 7.4(a) shows the model which contains the three compartments scalp, skull, and intra-cranial tissue.

Realistic $\boldsymbol{J}$- and $\boldsymbol{B}_J$-distribution were derived from FEM simulations using the Comsol Multiphysics software based on the GMRES solver. Therefore, the conductivity in the outermost scalp compartment was set to 0.22 S/m, in the skull compartment to 0.01 S/m, and in the innermost brain compartment to 0.33 S/m. The two stimulation electrodes were positioned roughly 10 cm apart, one on the forehead and the other one on the side. The conductivity of the electrodes was set to 1.4 S/m. The average tetrahedron side-lengths were approximately 3.5 mm in the brain and 2.5 mm in the

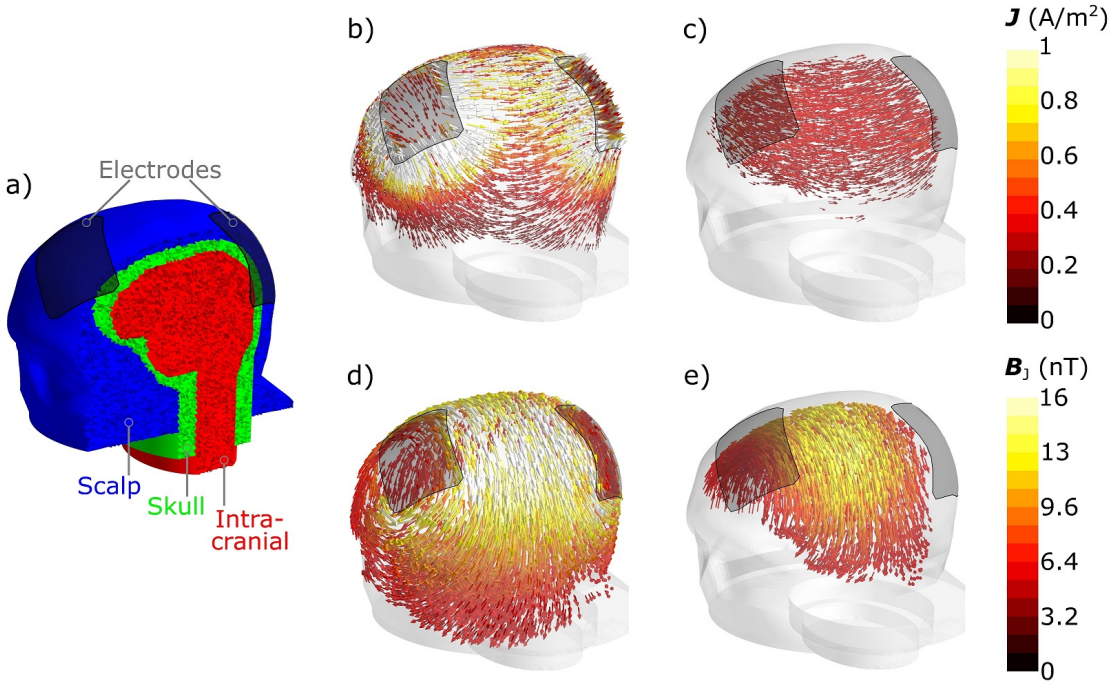

Figure 7.4: The tetrahedral FEM mesh of the three-compartment head model consisting of intra-cranial volume (red), skull (green), and scalp (blue) compartments (a). The electrodes are illustrated in transparent gray. The simulated current density $\boldsymbol{J}$ is visualized in the scalp (b) and in the brain compartment (c). The simulated magnetic field $\boldsymbol{B}_J$, due to all current flowing in the head, is plotted in the scalp (d) and in the brain (e). The arrow lengths are scaled logarithmically and each subfigure shows only the top 30 (magnitude) percentile of the field in the respective compartment.

scalp. Current-flow was realized by setting zero potential on the cathode's outer surface and applying a total current of ±4.5 mA on the outer surface of the anode. For the calculation of $\boldsymbol{B}_\mathrm{J}$, a spherical air compartment (2 m in diameter) was added to the model to ensure that the magnetic isolation boundary condition had a negligible effect on the result.

Patterns of the simulated current density and the associated magnetic field are shown in figure 7.4 (b–e). Due to the low conductivity of the skull, maximal current flows in the scalp compartment. In the vicinity of the electrode boundary the current density was up to 15 A/m^2. The maximal current density in the brain compartment under the electrodes was about 0.5 A/m^2. This is in accordance with literature values, reporting approximately 0.1 A/m^2 in the brain, for 1 mA applied current [27, 124]. In relation to $\boldsymbol{J}$, $\boldsymbol{B}_\mathrm{J}$ appeared smoother, yielding maximal field strengths of 20 nT in the scalp and 12 nT in the brain compartment. The maximum of the field magnitude in the brain compartment is localized in between the electrodes, just beneath the skull layer. In contrast to that, the maximal current density in the brain is localized beneath the electrodes.

7.2.3 Simulation parameters

The MRI simulation setup (section 7.2.1) was used to emulate the full zCDI sequences using the $\boldsymbol{B}_\mathrm{J}$-distribution derived from the FEM simulations (section 7.2.2). Figure 7.5(a) shows how the head model was positioned in the scanner arrangement, similar to how the positioning of a head would be in an actual measurement setup. The scalp-sensor distance was 16 mm, taking into account the warm-cold distance of the system plus 3 mm to compensate for the amplitude differences found in the comparison with

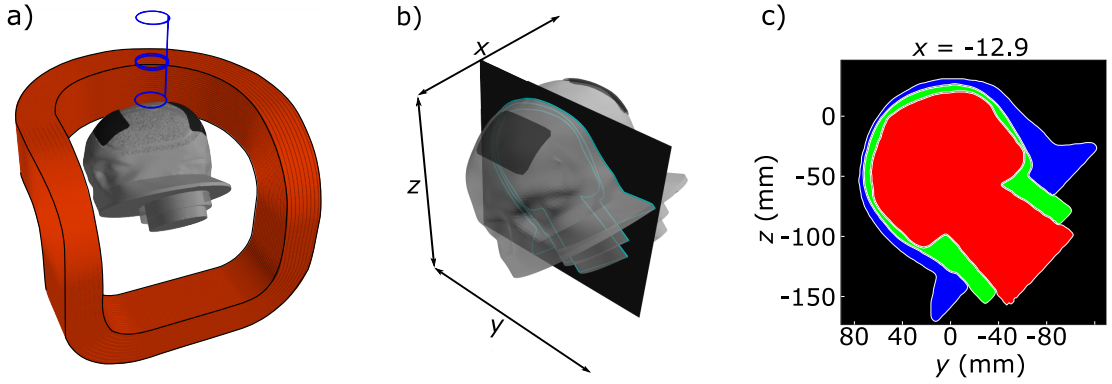

Figure 7.5: For the MRI simulations, the head model was positioned in the virtual scanner arrangement (a). Panel b) shows the model inside the FOV, defined by the MRI gradients, and c) displays a slice through the FOV centrally between the electrodes.

actual measurements, as described in appendix D.2.

A polarization current of 50 A was chosen corresponding to field maximum of 90 mT and mean of 65 mT in the brain compartment. Therefore, a best-case scenario was emulated assuming the coil can be operated in a nitrogen bath in the future. Nevertheless, the linear relation between polarization field strength and image SNR enables scaling the results to 30 A.

The magnetization was discretized to tetrahedral elements derived from the geometry of the FEM model. The time evolution of the magnetic moment was simulated for the center of each element. The T_2 relaxation time for the brain compartment was set to 106 ms and for the scalp compartment to 120 ms [87]. For simplicity, as the spin density in the skull is insignificant compared to soft tissue, this compartment was assumed to have no magnetization at all.

Gradients were set to give a voxel size of $(5 \times 5 \times 5)$ mm^3 and a FOV of 220 mm in the phase-encoded directions. Figure 7.5(b) presents the head model inside the coordinate system defined by the MRI gradients. The adjacent panel (c) displays a slice through the phantom, centrally between the electrodes. The compartment outlines were extracted from the FEM model, interpolated to a regular 1-mm grid. Both, the frequency- and phase-encoding dimensions were tapered with a *Tukey window* (shape parameter $\alpha = 0.5$) before computing the 3D-DFT.

7.2.4 Simulation results

Figure 7.6(a) displays the performance of the ULF-MRI setup, as derived from the simulations with 50 A polarization current and incorporating noise (350 aT Hz$^{-1/2}$).

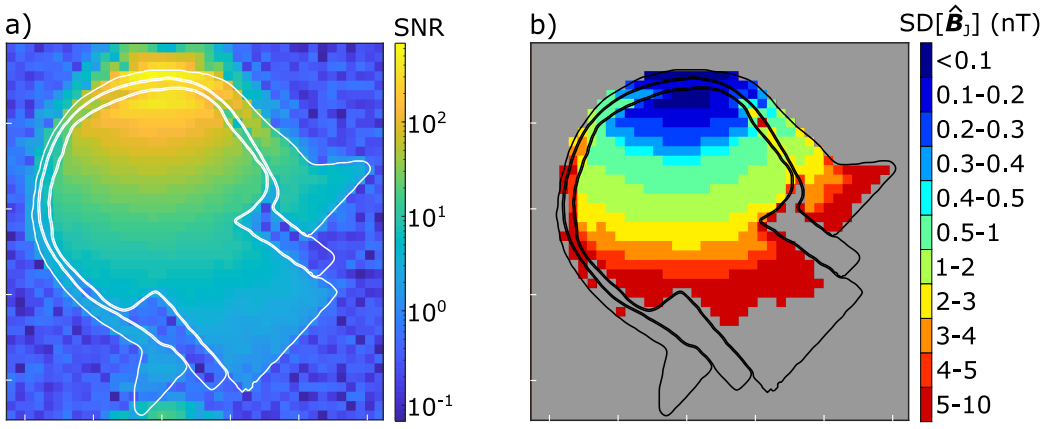

Figure 7.6: Performance of the optimized ULF-MRI setup. The panels show image SNR (a), and calculated SD $\left[\hat{\boldsymbol{B}}_J\right]$ (b), for simulations with 50 A polarization current and 350 aT Hz$^{-1/2}$ noise. The plane corresponding to the slice is given in figure 7.5(b, c).

As pointed out before, the reconstruction quality is highly dependent on the SNR of the underlying ULF-MR images. The simulations result in maximum SNR values above 600. The sensitivity drops with increasing distance to the sensor, but the image SNR remains well above 100 in a large region in the intra-cranial volume. In the previous chapter, the statistical uncertainty of the $\boldsymbol{B}_\mathrm{J}$-reconstruction in dependence of the image SNR was derived. Figure 7.6(b) gives confidence intervals for SD $\left[\hat{\boldsymbol{B}}_\mathrm{J}\right]$ calculated using equation (6.20) with $c = 1.3$. Over a large region of the brain compartment, SD $\left[\hat{\boldsymbol{B}}_\mathrm{J}\right]$ is smaller than 1 nT, giving an approximate SNR $\left[\hat{\boldsymbol{B}}_\mathrm{J}\right] > 10$, based on the estimations in chapter 6. Even if the polarization current was reduced to 30 A, the area of sufficient image SNR would be approximately 70×40 mm^2 (y, z).

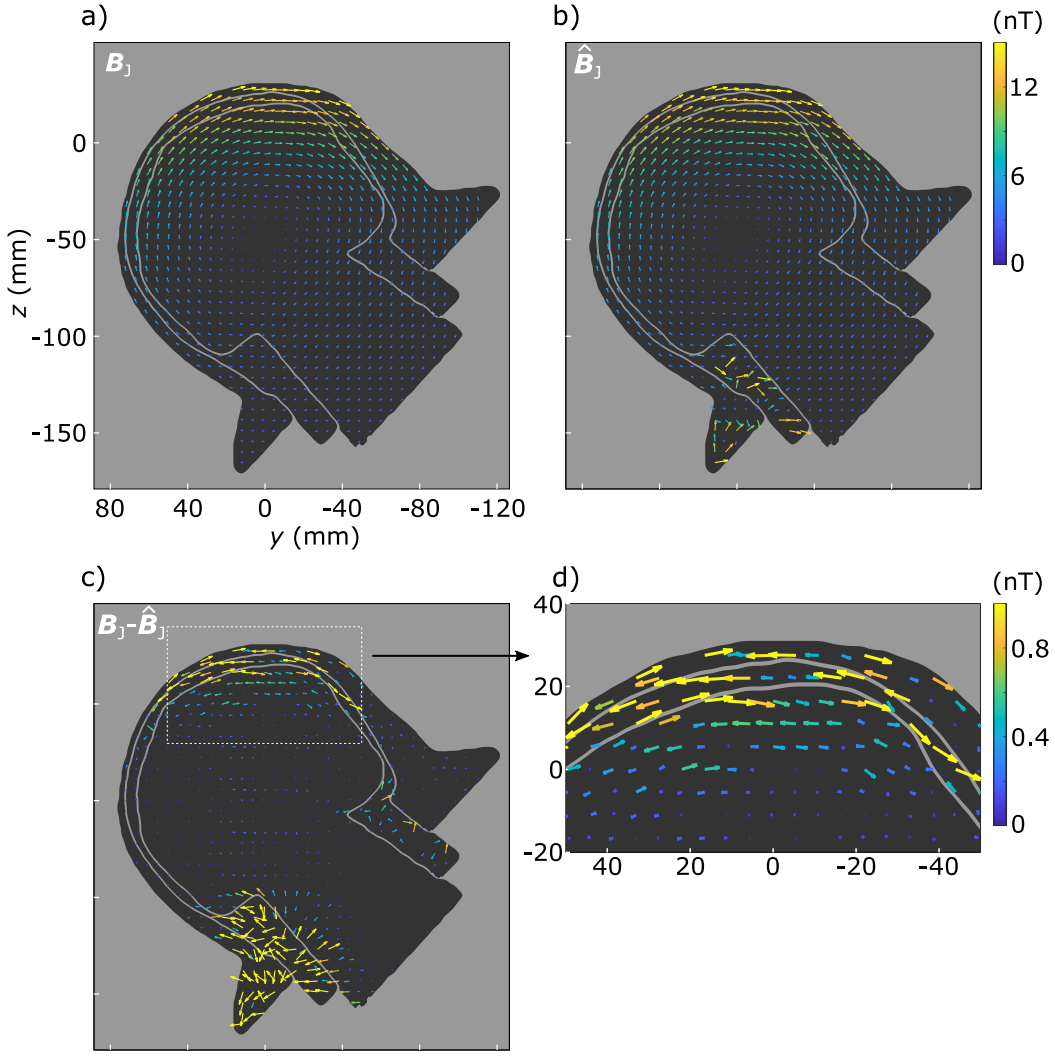

Figure 7.7: The input field $\boldsymbol{B}_\mathrm{J}$ from the FEM solution (a), the noise-free reconstruction $\hat{\boldsymbol{B}}_\mathrm{J}$ from the zCDI simulations (b), the difference field (c), and a zoom-in to c) (d) are shown in a yz-projection (compare figure 7.5(c)). Note: In a) and b) the colorbar and arrow lengths were limited to 15 nT and in c) and d) to 1 nT.

Figure 7.7 shows a comparison between the field reconstructions $\hat{\boldsymbol{B}}_{\mathrm{J}}$ of the simulated zero-field sequence (b) and ground-truth FEM solutions of $\boldsymbol{B}_{\mathrm{J}}$ (a). Both data sets are presented without noise. The reconstructed magnetic field $\hat{\boldsymbol{B}}_{\mathrm{J}}$ resembles closely the corresponding FEM solution, which was used as an input to the MR simulations. Notable differences are found inside the skull, which is expected due to the lack of magnetization, as well as on the top parts of the scalp at the field maximum. The difference image (c and d) reveals ringing artifacts in the intra-cranial volume, leading to error fields up to approximately 1 nT. Comparing the effects of ringing artifacts to the random fluctuations due to noise, as estimated in figure 7.6, it becomes evident that in the region directly below the sensor ringing and leakage cause the biggest reconstruction errors.

The difference between the reconstructed current density $|\hat{\boldsymbol{J}}|$ (figure 7.8(b)) and the corresponding FEM solution of $|\boldsymbol{J}|$ (figure 7.8(a)) is visualized in figure 7.8(c) and appears more prominent compared to the magnetic fields. Although no noise was added to the simulated data, errors in the finite-difference approximations and artifacts in $\hat{\boldsymbol{B}}$ add up, so that the $\hat{\boldsymbol{J}}$-field near the skull is highly distorted. The intra-cranial fields show greater resemblance, although a notable ringing-artifact from the skull can be

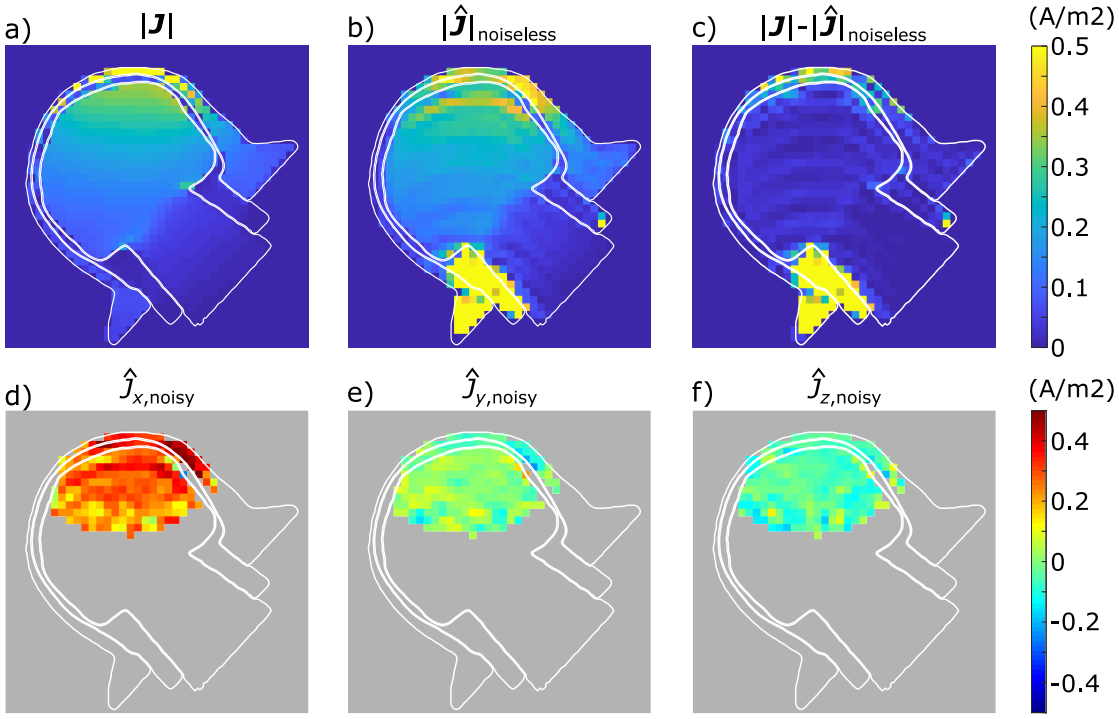

Figure 7.8: Panel a) displays the true $\boldsymbol{J}$-distribution from the FEM solution, interpolated to the voxel grid of the MRI simulations. b) gives the noiseless reconstruction $\hat{\boldsymbol{J}}$ and c) the difference between a) and b). The panels d)–f) show the noisy reconstructions $\hat{\boldsymbol{J}}$ for voxels with image SNR above 30, separately for $\hat{J}_x$, $\hat{J}_y$, and $\hat{J}_z$, respectively.

seen in $|\hat{\boldsymbol{J}}|$. In the reconstruction $\hat{\boldsymbol{J}}$ of the noisy data, shown in figure 7.8(d–f), the ringing artifacts are partly masked, but still clearly visible especially in the region near the skull and below the sensor.

7.3 A demonstration measurement using a realistic head phantom

7.3.1 Phantom and measurement parameters

The Ilmenau group used the data of the CT scan of the individual human head [143] to develop a three-compartment head phantom. Plastic forms were designed as negative moulds yielding tissue structures resembling the geometry of the head and the dielectric properties of biological tissue [144]. Hence, the phantom can be utilized to imitate current stimulation via surface electrodes under realistic conditions. The outer scalp compartment was created from conductive agar gel (2 wt% agar, 0.17 wt% NaCl) giving a nominal conductivity of 0.31 S/m. The relatively high percentage of agar results in a T_2 relaxation time of approximately 30 ms, thus about four times lower than what is expected in human scalp tissue in the microtesla regime. Because of the requirements on form stability, tuning the scalp compartment to realistic relaxation parameters was not possible. The rigid skull structure was manufactured from Stewaform (Glorex GmbH, Rheinfelden, Germany), providing a nominal skull conductivity of 0.0017 S/m in contact with 0.17 wt% NaCl solution. The original phantom development comprises an aqueous 0.17 wt% NaCl solution for the brain compartment. To tune the relaxation time constants $T_1 = T_2$ to approximately 100 ms, in this experiment the brain compartment was filled with an aqueous solution of $CuSO_4$ (0.079 wt%) and NaCl (0.112 wt%) giving a nominal conductivity of 0.33 S/m. As the skull material was not characterized in contact with an aqueous $CuSO_4$ solution, the actual skull conductivity in this experiment is uncertain.

Rubber electrodes from the tDCS setup DC-STIMULATOR MR (neuroConn, Germany) were attached to the right side of the phantom and supported by a plastic wrap (see figure 7.9(b)). The anode was placed fronto-temporal and the cathode occipital. The electrode wires were attached at the upper side and combined to a twisted pair (not visible in 7.9(b)). To fit the geometry of the polarization setup, a phantom neck was included that is much thicker than a human neck, providing the necessary support. The phantom was positioned on the temporal side in the polarization coil and below the dewar, such that current-flow was realized in the positive x-direction of the MR coordinate system (see figure 7.9(c)).

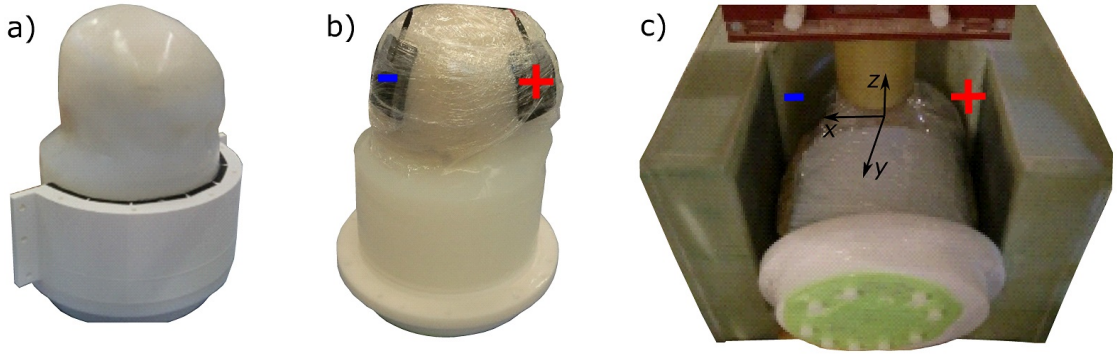

Figure 7.9: The realistic head phantom, shown in the half-open casting mold for the neck (a), with electrodes attached and secured with plastic wrap (b), and inside the ULF-MRI system (c).

When comparing the measurement setup to the simulations described in the previous section, it should be noted that in the simulations the electrodes were placed at the other side and slightly higher towards the top of the head. The direction was changed to retain positive current-flow in the positive x-direction of the MRI coordinates, which had to be rotated by 180° to accomplish the adiabatic field switch with the new polarization setup. Also, it should be kept in mind that the simulations did not include the electrode wires.

A total current of ±4.5 mA was applied to the phantom using the current source described in section 5.2.1. MRI gradients were set to derive a FOV of 180 mm and a voxel size $(6 \times 6 \times 6)$ mm^3. Due to limitations in the electronics of the decoupling scheme (figure 4.4) which were not yet adopted to carry currents as high as 30 A, the polarization current was set to 20 A yielding a polarization field of approximately 26 mT. The system noise was measured beforehand to be approximately 450 aT Hz$^{-1/2}$.

7.3.2 Results

Figure 7.10(a) gives the image SNR of the measurement with the head phantom in a central slice between the electrodes, similar to the illustrations of the simulations in figure 7.6. As expected, there is almost no signal from the scalp compartment which is due to the very low T_2 relaxation time of the 2%-agar solution. The brain compartment shows maximum image SNR of around 160, which is approximately one-third of the image SNR in the simulations. This agrees well with the reduced polarization current and slightly increased system noise.

Figure 7.10(b) shows the reconstruction of $\boldsymbol{B}_\mathrm{J}$ for voxels with SNR above 30. Maximum field strengths in the brain compartment are about three times higher than what was observed in the simulations. The rotation of the $\boldsymbol{B}_\mathrm{J}$-field due to the current density

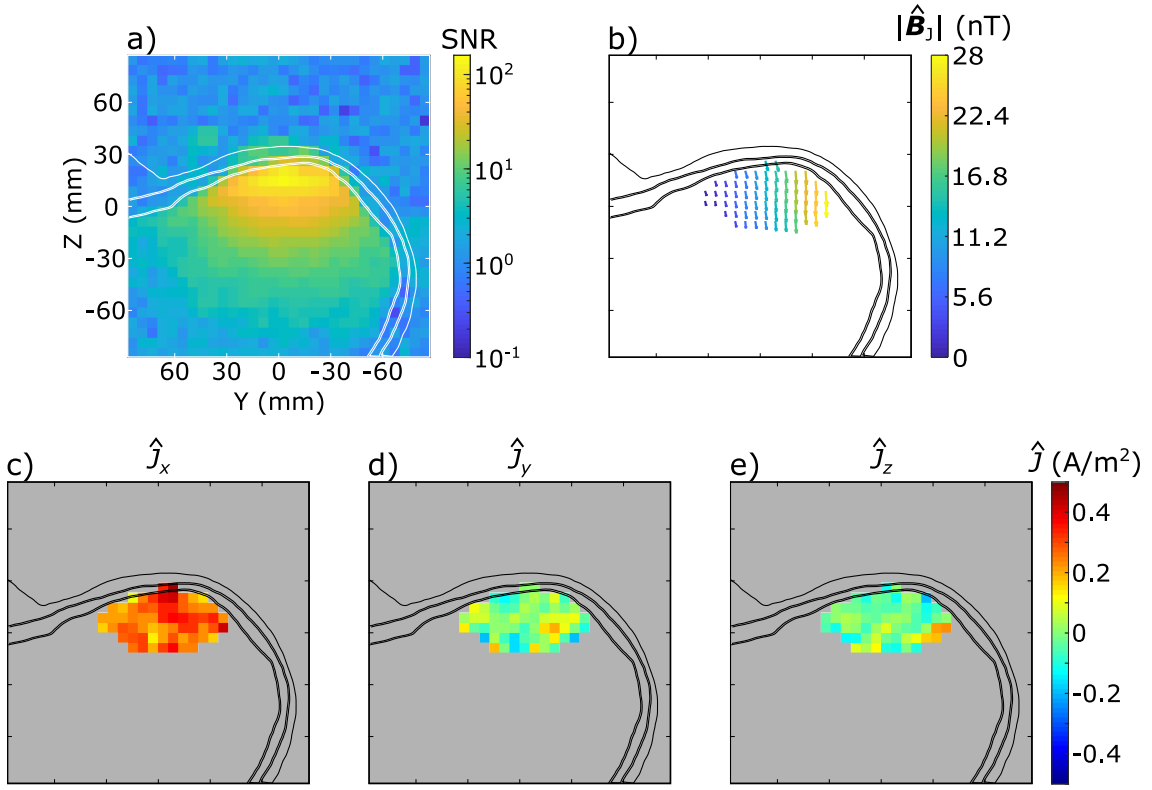

Figure 7.10: Image SNR (a), field reconstructions $\hat{\boldsymbol{B}}_J$ (b), and $\hat{\boldsymbol{J}}$ (c–e) of the verification measurements using the realistic head phantom.

is masked by a strong -z field which increases towards the top of the head. The origin of this field is most probably the electrode wires which pointed towards the top.

Current density reconstructions are visualized in the figures 7.10(c–e). Amplitude and direction towards x agree well with the simulations (figure 7.8(d–f)), indicating that the curl operator effectively removed the influence of the electrode wires on $\boldsymbol{B}_J$. The x-component of $\boldsymbol{J}$ amounts approximately 0.4 A/m^2 and the y-, and the z-components are close to zero.

7.4 An *In-vivo* demonstration measurement

7.4.1 A stimulation setup for *in-vivo* current impression

To show that the methods conducted in this thesis are suitable for an *in-vivo* application, a demonstration measurement, approved by a local ethics committee, was performed. Therefore, a commercial tDCS stimulator, the neuroConn DC-STIMULATOR MR, was utilized. The device comprises an *External Mode*, enabling to control the current waveform by a voltage input. Since the stimulator does not provide current monitoring, an external 1-kΩ-monitor resistor was attached to the circuit. The MR-version

of the stimulator features an rf-filter-module and high-impedance (10 kΩ) electrode wires. The filter helps to attenuate rf-interference that could degrade the SQUID performance. The electrode wires, however, are designed to avoid induction currents due to the fast field ramps in high-field MRI. Using the wires limits current application to approximately 1.5 mA. In the here developed ultra-low-field MRI setup, standard low-resistive electrode cables can be utilized, as the slopes of the magnetic-field ramps are not as steep. The turn-off of the polarization field is the only critical field ramp, having a slope $d\boldsymbol{B}/dt \approx 11.5$ T/s at the beginning, where the ramp-down is linear. A malfunction of the electronics, for instance a defect diode (compare figure 4.4), would result in a longer ramp-down time. In a worst-case approximation, where the loop spanned by the electrode wires is 30 cm in diameter and perfectly couples to the polarization field, the resulting induction voltage is about 800 mV. Taking into account the 1 kΩ-monitor resistor, the maximum current flow is limited to 800 μA, which is about four times lower than the stimulation current. Of note, the actual current due to induction will be much less as the loop is significantly smaller and the electrode-skin impedance adds several kΩ resistance.

7.4.2 Subject and measurement parameters

The volunteer was prepared with the rubber electrodes on the left side of the head. Figure 7.11(a) shows how the electrode position was fixed with a rubber band. Additionally, a standard EEG-cap was used to hold the electrodes in place. The anode was placed occipital and the cathode fronto-temporal, again, to obtain current-flow in the positive x-direction (compare figure 7.11(b)). The electrode wires were attached at the upper side and combined to a twisted pair (not visible in 7.11). A thick layer of conductive paste (Ten20®, Weaver and Company, Aurora, USA) was used to ensure good electrode contact. Impedance measurements before and after the zCDI measurements yielded 6.8 kΩ, and 3.5 kΩ, respectively. A total current of ± 3.5 mA was applied. A value of ± 4.5 mA could not be reached with respect to the slightly higher impedance at the beginning of the measurement.

The volunteer was lying on the right side on a non-magnetic table, such that the head was positioned in the polarization setup with the sensor between the electrodes (see figure 7.11(b, c)). As before, the polarization current was set to 20 A. The polarization time was increased slightly to 700 ms, still low regarding the assumed T_1 relaxation time of brain tissue in the millitesla regime of about 400 ms (compare figure 2.10). Again, due to the limitations in the decoupling circuitry, the polarization time could not be increased at that time. To reduce the overall measurement time compared to

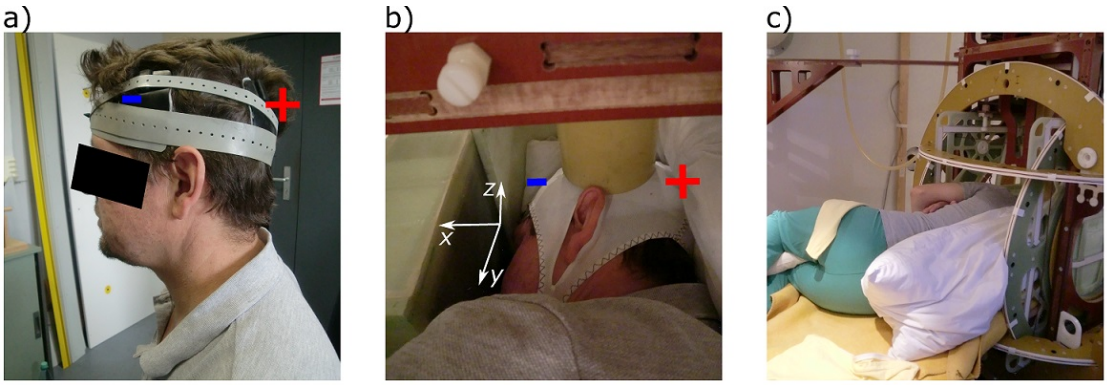

Figure 7.11: Preparation of the volunteer for the *in-vivo* demonstration measurement. a) shows the electrode positioning, b) the position of the volunteer in the ULF-MRI setup, and c) gives an overview of the volunteer lying in lateral position in the ULF-MRI setup.

the phantom measurements, MRI gradients were set to derive a FOV of 150 mm and a voxel size $(7 \times 7 \times 7)$ mm^3. Images of positive, and negative currents were taken to enable bipolar reconstruction according to section 6.2.2. A total of 3528 sequence runs was acquired in approximately 90 minutes, breaking down to 1.5 s per run. However, the nominal runtime is about 900 ms (700 ms polarization + 210 ms sequence run), indicating a long processing time of the LabVIEW™-based control software in between runs. The system noise was measured before the zCDI measurement with the volunteer in place to be approximately 520 aT Hz$^{-1/2}$.

7.4.3 Results

The image SNR of the *in-vivo* demonstration measurement is shown in figure 7.12(a) for a central yz-slice between the electrodes, similar to the illustrations in the figures 7.6(a) and 7.10(a). Maximum SNR values were about 72. The voxel dimensions were chosen too large to resolve the skull between scalp and intra-cranial compartment. The maximum SNR at voxels that are expected to be in the intra-cranial compartment was about 40, thus three-to-four times lower compared to the phantom measurements in the previous section, where only the intra-cranial compartment could be resolved. In consequence, the volume for a reliable reconstruction is reduced. This is due to the slightly higher time-domain noise, the reduced number of k-steps, and the higher T_1 relaxation time of brain tissue in the millitesla regime compared to the aqueous solution of $CuSO_4$ in the phantom. Figure 7.12(b) gives $\hat{\boldsymbol{B}}_\mathrm{J}$ for voxels with SNR above five. To remind the reader on the estimation of statistical uncertainty that was presented in chapter 6, an image SNR of five yields an SD$[\hat{\boldsymbol{B}}_\mathrm{J}] \approx 7.7$ nT which is on the order of $\boldsymbol{B}_\mathrm{J}$. Nevertheless, the reconstruction of $\boldsymbol{B}_\mathrm{J}$ looks qualitatively similar to the phantom

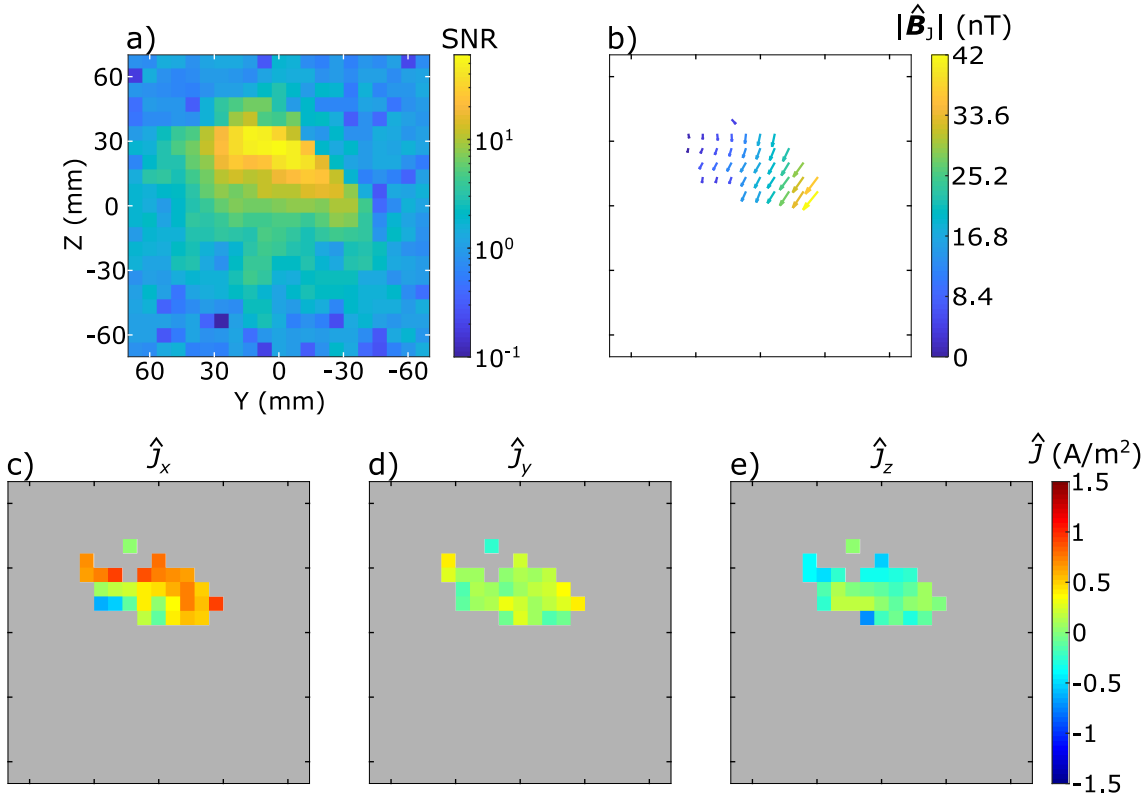

Figure 7.12: Image SNR (a), and field reconstructions $\hat{\boldsymbol{B}}_J$ (b) and $\hat{\boldsymbol{J}}$ (c–e) of the *in-vivo* demonstration measurement.

measurement. This is due to the large superimposing field from the electrode wires that dominates the reconstructed field.

The reconstruction of $\boldsymbol{J}$, as displayed in figure 7.12(c–e), shows large differences compared to the phantom measurements. Along the boundary of the head, which is expected to be the scalp, an x-directional current density could be resolved. The strength, slightly below 1 A/m^2, matches the value for the scalp that was estimated from the FEM simulations. For $\hat{J}_y$, slightly positive values are determined, whereas $\hat{J}_z$ shows a tendency towards negative values. Slightly negative $\hat{J}_z$-components are reasonable, as the sensor was positioned a bit closer to the anode (compare figure 7.11(b)). Below the scalp compartment, the reconstruction was dominated by noise.

7.5 Chapter summary and discussion

In this chapter, the necessary steps towards an *in-vivo* implementation of zCDI were taken. According to the results in chapters 5 and 6, a further boost in image SNR was necessary to reconstruct $\boldsymbol{B}_{\mathrm{J}}$ and $\boldsymbol{J}$ reliably in the intra-cranial head compartment. As the sensor noise of the developed setup is already outstanding, substantial improvements in image SNR were most likely possible by optimizing the polarization setup. A new self-shielded polarization coil was developed, that was specially designed for the shape of a human head. Immersed in an oil bath, the coil does not suffer from increased resistance due to heat and thereby overcomes the limitations regarding duty cycle and measurement breaks of the previous un-cooled setup.

To verify if the optimized design overcomes the SNR gap, a simulation toolbox was set up that emulates the zCDI sequence. Key features that determine the image SNR, such as the polarization field pattern, the coupling profile to the sensor, and noise, were accurately modeled. The estimates of $\boldsymbol{B}_{\mathrm{J}}$ and $\boldsymbol{J}$ were derived from FEM simulations using a three-compartment head model. The peak current densities in intra-cranial tissue are similar to literature values, when scaled to the applied current of 4.5 mA [27, 124]. However, the three-compartment model neglects the fact that current is partly shunted by cerebrospinal fluid (CSF), which has a higher conductivity compared to gray- and white-matter tissue [26, 27].

From the MRI simulations, and taking into account the insights on statistical uncertainty from chapter 6, it could be verified that the optimized setup provides image SNR sufficient for reliable $\boldsymbol{B}_{\mathrm{J}}$-reconstruction over a large volume in the intra-cranial compartment. However, it should be mentioned that the performance was evaluated with 50 A of polarization current, which represents a best-case scenario requiring liquid-nitrogen cooling of the polarization coil. At the moment, this cannot be realized with respect to the limited space in the existing coil setup. Nevertheless, a viable current of 30 A still yields sufficient image SNR in the intra-cranial volume, according to the simulations. However, the reconstruction volume would be reduced.

The simulations revealed that in addition to noise, spatial leakage from the 3D-DFT has a significant influence on the quality of the reconstruction. Appropriate windowing of the k-space data manipulates the spatial response function of the voxels, effectively reducing the far-reaching leakage at the cost of a smoothed resolution. However, with the applied imaging and reconstruction procedures, leakage artifacts could not be entirely eliminated, yielding noticeable reconstruction errors, especially visible in the $\hat{\boldsymbol{J}}$-distribution. Besides spatial filtering, an effective method to reduce ringing artifacts in MRI is to apply more k-steps. However, this might not be applicable to *in-vivo* CDI

as it would increase the measurement time significantly. Additionally, post-processing methods, for example "total variation constrained data extrapolation" [145], might reduce the artifacts without decreasing the image resolution.

The $\boldsymbol{J}$-reconstructions show limitations in thin tissue structures like the scalp. This is most probably due to the chosen resolution of $(5 \times 5 \times 5)$ mm^3, which does not allow sufficient gradient calculations in these areas. Reducing the voxel size to 1–2 mm would increase the quality of the $\hat{\boldsymbol{J}}$-distribution, but again at the cost of longer overall measurement time and lower image SNR. Generally, the simulations show that the $\boldsymbol{B}_\mathrm{J}$-reconstruction is more reliable than the $\boldsymbol{J}$-reconstruction, as artifacts strongly affect the gradient estimation.

A demonstration measurement was conducted on a realistic three-compartment head phantom based on the model from the simulations. Due to limitations in the polarization circuitry, only 20 A polarization current could be applied. The system's noise level of 450 aT Hz$^{-1/2}$ was significantly higher than the values reported in chapter 4 and 5. This is probably due to several reasons. First, the SQUID sensor was replaced due to a defect current limiter. Thereby, the sensor performance changed slightly. Additionally, the SQUID performance degraded slightly over time which might also be due to defects in the current limiter. Last but not least, the sensor is vulnerable to rf-noise. Eliminating the interference requires an extensive search for the noise sources, that was not possible during this experiment with respect to the stability of the phantom parameters over time. The resulting image SNR agreed well with the simulations, when scaled to the actual polarization parameters and noise. Due to a very low T_2 relaxation time, the scalp compartment did not yield sufficient image SNR for $\boldsymbol{B}_\mathrm{J}$-reconstruction. The reconstructed maximum $\boldsymbol{B}_\mathrm{J}$-values appeared about three times higher than what was found in the simulations. This is due to a large superimposing field component, originating from the electrode wires. Inferring from the stray-field estimations presented in appendix B these fields explain the additional magnetic field very well, when scaled to the applied current of 4.5 A. The $\hat{\boldsymbol{J}}$-field, on the other hand, agreed well with the simulations, as the field from the wires is curl-free. Due to the reduced reconstruction volume and the lower image SNR, leakage effects could not be distinguished from noise. Of note, even though the nominal scalp–skull conductivity ratio was much higher compared to the simulations, the strength of $\hat{\boldsymbol{J}}$ was comparable. Using an aqueous solution of $CuSO_4$ (0.079 wt%) and NaCl (0.112 wt%) probably caused increased ion infiltration into the skull material, yielding a skull conductivity comparable to the simulations.

Finally, a demonstration measurement was conducted on a volunteer, showcasing the performance of the method in an *in-vivo* application. The applied current of 3.5 mA was 1 mA lower than in the simulations and the phantom measurement. With

520 aT $\mathrm{Hz}^{-1/2}$, noise was even higher than in the phantom measurements. Besides the already mentioned circumstances that degrade the sensor performance, this experiment featured current impression via a commercial tDCS stimulator that is likely responsible for the additional noise. The long overall measurement time necessitated a smaller FOV and a slightly larger voxel size. Consequentially, a four-fold reduced image SNR compared to the phantom measurement was observed. This did not yield reliable reconstructions in the intra-cranial volume. Amplitude and direction of $\hat{\boldsymbol{J}}$ in the scalp compartment agreed with the values estimated from the FEM simulations. It was observed that the measurement time was about 30 % longer than expected, probably due to a long processing time of the LabVIEW™-based control software. This indicates a possible performance enhancement by improvements of the control framework. Despite the limitations, this measurement yielded the first full-vector $\boldsymbol{J}$-reconstructions from *in-vivo* CDI.

Chapter 8

General discussion and conclusions

8.1 Summary

Low-frequency CDI and CDI-based conductivity mapping would be beneficial for neuroimaging, neuromodulation, and possibly other applications. Existing methods that potentially enable non-invasive and *in-vivo* estimation of tissue conductivity suffer from distinct limitations, such as sensitivity to only one direction of the magnetic field associated with impressed currents, the need to solve an ill-posed inverse problem, or reconstructions based on indirect measures with unknown relation.

SQUID-based MRI in the ULF regime offers unique possibilities for CDI. The use of non-persistent magnets allows to switch all fields within a pulse sequence facilitating zCDI, a sequence designed by Vesanen et al. [6] that enables the detection of all components of a magnetic field, associated with impressed currents. However, before this work, zCDI could not be realized experimentally, due to hardware limitations in field switching and sensitivity.

In this thesis an ULF-MRI setup was developed that overcomes the limitations, allowing to perform *in-vivo* CDI. Key features are the manipulation of the magnetization's orientation via an adiabatic field change between the polarization field and defined guiding fields, the ability to switch all MRI fields nearly instantaneously, and an outstanding sensitivity. The latter was achieved through a combination of a sensor with ultra-high sensitivity and a cooled polarization setup, shape-optimized for the human head. Furthermore, the sequence was modified, now involving a calibration procedure that decomposes phase effects due to $\boldsymbol{B}_\mathrm{J}$ from those due to the imaging fields.

The method was successfully validated in phantom measurements, using a preliminary polarization setup that provided less sensitivity but had the benefit of a high

homogeneity and negligible transients after pulsing. $\boldsymbol{B}_\mathrm{J}$ and $\boldsymbol{J}$ could be reconstructed reliably for 2-mA currents in different directions and phantoms of various geometry. The measurements demonstrate the feasibility of zCDI and yielded the first reported reconstructions of the $\boldsymbol{J}$-vector based on a non-invasive method.

However, the validation measurements also revealed an influence of the electrode wires on the reconstruction of $\boldsymbol{B}_\mathrm{J}$, and artifacts due to leakage from the 3D-DFT. Additionally, a gap in SNR towards current density as low as expected in *in-vivo* applications was identified which led to the development of the improved cooled polarization setup.

MRI simulations using a realistic head model verified that the sensitivity of the final setup is sufficient to reconstruct the magnetic field $\boldsymbol{B}_\mathrm{J}$, associated with the current density $\boldsymbol{J}$, intra-cranially with an $\mathrm{SNR}[\boldsymbol{B}_\mathrm{J}] > 10$. To derive this information from the simulations, a preceding extensive investigation of the performance of the zCDI reconstruction based on image SNR was conducted.

Finally, two demonstration measurements were performed, one using a realistic head phantom, and the other on a volunteer in an actual *in-vivo* application. However, the full potential of the setup could not be exploited at the time. Compared to the parameters in the simulations, only two-fifth of the polarization current were applied, and noise was slightly increased. Nevertheless, the reconstructions agreed well with the simulations allowing the assumption that the performance of the setup is sufficient once the upgrade of all components is completed.

8.2 Discussion

The methods applied in this thesis yielded successful reconstructions of the full vector of $\boldsymbol{J}$ due to impressed currents. The derived $\boldsymbol{J}$-field incorporates information on absolute conductivity, and due to the spatially-resolved vector data maybe also information on directional conductivity, all subject to the discretization levels of the underlying MRI sequence.

However, it remains to be answered if this information can be extracted from the data. Generally, the measurements and simulations conducted in this thesis show that the $\boldsymbol{B}_\mathrm{J}$-reconstruction is more reliable than the $\boldsymbol{J}$-reconstruction. Shall the reconstructions be used to fit individual conductivity values, superior results are expected when the $\hat{\boldsymbol{B}}_\mathrm{J}$-field is used as the measurement data. However, magnetic fields arising from the electrode wires should be either modeled or eliminated. One way to exclude these fields would be to consider only closed path integrals of $\hat{\boldsymbol{B}}_\mathrm{J}$ and to apply the integral

form of *Ampère's* law. It is yet undetermined whether this only enables to derive bulk conductivity values, rather than spatially-resolved conductivity mapping. Methods for this have not been presented so far and should be subject to further research.

Furthermore, the conducted measurements are subject to a limited reconstruction volume as a single-channel sensor was used for signal detection. It is likely that conductivity fitting requires a broader sample coverage that could be gained by multi-channel devices that in the best case cover the shape of the head [108]. The sensitivity analysis in chapter 6 is universally applicable, requiring solely information on image SNR. In [75], the performance of the here presented ULF-MRI setup was compared to a setup comprising an MEG-based whole-head sensor system located at Aalto University in Espoo, Finland. Although that device provided a broad sample coverage, the sensitivity for deeper regions appeared low due to an inferior noise performance of the sensors. Hence, a multi-channel and ultra-low-noise sensor setup is desired. Of note, multiple channels could also help reducing the overall measurement time, and/or increase the spatial resolution to a level necessary to resolve $\boldsymbol{B}_{\mathrm{J}}$ and $\boldsymbol{J}$ in fine tissue structures, by means of parallel imaging [146].

8.3 Conclusions and outlook

This thesis gives a roadmap towards the successful implementation of zCDI. Modifications to the sequence have been identified and the implementation in hardware has been explained in detail. Key features, such as the manufacture of a sensor with ultra-high sensitivity, and a polarization setup that creates sufficient magnetization should be reproducible on the given data basis. Methods to assess the performance in the reconstruction based on image SNR were presented and can be applied to arbitrary setups.

Suggestions for further improvements include a multi-channel sensor setup. In addition, spectral leakage should be taken in closer consideration with the goal to reduce its effect on the reconstruction of $\boldsymbol{B}_{\mathrm{J}}$ and $\boldsymbol{J}$ during data acquisition, or by post-processing.

The data obtained through zCDI using ULF MRI is superior to that of other modalities as, for the first time, the full vector of $\boldsymbol{J}$ can be measured directly. Provided that the suggested improvements resolve remaining issues in sample coverage, measurement time, and image artifacts, this will facilitate reliable *in-vivo* and individual conductivity mapping. Besides, the data on $\boldsymbol{J}$ can be used to benchmark computational models, and monitor the propagation of currents, thereby improve electric stimulation.

Bibliography

[1] R. J. Ilmoniemi and J. Sarvas, Brain signals: Physics and mathematics of MEG and EEG. Mit Press, 2019.

[2] M. Bikson, P. Grossman, C. Thomas, A. L. Zannou, J. Jiang, T. Adnan, A. P. Mourdoukoutas, G. Kronberg, D. Truong, P. Boggio, A. R. Brunoni, L. Charvet, F. Fregni, B. Fritsch, B. Gillick, R. H. Hamilton, B. M. Hampstead, R. Jankord, A. Kirton, H. Knotkova, D. Liebetanz, A. Liu, C. Loo, M. A. Nitsche, J. Reis, J. D. Richardson, A. Rotenberg, P. E. Turkeltaub, and A. J. Woods, "Safety of transcranial direct current stimulation: Evidence based update 2016," Brain Stimulation, vol. 9, pp. 641–661, sep 2016.

[3] A. Antal, I. Alekseichuk, M. Bikson, J. Brockmöller, A. R. Brunoni, R. Chen, L. G. Cohen, G. Dowthwaite, J. Ellrich, A. Flöel, F. Fregni, M. S. George, R. Hamilton, J. Haueisen, C. S. Herrmann, F. C. Hummel, J. P. Lefaucheur, D. Liebetanz, C. K. Loo, C. D. McCaig, C. Miniussi, P. C. Miranda, V. Moliadze, M. A. Nitsche, R. Nowak, F. Padberg, A. Pascual-Leone, W. Poppendieck, A. Priori, S. Rossi, P. M. Rossini, J. Rothwell, M. A. Rueger, G. Ruffini, K. Schellhorn, H. R. Siebner, Y. Ugawa, A. Wexler, U. Ziemann, M. Hallett, and W. Paulus, "Low intensity transcranial electric stimulation: Safety, ethical, legal regulatory and application guidelines," Clinical Neurophysiology, vol. 128, pp. 1774–1809, sep 2017.

[4] R. Kraus Jr, M. Espy, P. Magnelind, and P. Volegov, Ultra-low field nuclear magnetic resonance: A new MRI regime. Oxford University Press, apr 2014.

[5] S.-J. Lee, J. H. Shim, K. K. Yu, S. min Hwang, S. Oh, I. Hilschenz, and K. Kim, "Toward a magnetic resonance electrical impedance tomography in ultra-low field: A direct magnetic resonance imaging method by an external alternating current," Applied Physics Letters, vol. 112, p. 153703, apr 2018.

[6] P. T. Vesanen, J. O. Nieminen, K. C. J. Zevenhoven, Y.-C. Hsu, and R. J. Ilmoniemi, "Current-density imaging using ultra-low-field MRI with zero-field encoding," Magnetic Resonance Imaging, vol. 32, pp. 766–770, jul 2014.

[7] J. O. Nieminen, K. C. Zevenhoven, P. T. Vesanen, Y.-C. Hsu, and R. J. Ilmoniemi, "Current-density imaging using ultra-low-field MRI with adiabatic pulses," Magnetic Resonance Imaging, vol. 32, pp. 54–59, jan 2014.

[8] M. Mohammadi, E. V. Silletta, A. J. Ilott, and A. Jerschow, "Diagnosing current distributions in batteries with magnetic resonance imaging," Journal of Magnetic Resonance, vol. 309, p. 106601, dec 2019.

[9] H. Gray, Anatomy of the human body. Philadelphia and New York: Lea and Febiger, 20 ed., 1918. Illustrator: Henry Vandyke Carter (SVG from `https://upload.wikimedia.org/wikipedia/commons/7/70/Gray726.svg`).

[10] "Illustration of meninges." `https://upload.wikimedia.org/wikipedia/commons/8/8e/Meninges-en.svg`. SVG by Mysid, original by SEER Development Team [1], Jmarchn (CC BY-SA - `https://creativecommons.org/licenses/by-sa/3.0`).

[11] J. Haueisen and T. R. Knösche, "Forward modeling and tissue conductivities," in Magnetoencephalography, pp. 1–22, Springer International Publishing, 2019.

[12] Ümit Aydin, J. Vorwerk, P. Küpper, M. Heers, H. Kugel, A. Galka, L. Hamid, J. Wellmer, C. Kellinghaus, S. Rampp, and C. H. Wolters, "Combining EEG and MEG for the reconstruction of epileptic activity using a calibrated realistic volume conductor model," PLoS ONE, vol. 9, p. e93154, mar 2014.

[13] R. Hoekema, G. H. Wieneke, F. S. S. Leijten, C. W. M. Van Veelen, P. C. Van Rijen, G. J. M. Huiskamp, J. Ansems, and A. C. Van Huffelen, "Measurement of the conductivity of skull, temporarily removed during epilepsy surgery," Brain Topography, vol. 16, no. 1, pp. 29–38, 2003.

[14] S. B. Baumann, D. R. Wozny, S. K. Kelly, and F. M. Meno, "The electrical conductivity of human cerebrospinal fluid at body temperature," IEEE Transactions on Biomedical Engineering, vol. 44, no. 3, pp. 220–223, 1997.

[15] M. Oozeer, C. Veraart, V. Legat, and J. Delbeke, "Simulation of intra-orbital optic nerve electrical stimulation," Medical & Biological Engineering & Computing, vol. 43, pp. 608–617, oct 2005.

[16] C. Ramon, P. Garguilo, E. A. Fridgeirsson, and J. Haueisen, "Changes in scalp potentials and spatial smoothing effects of inclusion of dura layer in human head models for EEG simulations," Frontiers in Neuroengineering, vol. 7, aug 2014.

[17] J. Jiang, D. Q. Truong, Z. Esmaeilpour, Y. Huang, B. W. Badran, and M. Bikson, "Enhanced tES and tDCS computational models by meninges emulation," Journal of Neural Engineering, vol. 17, p. 016027, jan 2020.

[18] M. Hämäläinen, R. Hari, R. J. Ilmoniemi, J. Knuutila, and O. V. Lounasmaa, "Magnetoencephalography—theory, instrumentation, and applications to noninvasive studies of the working human brain," Reviews of Modern Physics, vol. 65, pp. 413–497, apr 1993.

[19] M. A. Nitsche and W. Paulus, "Excitability changes induced in the human motor cortex by weak transcranial direct current stimulation," The Journal of Physiology, vol. 527, pp. 633–639, sep 2000.

[20] F. Yavari, A. Jamil, M. M. Samani, L. P. Vidor, and M. A. Nitsche, "Basic and functional effects of transcranial electrical stimulation (tES)—An introduction," Neuroscience & Biobehavioral Reviews, vol. 85, pp. 81–92, feb 2018.

[21] M.-F. Kuo, W. Paulus, and M. A. Nitsche, "Therapeutic effects of non-invasive brain stimulation with direct currents (tDCS) in neuropsychiatric diseases," NeuroImage, vol. 85, pp. 948–960, jan 2014.

[22] A. H. Moffa, A. R. Brunoni, S. Nikolin, and C. K. Loo, "Transcranial direct current stimulation in psychiatric disorders," Psychiatric Clinics of North America, vol. 41, pp. 447–463, sep 2018.

[23] A. Flöel, "tDCS-enhanced motor and cognitive function in neurological diseases," NeuroImage, vol. 85, pp. 934–947, jan 2014.

[24] T. Wagner, F. Fregni, S. Fecteau, A. Grodzinsky, M. Zahn, and A. Pascual-Leone, "Transcranial direct current stimulation: A computer-based human model study," NeuroImage, vol. 35, pp. 1113–1124, apr 2007.

[25] A. Datta, V. Bansal, J. Diaz, J. Patel, D. Reato, and M. Bikson, "Gyri-precise head model of transcranial direct current stimulation: Improved spatial focality using a ring electrode versus conventional rectangular pad," Brain Stimulation, vol. 2, pp. 201–207.e1, oct 2009.

[26] R. Salvador, A. Mekonnen, G. Ruffini, and P. C. Miranda, "Modeling the electric field induced in a high resolution realistic head model during transcranial current stimulation," in 2010 Annual International Conference of the IEEE Engineering in Medicine and Biology, IEEE, aug 2010.

[27] T. Neuling, S. Wagner, C. H. Wolters, T. Zaehle, and C. S. Herrmann, "Finite-element model predicts current density distribution for clinical applications of tDCS and tACS," Frontiers in Psychiatry, vol. 3, 2012.

[28] P. C. Miranda, M. A. Callejón-Leblic, R. Salvador, and G. Ruffini, "Realistic modeling of transcranial current stimulation: The electric field in the brain," Current Opinion in Biomedical Engineering, vol. 8, pp. 20–27, dec 2018.

[29] C. Gabriel, A. Peyman, and E. H. Grant, "Electrical conductivity of tissue at frequencies below 1 MHz," Physics in Medicine and Biology, vol. 54, pp. 4863–4878, jul 2009.

[30] H. McCann, G. Pisano, and L. Beltrachini, "Variation in reported human head tissue electrical conductivity values," Brain Topography, vol. 32, pp. 825–858, may 2019.

[31] S. Wagner, S. M. Rampersad, Ü. Aydin, J. Vorwerk, T. F. Oostendorp, T. Neuling, C. S. Herrmann, D. F. Stegeman, and C. H. Wolters, "Investigation of tDCS volume conduction effects in a highly realistic head model," Journal of Neural Engineering, vol. 11, p. 016002, dec 2013.

[32] M. K. Metwally, S. M. Han, and T.-S. Kim, "The effect of tissue anisotropy on the radial and tangential components of the electric field in transcranial direct current stimulation," Medical & Biological Engineering & Computing, vol. 53, pp. 1085–1101, may 2015.

[33] Y. Huang, A. A. Liu, B. Lafon, D. Friedman, M. Dayan, X. Wang, M. Bikson, W. K. Doyle, O. Devinsky, and L. C. Parra, "Measurements and models of electric fields in the in vivo human brain during transcranial electric stimulation," eLife, vol. 6, feb 2017.

[34] D. Holder, ed., Electrical impedance tomography: methods, history and applications. CRC Press, dec 2004.

[35] M. Joy, G. Scott, and M. Henkelman, "In vivo detection of applied electric currents by magnetic resonance imaging," Magnetic Resonance Imaging, vol. 7, pp. 89–94, jan 1989.

[36] P. Pesikan, M. Joy, G. Scott, and R. Henkelman, "Two–dimensional current density imaging," IEEE Transactions on Instrumentation and Measurement, vol. 39, no. 6, pp. 1048–1053, 1990.

[37] G. Scott, M. Joy, R. Armstrong, and R. Henkelman, "Measurement of nonuniform current density by magnetic resonance," IEEE Transactions on Medical Imaging, vol. 10, no. 3, pp. 362–374, 1991.

[38] G. Scott, M. Joy, R. Armstrong, and R. Henkelman, "Sensitivity of magnetic-resonance current-density imaging," Journal of Magnetic Resonance (1969), vol. 97, pp. 235–254, apr 1992.

[39] G. Scott, M. Joy, R. Armstrong, and R. Henkelman, "Electromagnetic considerations for RF current density imaging [MRI technique]," IEEE Transactions on Medical Imaging, vol. 14, no. 3, pp. 515–524, 1995.

[40] G. C. Scott, M. L. G. Joy, R. L. Armstrong, and R. M. Henkelman, "Rotating frame RF current density imaging," Magnetic Resonance in Medicine, vol. 33, pp. 355–369, mar 1995.

[41] N. Zhang, "Electrical impedance tomography based on current density imaging," Master's thesis, 1992.

[42] E. J. Woo, S. Y. Lee, and C. W. Mun, "Impedance tomography using internal current density distribution measured by nuclear magnetic resonance," in Mathematical Methods in Medical Imaging III (F. L. Bookstein, J. S. Duncan, N. Lange, and D. C. Wilson, eds.), SPIE, jul 1994.

[43] Y. Z. Ider and O. Birgül, "Use of the magnetic field generated by the internal distribution of injected currents for electrical impedance tomography (MR-EIT)," Turkish Journal of Electrical Engineering & Computer Sciences, vol. 6, no. 3, pp. 215–226, 1998.

[44] K. F. Hasanov, A. W. Ma, A. I. Nachman, and M. L. G. Joy, "Current density impedance imaging," IEEE Transactions on Medical Imaging, vol. 27, pp. 1301–1309, sep 2008.

[45] J. K. Seo, O. Kwon, and E. J. Woo, "Magnetic resonance electrical impedance tomography (MREIT): Conductivity and current density imaging," Journal of Physics: Conference Series, vol. 12, pp. 140–155, jan 2005.

[46] Y. Z. Ider, S. Onart, and W. R. B. Lionheart, "Uniqueness and reconstruction in magnetic resonance electrical impedance tomography (MR EIT)," Physiological Measurement, vol. 24, pp. 591–604, apr 2003.

[47] O. Kwon, E. J. Woo, J.-R. Yoon, and J. K. Seo, "Magnetic resonance electrical impedance tomography (mreit): Simulation study of j-substitution algorithm," IEEE Transactions on Biomedical Engineering, vol. 49, no. 2, pp. 160–167, 2002.

[48] O. Kwon, J.-Y. Lee, and J.-R. Yoon, "Equipotential line method for magnetic resonance electrical impedance tomography," Inverse Problems, vol. 18, pp. 1089–1100, jun 2002.

[49] O. Birgül, B. M. Eyüboglu, and Y. Z. Ider, "Current constrained voltage scaled reconstruction (CCVSR) algorithm for MR-EIT and its performance with different probing current patterns," Physics in Medicine & Biology, vol. 48, no. 5, p. 653, 2003.

[50] S. H. Oh, B. I. Lee, E. J. Woo, S. Y. Lee, M. H. Cho, O. Kwon, and J. K. Seo, "Conductivity and current density image reconstruction using harmonic bz algorithm in magnetic resonance electrical impedance tomography," Physics in Medicine & Biology, vol. 48, no. 19, p. 3101, 2003.

[51] J. K. Seo, J.-R. Yoon, E. J. Woo, and O. Kwon, "Reconstruction of conductivity and current density images using only one component of magnetic field measurements," IEEE Transactions on Biomedical Engineering, vol. 50, no. 9, pp. 1121–1124, 2003.

[52] C. Park, O. Kwon, E. J. Woo, and J. K. Seo, "Electrical conductivity imaging using gradient Bz decomposition algorithm in magnetic resonance electrical impedance tomography (MREIT)," IEEE Transactions on Medical Imaging, vol. 23, pp. 388–394, mar 2004.

[53] C. Park, E.-J. Park, E. J. Woo, O. Kwon, and J. K. Seo, "Static conductivity imaging using variational gradient Bz algorithm in magnetic resonance electrical impedance tomography," Physiological Measurement, vol. 25, pp. 257–269, feb 2004.

[54] L. Özparlak and Y. Z. İder, "Induced current magnetic resonance–electrical impedance tomography," Physiological Measurement, vol. 26, pp. S289–S305, mar 2005.

[55] Y. Liu, S. Zhu, and B. He, "Induced current magnetic resonance electrical impedance tomography of brain tissues based on the J-substitution algorithm: A simulation study," Physics in Medicine and Biology, vol. 54, pp. 4561–4573, jun 2009.

[56] O. F. Oran and Y. Z. Ider, "Feasibility of conductivity imaging using subject eddy currents induced by switching of MRI gradients," Magnetic Resonance in Medicine, vol. 77, pp. 1926–1937, jul 2016.

[57] E. M. Haacke, L. S. Petropoulos, E. W. Nilges, and D. H. Wu, "Extraction of conductivity and permittivity using magnetic resonance imaging," Physics in Medicine & Biology, vol. 36, no. 6, p. 723, 1991.

[58] H. Wen, "Noninvasive quantitative mapping of conductivity and dielectric distributions using RF wave propagation effects in high-field MRI," in Medical Imaging 2003: Physics of Medical Imaging, vol. 5030, pp. 471–477, International Society for Optics and Photonics, 2003.

[59] R. Stollberger and P. Wach, "Imaging of the active B1 field in vivo," Magnetic Resonance in Medicine, vol. 35, no. 2, pp. 246–251, 1996.

[60] U. Katscher and C. A. T. van den Berg, "Electric properties tomography: Biochemical, physical and technical background, evaluation and clinical applications," NMR in Biomedicine, vol. 30, p. e3729, may 2017.

[61] P. J. Basser, J. Mattiello, and D. LeBihan, "MR diffusion tensor spectroscopy and imaging," Biophysical Journal, vol. 66, no. 1, pp. 259–267, 1994.

[62] P. J. Basser, J. Mattiello, and D. Lebihan, "Estimation of the effective self-diffusion tensor from the NMR spin echo," Journal of Magnetic Resonance, Series B, vol. 103, pp. 247–254, mar 1994.

[63] D. S. Tuch, V. J. Wedeen, A. M. Dale, J. S. George, and J. W. Belliveau, "Conductivity tensor mapping of the human brain using diffusion tensor MRI," Proceedings of the National Academy of Sciences, vol. 98, no. 20, pp. 11697–11701, 2001.

[64] S.-M. Gho, J. W. Shin, M.-O. Kim, M. J. Kim, S. Kim, J.-H. Kim, and D.-H. Kim, "Observation of the correlation between electrical conductivity and apparent diffusion coefficient values," in Proceedings of the 24th Annual Meeting of ISMRM, Singapore, p. 1566, 2016.

[65] I. Hancu, J. C. Roberts, S. Bulumulla, and S.-K. Lee, "On conductivity, permittivity, apparent diffusion coefficient, and their usefulness as cancer markers at MRI frequencies," Magnetic Resonance in Medicine, vol. 73, pp. 2025–2029, jun 2014.

[66] J. Haueisen, D. Tuch, C. Ramon, P. Schimpf, V. Wedeen, J. George, and J. Belliveau, "The influence of brain tissue anisotropy on human EEG and MEG," NeuroImage, vol. 15, pp. 159–166, jan 2002.

[67] D. Ma, V. Gulani, N. Seiberlich, K. Liu, J. L. Sunshine, J. L. Duerk, and M. A. Griswold, "Magnetic resonance fingerprinting," Nature, vol. 495, pp. 187–192, mar 2013.

[68] O. Kwon, W. C. Jeong, S. Z. K. Sajib, H. J. Kim, and E. J. Woo, "Anisotropic conductivity tensor imaging in MREIT using directional diffusion rate of water molecules," Physics in Medicine and Biology, vol. 59, pp. 2955–2974, may 2014.

[69] M. Chauhan, A. Indahlastari, A. K. Kasinadhuni, M. Schar, T. H. Mareci, and R. J. Sadleir, "Low-frequency conductivity tensor imaging of the human head in vivo using DT-MREIT: First study," IEEE Transactions on Medical Imaging, vol. 37, pp. 966–976, apr 2018.

[70] M. Packard, "Free nuclear induction in earth's magnetic field," Physical Review, vol. 93, p. 941, 1954.

[71] J.-H. Storm, P. Hömmen, D. Drung, and R. Körber, "An ultra-sensitive and wideband magnetometer based on a superconducting quantum interference device," Applied Physics Letters, vol. 110, p. 072603, feb 2017.

[72] P. Hömmen, J.-H. Storm, N. Höfner, and R. Körber, "Demonstration of full tensor current density imaging using ultra-low field MRI," Magnetic Resonance Imaging, vol. 60, pp. 137–144, jul 2019.

[73] R. Körber, O. Kieler, P. Hömmen, N. Höfner, and J. Storm, "Ultra-sensitive SQUID systems for applications in biomagnetism and ultra-low field MRI," in 2019 IEEE International Superconductive Electronics Conference (ISEC), pp. 1–3, 2019.

[74] J.-H. Storm, P. Hömmen, N. Höfner, and R. Körber, "Detection of body noise with an ultra-sensitive SQUID system," Measurement Science and Technology, vol. 30, p. 125103, sep 2019.

[75] P. Hömmen, A. J. Mäkinen, A. Hunold, R. Machts, J. Haueisen, K. C. J. Zevenhoven, R. J. Ilmoniemi, and R. Körber, "Evaluating the performance of ultra-low-field MRI for in-vivo 3D current density imaging of the human head," Frontiers in Physics, vol. 8, p. 105, apr 2020.

[76] J. D. Jackson and K. Müller, Klassische Elektrodynamik. de Gruyter, 2006.

[77] E. M. Haacke, R. W. Brown, M. R. Thompson, and R. Venkatesan, Magnetic resonance imaging: physical principles and sequence design, vol. 82. Wiley-Liss New York:, 1999.

[78] W. Kahan, "Notes for math H110: Computing cross-products and rotations in 2- and 3-dimensional Euclidean spaces," tech. rep., Mathematics and Computer Science Depts. University of California, Berkeley CA 94720, 2016.

[79] F. Bloch, "Nuclear induction," Physical Review, vol. 70, no. 7-8, p. 460, 1946.

[80] D. G. Nishimura, Principles of magnetic resonance imaging. Standford Univ., 2010.

[81] K. P. Pruessmann, "Encoding and reconstruction in parallel MRI," NMR in Biomedicine, vol. 19, no. 3, pp. 288–299, 2006.

[82] A. J. Makinen, K. C. J. Zevenhoven, and R. J. Ilmoniemi, "Automatic spatial calibration of ultra-low-field MRI for high-accuracy hybrid MEG–MRI," IEEE Transactions on Medical Imaging, vol. 38, pp. 1317–1327, jun 2019.

[83] M. Burghoff, S. Hartwig, L. Trahms, and J. Bernarding, "Nuclear magnetic resonance in the nanoTesla range," Applied Physics Letters, vol. 87, p. 054103, aug 2005.

[84] R. Körber, A. Casey, A. Shibahara, M. Piscitelli, B. P. Cowan, C. P. Lusher, J. Saunders, D. Drung, and T. Schurig, "Nuclear magnetic resonance on room temperature samples in nanotesla fields using a two-stage dc superconducting quantum interference device sensor," Applied Physics Letters, vol. 91, p. 142501, oct 2007.

[85] J. Voigt, S. Knappe-Grüneberg, A. Schnabel, R. Körber, and M. Burghoff, "Measures to reduce low residual field and field gradient inside a magnetically shielded room by a factor of more than 10," Metrology and Measurement Systems, vol. 21, pp. 239–248, 2013.

[86] L. Q. Qiu, Y. Zhang, H.-J. Krause, and A. I. Braginski, "SQUID-detected NMR in earth's magnetic field," Journal of Physics: Conference Series, vol. 97, p. 012026, feb 2008.

[87] V. Zotev, A. Matlashov, I. Savukov, T. Owens, P. Volegov, J. Gomez, and M. Espy, "SQUID-based microtesla MRI for in vivo relaxometry of the human brain," IEEE Transactions on Applied Superconductivity, vol. 19, pp. 823–826, 2009.

[88] B. Inglis, K. Buckenmaier, P. SanGiorgio, A. F. Pedersen, M. A. Nichols, and J. Clarke, "MRI of the human brain at 130 microtesla," Proceedings of the National Academy of Sciences, vol. 110, no. 48, pp. 19194–19201, 2013.

[89] M. A. Espy, P. E. Magnelind, A. N. Matlashov, S. G. Newman, H. J. Sandin, L. J. Schultz, R. Sedillo, A. V. Urbaitis, and P. L. Volegov, "Progress toward a deployable SQUID-based ultra-low field MRI system for anatomical imaging," IEEE Transactions on Applied Superconductivity, vol. 25, pp. 1–5, jun 2015.

[90] K. C. J. Zevenhoven, H. Dong, R. J. Ilmoniemi, and J. Clarke, "Dynamical cancellation of pulse-induced transients in a metallic shielded room for ultra-low-field magnetic resonance imaging," Applied Physics Letters, vol. 106, no. 3, p. 034101, 2015.

[91] J. Nieminen, P. Vesanen, K. Zevenhoven, J. Dabek, J. Hassel, J. Luomahaara, J. Penttilä, and R. Ilmoniemi, "Avoiding eddy-current problems in ultra-low-field MRI with self-shielded polarizing coils," Journal of Magnetic Resonance, vol. 212, no. 1, pp. 154–160, 2011.

[92] P. T. Vesanen, J. O. Nieminen, K. C. J. Zevenhoven, J. Dabek, J. Simola, J. Sarvas, and R. J. Ilmoniemi, "The Spatial and Temporal Distortion of Magnetic Fields Applied Inside a Magnetically Shielded Room," IEEE Transactions on Magnetics, vol. 48, pp. 53–61, jan 2012.

[93] R. McDermott, S. Lee, B. t. Haken, A. H. Trabesinger, A. Pines, and J. Clarke, "Microtesla MRI with a superconducting quantum interference device," Proceedings of the National Academy of Sciences, vol. 101, pp. 7857–7861, may 2004.

[94] V. S. Zotev, A. N. Matlashov, P. L. Volegov, A. V. Urbaitis, M. A. Espy, and R. H. K. Jr, "Squid-based instrumentation for ultralow-field MRI," Superconductor Science and Technology, vol. 20, p. S367, oct 2007.

[95] I. Hilschenz, Design of a low field magnetic resonance imaging measurement system working below one kilohertz. PhD thesis, Fakultät für Physik und Geowissenschaften, Universität Leipzig, 2012.

[96] S.-J. Lee, J. H. Shim, K. Kim, K. K. Yu, and S. min Hwang, "Magnetic resonance imaging without field cycling at less than earth's magnetic field," Applied Physics Letters, vol. 106, p. 103702, mar 2015.

[97] R. E. de Souza, K. Schlenga, A. Wong-Foy, R. McDermott, A. Pines, and J. Clarke, "NMR and MRI obtained with high transition temperature dc SQUIDs," Journal of the Brazilian Chemical Society, vol. 10, pp. 307–312, aug 1999.

[98] I. Savukov, V. Zotev, P. Volegov, M. Espy, A. Matlashov, J. Gomez, and R. Kraus, "MRI with an atomic magnetometer suitable for practical imaging applications," Journal of Magnetic Resonance, vol. 199, pp. 188–191, aug 2009.

[99] I. Hilschenz, Y. Ito, H. Natsukawa, T. Oida, T. Yamamoto, and T. Kobayashi, "Remote detected low-field MRI using an optically pumped atomic magnetometer combined with a liquid cooled pre-polarization coil," Journal of Magnetic Resonance, vol. 274, pp. 89–94, jan 2017.

[100] J.-H. Storm, D. Drung, M. Burghoff, and R. Körber, "A modular, extendible and field-tolerant multichannel vector magnetometer based on current sensor SQUIDs," Superconductor Science and Technology, vol. 29, p. 094001, jul 2016.

[101] H. W. Fischer, P. A. Rinck, Y. van Haverbeke, and R. N. Muller, "Nuclear relaxation of human brain gray and white matter: Analysis of field dependence and implications for MRI," Magnetic Resonance in Medicine, vol. 16, pp. 317–334, nov 1990.

[102] A. L. Hopkins, H. N. Yeung, and C. B. Bratton, "Multiple field strength in vivo T1 and T2 for cerebrospinal fluid protons," Magnetic Resonance in Medicine, vol. 3, no. 2, pp. 303–311, 1986.

[103] P. A. Bottomley, T. H. Foster, R. E. Argersinger, and L. M. Pfeifer, "A review of normal tissue hydrogen NMR relaxation times and relaxation mechanisms from 1-100 MHz: Dependence on tissue type, NMR frequency, temperature, species, excision, and age," Medical Physics, vol. 11, pp. 425–448, jul 1984.

[104] H.-J. Krause and H. Dong, "Biomagnetic sensing," in Springer Series on Chemical Sensors and Biosensors, pp. 449–474, Springer International Publishing, 2017.

[105] C. Liu, B. Chang, L. Qiu, Y. Qiu, H. Dong, Y. Zhang, and X. Xie, "Multichannel ULF-MRI study in magnetic unshielded urban laboratory environment," IEEE Transactions on Applied Superconductivity, vol. 25, pp. 1–4, aug 2015.

[106] V. S. Zotev, A. N. Matlachov, P. L. Volegov, H. J. Sandin, M. A. Espy, J. C. Mosher, A. V. Urbaitis, S. G. Newman, and R. H. Kraus, "Multi-sensor system for simultaneous ultra-low-field MRI and MEG," International Congress Series, vol. 1300, pp. 631–634, jun 2007.

[107] V. S. Zotev, A. N. Matlashov, P. L. Volegov, I. M. Savukov, M. A. Espy, J. C. Mosher, J. J. Gomez, and R. H. Kraus, "Microtesla MRI of the human brain combined with MEG," Journal of Magnetic Resonance, vol. 194, pp. 115–120, sep 2008.

[108] P. T. Vesanen, J. O. Nieminen, K. C. J. Zevenhoven, J. Dabek, L. T. Parkkonen, A. V. Zhdanov, J. Luomahaara, J. Hassel, J. Penttilä, J. Simola, A. I. Ahonen, J. P. Mäkelä, and R. J. Ilmoniemi, "Hybrid ultra-low-field MRI and magnetoencephalography system based on a commercial whole-head neuromagnetometer," Magnetic Resonance in Medicine, vol. 69, pp. 1795–1804, jul 2013.

[109] M. Espy, A. Matlashov, and P. Volegov, "SQUID-detected ultra-low field MRI," Journal of Magnetic Resonance, vol. 229, pp. 127–141, apr 2013.

[110] M. Mößle, S.-I. Han, W. R. Myers, S.-K. Lee, N. Kelso, M. Hatridge, A. Pines, and J. Clarke, "SQUID-detected microtesla MRI in the presence of metal," Journal of Magnetic Resonance, vol. 179, no. 1, pp. 146–151, 2006.

[111] R. H. Kraus, P. Volegov, A. N. Matlashov, and M. Espy, "Toward direct neuronal current imaging by resonant mechanisms at ultra-low field," Neuroimage, vol. 39, pp. 310–317, 2007.

[112] M. Burghoff, H.-H. Albrecht, S. Hartwig, I. Hilschenz, R. Körber, N. Höfner, H.-J. Scheer, J. Voigt, L. Trahms, and G. Curio, "On the feasibility of neurocurrent imaging by low-field nuclear magnetic resonance," Applied Physics Letters, vol. 96, p. 233701, jun 2010.

[113] R. Körber, J. O. Nieminen, N. Höfner, V. Jazbinšek, H.-J. Scheer, K. Kim, and M. Burghoff, "An advanced phantom study assessing the feasibility of neuronal current imaging by ultra-low-field NMR," Journal of Magnetic Resonance, vol. 237, pp. 182–190, dec 2013.

[114] N. Höfner, H.-H. Albrecht, A. M. Cassará, G. Curio, S. Hartwig, J. Haueisen, I. Hilschenz, R. Körber, S. Martens, H.-J. Scheer, J. Voigt, L. Trahms, and M. Burghoff, "Are brain currents detectable by means of low-field NMR? A phantom study," Magnetic Resonance Imaging, vol. 29, pp. 1365–1373, 2011.

[115] N. Höfner, R. Körber, and M. Burghoff, "Towards direct neuronal current imaging via ultra-low-field mr," in PROCEEDINGS OF THE WORKSHOP BIOSIGNAL PROCESSING 2016, APRIL 7TH-8TH, 2016, BERLIN, GERMANY, 2016.

[116] S. Ogawa, T. M. Lee, A. R. Kay, and D. W. Tank, "Brain magnetic resonance imaging with contrast dependent on blood oxygenation.," Proceedings of the National Academy of Sciences, vol. 87, pp. 9868–9872, dec 1990.

[117] J. Clarke and A. I. Braginski, The SQUID Handbook, vol. 1. Wiley Online Library, 2004.

[118] J. Clarke and A. I. Braginski, eds., The SQUID Handbook, vol. 2. Wiley, aug 2006.

[119] R. L. Fagaly, "Superconducting quantum interference device instruments and applications," Review of Scientific Instruments, vol. 77, p. 101101, oct 2006.

[120] D. Drung, C. Assmann, J. Beyer, A. Kirste, M. Peters, F. Ruede, and T. Schurig, "Highly sensitive and easy-to-use SQUID sensors," Applied Superconductivity, IEEE Transactions on, vol. 17, pp. 699–704, jun 2007.

[121] R. Körber, "Ultra-sensitive SQUID instrumentation for MEG and NCI by ULF MRI," in EMBEC & NBC 2017, pp. 795–798, Springer Singapore, jun 2017.

[122] K. C. J. Zevenhoven, A. J. Mäkinen, and R. J. Ilmoniemi, "Superconducting receiver arrays for magnetic resonance imaging," Biomedical Physics & Engineering Express, vol. 6, p. 015016, jan 2020.

[123] A. Indahlastari, M. Chauhan, and R. J. Sadleir, "Benchmarking transcranial electrical stimulation finite element models: a comparison study," Journal of Neural Engineering, vol. 16, p. 026019, feb 2019.

[124] P. C. Miranda, M. Lomarev, and M. Hallett, "Modeling the current distribution during transcranial direct current stimulation," Clinical Neurophysiology, vol. 117, pp. 1623–1629, jul 2006.

[125] A. K. Kasinadhuni, A. Indahlastari, M. Chauhan, M. Schär, T. H. Mareci, and R. J. Sadleir, "Imaging of current flow in the human head during transcranial electrical therapy," Brain Stimulation, vol. 10, pp. 764–772, jul 2017.

[126] C. Göksu, L. G. Hanson, H. R. Siebner, P. Ehses, K. Scheffler, and A. Thielscher, "Human in-vivo brain magnetic resonance current density imaging (MRCDI)," NeuroImage, vol. 171, pp. 26–39, may 2018.

[127] P.-O. Löwdin, "On the non-orthogonality problem connected with the use of atomic wave functions in the theory of molecules and crystals," The Journal of Chemical Physics, vol. 18, pp. 365–375, mar 1950.

[128] J. G. Aiken, J. A. Erdos, and J. A. Goldstein, "On Löwdin orthogonalization," International Journal of Quantum Chemistry, vol. 18, pp. 1101–1108, oct 1980.

[129] R. N. Annavarapu, "Singular value decomposition and the centrality of Löwdin orthogonalizations," American Journal of Computational and Applied Mathematics, vol. 3, no. 1, pp. 33–35, 2013.

[130] B. D. Storey, "Numerical methods for differential equations." `http://faculty.olin.edu/bstorey/Notes/DiffEq.pdf`, 2003.

[131] K. C. J. Zevenhoven and S. Alanko, "Ultra-low-noise amplifier for ultra-low-field MRI main field and gradients," Journal of Physics: Conference Series, vol. 507, p. 042050, may 2014.

[132] I. Hilschenz, R. Körber, H.-J. Scheer, T. Fedele, H.-H. Albrecht, A. M. Cassará, S. Hartwig, L. Trahms, J. Haase, and M. Burghoff, "Magnetic resonance imaging at frequencies below 1 kHz," Magnetic Resonance Imaging, vol. 31, pp. 171–177, feb 2013.

[133] R. Körber, J.-H. Storm, H. Seton, J. P. Mäkelä, R. Paetau, L. Parkkonen, C. Pfeiffer, B. Riaz, J. F. Schneiderman, H. Dong, S. min Hwang, L. You, B. Inglis, J. Clarke, M. A. Espy, R. J. Ilmoniemi, P. E. Magnelind, A. N. Matlashov, J. O. Nieminen, P. L. Volegov, K. C. J. Zevenhoven, N. Höfner, M. Burghoff, K. Enpuku, S. Y. Yang, J.-J. Chieh, J. Knuutila, P. Laine, and J. Nenonen, "SQUIDs in biomagnetism: a roadmap towards improved healthcare," Superconductor Science and Technology, vol. 29, p. 113001, sep 2016.

[134] J. H. Dellinger, "The temperature coefficient of resistance of copper," Bulletin of the Bureau of Standards, vol. 7, p. 71, feb 1911.

[135] "Single-stage current sensors, magnicon GbR, Barkhausenweg 11, 22339 Hamburg, Germany; http://www.magnicon.com." See http://http://www.magnicon.com/squid-sensors/single-stage-current-sensors/ for description of electronics and data sheets.

[136] H. C. Seton, J. M. S. Hutchison, and D. M. Bussel, "Liquid helium cryostat for SQUID-based MRI receivers," Cryogenics, vol. 45, pp. 348–355, may 2005.

[137] T. Fedele, H. J. Scheer, M. Burghoff, G. Curio, and R. Körber, "Ultra-low-noise EEG/MEG systems enable bimodal non-invasive detection of spike-like human somatosensory evoked responses at 1 kHz," Physiological Measurement, vol. 36, pp. 357–368, jan 2015.

[138] J. Bork, H. D. Hahlbohm, R. Klein, A. Schnabel, et al., "The 8-layered magnetically shielded room of the PTB: Design and construction," in Biomag2000, Proc. 12th Int. Conf. on Biomagnetism, pp. 970–73, Espoo, Finland, 2001.

[139] M. Schmelz, V. Zakosarenko, T. Schönau, S. Anders, J. Kunert, M. Meyer, H.-G. Meyer, and R. Stolz, "A new family of field–stable and highly sensitive SQUID current sensors based on sub–micrometer cross-type Josephson junctions," Superconductor Science and Technology, vol. 30, no. 7, p. 074010, 2017.

[140] J. Luomahaara, M. Kiviranta, L. Gronberg, K. C. J. Zevenhoven, and P. Laine, "Unshielded SQUID sensors for ultra-low-field magnetic resonance imaging," IEEE Transactions on Applied Superconductivity, vol. 28, pp. 1–4, jun 2018.

[141] J.-H. Storm, O. Kieler, and R. Körber, "Towards ultrasensitive SQUIDs based on submicrometer-sized Josephson junctions," IEEE Transactions on Applied Superconductivity, vol. 30, pp. 1–5, oct 2020.

[142] I. Pykett, B. Rosen, F. Buonanno, and T. Brady, "Measurements of spin–lattice relaxation times in nuclear magnetic resonance imaging," Physics in Medicine & Biology, vol. 28, pp. 723–729, jun 1983.

[143] A. Hunold, D. Güllmar, and J. Haueisen, "CT dataset of a human head." `https://zenodo.org/record/3374839#.XXZNtHtCSUk`, 2019.

[144] R. Machts, A. Hunold, C. Drebenstedt, M. Rock, C. Leu, and J. Haueisen, "Measurement and analysis of partial lightning currents in a head phantom," PLOS ONE, vol. 14, sep 2019.

[145] K. T. Block, M. Uecker, and J. Frahm, "Suppression of MRI truncation artifacts using total variation constrained data extrapolation," International Journal of Biomedical Imaging, vol. 2008, pp. 1–8, 2008.

[146] V. S. Zotev, P. L. Volegov, A. N. Matlashov, M. A. Espy, J. C. Mosher, and R. H. Kraus, "Parallel MRI at microtesla fields," Journal of Magnetic Resonance, vol. 192, pp. 197–208, jun 2008.

[147] R. A. Schill, "General relation for the vector magnetic field of a circular current loop: A closer look," IEEE Transactions on Magnetics, vol. 39, pp. 961–967, mar 2003.

[148] J. D. Hanson and S. P. Hirshman, "Compact expressions for the Biot–Savart fields of a filamentary segment," Physics of Plasmas, vol. 9, pp. 4410–4412, oct 2002.

Appendix A

Additional material for the ULF-MRI setup

A.1 A potential-free and bipolar relay

All switching circuits presented in this thesis, are based on a potential-free relay, illustrated in figure A.1. Depending on the application, either two serial MOSFETs or IGBTs are set in opposite reverse direction, allowing bipolar current application (figure A.1 shows the relay equipped with MOSFETs). The relay disrupts the connection between circuit points A and B on 5-V-TTL-level input. Here, the non-inverting

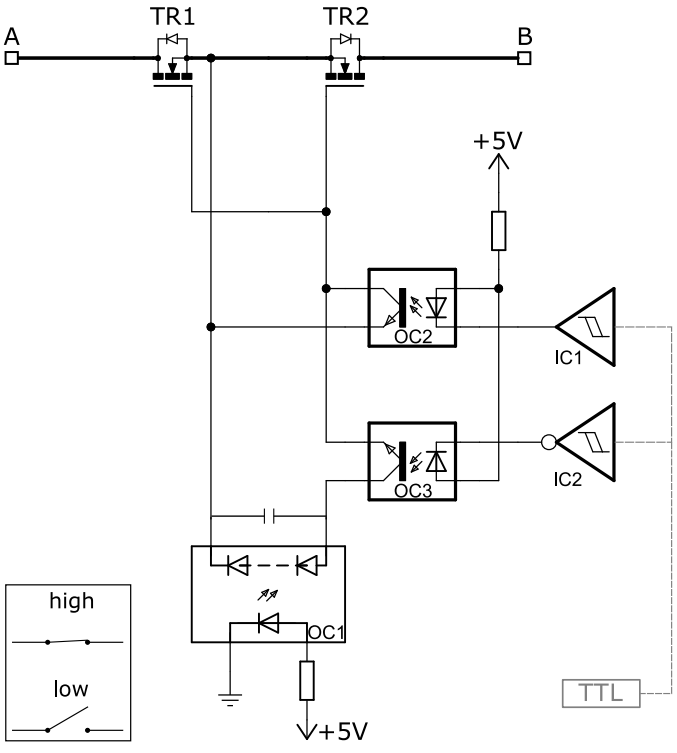

Figure A.1: Potential free relay, based on MOSFETs.

Schmitt-Trigger IC1 passes the 5 V to opto coupler OC2, shortening source and gate of the MOSFETs (or emitter and gate for IGBTs). Simultaneously, the inverting Schmitt-Trigger IC2 passes 0 V to OC3, which disconnects the gate-to-source bias, driven by photo coupler OC1. As a result, TR1 and TR2 are turned off, meaning there is no conduction between drain and source (or collector and emitter). Exchanging IC1 and IC2 provides a similar relay working at low-level operation. The potential-free design has the benefit of electrical isolation from the signal input, ensuring a low-noise operation of the circuit.

A.2 Checking the orthogonality of the guiding fields

In order to check, if the three-axis coil setup designed by Hilschenz meets the orthogonality requirements for zCDI, the field orientation and strength was measured. The nominal geometry of the coils is given in table A.1. A grid plate was developed that enabled to move a three-axis fluxgate (Mag-03MS from Bartington) in defined positions and orientations inside the coil system. The grid spaces matched the nominal distances between the fluxgate sensors for x-, y-, and z-direction, allowing vector field measurements for each grid position. In total, $3 \times 9 \times 3$ (x, y, and z) measurements were taken in a FOV of $(120 \times 120 \times 120)$ mm^3. A 5 s long sinusoidal 22 Hz current was applied to each coil separately, where the field was measured by the fluxgate.

The amplitudes were derived from a mean amplitude spectrum at 22 Hz, using a 1 s long *Hanning* windows with 0.5 s overlap. Figure A.2 shows the cubic FOV inside the three-axis coil system (left) and the FOV containing the field measurements in a zoom-in (right). Subsequently, the closest orthogonalization to the vector space defined by $\boldsymbol{B}(x\text{-coil})$, $\boldsymbol{B}(y\text{-coil})$, and $\boldsymbol{B}(z\text{-coil})$ at each grid point was derived by *Löwdin's*

Table A.1: Nominal parameters of the three-axis coil system.

Coil	∅ (mm)	d (mm)	Windings per coil arm [layers, rows]	Resistance (Ω)	Inductance (mH)	B/I in center (μT/A)
x-coil	947	472	[5, 5]	14.4	4.9	47.39
y-coil	1147	572	[6, 6]	24.3	12	56.36
z-coil	1047	522	[6, 6]	22	11	61.73

∅ – diameter; d – distance between coil arms;
B/I – field-to-current ratio

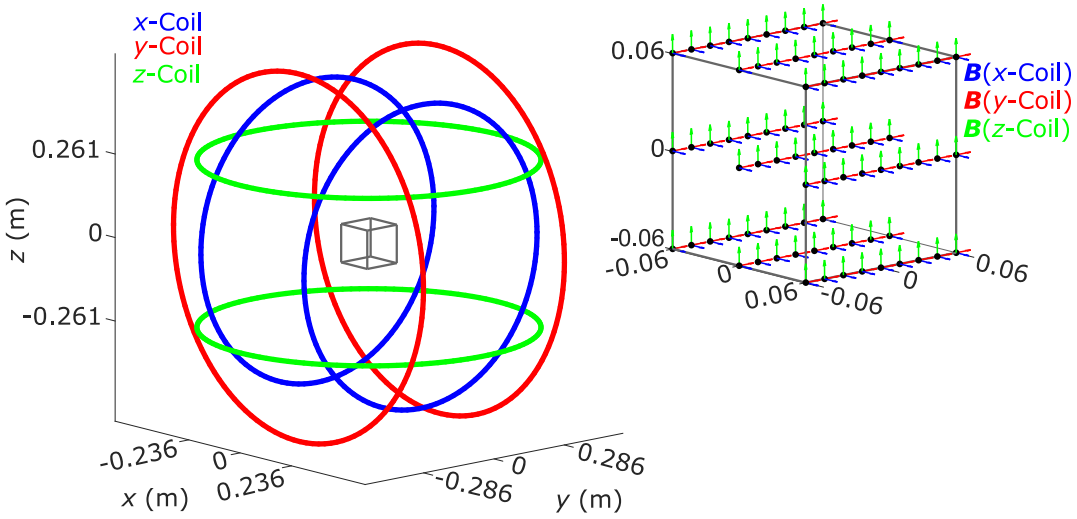

Figure A.2: Fluxgate measurement setup to estimate the orthogonality of the three-axis coil system. The cubic FOV inside the coil system is shown on the left and the FOV containing the field measurements is given on the right.

transformation (compare equation (3.13)). The distributions of misalignment, between the measured and the orthogonalized fields are displayed in figure A.3 in degree. These values do not include measurement uncertainties. Due to the large number of averages, measurement noise is assumed negligible. According to the manual, each sensor of the fluxgate has an alignment uncertainty of $\theta = \pm\ 0.1° = 1.745$ mrad and a calibration uncertainty regarding the amplitude of $\pm\ 0.5\%$. Using a small-angle approximation, the alignment uncertainty can be included by $\cos(\theta) \approx 1 - \theta^2/2$ in the direction of the field component and $\sin(\theta) \approx \theta$ in the direction perpendicular to the component. Table A.2 lists the measured field values for the central grid point, accompanied by the

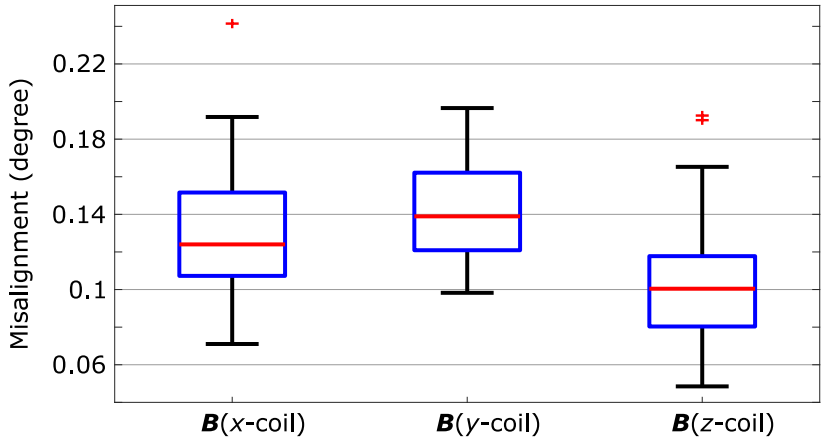

Figure A.3: Estimated orthogonality uncertainty of the three-axis coil system. The distributions of misalignment, between the measured and orthogonalized fields are in degree.

Table A.2: Fluxgate measurements at the center point of the three-axis coils system.

Coil	B/I measured in center X, Y, Z	Uncertainty due to misalignment sensor (< 0.1°) X, Y, Z	Total uncertainty including scaling error sensor (<0.5%) X, Y, Z
x-coil	48.136	±0.93 (nT/A)	±0.242 (μT/A)
	-0.114 μT/A	±0.085 μT/A	±0.086 μT/A
	0.374 μT/A	±0.084 μT/A	±0.086 μT/A
y-coil	0.318 μT/A	±0.1 μT/A	±0.1 μT/A
	57.352 μT/A	±0.96 nT/A	±0.288 μT/A
	-0.18 μT/A	±0.1 μT/A	±0.1 μT/A
z-coil	-0.649 μT/A	±0.11 μT/A	±0.11 μT/A
	0.025 μT/A	±0.11 μT/A	±0.11 μT/A
	63.64 μT/A	±1.3 nT/A	±0.319 μT/A

B/I – field-to-current ratio

uncertainty due to sensor misalignment and the total uncertainty including calibration. The calibration error adds negligible to the estimation of angles in the field measurements. The misalignment of the sensors, on the other hand, should be accounted for. In conclusion, the distributions of misalignment in figure A.3 need to be corrected by ± 0.1°. In the worst case, this results in a total sum of error angles in the vector space [$\boldsymbol{B}$(x-coil), $\boldsymbol{B}$(y-coil), $\boldsymbol{B}$(z-coil)] of approximately 0.9°, corresponding to an error field of 0.59 nT.

In conclusion, the coil system by Hilschenz fulfills the orthogonality requirements for zCDI using adiabatic turn off for manipulation of the magnetization orientation. The reconstruction uncertainty due to misalignment of the coil system is expected well below 1 nT and poses no risk for phase wrapping. Due to the systematic character of the misalignment uncertainty, full compensation of the reconstruction error, by means of background field subtraction and orthogonalization, is expected.

A.3 Estimation of the dewar's warm-cold distance

The SQUID probe is operated inside a lHe dewar. The warm-cold distance, i.e., the distance between the sensor loop and the outside of the flat bottom dewar could be measured using mutual inductance between a precisely positioned, single-turn excita-

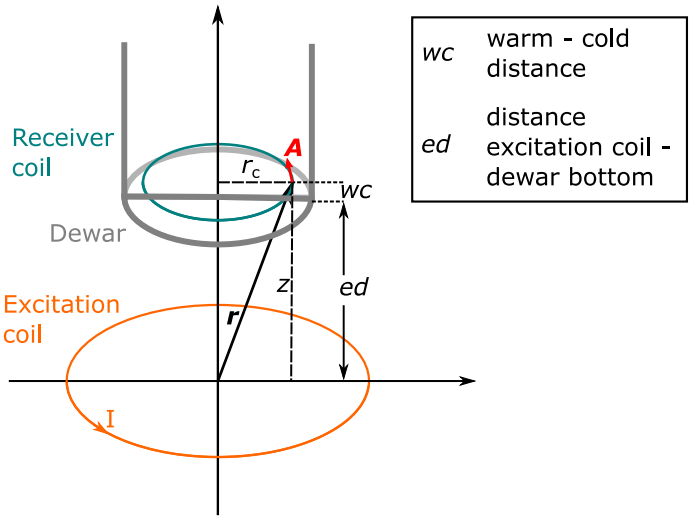

Figure A.4: Geometry for the warm–cold distance estimation. Measurements of $\varphi_{s,c}$ in the receiver coil for varying heights ed of the excitation coil allow the extraction of the warm cold distance.

tion coil, and the sensor loop. The coil was driven with an alternating current, where the measured amplitude spectrum at varying heights of the coil, relative to the dewar bottom, was related to flux through the sensor loop. This enabled fitting a model to the data to estimate the warm-cold-distance. Since both, excitation coil and receiver coil are centered collinearly on z, the magnetic vector potential $\boldsymbol{A}$, derived by equation (D.1), can be used to calculate the flux through the receiver coil $\Phi_{s,c}$, according to equation (2.36):

$$\Phi_{s,c} = \oint \boldsymbol{A} d\boldsymbol{l} = A_\varphi 2\pi a. \tag{A.1}$$

Here, a is the radius of the receiver coil and A_φ is the azimuth component of $\boldsymbol{A}$. Since the geometry is radially symmetric and the coil diameters are fixed, the radial component is constant and z is the only fitting parameter, yielding a minimization problem:

$$\min_z = ||\Phi_{s,c}(z) - \Phi_{s,m}(z)||_2^2. \tag{A.2}$$

Here, $\Phi_{s,m}$ is the measured flux and $z = z_{ed+wc}$, as explained in figure A.4.

Figure A.4 shows the geometry for the example of a magnetometer pick-up loop. The warm–cold distance was fit to 12.9 mm at 4.2 K (helium level at approximately 90%). It should be noted that the warm-cold distance might vary with the helium level, according to the thermal expansion of the dewar material and the SQUID probe.

A.4 Timings in zCDI

A sequence diagram of the entire zCDI sequence showing coil currents (I), control signals from the analogue outputs (AO), and TTL control levels for the decouplers and switches is given in figure A.5.

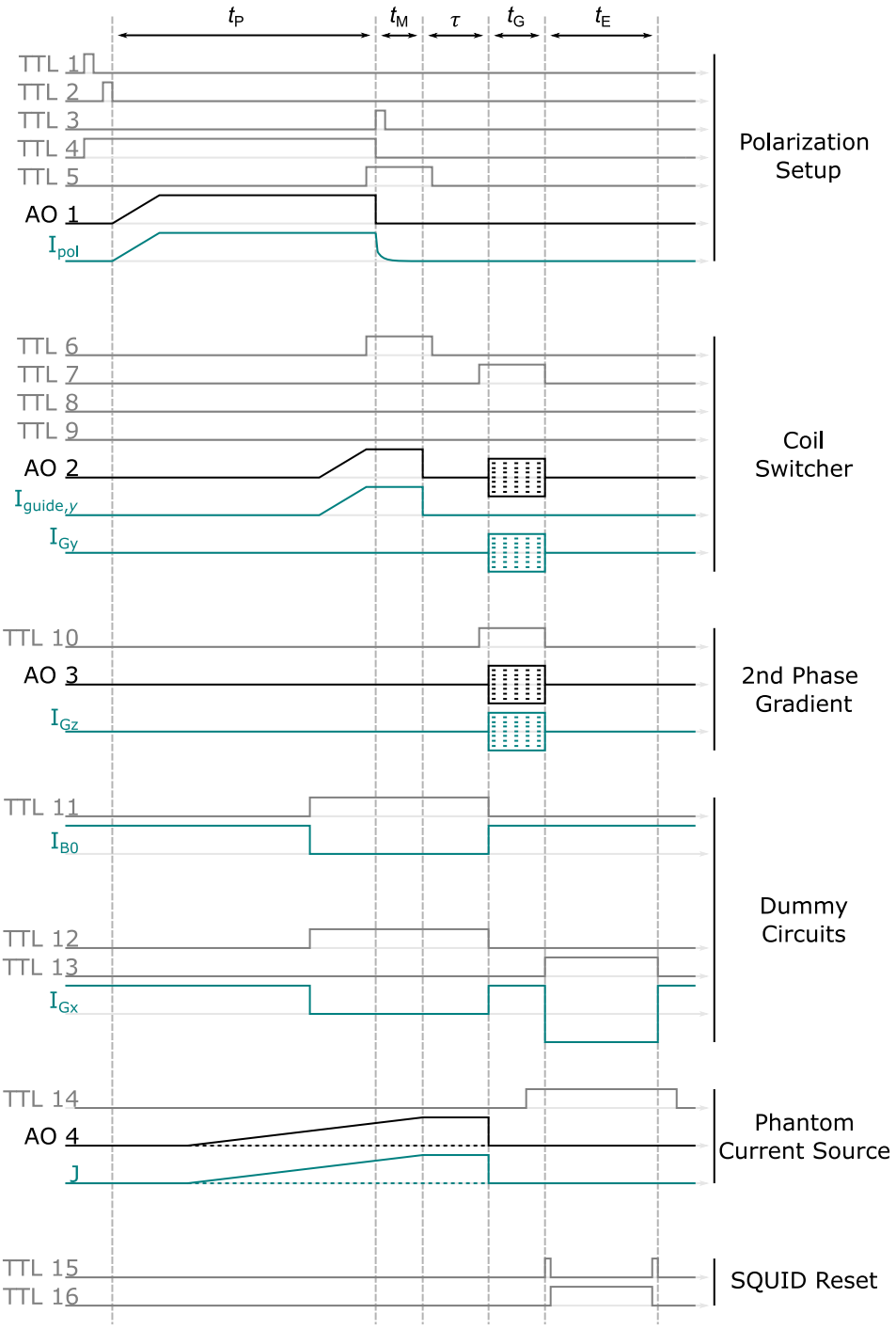

Figure A.5: Timing for the zCDI sequence. Please compare the circuit sketches for polarization setup (figure 4.4), coil switcher (figure 4.8), dummy circuits (figure 4.9), and phantom current source (figure 5.5).

Appendix B

Simulation of the stray fields of the electrode wires

To investigate the influence of the stray fields from the leads connecting the electrodes in the phantom experiments conducted in 5.2.5, the experiment with Phantom 3 was simulated. Therefore, the voltage distribution inside the phantom was derived from a finite difference method using a successive approximation with a tolerance-based stop criterion. The electrode surfaces had fixed potentials, according to the *Drichlet* condition (compare section 2.1) and the phantom boundaries were set to *Neumann condition*. In a defined 3-dimensional grid with 0.25 mm grid spaces the potential at each grid point (x,y,z) was successively adjusted using a seven-point star:

$$\begin{aligned} &U(x,y,z) = \\ &\frac{1}{6}\left[U(x-1,y,z) + U(x+1,y,z) + ... + U(x,y,z+1)\right]. \end{aligned} \tag{B.1}$$

The stop criterion was fulfilled when $\sqrt{\sum U(i)^2} - \sqrt{\sum U(i-1)^2}$, with i being the iteration step, was below a defined tolerance. The vector field $\boldsymbol{E}$ was calculated from the gradient field on $\boldsymbol{U}$ according to equation (2.10). A conversion to $\boldsymbol{J}$ was achieved by scaling the vectors to the total applied current of 2 mA. Finally, $\boldsymbol{B}_\mathrm{J}$ was estimated using the *Biot Savard* formula for volume elements

$$\boldsymbol{B}(\boldsymbol{r}) = \frac{\mu_0}{4\pi}\int_V \frac{\boldsymbol{J}(\boldsymbol{r}') \times (\boldsymbol{r} - \boldsymbol{r}')}{|\boldsymbol{r} - \boldsymbol{r}'|^3} dV, \tag{B.2}$$

at the discrete points i:

$$\boldsymbol{B}(\boldsymbol{r}) = \frac{\mu_0}{4\pi} v^3 \sum_i \frac{\boldsymbol{J}(\boldsymbol{r}_i) \times (\boldsymbol{r} - \boldsymbol{r}_i)}{|\boldsymbol{r} - \boldsymbol{r}_i|^3}. \tag{B.3}$$

The result is displayed in figure B.1(b) for a slice centrally through the phantom (compare the overview in panel a). It is visible that the rotation of the $\boldsymbol{B}$-field is symmetric inside the phantom.

In addition, the magnetic stray field from the leads connecting the electrodes was calculated using the *Biot Savard* formula for line elements (compare equation (D.6)). The leads were combined to a twisted pair about 22 mm below the phantom. The result, as displayed in figure B.1(c) shows that the stray field $\boldsymbol{B}_{\text{Leads}}$ is on the order of $\boldsymbol{B}_{\text{J}}$ and that the superposition of the two fields, as shown in panel d), nicely resembles the results of the phantom experiment visualized in figure 5.14(b). The current density reconstruction, displayed in figure 5.14(c) was not affected by the field of the leads as this is curl-free.

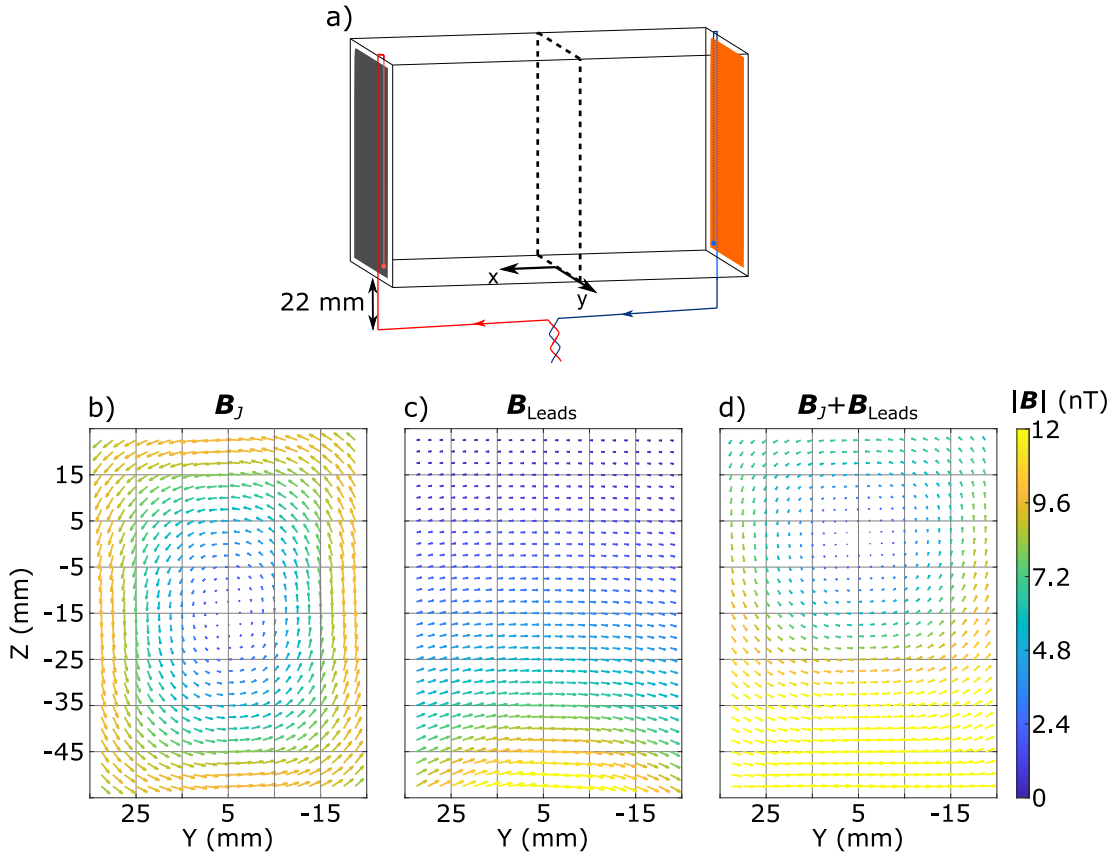

Figure B.1: The influence of stray fields by the electrode leads on $\boldsymbol{B}_{\text{J}}$. The figure shows a the simulated magnetic field in a slice centrally through the phantom (a) for $\boldsymbol{B}_{\text{J}}$ only (b), $\boldsymbol{B}_{\text{Leads}}$ only (c), and a superposition of $\boldsymbol{B}_{\text{J}}$ and $\boldsymbol{B}_{\text{Leads}}$ (d). Note: For reasons of illustration, axes were adjusted to match figure 5.14 approximately, and colorbar and arrow lengths were limited to 12 nT.

Appendix C

Noise in the rotation matrix estimate

The methods and results in this section have been previously published in the supplementary material to [75]. The text and equations are extracted from that publication. This section is mainly based on ideas of my fellow colleague Antti J. Mäkinen from Aalto University, Helsinky. For the sake of completeness it is included in this thesis.

A vector of the real and imaginary parts of zero-field-encoded raw voxel data could be defined as

$$\boldsymbol{a} = [\mathrm{Re}[v_x], \mathrm{Re}[v_y], \mathrm{Re}[v_z]]^\top, \text{and}$$
$$\boldsymbol{b} = [\mathrm{Im}[v_x], \mathrm{Im}[v_y], \mathrm{Im}[v_z]]^\top,$$

respectively, where v_x, v_y , and v_z are the voxel values for x-, y-, and z-directional starting magnetization. Now, the whole data can be expressed as a combination of these as $\boldsymbol{a} + i\boldsymbol{b}$ which is a 3D vector with complex elements. Applying the same phase correction obtained from a reference image for each element, one can write the data as $(\boldsymbol{a} + i\boldsymbol{b})e^{-i\delta}$. Note that applying the phase correction does not change the noise distribution in the real and imaginary parts when they both have an equal amount of noise.

The phase-corrected zero-field-encoded data can be converted to a rotation matrix by normalizing the rows corresponding to $\boldsymbol{a}$ and $\boldsymbol{b}$. Apart from noise, vectors $\boldsymbol{a}$ and $\boldsymbol{b}$ should have the same norm, giving rise to the approximation $|\boldsymbol{a}| \approx |\boldsymbol{b}| \approx |u_0|$, where u_0 is the voxel value in a (ideal) reference image. Thus, one can normalize the imaginary and real parts with a common factor $(\boldsymbol{a} + i\boldsymbol{b})e^{-i\delta}/|u_0|$. The elements of the third and second row of the rotation matrix can now be read from the real and imaginary parts of this quantity and the first row could be derived as a cross product of the normalized rows.

To derive the effect of noise in the matrix elements, it is assumed that v_x, v_y, and v_z are all contaminated by complex Gaussian noise. If the normalization and reference phase were noise-free, the standard deviation of the elements of the rotation matrix would read

$$\sigma_{\mathbf{\Phi},0} = \frac{1}{\sqrt{2}\,\mathrm{SNR}}\,,$$

where SNR is defined as in (6.7). Since the noise in the elements is uncorrelated, the noise covariance matrices for both of the rows can be written as $\sigma^2_{\mathbf{\Phi},0}\mathbf{I}$.

Next, it is studied how the noise in the reference phase and normalization affect the noise covariance matrix of the third row corresponding to $\boldsymbol{a}$ when $\delta = 0$. Adding noisy reference phase increases noise in $\boldsymbol{a}$ in the direction of $\boldsymbol{b}$ as it can be considered as a small rotation in the plane spanned by $\boldsymbol{a}$ and $\boldsymbol{b}$. In the limit of high SNR, the standard deviation of the phase noise $\Delta\delta$ is approximately $1/(\sqrt{2}\,\mathrm{SNR})$. The noise in the phase factor can be expanded as $e^{i\Delta\delta} \approx 1 + i\Delta\delta$, and in the limit of a small perturbation in the noise in $\boldsymbol{a}$ would be $\Delta\delta\boldsymbol{b}$, giving $|\boldsymbol{b}|^2/(\sqrt{2}\,\mathrm{SNR})^2 \approx |u_0|^2/(\sqrt{2}\,\mathrm{SNR})^2$ extra variance in the direction of $\boldsymbol{b}$. The noise covariance of the non-normalized but phase-reference-noise-affected third row would be approximately $|u_0|^2\sigma^2_{\mathbf{\Phi},0}(\mathbf{I} + \mathbf{P_b})$, where $\mathbf{P}_{\boldsymbol{b}} = \boldsymbol{b}_0\boldsymbol{b}_0^\top/|\boldsymbol{b}_0|^2$, where $\boldsymbol{b}_0$ is the expected value of the vector $\boldsymbol{b}$.

The effect of noise in the normalization constant can be analyzed by interpreting the noise $\boldsymbol{\epsilon}$ in the vector elements of $\boldsymbol{a} = \mathrm{E}[\boldsymbol{a}] + \boldsymbol{\epsilon} = \boldsymbol{a}_0 + \boldsymbol{\epsilon}$ also as a small perturbation

$$\frac{1}{|\boldsymbol{a}|} \approx \frac{1}{|\boldsymbol{a}_0|}\left(1 - \frac{\boldsymbol{a}_0^\top\boldsymbol{\epsilon}}{|\boldsymbol{a}_0|^2}\right),$$

where only the first-order term in $\boldsymbol{\epsilon}$ is considered. In this case, $\boldsymbol{\epsilon}$ will also contain the effect of noisy phase referencing. Normalizing the third row then gives approximately

$$\begin{aligned}
\frac{\boldsymbol{a}}{|\boldsymbol{a}|} &\approx \frac{\boldsymbol{a}_0}{|\boldsymbol{a}_0|} + \frac{\boldsymbol{\epsilon}}{|\boldsymbol{a}_0|} - \frac{\boldsymbol{a}_0^\top\boldsymbol{\epsilon}}{|\boldsymbol{a}_0|^2}\frac{\boldsymbol{a}_0}{|\boldsymbol{a}_0|} \\
&= \frac{\boldsymbol{a}_0}{|\boldsymbol{a}_0|} + \left(\mathbf{I} - \frac{\boldsymbol{a}_0\boldsymbol{a}_0^\top}{|\boldsymbol{a}_0|^2}\right)\frac{\boldsymbol{\epsilon}}{|\boldsymbol{a}_0|} \\
&= \frac{\boldsymbol{a}_0}{|\boldsymbol{a}_0|} + (\mathbf{I} - \mathbf{P}_{\boldsymbol{a}})\,\frac{\boldsymbol{\epsilon}}{|\boldsymbol{a}_0|}\,,
\end{aligned}$$

where the matrix $\mathbf{I} - \mathbf{P}_{\boldsymbol{a}} = \mathbf{I} - \boldsymbol{a}_0\boldsymbol{a}_0^\top/|\boldsymbol{a}_0|^2$ projects out any component in the direction of $\boldsymbol{a}_0$, *i.e.*, $(\mathbf{I} - \mathbf{P}_{\boldsymbol{a}})\boldsymbol{a}_0 = 0$, but leaves components orthogonal to $\boldsymbol{a}_0$ unaffected. The noise is thus the same as in the case of noiseless normalization but the noise contribution in the direction of $\boldsymbol{a}_0$ is canceled. For example, when $\boldsymbol{a}$ is roughly y directional, the noise in the direction of y is removed by the normalization.

Normalizing the row exactly to unit norm modifies the noise approximately with the linear transformation $|\boldsymbol{a}_0|^{-1}(\mathbf{I}-\mathbf{P}_{\boldsymbol{a}}) \approx |u_0|^{-1}(\mathbf{I}-\mathbf{P}_{\boldsymbol{a}})$ giving a new covariance matrix

$$(\mathbf{I}-\mathbf{P}_{\boldsymbol{a}})\sigma^2_{\boldsymbol{\Phi},0}(\mathbf{I}+\mathbf{P}_{\boldsymbol{b}})(\mathbf{I}-\mathbf{P}_{\boldsymbol{a}}) = \sigma^2_{\boldsymbol{\Phi},0}(\mathbf{I}-\mathbf{P}_{\boldsymbol{a}}+\mathbf{P}_{\boldsymbol{b}})\,,$$

as $\mathbf{P}_{\boldsymbol{a}}\mathbf{P}_{\boldsymbol{b}} = 0$ because $\boldsymbol{a}_0$ and $\boldsymbol{b_0}$ are orthogonal and $\mathbf{P}^2_{\boldsymbol{a}} = \mathbf{P}_{\boldsymbol{a}}$ because the operator is a projection.

The noise covariance can be diagonalized in the row basis of the (noiseless) rotation matrix $\boldsymbol{\Phi}_0$,

$$\sigma^2_{\boldsymbol{\Phi},0}(\mathbf{I}-\mathbf{P}_{\boldsymbol{a}}+\mathbf{P}_{\boldsymbol{b}}) = \boldsymbol{\Phi}_0^\top \begin{bmatrix} \sigma^2_{\boldsymbol{\Phi},0} & 0 & 0 \\ 0 & 2\sigma^2_{\boldsymbol{\Phi},0} & 0 \\ 0 & 0 & 0 \end{bmatrix} \boldsymbol{\Phi}_0\,,$$

i.e., there is zero variance in the direction of $\boldsymbol{a_0}$, double variance in the direction of $\boldsymbol{b_0}$ and non-modified variance in the direction of the first row.

Similar analysis can be made for the second row of the rotation matrix estimate giving the following noise covariance:

$$\sigma^2_{\boldsymbol{\Phi},0}(\mathbf{I}+\mathbf{P}_{\boldsymbol{a}}-\mathbf{P}_{\boldsymbol{b}}) = \boldsymbol{\Phi}_0^\top \begin{bmatrix} \sigma^2_{\boldsymbol{\Phi},0} & 0 & 0 \\ 0 & 0 & 0 \\ 0 & 0 & 2\sigma^2_{\boldsymbol{\Phi},0} \end{bmatrix} \boldsymbol{\Phi}_0\,.$$

For small rotation angles, the noise in B_y and B_z is explained by the noise variance in the rotation matrix. To explain the noise in the estimates of the effective magnetic field component B_x, one still has to take in to account that, due to the same reference phase noise, the noise in $\Phi_{3,2}$ and $\Phi_{2,3}$ is correlated. The covariance between the elements can be derived to be $-\sigma^2_{\boldsymbol{\Phi},0}$. In consequence, the variance of $\gamma\tau B_x \approx (\Phi_{3,2}-\Phi_{2,3})/2$ becomes

$$\begin{aligned}\mathrm{Var}[\gamma\tau B_x] =& \frac{\mathrm{Var}[\Phi_{2,3}]}{4} + \frac{\mathrm{Var}[\Phi_{3,2}]}{4} \\ & - 2\frac{\mathrm{Cov}[\Phi_{3,2},\Phi_{2,3}]}{4}\,,\end{aligned}$$

which results in $3\sigma^2_{\boldsymbol{\Phi},0}/2$ corresponding to the Monte-Carlo estimate in figure 6.1(b). This analysis considers a single reconstruction of effective B_x. In bipolar reconstruction, as presented in equation (6.13), the additional noise due to the noisy phase reference cancels out.

Appendix D

The MRI simulation toolbox

D.1 Magnetic field calculations

This thesis includes several methods that involve the calculation of magnetic fields due to coils of various geometries. For example, the coupling profile to the sensor is calculated by reciprocity, where the flux at the sensor due to a magnetization source is explained by a field at the position of the magnetization source due to a current in the sensor (see section 2.2.4).

The sensor and most of the MRI coils are formed by circular loops, facilitating the use of elliptical integrals for magnetic field integration. According to the derivations presented by Schill [147], the magnetic vector potential of a circular current loop of diameter a and oriented in z can be formulated at $\boldsymbol{r} = [x, y, z]$ in a cylindrical coordinate system (r_c, φ, z) by:

$$\begin{aligned} \boldsymbol{A}(r_c, \varphi, z) &= \hat{\varphi}\boldsymbol{A}_\varphi \\ &= \frac{\mu_0 I_0}{\pi k_c}\left(\frac{a}{r_c}\right)^{1/2}\left[\left(1-\frac{k_c^2}{2}\right)K(k_c) - E(k_c)\right]\hat{\varphi}, \end{aligned} \tag{D.1}$$

where r_c is the radial component given in the Cartesian coordinate system by $\sqrt{(x-x')^2+(y-y')^2}$, with $\boldsymbol{r}' = [x', y', z']$ being the center point of the loop. $E(k_c)$ and $K(k_c)$ are the complete elliptical integral functions of the first and second kind, respectively, corresponding to

$$k_c^2 = \frac{4ar_c}{(r_c+a)^2 + (z-z_0)^2}. \tag{D.2}$$

The magnetic flux density is given by the curl $\nabla \times \boldsymbol{A}$ by

$$\begin{aligned} \boldsymbol{B}(r_c, \varphi, z) &= -\frac{d\boldsymbol{A}_\varphi}{dz}\hat{r}_c + \frac{1}{r_c}\frac{d(r_c\boldsymbol{A}_\varphi)}{dr_c} \\ &= B_{r_c}\hat{r}_c + B_z\hat{z}, \end{aligned} \tag{D.3}$$

giving rise to the axial and radial components of $\boldsymbol{B}$ per unit current I_0 by:

$$\begin{aligned} B_z(r_c,\varphi,z)/I_0 =& \frac{\mu_0}{2\pi}\frac{1}{\left[(r_c+a)^2+(z-z')^2\right]^{1/2}} \\ & \cdot\left[K(k_c)-\frac{r_c^2-a^2+(z-z')^2}{(r_c-a)^2+(z-z')^2}E(k_c)\right] \\ B_{r_c}(r_c,\varphi,z)/I_0 =& \frac{\mu_0}{2\pi}\frac{(z-z')}{r_c\left[(r_c+a)^2+(z-z')^2\right]^{1/2}} \\ & \cdot\left[-K(k_c)+\frac{r_c^2-a^2+(z-z')^2}{(r_c-a)^2+(z-z')^2}E(k_c)\right] \end{aligned} \tag{D.4}$$

Transferring back to Cartesian representation, yields the desired coupling coefficients:

$$\boldsymbol{C}(\boldsymbol{r}) = \begin{pmatrix} C_x \\ C_y \\ C_z \end{pmatrix} = \begin{pmatrix} B_x \\ B_y \\ B_z \end{pmatrix} I_0^{-1} = \begin{pmatrix} B_{r_c}(r_c,\varphi,z)(x-x')r_c^{-1} \\ B_{r_c}(r_c,\varphi,z)(y-y')r_c^{-1} \\ B_z(r_c,\varphi,z) \end{pmatrix} I_0^{-1}. \tag{D.5}$$

Please note, that the magnetization precesses in a plane perpendicular to the main field, which is why only two components, B_z and one of the components B_y or B_x, add to the coupling field.

The above presented method is computationally efficient. The complete elliptical integrals and subsequent $\boldsymbol{B}$ calculation yield two sets of equations per field point $\boldsymbol{r}$. However, it is limited to circular current loops. Arbitrary coil arrangements, such as the head-shaped polarization coil introduced in chapter 7, require to integrate over the line integral bounding the coil, numerically. An often employed method is the numerical integration of the closed loop via straight filamentary line approximation:

$$\boldsymbol{B}(\boldsymbol{r})/I_0 = \frac{\mu_0}{4\pi}\sum_{j=1}^{N_{Seg}}\int_{\boldsymbol{r}'=\boldsymbol{r}_j}^{\boldsymbol{r}_{j+1}}\frac{d\boldsymbol{r}\times(\boldsymbol{r}-\boldsymbol{r}')}{|\boldsymbol{r}-\boldsymbol{r}'|^3}. \tag{D.6}$$

Here, N_{seg} is the number of line segments that approximate the coil. A compact integration of expression (D.6) was presented by Hanson and Hirschman [148]

$$\boldsymbol{B}(\boldsymbol{r})/I_0 = \frac{\mu_0}{4\pi}\sum_{j=1}^{N_{seg}}\frac{c_j+c_{j+1}}{c_jc_{j+1}}\frac{\boldsymbol{c}_j\times\boldsymbol{c}_{j+1}}{c_jc_{j+1}+\boldsymbol{c}_j\cdot\boldsymbol{c}_{j+1}}, \tag{D.7}$$

where $\boldsymbol{c}_j = \boldsymbol{r}-\boldsymbol{r}_j$ and $c_j = |\boldsymbol{r}-\boldsymbol{r}_j|$. Zevenhoven et al. [122] showed that (D.6) exactly integrates to (D.7) and used the expression to calculate coupling fields for various receiver arrangements.

D.2 Validation measurement

For the evaluation of the simulations, a comparison with actual measurements using the PTB setup was executed. Therefore, a spherical single-compartment phantom (80 mm diameter), filled with an aqueous solution of $CuSO_4$+H_2O to tune the T_2 relaxation time to approximately 100 ms, was placed 10 mm below the dewar (nominal warm-cold distance 13 mm). The current in the polarizing coil was set to 20 A, resulting in an inhomogeneous polarizing field of approximately 25 mT. Gradients were set to give a voxel size of $(4.8 \times 4.8 \times 4.8)$ mm^3 and a field of view (FOV) of 115 mm in the phase-encoded directions y and z. The resulting time signals of the gradient echos

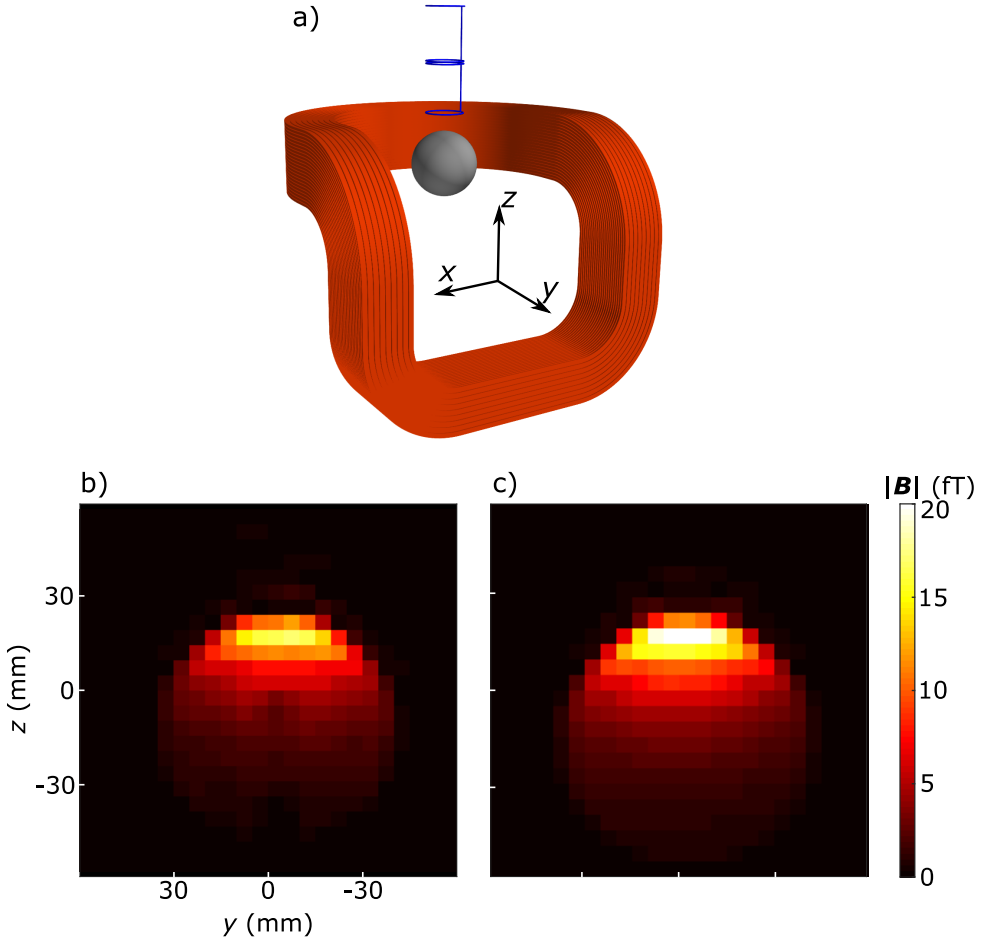

Figure D.1: Comparison of measured and simulated MRI images. (a) shows the utilized setup, including the polarizing coil (orange), the spherical phantom (gray), and the receiver coil of the sensor (blue). Central slices of reconstructed images, not corrected for the sensitivity profile, are presented for measurement (b) and simulation (c). Please note that the actual phantom contains a mount for dipolar current electrodes, that is recognisable in the central lower half of the reconstructed measurement, but was not accounted for in the simulations.

were processed to form an array of k-space data. To reduce Gibbs ringing, both the frequency- and the phase-encoding dimensions were tapered with a Tukey window (shape parameter = 0.5) and the 3D-DFT was applied to reconstruct the images. For the simulations, the sphere was approximated by a regular 1-mm spaced grid.

Figure D.1 illustrates the setup, accompanied by magnitude images of measurement and simulation. The results reveal a difference in the amplitude of measured and simulated MRI of approximately 25%, probably subject to multiple origins. A shielding coil reduces the polarizing field of the actual setup, which was not accounted for in the simulations. Also, winding errors due to the relatively complex geometry of the polarizing coil reduce the current-to-field ratio. In addition, the true warm–cold distance of the dewar could vary depending on the helium level and the phantom mount also might have inaccuracy in the millimeter range. Taking all these uncertainties into account, the simulated MRI sequence resembles the realistic conditions found in actual measurements.